BCAST

Brunel Centre for Advanced
Solidification Technology

STRAIN ENHANCED STRENGTHENING DURING THERMOMECHANICAL AGEING OF AN AUTOMOTIVE ALUMINIUM ALLOY

A thesis submitted for the degree of
Doctor of Philosophy by

Aniekanabasi Essien

Department of Mechanical and Aerospace Engineering
Supervision: Yan Huang, Chamini Mendis, Carla Barbatti, Zaidao Li
Submission Date: January 2024

Brunel University
Uxbridge, UB8 3PH
United Kingdom

Abstract

Thermomechanical treatments as a means of strengthening Al alloys have been of particular interest in recent years. Fabrication of aluminium alloys that can outperform conventional steels are especially attractive for applications in automotive industries. This study aims to gain a fundamental understanding of the effect of metal forming processes on the mechanical properties in shaped aluminium components for optimal performance in automotive applications. This thesis presents a study on the application of a novel thermomechanical process in a 6xxx series Al-Mg-Si-Cu alloy system comprised of 3 key steps: artificial preaging, cold working and artificial final ageing. A process designed to attain improved mechanical performance from the alloy, particularly strength-ductility optimisation. The current work aims to develop an optimised treatment recipe and characterise pertinent microstructural changes affording these mechanical responses. Vickers Hardness and Tensile Testing were used as the main procedures of obtaining mechanical properties. Optical Microscopy, Electron Dispersive Spectroscopy, Scanning Electron Microscopy, Electron Backscattered Diffraction and Transmission Electron Microscopy were used as analytical tools of microstructural evolution in prepared sample specimens. The understanding garnered will be applied in relevant scenarios to generate desired manufacturing induced properties.

Flat strips of 3mm in thickness were prepared through DC casting and hot extrusion followed by immediate water quenching, retaining the super saturated solid solution state (SSSS). Experimental results from hardness and tensile tests illustrate enhancements in material properties subject to the preaging treatment at 150^{o} C and 170^{o} C and the subsequent low strain deformation of 4% and 8% through either rolling or stretching. These strength increments are induced by significant increases in dislocation density resulting from the interactions with the precipitate particles formed in the preaging step, which were characterised by EBSD and TEM analysis. These precipitate-dislocation complexes in turn promoted heterogenous nucleation and growth of secondary phase precipitate particles in the final ageing step of the treatment.

Thermomechanical conditions in this study investigated changes in material response due to parameters such as ageing conditions and strain mode. It was found that strain mode exhibited considerable impact on the final properties of the material. Based on EBSD data, stretching, and rolling plastic deformation elicited different changes in crystallographic texture components as compared to the as-extruded material. In particular, the development of cube {001}<100> and goss {110}<001> texture components led to differences in the final mechanical properties. Further, selected preaging condition determined the degree of dislocation storage enhancement. The alloy samples preaged to a further point in the precipitation sequence exhibited a greater increase in the dislocation density than those less preaged conditions due to the development of atomic clusters, Guinier-Preston zones and β'' phase particles. Evidence also suggests that the dislocation structures formed at these varying preaging stages resulted in notably different final ageing kinetics.

Optimisation of the novel thermomechanical treatment in the study showed that preaging temperature differences also played a role in determining final mechanical properties.

Preaging at 170° C presented a greater hardening response with the optimum thermomechanical treatment recipe: an artificial preaging at 170° C for 4 hours followed by a plastic deformation of 8% stretching strain at room temperature and a final artificial ageing at 170° C for 4 hours.

The Optimal thermomechanical treatment route investigated in this research exhibited mechanical properties that were superior those achieved in other studies using similar alloys. Microstructural changes and interactions between crystallite defects discovered in this study improved the understanding of alloy strengthening through application of a thermomechanical process.

Acknowledgements

I would like to begin with giving up praise to the Almighty God for provision and good health throughout my studies, it is through God that any of this has been possible.

I would like to sincerely thank my supervisors Drs Yan Huang and Chamini Mendis for their continued support throughout my PhD study. Their excellent encouragement and supervision enabled me to pursue and achieve completion of this degree. Dr Yan Huang, I am grateful for your unwavering patience during the writing of my thesis. It is your wealth of knowledge and amicable aura that inspired me to breakthrough challenges throughout the past 4 years. I would also like to extend a tribute to Dr Chamini Mendis for continued help throughout the iterative experiments. Thank you for training me in the many techniques used in this study in ways that bolstered my understanding despite the many unforeseen obstructions that were presented. I want to express my appreciation to Brunel University London, EPSRC and Constellium SE for financial support, allowing me to focus on my studies. Many thanks to my industrial supervisors at Constellium, Drs Carla Barbatti and Zaidao Li for devoting time to attend weekly meetings and aiding in my publication. Throughout my studies, you both have been extremely gracious.

I would like to acknowledge appreciation for experimental support from my colleagues throughout my work. Special thanks to Dr Raluca Negrea for help in attaining and interpreting the results in TEM and Dr Shihao Wang for support in operating the EBSD system. I am indebted to the technical staff for training and kind help in use of the many facilities, Miss Loredana Saccone, Miss Aneta Walsh, Mr Philip Nicola, Mr Paul Krawczynski, Miss Sam Melvin, Mr Warren Lee, Mr Stephen Cook, Mr Jon Gadd, Dr Ashley Howkins, Dr Lorna Anguilano and at the rest of the Experimental Techniques Centre (ETC) staff members.

I take this opportunity to thank Dr Maaouia Souissi for kind help in my research and for comments on my work. Thank you to Dr Chrysoula Tzileroglou and Sajun Prasad Kasi for the shared work that complemented my studies.

Finally, I immensely appreciative for my family and friends who fuelled my endurance and kept my spirits high with continuous encouragements for so many years.

Table of Contents

Chapter 1. Introduction

1.1 Background

The automotive industry is facing increasing ecological and economical stresses according to (Rochet et al., 2020). Reducing the dependence on fossil fuels as well as the emission of greenhouse gasses has become of paramount importance to automotive manufacturers. Typically, and traditionally, steel alloys were/are used for most car parts in car production, but these are slowly becoming phased out for new materials, primarily for aluminium and magnesium alloys. According to (Rochet et al., 2020), this is done in order to reduce both weight and the cost of automotive components. The lesser cost of transportation of lighter materials is an additional economic benefit for automotive manufacturers.

Additional prospects for the increased demand for aluminium alloys come from the rise in production of electric vehicles, with many more entering the market sooner and faster than ever expected before (Djukanovic, 2018). In the electric vehicle industry, the greatest push apart from lowering costs is to increase the driving range of the vehicle from a full charge. To attain this augmented range for a given battery size and weight, weight reduction of the electric vehicle is the agreed to be the most determining factor. Thus, the preferred material for electric vehicles proves to be aluminium (Djukanovic, 2018).

Currently to reduce the weight of said vehicles, a combination of aluminium alloys, high strength steels, magnesium, composite materials (carbon fibre) and types of plastics have been grouped to achieve this goal. However, lightening of these automobiles must be done without the compromise of safety and performance. Vehicle structural parts must have a good balance of strength and ductility.

Aluminium alloys have been used in many vehicles, mostly in engines, in power trains and wheels, of which most are formed through cast parts and extrusions. These new aluminium alloys as well as new production and assembly methods enable significant increases in aluminium sheet use (Djukanovic, 2018).

Although aluminium is known and desired for its lightweight properties, automotive manufacturers are also interested in the high durability as well as its superior corrosion resistance (Djukanovic, 2019). Aluminium alloy manufacturers have begun research to develop aluminium alloys with even greater enhancements in strength and ductility than older aluminium alloys. This is achieved by altering volumes of the constituent elements and producing fresh mixes. This gives rise to a myriad of aluminium alloys, all with differing properties (Djukanovic, 2019). Different aluminium alloys display different mechanical/desired properties and are thus put to different uses.

Relative to the Al-Cu-Mg (2xxx series) and Al-Zn-Mg-Cu (7xxx series) alloy systems, Al-Mg-Si (6xxx series) Al Alloys possess lower strengths, narrowing their band of application in manufacturing scenarios. Mechanical performance enhancements to this alloy group are therefore of particular interest, notably, the strength-ductility compromise. A vast majority of aluminium production parts are created through metal forming techniques, which as well as shaping the final component geometry, alter the mechanical properties through strain hardening from the applied plastic deformation. Generally, the manufacturing process' effect on final material properties is not considered in determining material capabilities.

In recent years, many studies have investigated the effect of a thermomechanical process in strengthening 6xxx series alloys which comprises an ageing and work hardening step or any combination of them to further manipulate and enhance the mechanical properties of these alloys, such as strength and ductility (Ashby, 2003). The various steps can be altered as required, yielding advantageous material properties. The strain levels considered in these studies, however, are extremely high and are not relevant in a manufacturing setting, thus an understanding of more relevant strain levels allows for integration of the manufacturing process into the holistic component design of these engineering materials. Recent work by Ryen et al. and Zhong et al. displayed the preaging effect on the work hardenability of the different 6xxx series aluminium alloys where the respective preaging steps proved advantageous, demonstrated through formability tests.

Through application of these novel thermomechanical processes, unique microstructural complexes are developed consequent of the main strengthening mechanisms through which these mechanical properties are attained, namely kinetic precipitation and dislocation structure evolution. Investigating and understanding of these micron level interactions will clarify the link between these microstructural evolutions and the enhancements in mechanical properties of the 6xxx series alloys used in automotive part scenarios.

In the automotive industry, energy absorption plays a vital role in crash analysis of formed vehicular components likely to experience minor crash collision, ensuring overall safety of the component's use (Mamalis, 2008). Crashworthiness performance testing and analysis for structural parts is required before implementation in actual field (Nasiruddin, 2017) with studies by Maghami et al and Kohar et al, using rectangular thin-walled tube structures with energy absorption and mean crushing force being used as crucial crashworthiness indicators. Tests performed on samples must be quasistatic for energy absorption performance due to rate-sensitivity of aluminium alloys used, these tests are sufficient to represent the crash performance.

1.2 Research Objectives

The overarching aim of the study is to develop a thermomechanical process incorporating artificial heat treatments as well as plastic deformation that yield enhanced material properties defined by great strength to ductility compromise. The effects of artificial ageing temperatures – 150° C and 170° C and strain path – stretching, rolling and EMPT are to be understood and described. Microstructural contributions to these improved mechanical properties are to be determined using a myriad of imaging and analytical tools. All in the scope of being implemented in manufacturing processing of parts. The following research objectives provide a means through which this was accomplished.

Objective 1: to determine the conditions for thermomechanical stages, including artificial PreAging temperatures and durations, plastic deformation modes and strain levels and artificial final ageing temperatures and durations.

Objective 2: to investigate the strengthening of the Al-Mg-Si-Cu alloy through mechanical property measurement.

Objective 3: to analyse and characterize microstructural features (e.g. precipitate nucleation, dislocation densities and evolution, intermetallic phases) responsible for increased mechanical behaviour.

Objective 4: to cross reference findings between results and conclude the relevant features and intragranular interactions for obtaining enhance strength-ductility compromise.

1.3 Thesis Outline

The work is constituted of a total of 7 chapters. This Chapter 1 is Introductory. Chapter 2 covers a review of pertinent literatures in the study of thermomechanical strengthening of 6xxx series aluminium alloys. In Chapter 3, the starting material, the procedure of all experimental works and the techniques used for characterisation in this research study are described. Chapter 4 presents the results and descriptions of processing the Al-Mg-Si-Cu alloy through the determined mechanical strengthening route of specific artificial ageing and plastic deformation. These results include an in-depth characterisation of the starting material, preaging kinetics and mechanical property examinations of the various stages of the employed thermomechanical process for both 150° C and 170° C preaging conditions. Microstructural analysis of critical specimen conditions was implemented, using a multitude of technologies, including Scanning Electron Microscopy, Electron Backscattered Diffraction and Transmission Electron Microscopy. The results of these trials are analysed and discussed in Chapter 5, interpreting the preaging effect on the final material behaviour as well as the recognised dislocation-precipitate interactions. Chapter 6 summarises the study with the main conclusions reached and the suggestions for future work.

Chapter 2. Literature Review

This chapter outlines and reviews the current body of knowledge and the most recent and up to date theories of metallurgy, especially those regarding aluminium alloys. Commonly used alloys and strengthening mechanisms are described as well as the best, most conventional processing methods. A recently developed thermomechanical process is discussed and how it yields beneficial or desired results from specific alloys. The mechanical properties of these alloys are covered as well as how they can best be measured and recorded. The chapter then goes on to describe the gold standard in metal alloy characterisation. These include Optical Microscopy, Scanning Electron Microscopy, Electron Backscattered Diffraction, Electron Channelling Contrast Imaging and Transmission Electron Microscopy. Their mechanisms are described and how they can be utilised to unveil the features and mechanisms at work in the material microstructure to better understand the local and global effects that yield these enhanced mechanical properties.

2.1 Introduction to Aluminium Alloys

Aluminium's properties make it one of the most advantageous and versatile materials in use today. It is lightweight; it weighs 1/3 of equal volumes of steel, copper, and iron with a density value of approximately 2.7g/cm^3. It is strong; at appropriate tempers, certain aluminium alloys have strengths that surpass some steels. Due to these lightweight properties, aluminium has been used in many applications in industry to replace steel parts, as weight reduction is of great advantage in the field. Aluminium is also commonly acknowledged for having good corrosion properties as well as good formability and ease in recycling.

Aluminium as a pure metal is a polycrystal. Pure aluminium is not as strong or hard as steel, and thus, in order for an aluminium part to possess the same strength qualities as its steel counterpart, it would need to be thicker and bigger – this defeats the purpose of utilizing aluminium for its lightweight properties as the parts end up being just as heavy. The resolve to this problem is alloying aluminium with other elements in order to take advantage of the various strengthening mechanisms associated with the common aluminium alloys.

To strengthen the metal and improve ductility, alloying elements are added to form more advanced alloys with more complex systems. Aluminium is often alloyed with elements like: Copper, Zinc, Magnesium, Silicon, Manganese and Lithium. Small levels of Chromium, Titanium, Zirconium, Lead, Bismuth and Nickel are also common constituents of alloying recipes. Iron is invariably present in small quantities (Tanwir & Ansari, 2017) and can be seen as an impurity.

Strong aluminium alloys date back to the accidental discovery of the age hardening phenomenon by Alfred Wilm in the year, 1901. Wilm discovered an alloy known as Duralumin (which is Al-3.5%Cu-0.5%Mg-0.5%Mn by weight) this novel alloy was applied for use in the structural components of Zeppelin airships and other aircrafts (Polmear, 1995).

2.1.1 Cast & Wrought Alloy Designation and Characteristics

Aluminium alloys have various characterizations. They are commonly separated into cast aluminium alloys and wrought aluminium alloys.

Cast alloys are identified by a 3-digit, with a decimal point designation system (xxx.x) whilst wrought alloys are classified with a 4-digit system. In aluminium alloys, the digits are usually preceded with the capital letters “AA”, denoting “Aluminium Alloy”. In cast alloys, the digit in the hundreds space indicates the main alloying element present, whilst the decimal place signifies the form of the material, whether in cast shape (0) or as an ingot (1 or 2). In wrought alloys, the digit in the thousands space indicates the principal/major alloying element added to the aluminium alloy, the digit in the hundreds space indicates the modification of the specific alloy, and the remaining two digits are arbitrary numbers given to alloys in that alloy series. Unlike the cast alloys, the form of the material is not described in the designation system.

Aluminium Cast Alloy by Series:

1xx series – Pure Aluminium. Composed of > 99.000% aluminium.

2xx series – Aluminium and Copper alloys

3xx series – Aluminium and Silicon alloys with added Copper and or Magnesium

4xx series – Aluminium and Silicon alloys

5xx series – Aluminium and Magnesium alloys

6xx series – Aluminium and Zinc alloys

7xx series – Aluminium and Tin alloys

8xx series – Aluminium and Other Element alloys

(Starke, 1996)

Aluminium Wrought Alloy by Series:

1xxx series – commercially pure aluminium. Composed of 99% or more aluminium.

2xxx series – the main alloying element in this series is **Copper**. These alloys are strong and tough but are not corrosion resistant and thus are usually coated or painted.

3xxx series – in this series of aluminium alloys, the primary alloying element is **Manganese** with small amounts of magnesium. These alloys are moderately strong and are workable. Uses include cooking utensils.

4xxx series – **Silicon** is mixed with aluminium in this alloy series. This reduces the melting point without reducing its ductility. Used for welding wires.

5xxx series – the primary alloying element is **Magnesium**. This alloying makes the material strong, weldable, and resistant to marine corrosion. Used to manufacture storage tanks and put to marine applications.

6xxx series – both **Silicon** and **Magnesium** are used in these alloys. Alloys of this composition are formable, weldable and heat treatable. They are resistant to corrosion and have moderate strength. Used in architecture.

7xxx series – **Zinc** is the alloying metal. the resultant alloys are heat treatable and very strong. Used for aircraft applications.

8xxx series – these alloys are made with other combinations of elements including **Tin** and **Lithium.**

(Polmear, 1995) (Helmenstine, 2020)

Each series contains many subgroups and are slightly varied. The variation is down to the manufacturing techniques used to prepare the alloy, the chemical compositions, and the temper conditions (for example, T4, T6, T7 etc.) (Djukanovic, 2019). As described above, aluminium alloys are divided into two main, broad categories: wrought alloys and casting alloys. These categories are then further subdivided into heat treatable and non-heat treatable alloys. Wrought alloys generally have a higher tensile strength but in most cases, casting alloys are cheaper to produce due to their relatively lower melting points (Helmenstine, 2020).

Alloys that are to be used in the automotive industry are classed under numerous groups: cast, extruded and rolled alloys. They all individually have different applications and are utilized at different locations in the vehicle. As shown in the matrix above, the chemical composition and properties of the alloys siphoned into designated series. The majority of automotive alloys fall in the 5xxx and 6xxx series (Djukanovic, 2019). Higher strength aluminium alloys are much more sought after in this industry. The balance leans more to the 6xxx series alloys as they are more versatile and are also heat treatable.

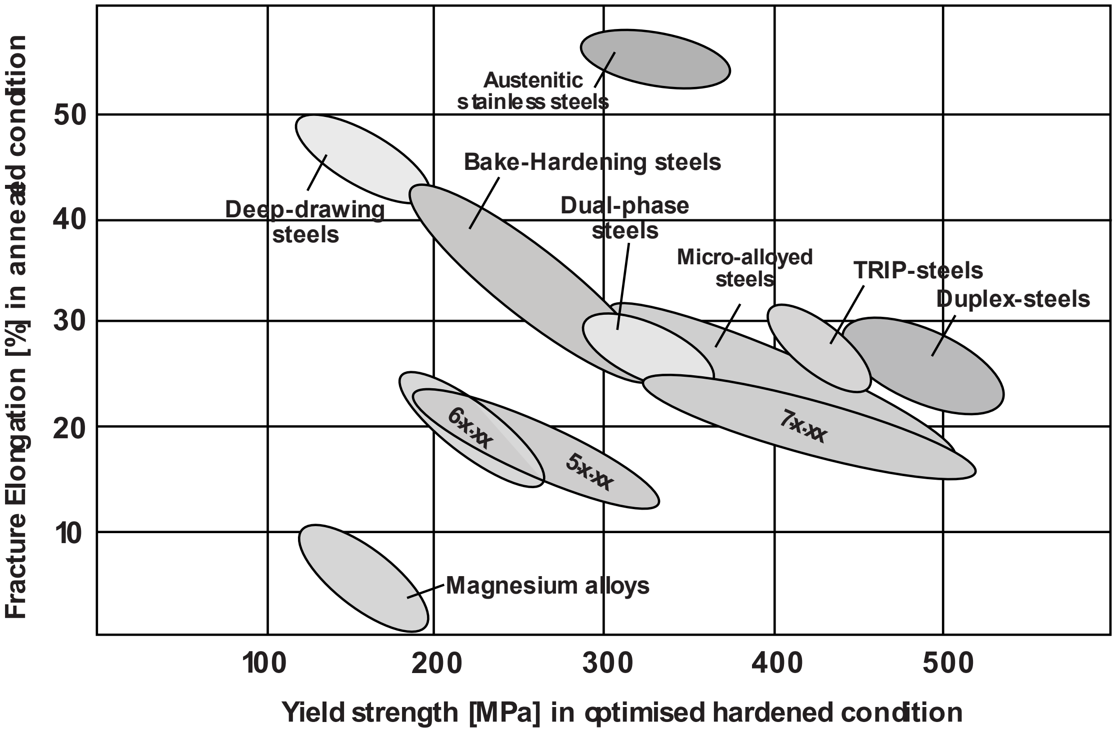

Figure 2.1: Comparison of Aluminium Cast Alloy Series. %Fracture elongation against yield strength. (Raabe, 2020)

In the graph above, ductility is graphed against yield strength for numerous alloys. The notable alloys are those in the rings annotated “5xxx” “6xxx” “7xxx”. These are aluminium alloys. As displayed in the graph, the 7xxx series alloys have the greatest strength value out of these aluminium alloys followed by the 5xxx and then closely followed by the 6xxx series. The 7xxx series alloys has a much greater strength than the other two alloy series. This is due to its zinc and magnesium constituents. The weight percentage of zinc in these alloys vary between 1-8%. These alloys are said to have moderate to very high strength (Raabe, 2020).

The yield strength of the 5xxx and 6xxx series alloys are very similar. However, the graph shows that the ductility properties of the 6xxx is slightly greater than those of the 5xxx series alloys. This property is more advantageous in the automotive industry as a material that will not fracture in a brittle manner is required. This explains why the 6xxx series alloys are preferred in industry.

2.1.2 Al Alloy Crystallography and Structure

Aluminium and its alloys form crystalline polycrystal structures. These structures have regular and repeating arrangements and have specific melting points as opposed to amorphous crystals that are irregular in pattern and melt over a range of temperatures. Most aluminium materials used for engineering are polycrystals. Each crystal in a polycrystalline material is also called a grain. If these grains are randomly oriented, the properties of the material and non-directional and the material is classed as isotropic. If the grains are textured however, the material will exhibit anisotropic behaviour (Callister , 2007).

As aluminium is a metal, the bonds formed between the atoms in its crystals are metallic bonds. Metallics bonding is described as the sharing of free electrons among a lattice of positively charged metal ions (Callister, 2007). Atomic bonding in these materials are nondirectional and thus there are minimal restrictions on the number and positions of nearest neighbouring atoms, leading to dense atomic packings (Callister, 2007). Aluminium forms a face centred cubic (FCC) structure, which is the densest geometric packing of spheres. There is a distinct 3-layer sequence of atoms in FCC structures and it repeats as ABCABCA… (Nakashima, 2018).

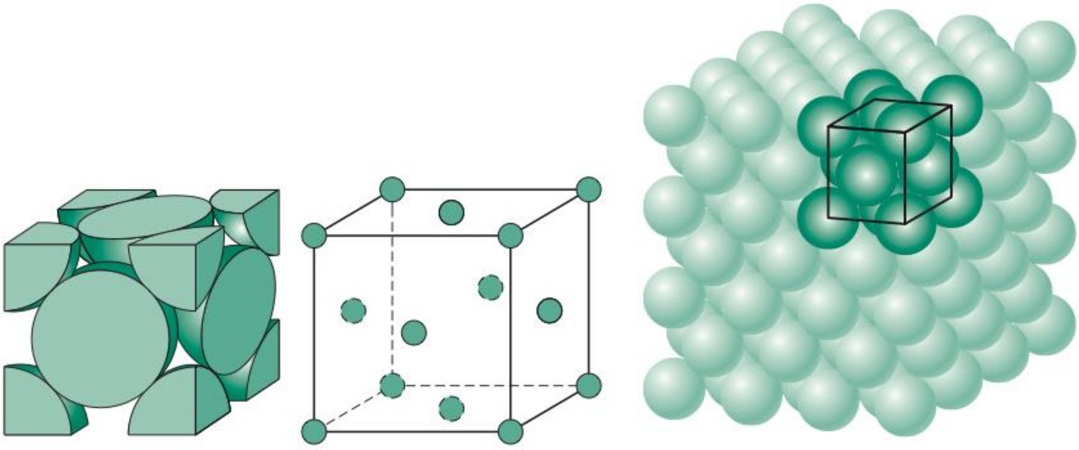

Figure 2.2. Face centred cubic structure. (Callister, 2007)

The unit cell, shown in Figure 2.2 is a small repeat structure that represents the repetitive arrangement of atoms in an aluminium crystal lattice. The symmetry of the crystal can be seen through this figure. Cubic structures crystallographic planes can be determined using this unit cell, described through miller indices (hkl). Parallel planes are equivalent and have the same hkl indices. Commonly referenced planes are shown in Figure 2.3.

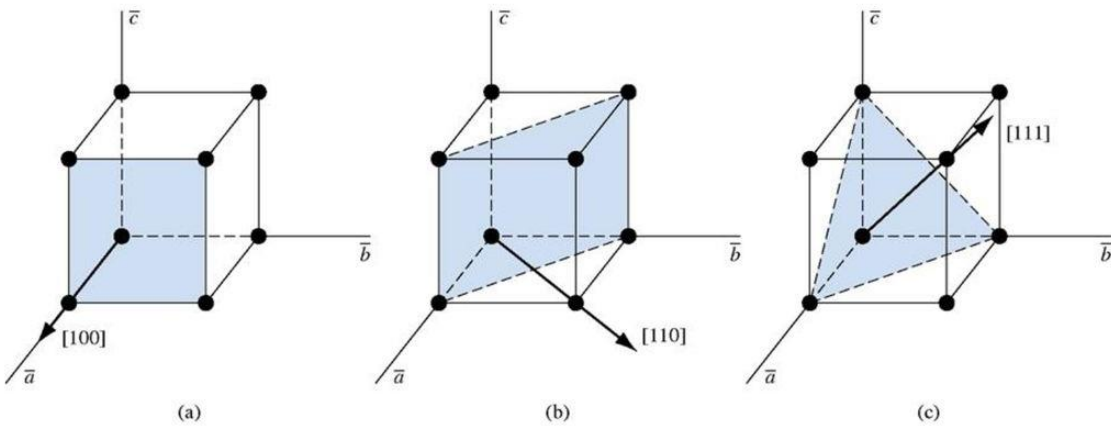

(100) Plane with normal direction [100]

(110) Plane with normal direction [110]

(111) Plane with normal direction [111]

Figure 2.3. Lattice planes in cubic structures (Sparks, 2015)

There are numerous equivalent atomic planes that can be drawn in the unit cell, and these are conventionally grouped into families of planes. Planes of the same family have the same atomic packings. Families of planes are enclosed in {} braces. As an example, the family of {111} planes are (111), ($\bar{1}\bar{1}\bar{1}$), ($\bar{1}11$), ($1\bar{1}\bar{1}$), ($11\bar{1}$), ($\bar{1}\bar{1}1$), ($\bar{1}1\bar{1}$) and ($1\bar{1}1$) (Callister, 2007).

2.1.3 Al Alloy Temper Nomenclature

The mechanical properties of aluminium alloys are highly dependent on the processing status of the material, these include heat treatment schedules as well as cold working or other means of plastic deformation. These primary processes increase the materials properties through different combinations and sequences of these strengthening processes, and thus a shorthand temper designation system which appears as a hyphenated suffix was developed, called the International Alloy Designation System (IADS).

These temper designations are assigned to inform of the materials processing history and can advise manufacturers of expected material performance as well as how to achieve them. The main standardised labels recognised by the IADS are listed below (Benedyk, 2010).

F specifies an As-Fabricated Alloy (cast, extruded, forged, hot worked).

H indicates an Alloy subjected to Strain Hardening.

H1x – cold worked only (x states the amount of cold work and strengthening).

H2x – cold worked and partly annealed.

H3x – cold worked and stabilised to prevent natural ageing.

O describes an Annealed Alloy (softest possible state).

W is a Solution Heat Treated Alloy (unstable due to natural ageing at room temperature).

T describes an Age Hardened Alloy (stable).

T1 – cooled and naturally aged.

T2 – cooled, cold worked, and naturally aged.

T3 – solution heat treated, cold worked, and naturally aged.

T4 – solution heat treated, and naturally aged.

T5 – cooled and artificially aged.

T6 – solution heat treated and artificially aged.

T7 – solution heat treated and overaged (to stabilise).

T8 – solution heat treated, cold worked, and artificially aged.

T9 – solution heat treated, artificially aged and cold worked.

T10 – cooled, cold worked and artificially aged.

2.2 Application of Aluminium Alloys in the Automotive Industry

Aluminium extruders are working on producing new types of 6xxx series aluminium alloys for application in the automotive industry. These are for parts such as bumper systems, crash boxes and side sills, which require higher strength. These 6xxx series alloys serve as an alternative to high strength 7xxx series alloys. These new 6xxx series alloys are better preferred, as they a far easier to extrude and at lower costs. They do not compromise on strength either, as they still achieve similar tensile yield strengths to some of the 7xxx alloys (Djukanovic, 2018).

The 6xxx series aluminium alloys are the most commonly used alloys in extrusion. The additions of magnesium and silicon alloying elements give the materials the ability to be strengthened through work hardening through heat treatment processes. These Mg and Si elements bond to form precipitates in the matrix of the microstructures of the alloys that aid in the strengthening of these aluminium alloys.

2.2.1 Main 6xxx & 7xxx series Al Alloys in the Automotive Industry:

Aluminium alloy “AA6016A”, released by Alusuisse at the start of the millennium. It has excess silicon content and is the main alloy selected in Europe for the external panels of vehicles (Djukanovic, 2019). It is now produced by most of the major aluminium sheet providers such as Novelis, Aleris, Constellium, Hydro and AMAG. (Scamans, 2020) states that the specification of this alloy is wide and large, consequently there is a lot of variation. This leads to a myriad of variants of the alloy that can provide specific properties like, higher strength, formability, or hemming quality.

AA6082 made up approximately 9% of all extruded products in the year 2000 (Reiso, 2004). The alloy is a medium to high strength rated alloy with high levels of manganese – a constituent element at between 0.40-1.00 wt%. The composite is commonly added to introduce manganese dispersoids to the material which form during the homogenisation process. The main function of these dispersoids in aluminium is to prevent recrystallization (Hu, 2010).

AA6060 is another medium to high strength alloy that is notably easy to extrude, forming complex profiles with complex cross sections. With low levels of manganese, there are a limited number of dispersoids in the crystal and this results in a material that recrystalises through processing.

AA6111 is another well-developed aluminium alloy, it is used by Jaguar and Land Rover in their aluminium intensive models. AA6111 is essentially the same as alloy AA6082 with significant additions of copper. Copper is one of the main alloying metals (levels of 0.6 to 1.1 wt%). The addition of copper enables the alloy to strengthen in the short time available in the bake hardening process. The bake hardening process is an integral part of the automotive production line, where the vehicle has been painted and is heated to cure the paint. This alloy is even stronger than AA6016A, but its corrosion resistance is a little less (Rochet et al., 2020).

In the writing of (Scamans,2020), AA6451 is an alloy developed by manufacturer Alcan. It combines properties of both AA6111 and AA6016A. This alloy was initially marketed for use in external panels. AA6451 has a lower copper level (<0.4 wt%) than AA6111 and a lower silicon level than AA6016A, with an addition of vanadium instead of titanium. AA6451 is the favoured alloy for production from recycled scrap.

Alcoa developed an outer panel alloy by name, AA6022, first put to market in 1996. The alloy had the strength of AA6111 and the formability of AA6016A. However, the A6022 alloy is a low copper alloy (<0.11 wt%) and a low iron alloy (<0.2 wt%) which makes it relatively difficult to recycle from scrap stock.

AA7075 – (T6 temper). In the 2014 C & Corvette stingray, this alloy is used in the front crush zone, the extrusion is made using a high yield, high strength 7000 series aluminium alloy. It “folds up like an accordion” during collision, to absorb the impact energy.

2.3 Dislocation Structure

The majority of strengthening in a material or polycrystal is based on the interactions of dislocations and the obstacles present (solutes, strain fields, grain boundaries, precipitates etc). This is because dislocation slip is the mechanism through which plastic deformation is facilitated. Creating obstacles to dislocation motion increases the stresses required to cause further plastic deformation.

A dislocation is a one dimensional or linear defect in which a number of the crystal lattice atoms are misaligned. This can be in the way of an extra half-plane of atoms. This kind of dislocation is termed as an edge dislocation. This type of dislocation occurs when there is an extra plane of atoms that are generated in the crystal structure, straining to the breaking point the bonds that hold the atoms together.

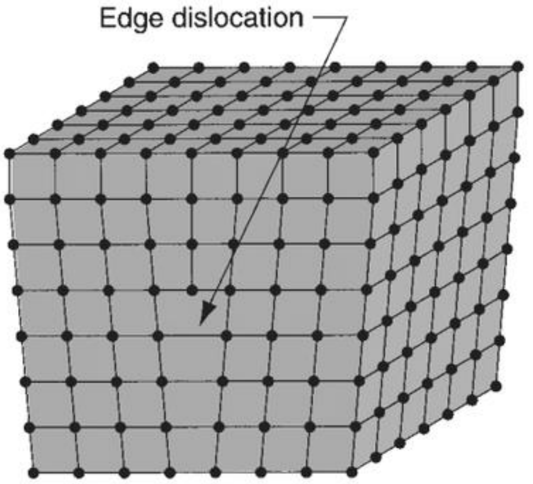

Figure 2.4. Edge dislocation. (Li, 2018).

The dislocation line for an edge dislocation is perpendicular to the plane of the page. The presence of the dislocation line generates a lattice distortion in the area around it. The atoms above the dislocation are squeezed together and experience compressive forces, whilst the atoms below the dislocation are pulled apart showing tensile strains. The magnitude of this distortion field reduces with increased distance from the dislocation position. In other words, atoms much closer to the dislocation experience a greater distortion than those further away.

Another type of dislocation is the screw dislocation. This type of dislocation is formed by shear stresses which are applied to the lattice that produce a distortion as seen in Figure 2.5.

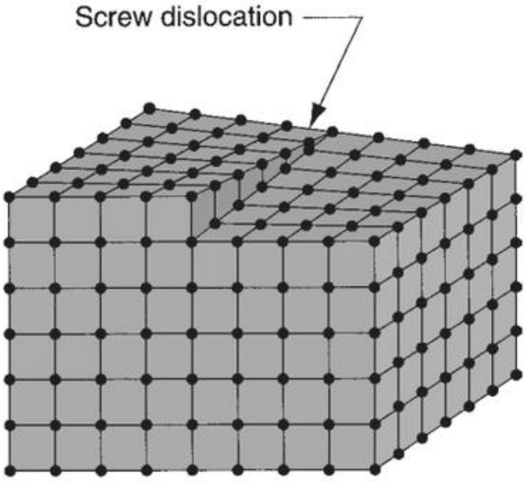

Figure 2.5. Screw dislocation. (Li, 2018)

A screw dislocation can be visualized as one plane of the crystal being turned against the other plane. One region of the lattice is shifted by one atomic distance to one side relative to another region. The screw dislocation has a helical/ spiral path that is traced around the dislocation line.

In reality crystalline materials are neither pure edge nor screw dislocations, they are in fact a fair mixture of both types known as mixed dislocations.

The burgers vector which expresses the magnitude and direction of a dislocation is denoted **b.** The burgers vector of a dislocation is defined by the orientation of the edge or screw dislocation line. The burgers vector of an edge dislocation is perpendicular to the dislocation line, whilst the burgers vector for a screw dislocation is parallel to its dislocation line. In a system with mixed dislocation types, the burgers vector is neither perpendicular nor parallel. For a metallic material, the burgers vector for a dislocation point in the direction of the closed packed crystallographic direction and its magnitude is equal to that of the interatomic spacing.

Dislocation motion in a crystalline material brings about permanent deformation (plastic deformation). These dislocations move along slip planes dependent on the material's atomic arrangement.

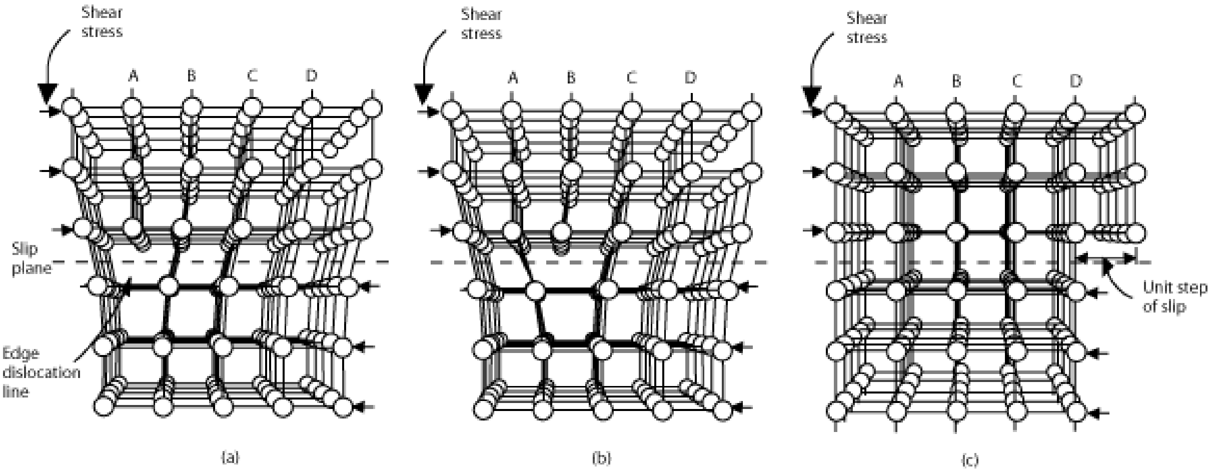

Figure 2.6. Dislocation motion (Davoudi, 2018).

Plastic deformation takes place when a large number of dislocations move. Edge dislocations are moved by shear stresses that are applied perpendicular to the line of the dislocation. Figure 2.6 illustrates how this dislocation propagates. In the image, the shear stress is applied to the lattice, and this forces the extra half plane to the right. Bonds are broken between the chains and reformed, this causes the adjacent plane (B) to become an extra half plane. This continues until the half plane moves to the terminal. In order for this motion to occur, the applied shear stress must be of sufficient magnitude. The motion of this dislocation in the lattice structure is called slip. The crystallographic plane by which this dislocation moves is called the plane of slip, or the slip plane, shown in the figure as the dotted line.

All metal and metal alloys contain some dislocations that are formed during solidification, during plastic deformation and as a consequence of thermal stresses withheld in the system from the quenching steps. The density of dislocations in the lattice is expressed as the sum of the dislocation length per unit volume, or as the total number of dislocations that cross a unit area of a region. This is measured in millimetres of dislocations per cubic millimetre or per square millimetre. Dislocation densities usually lie between 10^3 mm^{-2} and 10^{10} mm^{-2}, although, heavily deformed materials can attain dislocation densities up to 10^{14} mm^{-2}. Heat treatments of a deformed alloy can lower its dislocation densities to somewhere in the midpoint of this range.

Slip planes are on the planes with the minimum resistance to dislocation motion. Dislocations do not move as easily on every crystallographic plane of atoms in all crystallographic directions. The slip plane is the preferred plane. The slip planes are those with the highest planar densities. The direction of motion along this slip plane is called the slip direction. The slip direction corresponds to the direction in this plane that is most closely packed with atoms. Together, the slip plane and slip direction are called the slip system. Each slip system is different, dependent on the crystal structure of the metal. The slip system allows that the atomic distortion from the dislocation motion is to a minimum.

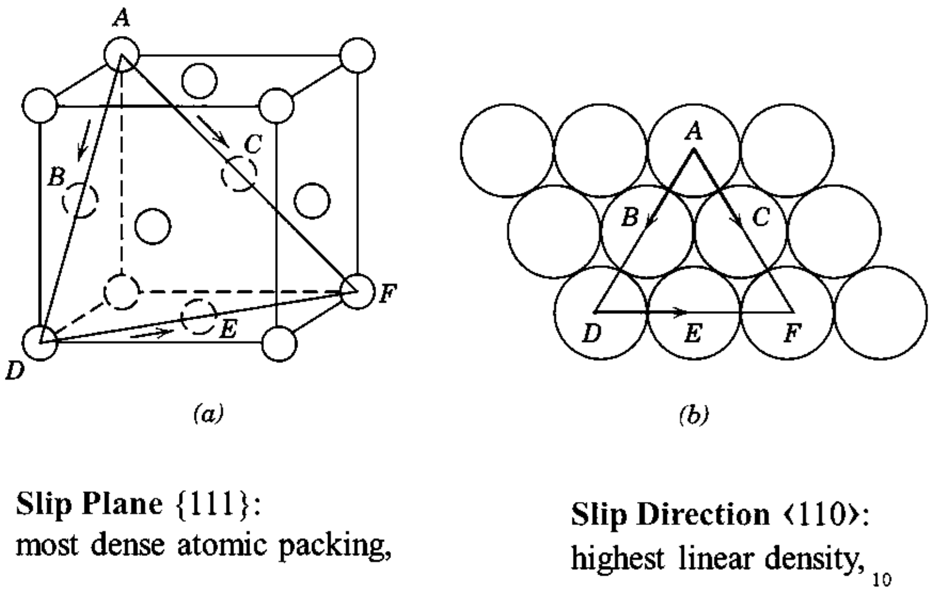

Figure 2.7. FCC slip system. (Jackson, 2019).

As aluminium has a face centred cubic lattice crystal structure (FCC), its preferential slip plane is the {111} plane. This plane contains closed packaged planes. Its slip direction is in the <110> direction within the {111} plane, which is a closed packed direction. For this FCC lattice crystal structure, the slip system is represented by {111}<110> (Callister, 2007).

A given slip plane may contain more than one slip direction, thus there are numerous slip systems present in a particular crystal lattice structure. In the FCC lattice crystal structure, there are four unique {111} planes and each of these planes contain three independent, <110> directions. This sums up to a total of 12 slip systems in this lattice structure.

Although a stress that is applied to an alloy sample may be tensile or compressive, there are shear components of this force that exist and are oriented at a myriad of angles and directions. These may not be parallel or perpendicular to the stress direction. These shear components are called resolved shear stresses. The magnitude of these stresses is dependent on both the applied stress and the orientation of the slip plane and the slip direction within that plane.

The resolved shear stress is given by the following equation:

$$\boldsymbol{\tau_R = \sigma(cos\phi cos\lambda)} \qquad (2.1)$$

ϕ represents the angle between the normal to the slip plane and the direction of the plane.

λ represents the angle between the slip and stress direction.

σ is the magnitude of the applied stress.

A metal crystal has many slip systems that can be activated. The resolved shear stress for each one is different because the orientation of each is different relative to the applied stress axis. However, the slip system that has the largest resolved shear stress is generally the one that is most favourably orientated.

When a stress is applied, whether it is tensile or compressive, the most favourable slip system is where the slip begins. The slip commences when the resolved shear stress reaches a critical magnitude. This is termed the critical resolved shear stress, and it represents the minimum shear stress that is required to evoke slip. This is different in each material and is instrumental in determining when yielding of the material takes place. The minimum stress required to cause yielding is when ϕ and λ are at 45°.

During this process of deformation through slip, atoms move along the slip systems, but the orientation of the crystal stays the same. The slip appears such that the crystal has been divided into two blocks. When the tensile load is further increased the block becomes divided again. The sequence of slip of dislocations continues, as shown in the following figure, until a macroscopic change can be visualized (Kopeliovich, 2012).

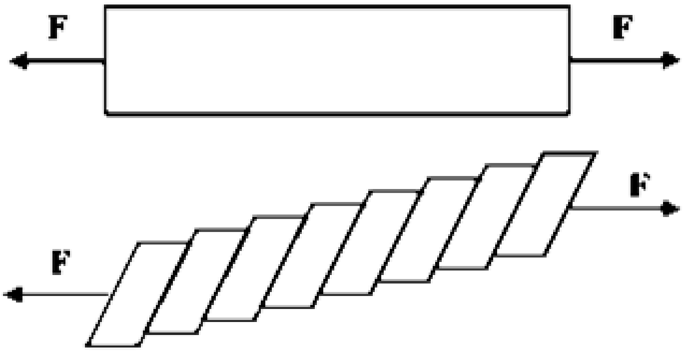

Figure 2.8. Deformation – Slip sequence. (Kopeliovich, 2012)

As a material is deformed, the number of dislocations in the crystal lattice increases. Dislocations are generated and multiplied through Frank-Read sources. The external stress applied to the material begins dislocation movement through slip in the grains/crystals of the material. When these glissile dislocations encounter obstacles, such as, impurities, hard particles or other dislocations, they become pinned, or sessile (Caillard, 2003). This causes a pile up of immobile dislocations at the obstacle site and these structures become Frank-Read sources, accommodating the creation of new, mobile dislocations.

The dislocation pinned between two points experiences a force from further applied external stresses perpendicular to the dislocation line, this causes the dislocation to lengthen and bend into an arc as illustrated in Figure 2.9. The shearing stress applied to the dislocation line increases till it reaches a critical point, at which the converging sides of the expanding dislocation meet and cancel, forming a dislocation loop and a new dislocation between the two pinning points. Continued applied stress to the material will cause the process to be repeated.

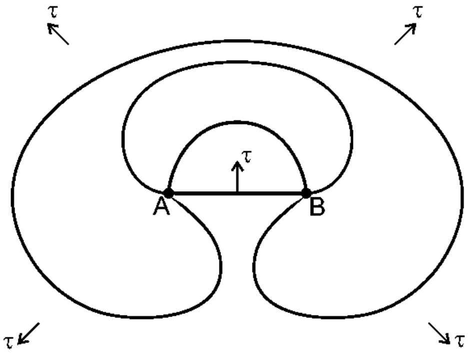

Figure 2.9. Frank Read Source. A pinned dislocation line subjected to a shear stress. (Monavari, 2009)

Geometrically necessary dislocations (GNDs) and statistically stored dislocations (SSDs) are generally the two categories of dislocations frequently referred to. As plastic deformation progresses, the storage of these SSDs occurs primarily through random trapping processes of mobile dislocations such as Frank-Read sources. GNDs on the other hand form to accommodate local orientation gradients from plastic bending in the crystalline material, first described by Nye in 1953 (Zhu, 2016).

GNDs are of the same sign whereas SSDs statistically consist of equal numbers of positively and negatively signed dislocations. As there are both GNDs and SSDs accumulated in the lattice matrix, the total density of dislocations is given as the addition of the two densities.

$$\boldsymbol{\rho_{tot} = \rho_s + \rho_g} \qquad (2.2)$$

Where $\boldsymbol{\rho_{tot}}$ is the total density, $\boldsymbol{\rho_s}$ is the SSD density, and $\boldsymbol{\rho_g}$ is the GND density.

Nyes Tensor is used to calculate the density of GNDs in a three-dimensional crystal. The dislocations can be determined by burgers vectors when the effects if the dislocations are averaged (Nye, 1953) (Fleck, 2002).

If the burgers vector of the unit area normal to the unit vector $\boldsymbol{l_j}$ has a burgers vector $\boldsymbol{B_i}$, then.

$$\boldsymbol{B_i = a_{ij} l_j \, (i, j = 1, 2, 3)} \qquad (2.3)$$

Where $\boldsymbol{a_{ij}}$ is the Nyes tensor relating to the unit vector and burgers vector. This defined tensor determines the state of dislocations in the region.

Assuming $\boldsymbol{B_i} = \boldsymbol{b_i}\,(\boldsymbol{n r_j l_j})$, where **r** is the unit vector parallel to dislocations and **b** is the burgers vector, **n** is the number of dislocations crossing unit area normal to **r**. Therefore, $\boldsymbol{a_{ij}} = \boldsymbol{n b_i\, r_j}$**,** meaning the total $\boldsymbol{a_{ij}}$ is the sum of the different values of $\boldsymbol{n b_i\, r_j}$.

It can be proved that the dislocation potential can be written as

$$\boldsymbol{W} = \frac{\boldsymbol{1}}{\boldsymbol{2}}\boldsymbol{a_{ij} k_{ij}} \qquad (2.4)$$

It is understood that as the density of dislocations increases, interaction between them increase, leading to formations of tangles and other more complex structures. This work hardening behaviour of metals is termed dislocation evolution (Davoudi, 2018). With increasing volume fractions of dislocations, forests and cells begin to form. Upon further deformation, there is annihilation of dislocations inside of these cells forming more defined wall structures and dislocation free zones inside of these deformation induced cells. These dislocation cells are defined by characteristic three-dimensional tangles of dislocations that serve as “walls” with a less dense region inside of them (Yu, 2013) occurring at high levels of plastic deformation. The formation of these sub grain cells have great impact on the strain hardening of the materials.

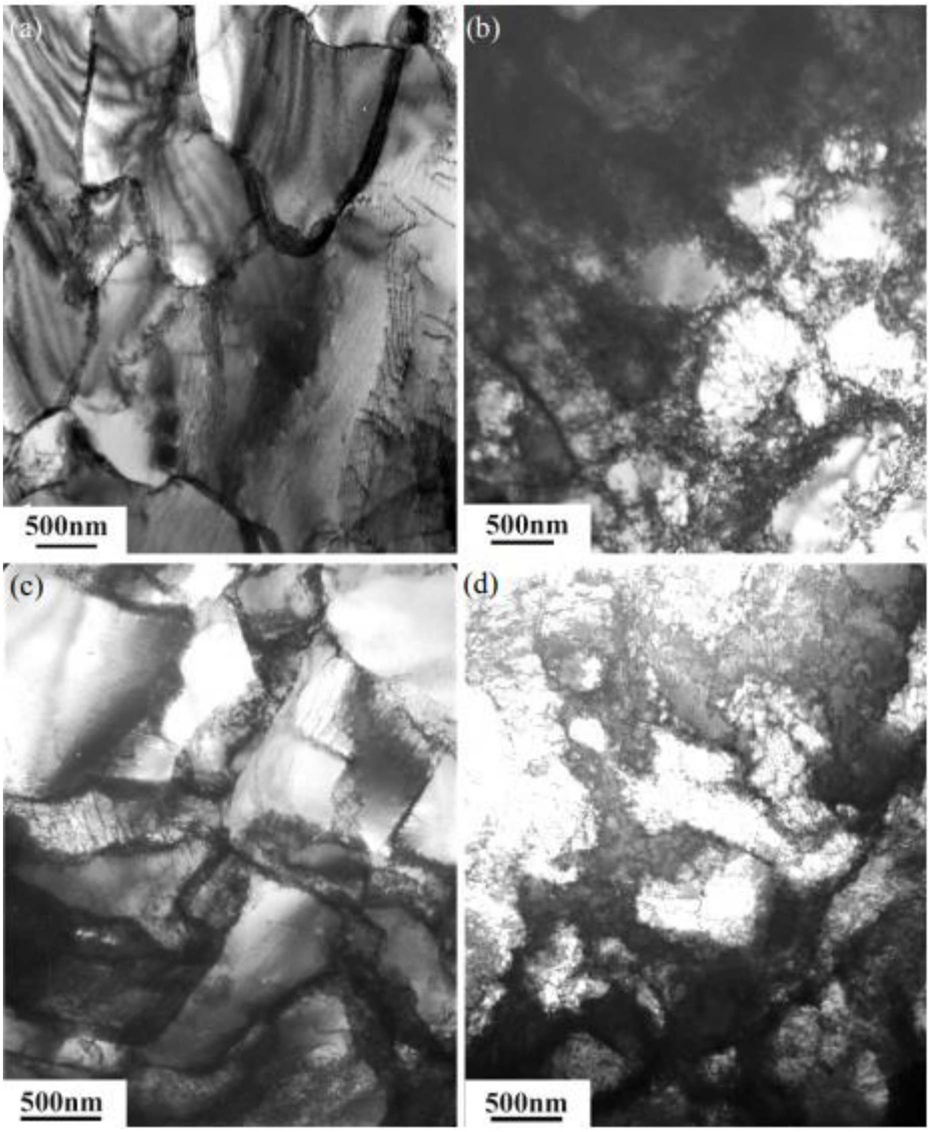

Figure 2.10. TEM micrograph showing cellular structure formation following room temperature deformation in an FCC metal (Landau, 2009).

Strains applied to the material cause the formation of cellular equiaxed structures as illustrated in Figure 2.10. with increasing strain, the size and morphology of the cells changed, with the cells becoming smaller and the boundaries of dislocations becoming sharper which indicates a higher density of dislocations inside them (Landau, 2009). The dislocations inside the boundaries change in a way that forms parallel arrays of dislocations when a critical degree of strain is reached.

Taylors equation gives an expression that describes work hardening, forming a relation between the flow stress of a material to the density of dislocations. It is required that the flow stress is assumed to be the external stress required to move dislocations on parallel slip planes past each other. The maximum shear stress that can be associated with a dislocation is given by $\mu b/r$, where μ is the shear modulus and r is the distance to the dislocation (Davoudi, 2018). The flow stress of the material can be written as

$$\boldsymbol{\tau} = \boldsymbol{\tau_0} + \boldsymbol{\alpha\mu b}\sqrt{\boldsymbol{p}} \qquad (2.5)$$

Where **a** is a parameter without dimension with a nominal value of 0.05 to 2.6 dependant on the material, $\boldsymbol{\tau_0}$ is the flow stress of the material when $\boldsymbol{\rho}$ the dislocation density is equal to 0. i.e $\boldsymbol{\tau_0}$ is the shear resistance to dislocation motion in the absence of dislocation interaction.

The equation can be rewritten as

$$\boldsymbol{\tau} - \boldsymbol{\tau}^* = \boldsymbol{\alpha\mu b}(\sqrt{\boldsymbol{p}} - \sqrt{\boldsymbol{\rho}^*}) \qquad (2.6)$$

$\boldsymbol{\tau}^*$ and $\boldsymbol{\rho}^*$ are the flow stress and dislocation density when the material initially becomes fully plastic.

The reversal of the dislocation features achieved through cold working is achieved when the material is heat treated. The elevated temperature alloys the material to reduce stored energy through the resolvent of these crystal line defects achieved through atomic diffusion accommodated by the elevated temperature. Resultantly, the reduction in the volume fraction of dislocations results in a decrease in the yield strength of the material. The strain hardening in reversed. The process through which these dislocations are released from the crystal matrix is called dislocation recovery (Callister, 2007).

Doherty, 1998 described recovery as annealing processes applied to a deformed material which takes place to reduce the density of dislocations without the migrations of high angle grain boundaries, which would entail the processes of recrystallization and grain growth. Recovery can occur during heat treatment which is standard or called 'static' but also whilst the material is being deformed, common in hot working (Rivera, 2012). During this process of hot working where the material is deformed at elevated temperatures, new dislocations are generated as a result of the deforming of the material whilst dislocations are being removed from the material through the heat treatment process for reduction of overall energy, this forms a dynamic equilibrium and is termed dynamic recovery (Rivera, 2012).

Recovery was proven in an experiment by Cahn in 1949, where a single crystal was bent. This single crystal deformed along an individual slip system. It was observed that the edge dislocations orientated along and into tilt boundaries otherwise known as a low angle grain boundary. The process through which these dislocations are recovered can be described through 2 distinct processes, annihilation, and rearrangement. When the temperature no more than one-third of the absolute melting point is reached, the dislocations become mobile, like signed dislocations are repelled and opposing signed dislocations attract one another. Once these dislocations meet, they are annihilated, or in other words, cancel out each other and the stored energy associated with each is reduced (Galindo, 2012). Dislocations existing in the material after the annihilation process are aligned in arrays where their strain fields overlap, this has the effect of reducing their contributions to the stored energy of the system.

Stages of deformation can be divided into 5 distinct stages as described by Diehl et al in their 1955 study on tensile deformation of single crystals and also corroborated by Nabarro et al, 1964.

Stages I and II are closely linked and the point of transition between the two stages is not easily reproduced, varying with handling, sample surface conditions, crystal orientation and chemical purity (Nabarro, 1964). Stage I is referred to as easy glide which is observable in single crystals. This stage is identified by the fairly low hardening rate of $2\text{x}10^{-4}G$, where G is the shear modulus of the material. The material is said to behave relatively soft in this state. Stage II occurs after a certain amount of applied strain where a significant increase in strain hardening rate is observed. A clear transition between the stages takes place (Nabarro, 1964). The strain hardening rate observed in stage II is independent of temperature and straining rate with only a slight dependency on the crystal orientation, reaching values of up to G/20. (Reed, 1972) however stated that in pure aluminium, a slight temperature dependency can be seen. In polycrystals however, Stage II occurs before Stage I in some cases.

Stage III replaces Stage II and is characterised by a decreasing strain rate with the increasing stress as well as displaying a strong dependence on strain rate and temperature. Stage III is defined as the most significant stage of a tensile test where the primary process of dislocation annihilation occurs through dynamic recovery (Kocks, 1976) (Kocks, 2003). The annihilation process takes place with through cross slip of screw dislocations in the material matrix.

Stages IV and V follow stage III. In stage IV, the strain hardening rate is at a constant rate with a value similar to that of stage I. (Sekine, 1981) et al investigated large strain deformations. Stage IV is not too often observed in material tensile testing as necking occurs in the specimen before this phenomenon can be seen. For this reason, torsional testing often replaces tensile testing to reveal these later stages of the deformation sequence (Rollet, 1988) (Seumer, 1993) (Zehetbauer, 1993) (Les, 1997) or compressive tests in the case of (Asgari, 1997). Initial characterisation of Stage IV was done in wire drawing followed by tensile testing experiments by (Langford, 1969). (Ryen, 2006) found interestingly that this stage is insensitive to alloy chemical composition. Stage V is the final step of the strain hardening evolution and is described as stress saturation (Seumer, 1993).

2.4 Aluminium Alloy Strengthening Mechanism

In a lot of metallurgical applications, it is required that alloys are designed that have high strengths yet possess good ductility and toughness. In most scenarios, ductility is reduced at the expense of strength properties. This segment outlines the existing theories of strengthening mechanisms in work-hardenable and precipitate hardening aluminium alloys. There are a great number of hardening mechanisms present in metallic alloys based entirely on the addition of elements to the base metal to greatly improve its mechanical properties and performance. This chapter will review many of the existing theories of aluminium and aluminium alloy strengthening mechanisms.

Alloying aluminium with other metals and elements proves to improve its mechanical properties. However, apart from their chemical properties which are resultant from their chemical composition, the final alloy characteristics can be altered by various techniques. There are several strengthening techniques available to engineers when working with aluminium alloys. These techniques incorporate slowing the motion of dislocations, since the motion of these dislocations is linked to the degree of plastic deformation. Reducing the dislocation motion evokes increased strength and hardness properties as more work is required to further mobilise the dislocations to allow flow to proceed. These strengthening mechanisms are plenty used in industry. Namely, they are Grain size strengthening, work hardening, solute strengthening, and precipitate hardening (Djukanovic, 2019). These processes can provide an alloy with improved properties like higher strength, increased ductility, and workability. In aluminium alloys, all these methods of augmenting material strength are widely used in cohesion, but the mechanism promoting the greatest increment in strength is precipitation hardening.

2.4.1 Work Hardening

Dislocations are the means through which most mechanical strengthening mechanisms work and is how plastic strain is applied.

The work hardening technique works on the premise that when a ductile metal is plastically deformed, it becomes harder. This phenomenon is also known as cold working, this is due to the temperature at which the deformation occurs, which is “cold” relative to the absolute melting temperature of the metal. Most metals are work hardened at room temperature.

The percent cold work (%CW) is a more convenient parameter to work with when dealing with work hardened metals. This parameter can be given by the following equation:

$$\%CW = \left(\frac{A_0 - A_d}{A_0}\right) \times 100 \qquad (2.7)$$

A_0 is the original cross-sectional area that experiences deformation. A_d is the cross-sectional area post deformation.

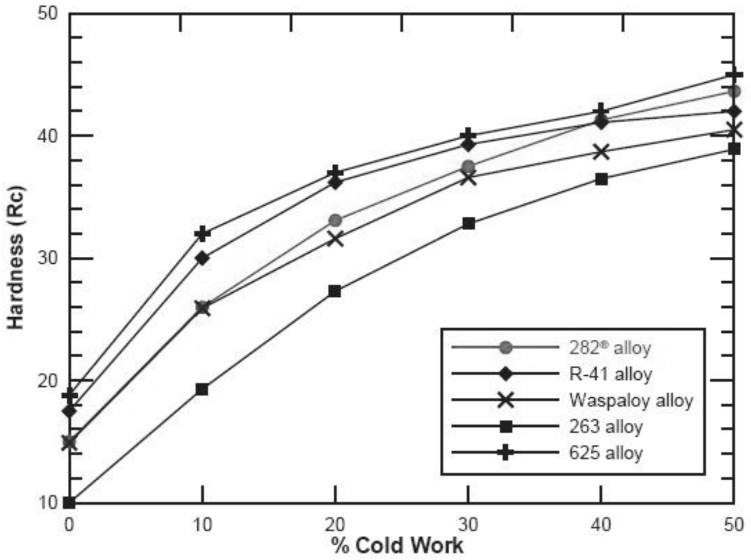

Figure 2.11. Alloy hardness versus % cold work on different alloys. (Haynes, 2020).

Figure 2.11 above shows the effect of different cold working on different alloys. The relationship is such that, as the percentage cold work increases, so does the hardness.

However, the response to the increase of cold work gradually reduces as the degree of cold working is increased. In this kind of strengthening, the gain in strength, hardness and other mechanical properties is at the expense of the materials ductility (Callister, 2007).

The work hardening phenomenon can be explained through the interaction between dislocations and strain fields similar to those in solute hardening. The dislocation density increases when the material is plastically deformed or cold worked. As a consequence of this, the average distance between dislocations is reduced. i.e. the dislocations are located closer to one another. The average dislocation – dislocation strain interaction is repulsive. This overall results in the dislocations being impeded by the presence of other dislocations.

With further plastic deformation and further increased dislocation densities, the obstruction to dislocation motion by other dislocations present becomes more and more pronounced. This in turn means a larger stress is required to further deform the cold worked material.

Work hardening usually involves the reduction in thickness of a material. the thickness of plates and sheets can be lessened using cold rolling, whilst wires and tubes can be cold worked using drawing techniques.

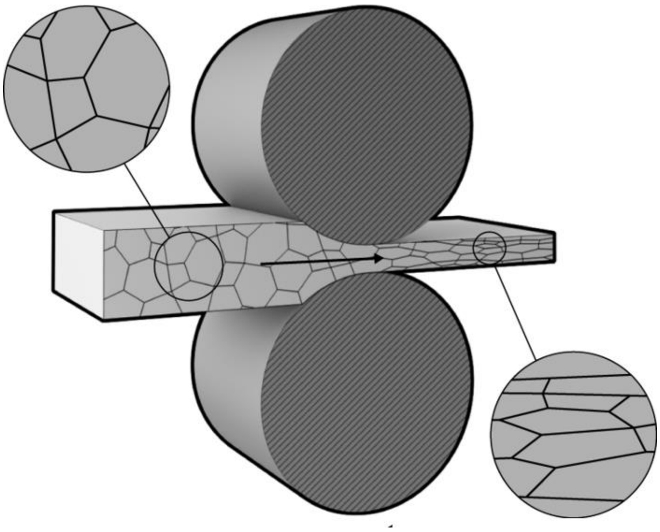

Figure 2.12. Cold rolling of a metal sheet. (Wearing, 2018).

The sheet is work hardened through the rolling process. In this rolling process, the material sheet is pressed between two rotating rollers. As a result, its thickness is reduced without the recrystallisation of the material grain structure. The process is carried out at room temperature to harness the effects of cold working.

In a study by J. Hirsch, 2011, the microstructure of the metal undertook evolution during cold rolling. The bulk deformation flattens the grains which are mostly equiaxed and recrystallized. The typical FCC rolling texture is generated.

2.4.2 Grain size (Hall-Petch) Strengthening

Grain boundary strengthening as a mechanism works on the premise of the size and average grain diameter in a polycrystal and how they affect its mechanical properties as a whole (Calister pg.188). In a polycrystal, there are numerous crystals or grains lined adjacent to one another in all planes forming a 3-dimensional crystal matrix. A grain in a metal is an individual crystal in which with its constituents (aluminium atoms in this context) are all arranged in an orderly manner. Each grain can have a random size and random orientations along planes. In a polycrystal there are a large number of grains, and since they can have any random orientation, these grains are said to be mis-orientated (as adjacent grains have different crystallographic orientations). A grain boundary is the position at which two grains meet. Several grains and the boundaries that lie between them can be seen illustrated in the figure below:

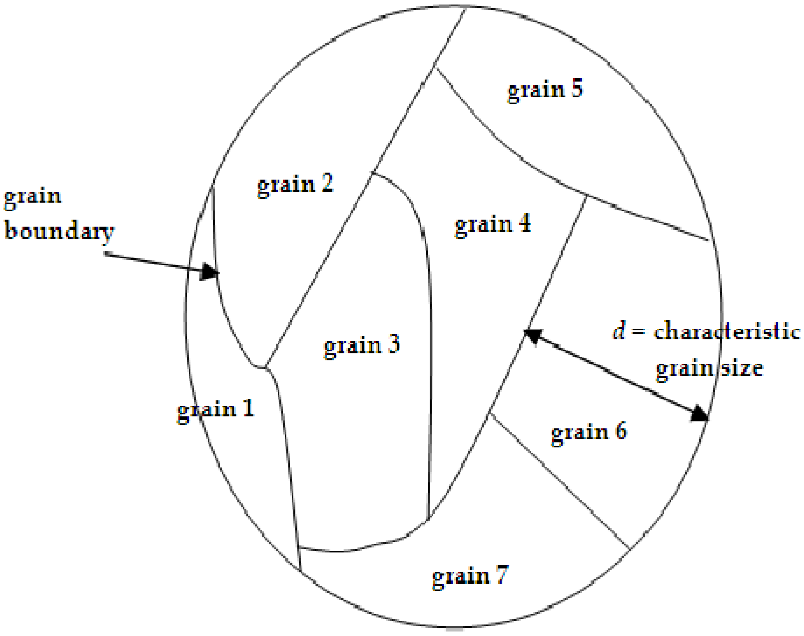

Figure 2.13. Grain Boundaries of a Polycrystal. (Bidin, 2012)

During plastic deformation, slip and dislocation motion must take place across the grain boundary that is shared between two or more grains. Grain boundaries act as barriers to dislocation motion as the dislocations cannot move across this boundary as easily as it had moved across the grains. This property can be harnessed, to increase the strength of the polycrystalline metal alloy.

The way in which dislocations are stopped by grain boundaries are:

a) The two neighbouring grains have different orientations (as mentioned above). Thus, a dislocation that is crossing this boundary into the next grain would have to change direction in order to continue propagating and moving across this new grain. As the crystallographic misorientation between the two grains increases, the more difficult it is for the dislocation to cross the grain boundary.

b) The atomic disorder within the grain boundary region means the slip planes are not continuous between the two grains.

In high angle grain boundaries, it may be increasingly difficult for the dislocations to traverse the grain boundaries even at increased stresses. Dislocations then pile up at the grain boundaries. The pile up of these dislocations produces stress concentrations ahead of their slip planes. New dislocations are then resultantly generated in the adjacent grains.

To increase the strength of a polycrystalline metal alloy, the grains are refined to produce a finer grained material (a material with grains of a smaller radius). This increases the hardness and strength of the material as compared to a coarser grained version of the same alloy. This is because the alloy with the finer grain structure has a greater number of grains for the same volume, meaning there are more grain boundaries present. Since these grain boundaries act as obstacles to dislocation motion, more grain boundaries result in increased impediment of dislocation motion. The toughness of an alloy is also increased as a result of grain size reduction.

The yield strength of the material can vary as a function of the grain size and this relationship can be expressed in the Hall-Petch equation:

$$\boldsymbol{\Delta\sigma \propto kd^{-1/2}} \qquad (2.8)$$

In the equation ***Δσ*** represents the change in yield strength of the material. ***k*** is the Hall-Petch coefficient, which is a constant that varies for each specific material. ***d*** is the average grain diameter.

The Hall-Petch coefficient has contrasting values, dependent on the grain size due to deformation mechanisms. It quantifies how much the yield strength increases as the grain size decreases. The Hall-Petch equation cannot be used and fails for very coarse and extremely fine-grained polycrystalline materials, as in very coarse grains, the grain diameter is so large, meaning that the strengthening resulting from grain size and grain boundary hardening is far less significant and is more determined by other factors such as dislocation densities, alloying elements, and heat treatment. (Li, 2016)

The texture of the alloy can determine how the alloy behaves in different directions of applied stress. If the alloy has an overall uniform texture, it behaves predictably in all directions (isotropic) when a stress or load is applied to the material.

This relationship is depicted in Figure 2.14 below.

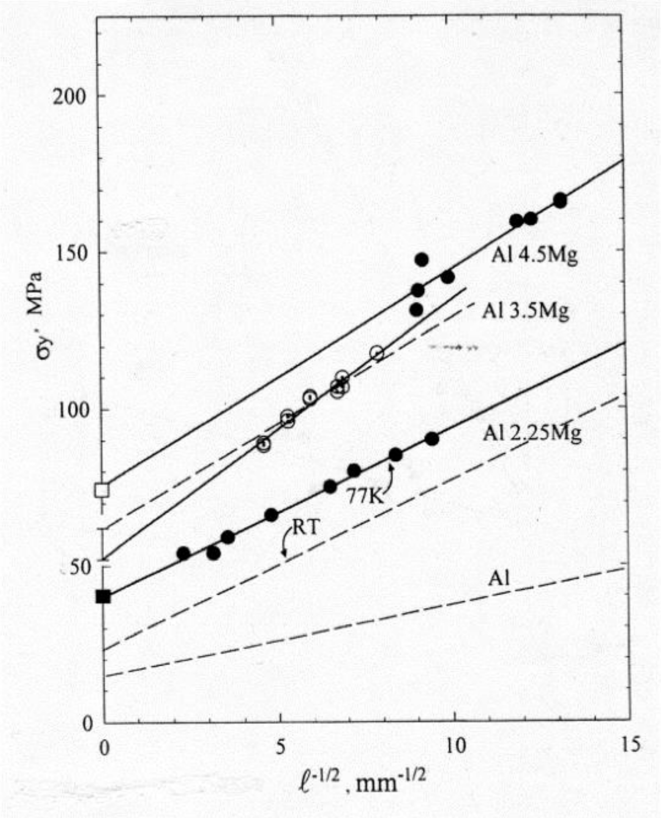

Figure 2.14. Hardness as a function of grain size of Al-Si alloys (Armstrong, 2016)

The horizontal axis displays the inverse of the square root of the grain size and thus, a greater value is linked to a smaller grain size. The grain diameter increases from right to left and the graph is not linear.

The size of the grains can be controlled using specific temperatures as grain boundaries have energies associated with them. Bigger grains in a crystal mean the total boundary area decreases and thus the total energy reduces. Due to this there is a driving force for grain growth as a lower energy is preferred by the system. To attain finer grains, grain growth must be halted. The alloy must be heated to a critical temperature and then quenched rapidly to prevent the growth of the grains. The shorter time for solidification means, there are more spontaneously generated nuclei and reduced growth of these nuclei.

Grain refinement is another technique through which the grain size can be controlled. This is usually achieved with the addition of specific elements such as Zirconium (Zr), Zinc (Zn), Titanium (Ti) and Boron (B). This kind of grain size control is used primarily in as cast alloys.

In a study by Schempp (2013), grain refinement was achieved through the addition of grain refiner AL Ti5B1 to gas tungsten arc weld metal of aluminium alloys 1050A (Al 99.5) and 5083A (Al Mg4.5Mn0.7). The additions of the grain refiner led to significant reductions of the mean grain diameter (alloy 1050A, 86%; 5083A, 44%) with a change in grain shape from columnar to equiaxed. Tensile tests taken for the 5083A alloy showed that the materials ductility was increased through the use of grain refinement.

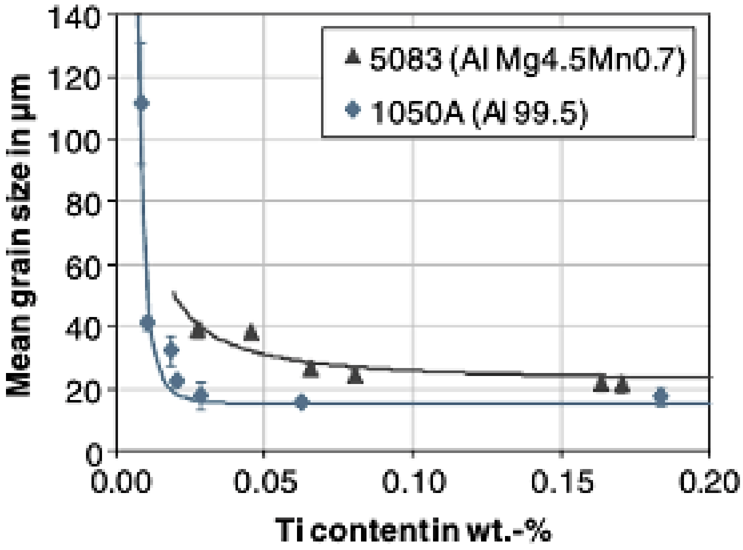

Figure 2.15. Weld metal mean grain size dependent upon weld metal Ti content. (Schempp, 2013)

As illustrated in the graph, as the Ti content was increased in wt% the mean diameter of the grains was reduced. The relationship is not linear. The graph shows that the 1050A alloy was most affected by the addition of this elemental grain refiner. This alloy however had a much greater initial mean grain diameter.

For wrought alloys, the more effective grain size control is achieved through specific high temperature treatments as aforementioned. The temperatures and quench times are all dependent on the alloy and its chemistry which can be optimised.

2.4.3 Solute Strengthening

In this type of strengthening, the metal material is alloyed with elements that would go into either substitutional or interstitial solid solution. This is also known or referred to as solid solution strengthening (Callister, 2007). Higher purity metals are almost always softer than when merged with alloying elements. There is a positive correlation, where the increase in the concentration of the impurity (alloying element) causes an increase in the alloys tensile and yield strength (Wang, 2019).

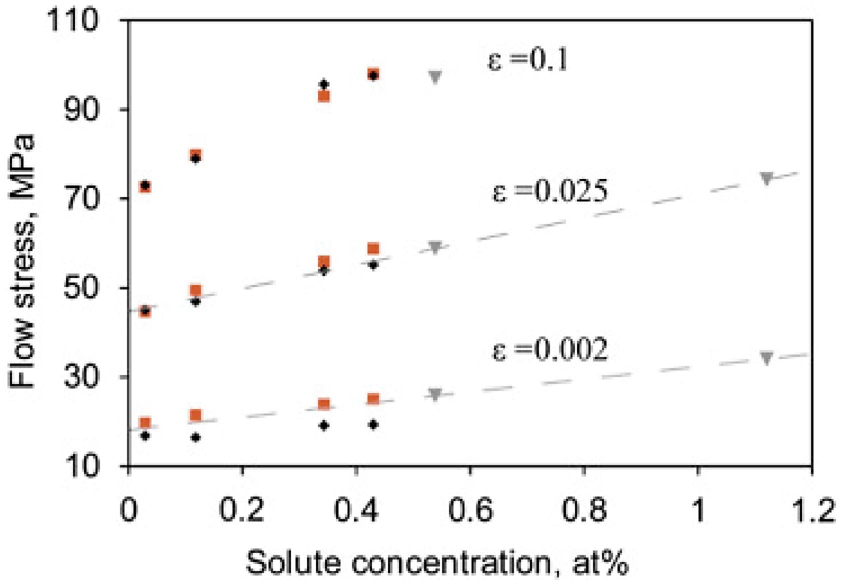

Figure 2.16. Flow stress against Si wt% concentration | Al-Si alloy. (Zhao, 2013).

The figure above shows the relationship mentioned above. Alloys are stronger than pure metals because the impurity atoms that are added go into the solid solutions. Their presence in the lattice generates lattice strains around the adjacent, surrounding atoms. The lattice strain field around these atoms interact with the dislocations that traverse their slip planes. Consequently, the dislocations motions are restricted.

The strain fields produced by the addition of these impurities can either be compressive or tensile. For example, an impurity atom that is smaller than the surrounding host atoms imposes tensile strains on the surrounding crystal lattice.

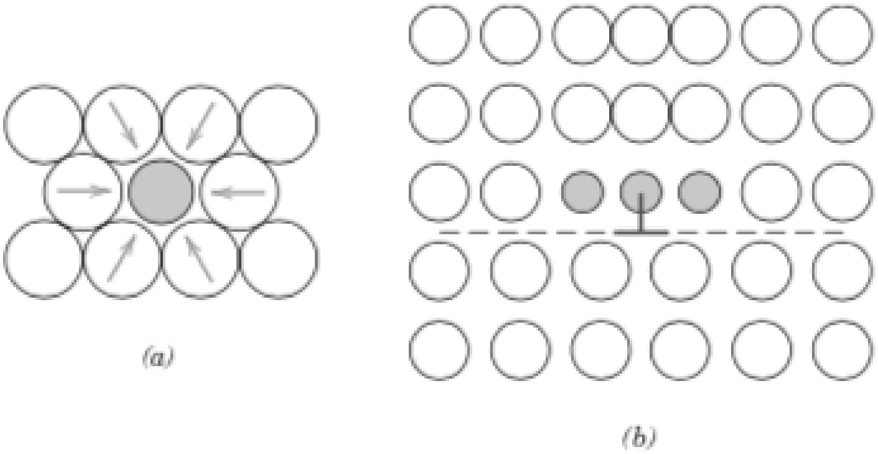

Figure 2.17. Tensile strains in crystal lattice. (a)Tensile strains caused by smaller substitutional impurity atom. (b) Location of smaller substitutional impurity atoms. (Oneal, 2016)

However, when a relatively larger impurity atom is substituted into the crystal lattice, the atom imposes compressive strains to its surrounding region:

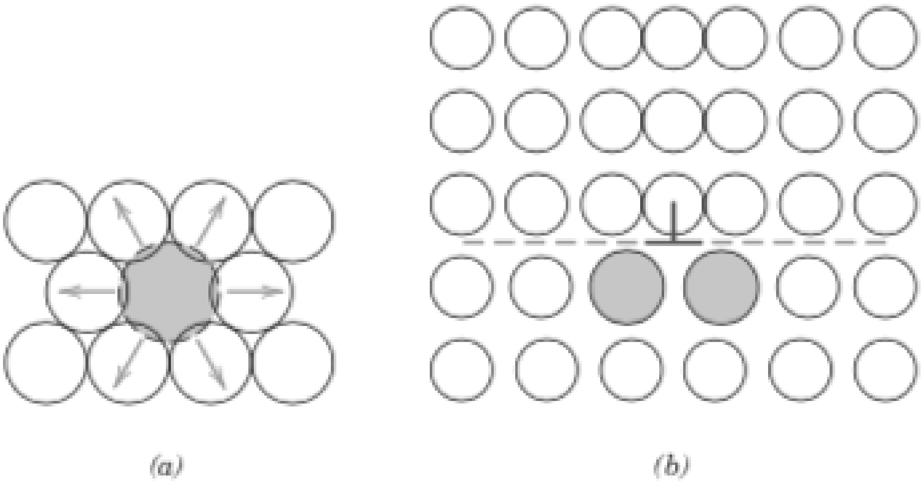

Figure 2.18. Compressive strains in crystal lattice. (a) Compressive strains caused by presence of larger substitutional impurity atom. (b) Possible locations of larger substitutional impurity atoms. (Oneal 2016)

These solute impurity atoms tend to diffuse to and segregate around dislocations. This is done in a way that reduces the overall strain energy of the system through cancelling some of the strain of the lattice that surrounds the dislocation.

Where the impurity atom is smaller than the host's atoms, its tensile strain will partially cancel out some of the dislocation's compressive strain. Where the impurity atom is larger than the host's atoms, its compressive strains would nullify the tensile strains around the dislocation.

The resistance to slip is greater when the impurity atoms are present as they interact with the dislocations that approach them. These interactions with the dislocations are how the slip motion of the dislocations are lessened (Zhao, 2013). The overall lattice strain must increase if the dislocation is to be drawn away from the impurity atoms. Furthermore, these interactions are also present among the impurity atoms and the dislocations when the dislocations slip during plastic deformation. For this reason, a greater stress must be applied in order to initiate and cause the progression of plastic deformation for these solid-solution alloys as compared to pure metals. This opposition to the dislocation motion elicits the increased strength and hardness properties.

2.4.4 Precipitation Hardening

Precipitation hardening is a technique by which metal alloys can be strengthened and hardened. This mechanism is the most widely used in industry. The strongest aluminium alloy series (2xxx, 6xxx and 7xxx) are produced through the physics behind this process. (Osten, 2019). This enhancement of mechanical properties is achieved due to the presence of tiny uniformly dispersed precipitate particles of a secondary phase which are situated within the original phase matrix. This phenomenon was first discovered in 1911 by Alfred Wilm through and Al-Cu-Mg alloy. In order for an alloy system to be precipitation-strengthened, there must be a terminal solid solution that has a decreasing solid solubility as temperature decreases. This secondary phase is only made present by phase transformations that are brought about by specific and controlled heat treatments (Callister, 2007). The second phase particles that are formed as a result of this ageing must be hard/brittle and the material must be able to form coherent secondary precipitates in order to attain the best mechanical properties.

These small secondary phases particles are better known as precipitates. This method of hardening is also widely known as age hardening. Many aluminium based alloys, copper-tin, certain steels, nickel-based super-alloys, and titanium alloys can be strengthened through this precipitation hardening process.

The generation and development of the secondary phase particles can be described with the aid of the alloy phase diagram. For simplicity, only one alloying element is considered although in real life applications, most precipitation hardened metals contain two or more alloying elements. The phase diagram of an Al-Cu system is imaged in the figure below:

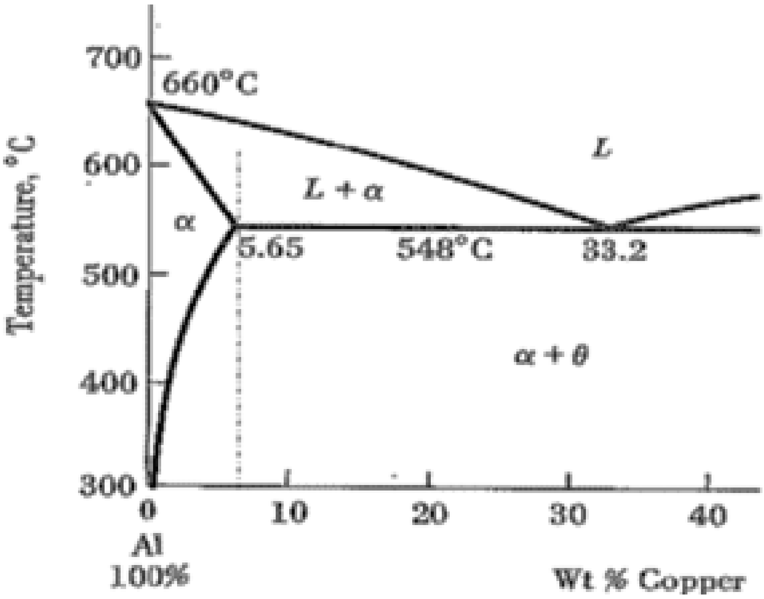

Figure 2.19. Al-Cu phase diagram. (Rao, 2015).

A phase diagram is a hypothetical graph made for precipitation-hardenable binary alloy.

Precipitation hardening is achieved through two different complementary heat treatment stages. The first stage of the heat treatment process is known as solution heat treatment. In this stage, all of the solute atoms are dissolved and only a single phased solid solution is present. This treatment consists of heating the alloy to a temperature within the α phase region of the phase diagram. The metal is held at this temperature for a duration of time to ensure that all of the θ phase that may be present has had sufficient time to completely dissolve into the solution. The alloy now only fully consists of an α phase. The solution is then rapidly cooled through quenching to around room temperature. The main purpose of such a rapid cooling is to prevent any diffusion and resultant formation of any of the θ phase. The current solution is not at equilibrium. The α phase solid solution is supersaturated with θ atoms. In this state, the alloy is relatively weak and soft.

The second stage, known as the precipitation heat treatment. In this stage, the supersaturated α solid solution is heated to an intermediate temperature within the α + θ two-phase region. Diffusion rates at this selected temperature are more significant. A θ precipitate phase begins to form, fine particles of the alloying element, forming the required secondary phase in the α phase. The alloy is held at this temperature for an appropriate period, allowing it to "age". After the allocated period, the alloy is cooled down to around room temperature. The rate of the cooling in this step is not as important as that of the previous stage (solution heat treatment). Both the solution and the precipitation heat treatment stages can be graphed on a temperature versus time graph.

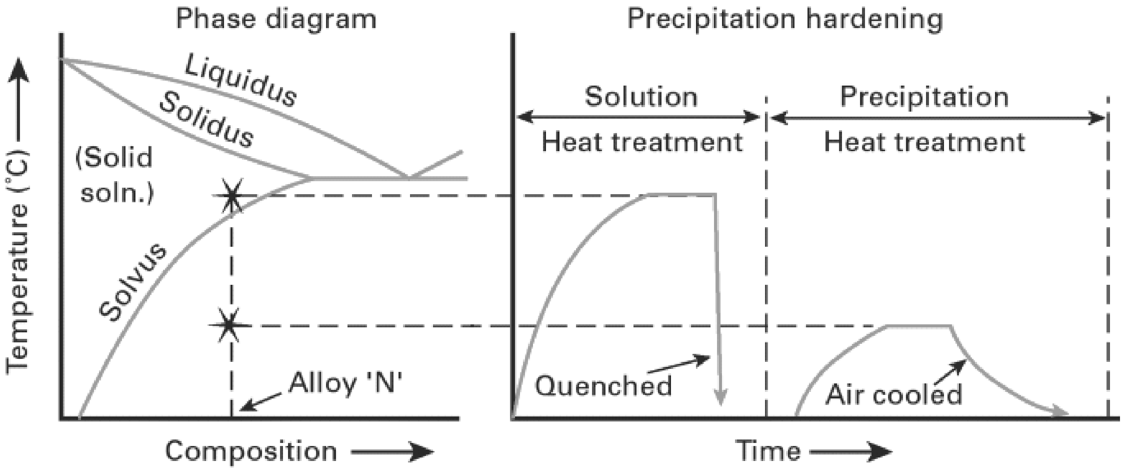

Figure 2.20. Aluminium phase diagram linked to precipitation hardening. (Mathers, 2020)

The above figure displays both the solution and precipitation heat treatment stages. The temperature is placed next to the phase diagram to clearly display what part of the phase diagram and what phases are present at each respective temperature.

The strength and hardness of this alloy caused by the presence these θ particles depend primarily on both the precipitation treatment temperature and the aging time for which the alloy was held at this temperature. In some alloys, spontaneous aging occurs even at room temperature over long periods of time. This is called natural ageing.

The effect of these θ phase particles on the strength can be illustrated on a yield strength versus time graph at a constant temperature:

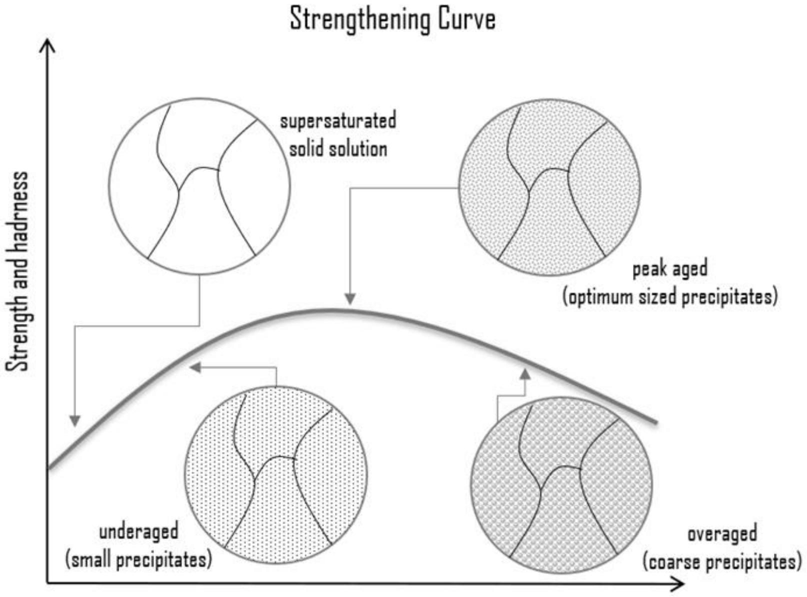

Figure 2.21. Precipitation hardening – strengthening curve. (Abbass, 2015)

There is an optimum time for which aging can occur, this is depicted in the figure as the peak aged condition. At this specific time, the precipitates have reached an optimum size and dispersion. Before this stage, the precipitates are too small. A time longer than this results in precipitates that are coarser, denoted overaged. Past the peak aged condition and into the overaged stage, the strengthening and hardening begins to diminish as time increases.

The temperature at which the precipitation heat treatment occurs has a large effect on what yield strength can be achieved. A lower temperature means a greater yield strength can be attained, but it may take an insensible time to attain such strength values. A higher precipitation temperature results in reaching peak hardness and strength in a shorter time, but the value of this peak strength is lesser.

The small uniformly dispersed particles formed through this mechanism are the means through which the alloys are strengthened. They do this by presenting an obstacle to the motion of dislocations. The presence of these second phase particles represents a distortion in the matrix lattice (Power, 2017).

The obstacles which hinder slip can either be, the strain fields formed around the second phase particles, the particles themselves or both (Power, 2017).

In a study by Gornonstyrev, 2015, in the precipitation heat treatment process, there are several precipitate phases that form in a specific sequence. For example, in an aluminium-copper alloy of composition 96 wt% Al – 4 wt% Cu, there are four precipitate structures that can be recognised: (1) GP-1 zones, (2) GP-2 zones (also called θ’’), (3) the θ’ phase, and (4) the θ - ($CuAl_2$) Phase. In the early stages of the aging process, a large number of very small solute-rich clusters form and they are completely coherent (Gornonstyrev, 2015). Coherent particles are those that form on the FCC lattice of the matrix. The atomic dimensions of these solute-rich regions differ to that of the lattice, and thus, strains occur in the lattice around the clusters. The strain field that are resultantly formed are known commonly as Guinier-Preston zones or GP-1 zones.

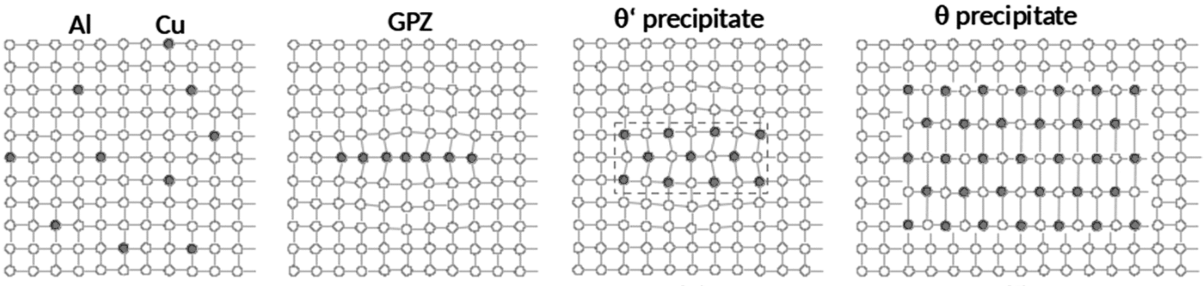

Figure 2.22. Precipitation in Al-Cu supersaturated solution (Gornonstyrev, 2015).

These GP-1 zones rapidly grow until they are of a certain size, typically of the temperature of aging and then all growth stops. The size of these particles is between 3-7 nm thick at room temperature and 10-15 nm at 70-130 ° C. With increased growth of these GP-1 zones, comes increased hardening and decreased ductility. This hardening comes from the restriction to dislocation slip caused by the strain and distortion of the lattice (Gornonstyrev, 2015). As the aging process progresses, the GP-1 zones are soon replaced by GP-2 zones. These Gp-2 zones are larger than the Gp-1 one zones. Their size ranges from between 10-100nm and 1 – 4nm thick. Optimal mechanical properties can be attained by growing the GP-2 zones as large as possible without the formation of the θ′ phase.

As the aging continues, the θ′ phase forms, causing recrystallisation, softening (a decrease in hardness), this is the process of over aging. The lattice parameter of the θ′ phase is different to that of the matrix and its shape is a tetragonal structure. The strains that exist are not coherent and each particle is surrounded by a ring of dislocations (Gornonstyrev, 2015). Sizing of this θ′ phase ranges from 10-600nm in diameter with a thickness of between 10 – 15nm, depending on time and temperature. With increased time, the θ′ phase is slowly replaced by the θ ($CuAl_2$).

Not all structures form at all aging temperatures. For instance, below 80 ° C it is very unlikely that the formation of precipitates progresses beyond the GP-1 phase. If given a sufficient time period and a temperature of above 220 ° C, the θ′ phase is present. At higher temperatures, the Gp-1 zones do not appear at above 180 ° C; the θ′′ phases do not form above 230 ° C. maximum hardness is reached sooner at higher temperatures, but this hardness value is generally lower (Gornonstyrev, 2015).

In Al-Mg-Si alloys, 6xxx series alloys, the precipitation phases found also follow a specific sequence, however this sequence is different to that found in the Al-Cu system. In a study by Edwards 1998, the sequence that the precipitates formed was as follows:

Co clusters containing Mg and Si atoms -> Small precipitates of unknown structures -> B′′ needle shaped precipitates -> B′ lath shaped precipitates and B′ rod shaped precipitates. (Edwards, 1998)

Later in a study in 2010 by Fang, the unknown structures were then later defined as Guiner-Preston zones with the sequence found being labelled as:

Supersaturated solid solution -> G.P zones -> metastable B′′ precipitates -> metastable B′ precipitates -> stable B phase + Si particles. (Fang, 2010)

Guiner-Preston zones(GP Zones) were identified long before this by two scientist, Andre Guinier, and G. V. Raynor Preston. This led these structures being named after the two scientists. GP Zones are nanoscale clusters or precipitates that are found to form mainly in 6xxx series alloys. These precipitates are the first formed through artificial ageing and are instrumental in the strengthening of 6xxx series alloys.

The goal of precipitation in these Al-Mg-Si alloys is to achieve a uniform distribution of fine precipitates, mainly B′ and B′′ which subsequently act as obstacles to dislocation slip when the material is exposed to external stresses or forces. This results in increased strength in the material through plastic deformation, yielding the desired improved mechanical properties. Dependent on the specific alloying system and composition of the specific alloys, this precipitation sequence can be varied (Andersen, 1998).

In Julia Osten's literature: development of precipitation hardening for high strength alloy AA7068, it is understood that the conditions such as temperature and timings of each step in the precipitation hardening process largely alter the strength of the final product (the alloy material). A compromise must be struck to ensure high strength but still a sufficient ductility for the material.

In Osten's paper, aluminium wrought alloy AA7068 (AlZn7.5Mg2.5Cu2) was supplied as an 8mm rolled bar. The mass fractions used in the study are as shown in table one. The following composition was chosen as it allowed for adjustments for very high strength.

Table 2.1. Mass fraction of alloying elements of the investigated material in %. (Osten, 2019)

Aluminium Alloy	**Mass Fraction in %**								
	Si	**Fe**	**Cu**	**Mn**	**Mg**	**Cr**	**Zn**	**Ti**	**Zr**
AA 7068	0.052	0.076	**1.60**	0.008	**2.96**	0.013	**8.43**	0.022	**0.084**
AMS 4331	≤0.12	≤0.15	**1.6-2.4**	≤0.10	**2.2-3.0**	≤0.05	**7.3-8.3**	≤0.10	**0.05-0.15**

The quench rates or cooling rates were ranged between 0.01 to 10K/s in this investigation. For this specific alloy, Osten et al found, using SEM techniques, that for slower rates the grain boundary precipitates became fairly large as a result of a longer time to alloy growth of the particles. Within those large particles, often, even brighter particles could be visible which the study states could have been Fe rich primary particles. And the opposite could be said for the faster cooling rates, the quenching induced particles were stated to become smaller with increasing cooling rates.

For this specific alloy, it was found that an appropriate solution treatment temperature was to be 475C – 480C.

The soaking duration was to be set to 30 minutes, as there was no difference between 10 mins and 60 mins at 475C.

There was a 3% stretching performed on the sample before any age condition was applied. This aging condition was described as 10 hours at 130C.

The aforementioned conditions gave rise to a yield strength of 626 MPa. A tensile strength of 651 MPa and a fracture elongation of 10%.

In a study by Shuiqing Chi et al.: The Influence of Zn addition on precipitate behaviour and intergranular corrosion of Al-Mg-Si alloys, the effect of additions of 0.2wt% Zn on the microstructure, age hardening and intergranular corrosion (IGC) properties of Al-Mg-Si alloys were observed. These parameters were investigated using: a scanning electron microscope (SEM), a transmission electron scanning microscope (TEM), hardness testing and electrochemistry testing.

Shuiqing and his partners found that the addition of these minor levels of Zn significantly accelerated the conversion of GP Zones into B'' precipitates. They also found that through this, the intragranular precipitates became more densely distributed in the crystal matrix and also were morphologically smaller. All these features proved to be advantageous to the precipitation strengthening of the material leading to increases in hardness as well as the age hardening response. The material displayed a peak hardness of 125.8HV which was an increment of 12.7HV in comparison to the alloy without the added Zn.

2.4.5 Dislocation- Precipitate Interactions

As in all other strengthening mechanisms discussed, dislocation interactions are vital in attaining the desired strength properties. The presence of dislocation lines and their motion are integral in strengthening a material. Dislocations are formed during the solidification processes as well as when the lattice undergoes plastic deformation. Grain boundaries are also a source of dislocations as there are many vacancies present in this region due to the mis-orientation of the two adjacent grains on either side of the boundary. Dislocations can also be generated through many other defects found in crystal lattices including, twin boundaries, stacking faults, precipitates, and inclusions, disclinations, impurities and internal strain fields.

Dislocations reduce the stress required to plastically deform materials. The dislocation-precipitate interactions however are useful in enhancing the strength and hardness of the metallic material that has been aged.

As aforementioned, precipitates become present in the matrix through the strengthening mechanism of age hardening. The combination of the temperature and the time at this temperature determine the size of these particles (Abbass, 2015). The size and dispersion of these secondary phase particles largely affects the degree of strengthening achieved by the technique. The reason for this increased strength can be explained by the size of the precipitate particles formed and consequently how these particles are to interact with the dislocation lines that attempt to traverse the region they reside in. Small finer precipitate particles interact with dislocation lines in a different way to larger, coarser precipitate particles.

During dislocation motion, when a dislocation line comes across a precipitate and attempts to pass it, the precipitate acts as a pinning point for the dislocation and causes an obstacle to its slip. These precipitate that are present in the material matrix have the effect of increasing dislocation storage when they pin the dislocations as this action promotes dislocation accumulation withing the material. this increased density of dislocations stored around precipitates can result in work hardening, further strengthening the material.

Another way through which dislocation storage is increased by these precipitates is in where they act to generate new dislocations. When this interaction occurs between dislocations and precipitates, especially during plastic deformation, stress fields around these precipitates lead to nucleation of dislocations.

These multidirectional interactions between dislocations and precipitates also significantly affect the evolutions of precipitates. The nucleation, growth, coarsening and dissolution of these precipitates are heavily affected by the presence of dislocation structures in the crystal lattice. During the ageing process, dislocations act as favourable sites for the nucleation of the new precipitates formed in the process. The regions around dislocations have higher relative energies, reducing the activation energy required for nucleation. These means precipitates nucleate more preferentially in these areas. This heterogeneous nucleation of precipitates is further enhanced by the strain fields that preside around said dislocations. These strain fields work to alter the local chemical potential which promotes clustering of solute atoms, consequently leading to nucleation of new precipitate particles.

Once these precipitates have been nucleated, the presence of dislocations aid in the diffusion of these solute atoms. Dislocation cores act as quick diffusion paths as compared to the perfect crystal lattice which accelerates the growth of the precipitates as solute transport is increased to the growing precipitate. Dislocation networks further the coarsening of the precipitates present in the matrix. The dynamics of the coarsening are rapidly affected by the defect networks through the redistribution of solute atoms and enhanced solute mobility.

One way in which the precipitate impedes the motion of the dislocation is when the precipitate particles are fine, or coherent and/or not overly hard, the dislocation line uses energy to cut through the precipitate particle.

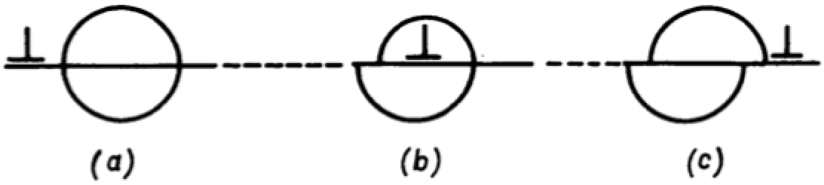

Figure 2.23. Cutting of a precipitate. (Smallman, 2017).

In the figure above, the mechanism through which the dislocation line cuts the precipitate particle is shown. The particle passes through a coherent particle which is on the same slip plane as in the matrix. This motion requires more stress than the movement through the normal matrix.

When the precipitate particles are large, the precipitate impedes the motion of dislocation lines through Orowan looping, otherwise known as bowing:

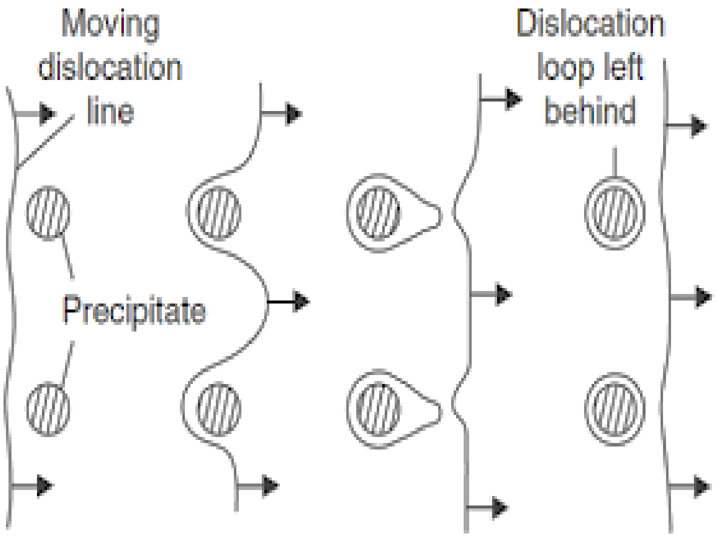

Figure 2.24. Dislocation-Precipitate Interaction, Orowan Looping. (Smallman, 2007)

Orowan looping occurs primarily when the precipitate particles are large and coarse or are incoherent to the crystal matrix or if the precipitate is extremely hard. As the dislocation line attempts to pass the precipitate particle, it begins and continues to bend around it as it cannot shear the particle. This process continues until it completely encloses the precipitate forming and leaving behind a dislocation loop around the particle. Once this mechanism has taken place, the dislocation can then move on. This looped precipitate particle will then form further obstacle to any other dislocation lines that attempt to pass it.

Orowan stress is the stress required for a dislocation to push between particles. It is given by the following formulaic equation:

$$\Delta\boldsymbol{\tau}_{\boldsymbol{OR}} = \frac{\boldsymbol{2E_L}}{\boldsymbol{b}(\boldsymbol{L}-\boldsymbol{D})} \qquad (2.4)$$

Where $E_L = \alpha Gb^2$ is the dislocation line tension. L is the interparticle distance and D is the particle diameter.

There is a critical size of coherent precipitates as this leads to the greatest strengthening caused by the precipitates. As the particle size increases, cutting through it becomes more difficult:

$$\Delta\boldsymbol{\tau}_{\boldsymbol{cutting}} \propto \boldsymbol{r} \qquad (2.5)$$

The dislocations will then tend to bow around these larger particles by Orowan looping:

$$\Delta\boldsymbol{\tau}_{\boldsymbol{cutting}} \propto \frac{\boldsymbol{1}}{\boldsymbol{r}} \qquad (2.6)$$

Strengthening mechanisms by which the hardening is increased is through antiphase boundary formation (APB), Interfaces, coherency strain hardening, stacking fault defect and the modulus effect. These mechanisms all contribute to the strength achieved by the precipitation hardening process. They are listed in order of mean strength contribution of the processes.

The total strengthening is given by the sum of the individual contributions:

$$\boldsymbol{\tau}_{\boldsymbol{total}} = \boldsymbol{\tau}_{\boldsymbol{APB}} + \boldsymbol{\tau}_{\boldsymbol{int}} + \boldsymbol{\tau}_{\boldsymbol{coh}} + \boldsymbol{\tau}_{\boldsymbol{SF}} + \boldsymbol{\tau}_{\boldsymbol{mod}} \qquad (2.7)$$

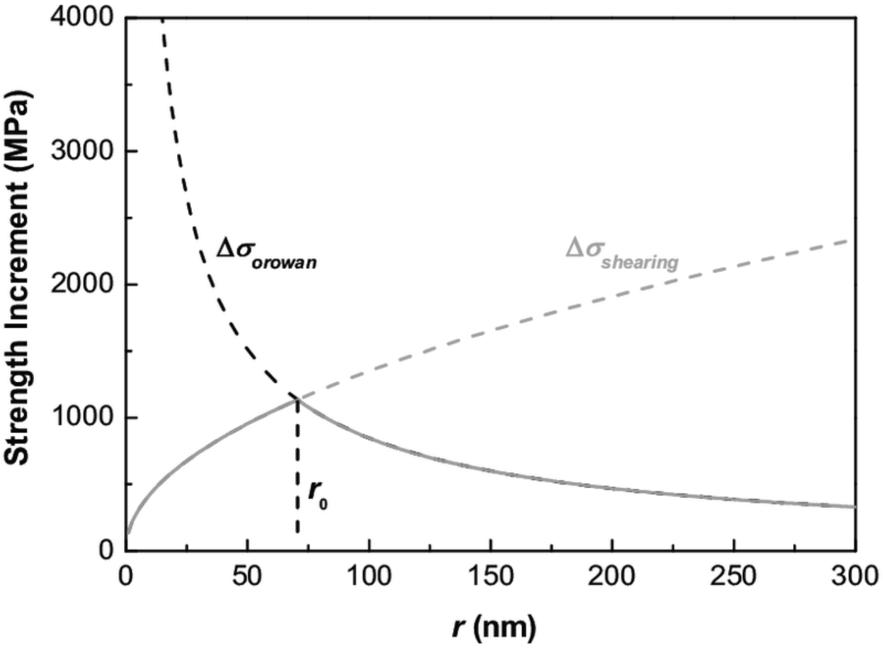

Figure 2.25. Strength versus precipitate particle radius. (Wang, 2018)

A critical radius of the particle at which the maximum strengthening occurs exists and this lies where the two lines overlap. This critical radius is usually between 5 – 30 nm. This explains the aging graph where strength is plotted against time. Extremely fine particles which are present in the underaged condition cause less strengthening and large coarse grains present in the overage condition are detrimental to the strengthening of the alloy.

There are a number of precipitate interfaces that a dislocation in motion may come across and these all affect its ability to continue motion. The precipitate can be coherent, semi coherent, and incoherent with the lattice matrix.

If the precipitate phase is coherent, there is perfect registry between it and the lattice matrix. They are said to be continuous. Elastic strains may exist around them and a widespread distortion of the crystal lattice. As the size of this coherent particle increases, so does the magnitude of the strain field around it. Semi-coherent precipitates are those that are coherent with the matrix on some faces but not all. This incoherency is compensated by misfit dislocations. The introduction of dislocations reduces the strain energy. Incoherent precipitates are said to have no continuity with the lattice matrix. Incoherent precipitates only block slip if it lies directly in the path of the dislocation. There are negligible strains in this type of particle.

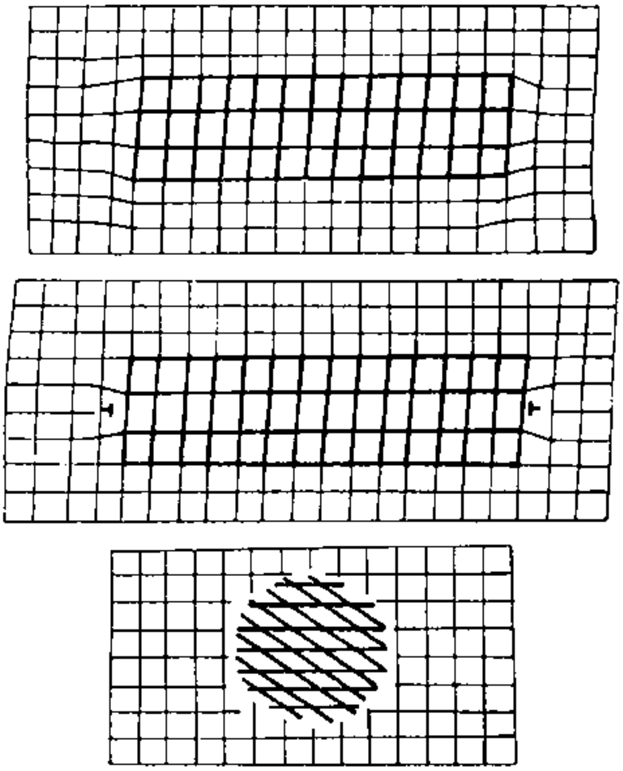

Figure 2.26. Precipitate coherency. (Phaniraj, 2017)

In Figure 2.26, there are three images, the image at the top displays the precipitate and how it is coherent with the matrix, the second picture (in the middle) demonstrates a precipitate particle with a semi-coherent orientation relative to the matrix. The illustration at the bottom is of an incoherent particle.

Generally, the interfacial free energy is minimized when the secondary phase and the primary phase are better matched. Incoherent particles have a higher energy and are more mobile due the increased freedom of atomic motion. The stresses present in the system as the precipitates age and grow largely influence the shape the precipitate presents. The following figure can illustrate how the shape is changed as the strain energy is altered:

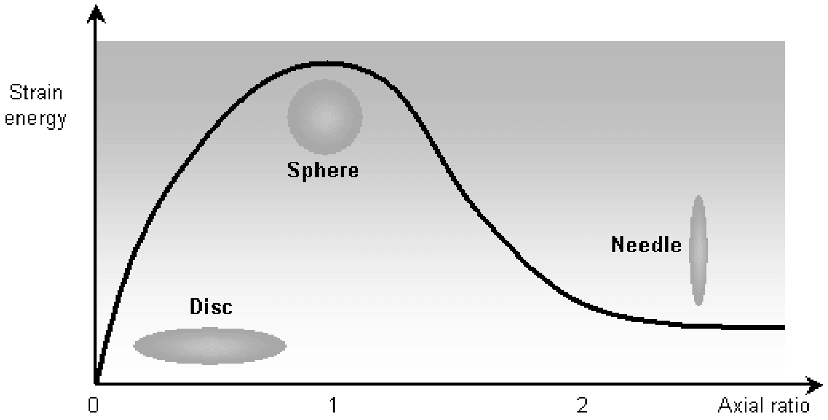

Figure 2.27. Precipitate shape. (Awan, 2017).

Generally, growth as discs is preferred. In reality, precipitates have both coherent and incoherent interfaces to the matrix. The greater mobility of the incoherent interfaces leads to faster growth in these directions. The growth in these directions is what brings about the disc like shape.

The presence of defects in the material causes an increase in energy of particles in the lattice as a perfect lattice with a regular structure has the lowest energy as the atoms sit in energy wells. These energy fields around dislocations and precipitates means that they can also interact in a diffuse manner, where the dislocations are interacting with the strain fields caused by the precipitates (Hull, 2011)

2.5 Aluminium Alloy Faults and Limits to Strength

In Chi's (2020) study, as heat-treatable alloys, Al-Mg-Si alloys have been and are widely used in the automotive manufacturing industry. They have become the preferred material for automotive body plate panels. This is said to be due to their high specific strengths, good formability, excellent corrosion resistance and great weldability.

The study however goes onto to say that these alloys still face some challenges in regard to their applications such as how to further improve the aforementioned mechanical properties as well as attaining a quick age hardening response.(Chi, 2020)

There are therefore limitations to the mechanical strength of these alloys as well as other these mechanical properties. Work, research, and further developments are important in stretching these boundaries to amass even yet increased mechanical properties.

Studies such as that carried out by Zhi-Xiu et al in 2012, investigating the effect Cu content on microstructures and properties of aluminium alloys show that the incremental addition of Cu in Al-Mg-Si-Cu alloys can indeed increase the age hardening response but simultaneously causes increased susceptibility to corrosion. The Cu content ranged from 0.6 – 0.9 wt%. The higher the Cu content, the more sensitive the alloy is to intergranular corrosion. The addition of Si to the alloy is also shown in this study to lead to enhanced mechanical properties. However, the detriment of this element's addition is the area known as the precipitate free zone (PFZ) dissolves as the anode. This is as a result of the silicon particles precipitating in the grain boundary. Al-Mg-Si alloys with excess magnesium can have much improved corrosion properties, but their age hardening responses are hindered.

When comparing Al-Mg-Si (6xxx) alloys to Al-Zn-Mg (7xxx) alloys (which are widely used in aerospace applications as a result of their high strength). It is shown that the precipitation sequence of the Al-Zn-Mg alloys is super saturated solid solution (SSSS) --> Guinier-Preston (GP) zones --> η' --> η($MgZn_2$).

The η' phase as described in the literature of Chi et al (2020) is considered to be the main strengthening precipitates of the Al-Zn-Mg alloys at the peak age state. Further, the atomic radius of a Zn atom is close to the atomic radius of an aluminium atom, 135 and 125 picometers respectively. This means there is low lattice distortion in the crystal structure of said alloys. Therefore, under the premise of ensuring the good forming capability of the alloy, the age hardening response of these Al-Mg-Si alloys can be improved with the addition of Zn atoms.

The precipitation sequence of Al-Mg-Si alloys is typically: SSSS --> Si clusters and Mg clusters --> dissolution of Mg clusters --> Mg, Si co-clusters --> GP zones --> β'' --> β' --> β. In a recent study by Saito et al. the addition of Zn atoms did not change this precipitation sequence of Al-Mg-Si alloys. Cai et al. found that the addition of Zn atoms aided in producing a faster and higher age hardening response. The electrical conductivity at the beginning of aging was also reduced.

2.6 Deformation Modes

Deformation is the action of changing or distorting the geometrical dimensions of a solid object. This is usually caused through the application of an external force. When the force is applied to the material or the solid object, the deformation caused may be either elastic or plastic (reversible and irreversible respectively) and this is dependent on the material properties and the magnitude of the force applied. Two terms describe the force on objects that are undergoing deformation: stress and strain, where stress is a force acting on a solid object that produces a strain. Stress is a force applied over an area and is given in units of Force/Area (Pascal (Pa)) (Rappaz, 2010).

Deformation or stress can be applied to the material in a number of ways:

- Tensile Stress – this is when forces pull on the object, elongating it. This is similar to the way a rubber band stretch.
- Compressive Stress – this occurs when the forces incident on the object results in it becoming compressed.
- Bulk Stress – when an object is squeezed from all of its sides. This is similar to a submarine experiencing forces from all over in the depth of the ocean.
- Shear Stress – this type of stress arises when the deforming forces are applied tangentially to the surface of the object.

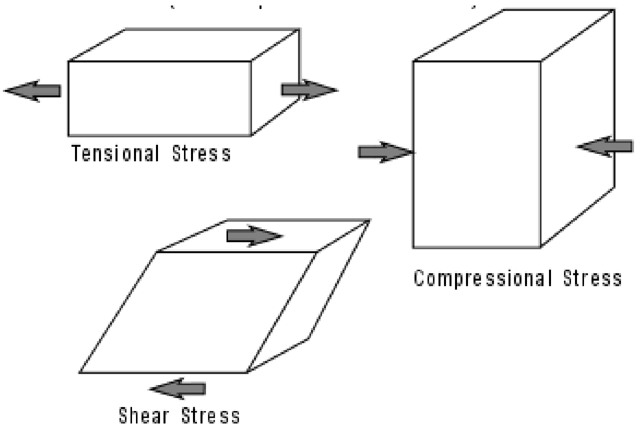

Figure 2.28. Deforming forces (Nelson, 2015)

The aforementioned forces can be applied to aluminium structures through processes such as rolling, bending, and stretching.

Rolling is a technique through which compressive stresses can be applied to the metal. The rolling can produce a piece of metal that is a plate or sheet. The dimensions of the structure are reduced during this kind of mechanical processing. The sample to be rolled is rolled through two large hard steel rolls, the gap left between the two rolls determines the degree of deformation that takes place. Rolling can be done either hot – with hot softened aluminium – or cold with aluminium at room temperature. Hot rolling aluminium prevents strain hardening of the metal as the metal undergoes deformation whilst cold rolling means that the work hardening can occur. Cold rolling requires more energy as the metal is harder, but it generally produces a product with a smoother final surface.

Stretching is a technique that brings about tensile stresses. The piece of metal experiences elongation along the stretching direction. This deformation takes place on a piece of apparatus known as a stretcher, the sample is clamped down on both sides and pulled in opposing directions. The degree of deformation can be controlled by achieving differing amounts of strain.

Bending is a technique that combines a mixture of compressive and tensile stresses. When a piece of metal is bent, the inner side of the sample undergoes compression, whilst the outer experiences tensile stresses. The degree to which the material is bent changes the amount of deformation that is introduced to the material.

2.7 Texture

Crystallographic texture refers to the distribution of grain orientations in a metal. The grain orientation can be defined as the crystal unit cell orientation relative to the external coordinate system. For example, in an extruded sample, the texture of the crystals in the material are characterised parallel to the extrusion direction, normal direction and transverse direction.

In a given material, there may be a preferred orientation of the grains in the crystalline structure. This preferred orientation can be generated from a range of processes including recrystallization and deformation. The texture found in a polycrystalline material greatly affects its measured mechanical properties as there can be anisotropy where the mechanical properties vary with direction. Properties such as yield strength, tensile strength and hardness can vary based on the texture of the material. These properties are all directionally dependent due to the slip systems in the respective grains and how they orientate relative to the direction of the applied force. Specific crystallographic orientations have more active slip systems meaning deformation along these directions occur more easily resulting in lower measured nominal values. When the external force is applied in other directions however, the measured properties would differ leading to anisotropic strengths and hardnesses of the material. If an aluminium sample had a strong (111) texture, slip would occur more easily on the (111) plane. It is therefore critical to understand the effects of texture and control the measurements of these mechanical properties when testing anisotropic materials.

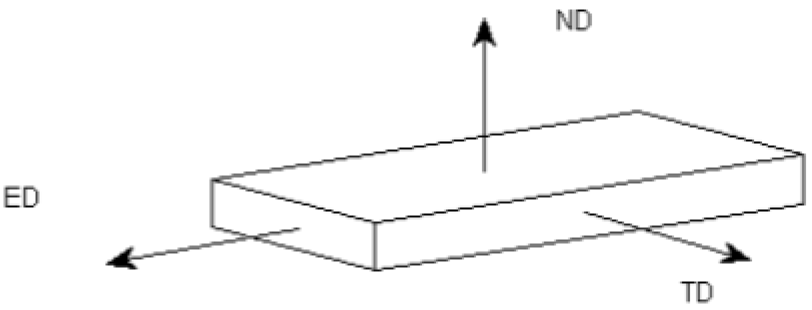

Figure 2.29. Extruded specimen sample directions. (Padovano, 2012)

Pole figures, also known as stereographic projections, illustrate orientation distributions of crystalline grains/planes in graphical form. These graphical representations aid in visualising and analysing crystallographic textures in polycrystalline materials.

Pole figures generation can be illustrated by putting the sample in the centre of a unit sphere. Each crystal in the sample with its crystallographic orientation projects and corresponds to a point on the resultant pole figure respective to the macroscopic coordinate system. In rolled and extruded flat profiles, the normal direction points toward north of the sphere.

Pole figures are built by drawing a line parallel to the characteristic direction. This parallel line intercepts the sphere's northern hemisphere. A line of intersection is then drawn connecting the point of the intersection to the south pole. At some point of this line, there is an intersection with the equatorial plane, creating a pole. Each unique intersection of this equatorial plane corresponds to the crystallographic orientation of a single grain. By collecting this information from all grains in a sample, understanding of the overall texture of the polycrystal can be garnered and analysed.

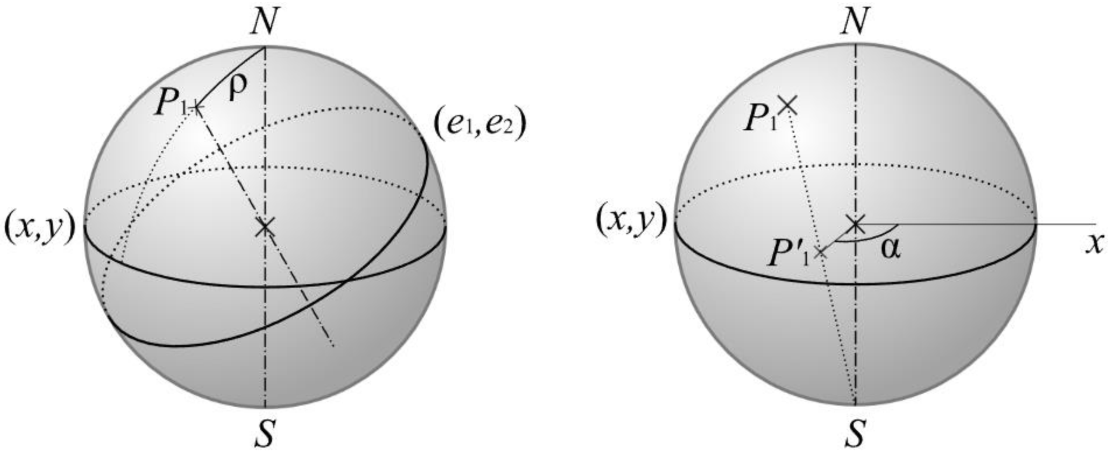

Figure 2.30. Stereographic projection of a pole. (Depriester, 2014)

Euler orientation space is a 3-dimensional space that gives a mathematical system through which crystallographic orientation of grains can be described. Euler angles are sets of three angles in this 3-dimensional space that define the rotation about the three zone axes (x, y and z). These rotations represent the grain orientation rotated from a cube position. Euler angles ϕ_1, Φ, and ϕ_2 describe rotation about the z-axis, x-axis and z-axis respectively. By convention, in material science, the Bunge definition corresponding to the ZXZ notation is applied.

Figure 2.31 displays how the Euler angles represent sample texture in Euler space. This space is described as a Cartesian plot of 3 dimensional space with axis set as the three Euler angles. ϕ_1 and ϕ_2 give values from 0 to 360 degrees whilst Φ only goes up to 180 degrees.

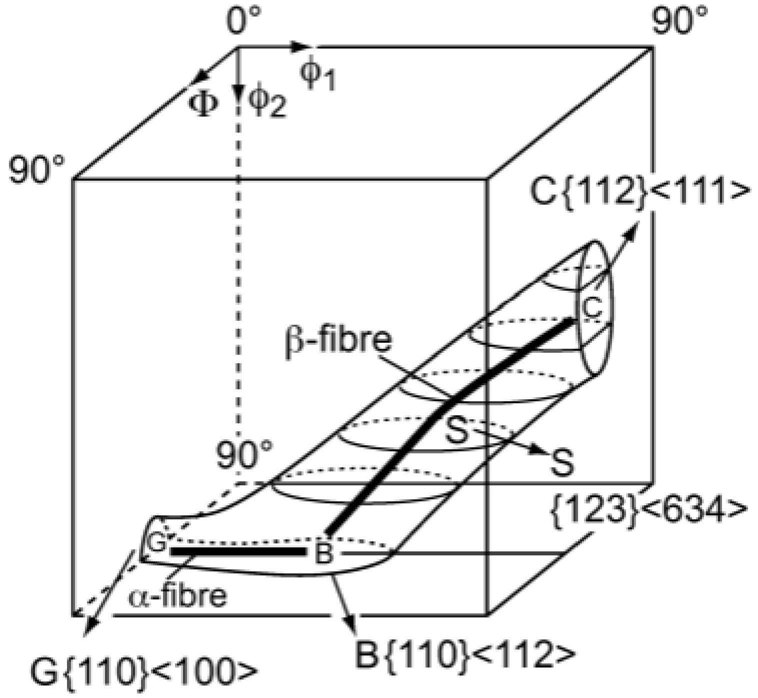

Figure 2.31. Euler space showing orientation distribution of texture fibre components (Goyal, 2011)

In cubic structure where there is symmetry, the range for these angles are reduced to 0-90 degrees as illustrated in Figure 2.31 which is an Orientation Distribution Function (ODF).

2.8 Thermomechanical Process (aDA)

The alloy to be used is a modified version of the 6008-aluminium alloy. This alloy is said to be a crush alloy, as it has great crush properties. The main alloying components are magnesium and silicon with small additions of Vanadium.

Thermomechanical processing is an umbrella term used in the automotive industry and refers to a process where workpieces are subjected to high temperature treatment as well as mechanical deformation. An example of a thermomechanical process is extrusion, stretching and artificial ageing. This sequence results in a material with further improved mechanical properties. However, the thermomechanical process is not exclusive to just extruded samples and can be incorporated with hot rolled and forged processed materials. The thermomechanical processes are chosen based on the properties required of the material in its final product state.

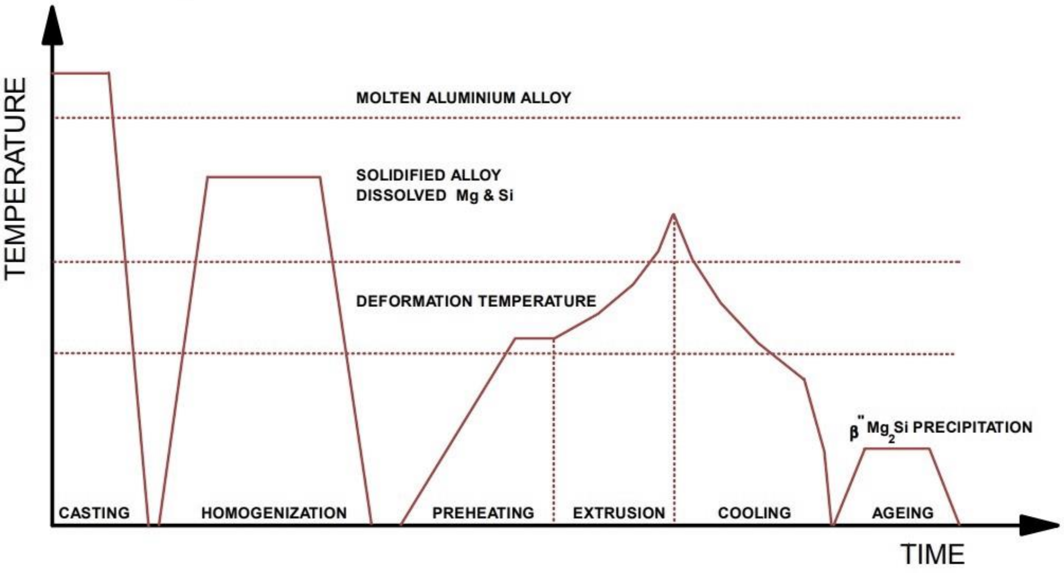

Figure 2.32. Schematic of Aluminium alloy thermomechanical sequence. (Li, 2021)

The figure above shows a common processing path for thermomechanical processing of extruded aluminium alloys.

The aDA process is one developed and adapted by Constellium, it produces an alloy with overall increased mechanical properties. The steps in this adapted process include a pre-aging treatment (small a), a deformation (D) of the sample and a final ageing step.

In the process, the alloy is in the deformed (extruded) state. The alloy is deformed at a high temperature and is then quenched. The sample is thus in the solution treated and quenched state. Where this process differs to that normally found is industry (normal T6), is that rather than this being followed directly by the precipitation hardening treatment, the aDA process is put in its place. There is a deformation process before the precipitation hardening in the final step. The introduction of this deformation causes the formation of more dislocations in the sample material. Consequently, the precipitation nucleation and kinetics are noticeably improved. In this aDA process, the deformation process in turn boosts the performance of the final age hardening treatment.

Application of these novel thermomechanical processes to understand the effect of the aDA process on the manufacturing induced properties in aluminium alloy parts will aid in obtaining optimal performance in shaped automotive parts for industrial applications in their final product states. in the aDA step, the deformation step can be altered to represent common forming processes, ranging from more simple deformation modes such as tensile, compression, shear and torsion; to more complex modes of deformation such as: roll bending, stretch bending, press bending, rotary stretch and electromagnetic pulse forming. This will help in gaining an understanding of the potential for generating manufacturing induced properties.

2.8.1 Extrusion

Extrusion is a relatively modern process. The processes used before its development were rolling and forging. Extrusion is unique, in that the potential for shapes formed are plenty and the complexity of these shape cannot be matched by any other forming method. In extrusion, a billet is forced to flow through a die to form a continuous length of a sample shape. The die has a complementary shape to that of the expected shape of the product. The billet is usually cylindrical and is forced through the specific die using a hydraulic ram as can be seen in Figure 2.33. The process can be viewed as a hot working process, as the metal is heated appropriately to give it a suitable flow stress – increasing its softness and ductility. (Sheppard, 1999).

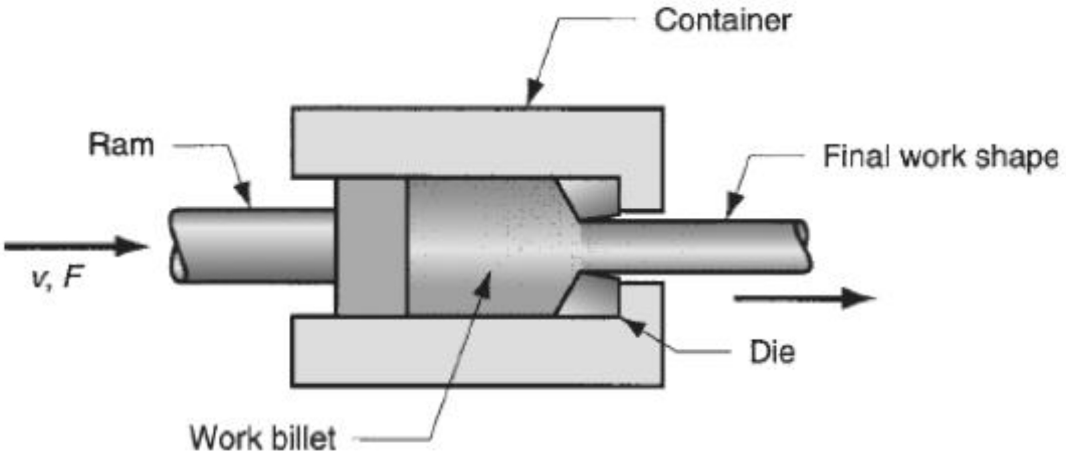

Figure 2.33. Hot Extrusion (Botha, 2016).

The extrusion process can either be direct or indirect. This is largely dependent on the arrangement of the equipment. In direct extrusion, the die is located at one terminal of the container and the billet is pushed from the other end towards it. Whereas in an indirect extrusion process, the die is placed on the end of the ram. The ram is bored out to allow the extruded portion of the billet to pass through it, it moves through the container from one end to the other with the opposite end being closed (Sheppard, 1999).

The extrusion ratio (R_{ext}) or the reduction ratio is a termed used to describe the ratio between the initial cross-sectional area of the material billet (A_0) and the cross-sectional area of the extruded product (A_f). It is given by the following equation: $R_{ext} = A_0/A_f$. The extrusion ratio is important as it affects numerous aspects of the process, including the required force for the extrusion, the material flow, and the final properties that the extruded piece would have. Higher extrusion ratios indicate a greater reduction in the material's cross-sectional area which requires a greater force to push the material through the die which can often result in changes in the materials post extrusion properties i.e. greater hardness, altered grain structure as well as surface/cosmetic defects (Babu, 2022).

The average strain can be calculated roughly using $\in = \ln(R_{ext})$ however this strain varies depending on the position of the extruded material.

For round extruded samples, the deformation mode in the centre of the profiles is near uniaxial elongation according to the work of Verlinden et al 2007. In rectangular extruded samples however, the deformation in the centre of the piece is said to be at first close to that in the round samples, round, but at the later stages of the extrusion it is switched to be closer to plane strain deformation. In the surface of these extruded rectangular workpieces, shear deformation components are experienced as well as plane strain components (Verlinden, 2007).

Chapter 3. Experimental Procedure

This chapter outlines the entirety of experiments carried out, the relevant specifications for each procedure are described in detail. All experiments were carried out on extruded strips of the 6xxx series alloy of thickness 3mm. The samples were solution heat treated and subsequently treated using a specific thermomechanical process. The deformation mode used in the process was alternated to view their respective effects. The forms of deformation used in the investigation were Uniaxial Stretching, Rolling, a combination of Stretch & Roll, and Electromagnetic Pulse Technology (EMPT). The samples were then examined and analysed using advanced techniques such as Optical Microscopy (OM), Scanning Electron Microscopy (SEM), Electron Backscattered Diffraction (EBSD) and Transmission Electron Microscopy (TEM). Mechanical tests such as hardness testing and tensile testing were performed to quantify the enhancements in mechanical properties.

The chart below shows the workflow and the different experimental results collected.

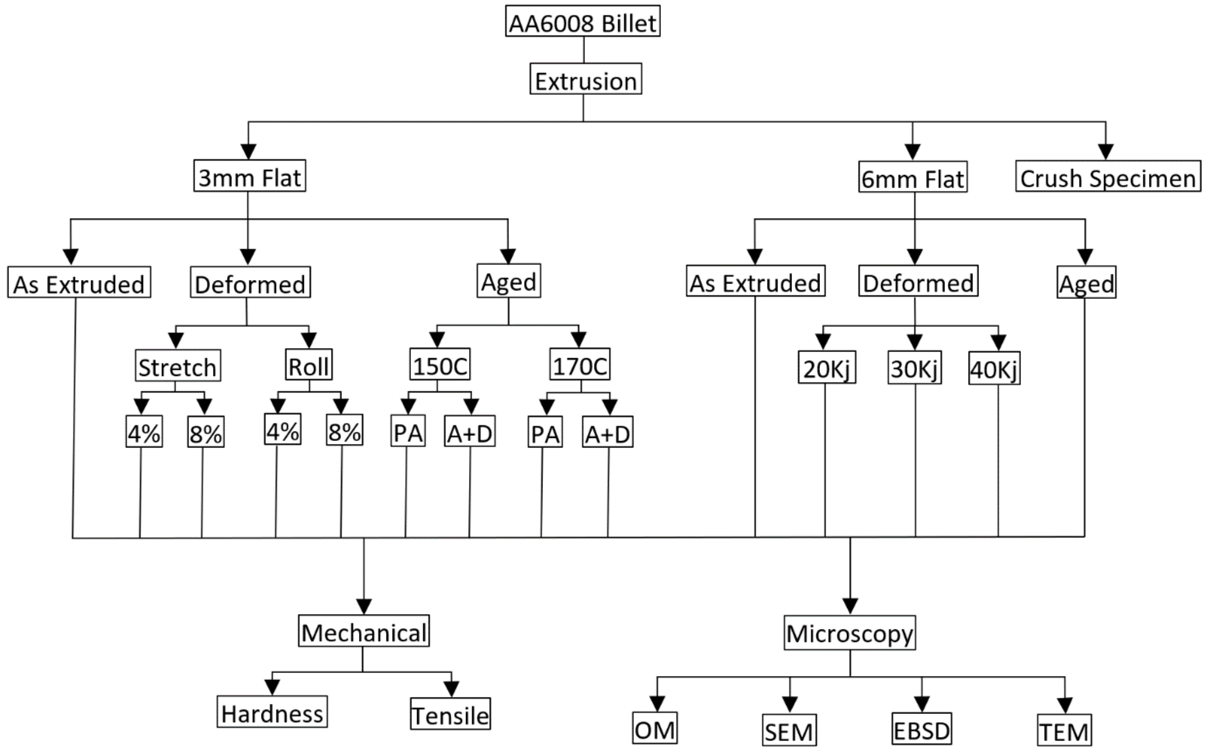

*PA: Preaged; A+D: Aged + Deformed

Figure 3.1. Outline of experimental workflow.

3.1 Materials

3.1.1 Alloy Description

The alloy used is a wrought aluminium alloy described under the designation nomenclature of AA6008. The main alloying elements of the alloy include Magnesium, Silicon, and Copper, plus trace amounts of other elements. As 6xxx series aluminium alloy, the alloy is known to be heat treatable and displays favourable mechanical properties such as high strength and ductility, excellent extrudability and corrosion resistance. This specific alloy is also termed as a "Crush Alloy," which means that its elemental constituents have been mixed to have improved toughness and crush test properties. This alloy is therefore suitable for use in crash exposed areas of vehicles where a good balance of strength energy absorption are required. Studies on the alloy are limited compared to other more common aluminium alloys.

Normal applications for the alloy include automobile product components such as bumper beams. For this application it is essential that the material is strong enough to absorb the impact energies in the event of a collision as well as effectively stabilising the crush response.

The chemical composition by percentage laid between a specified range as described for the material in Table 3.1 below. Standard flat tensile samples were cut from these as-received samples and tested to obtain the properties of the as-extruded material.

Table 3.1. Elemental Composition Acceptable Ranges.

Element	Si	Fe	Cu	Mn	Mg	Cr	Ni	Zn	Ti	V	Zr
Min (wt%)	0.5x	0.1x	0.5x	0.0x	0.5x	0.0x	0.0x	0.0x	0.0x	0.0x	0.0x

Due to commercial security/interest, some details have been omitted.

3.1.2 Extrusion Process

The as-received material was in the form of extruded sheets produced by Constellium with the following dimensions: 200 x 50 x 3mm for the stretching and rolling samples, and 200 x 20 x 6mm for the EMPT samples. The alloy was prepared by DC casting and homogenisation.

The material was cast into billets by Constellium of size 152mm diameter.

The billets were heated to 550°C for 30 minutes to dissolve all Mg_2Si particles and then extruded using a die that produced flat/sheet samples, followed by a rapid cooling via a water quench post-extrusion to prevent the reformation of Mg-Si particles.

The apparatus used for producing the samples was an extrusion press. This set up was able to both heat the material to the correct temperature, taking frictional heat into account, and extrude the material. There was a water quench bath positioned conveniently at the end of the extruder to allow for rapid immediate cooling, post extrusion.

The first die used for the extrusion of the samples used in stretching and rolling can be seen in schematic below displaying the dimensions of the die (Figure 3.2). The die used for the EMPT samples is shown in Figure 3.3.

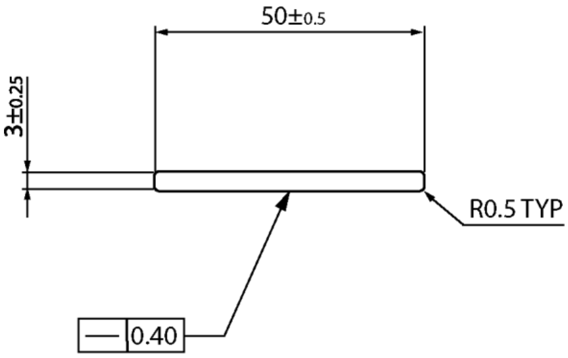

Figure 3.2. Schematic showing die dimension specifications of die used in stretching and rolling experiments, all given numbers are in mm.

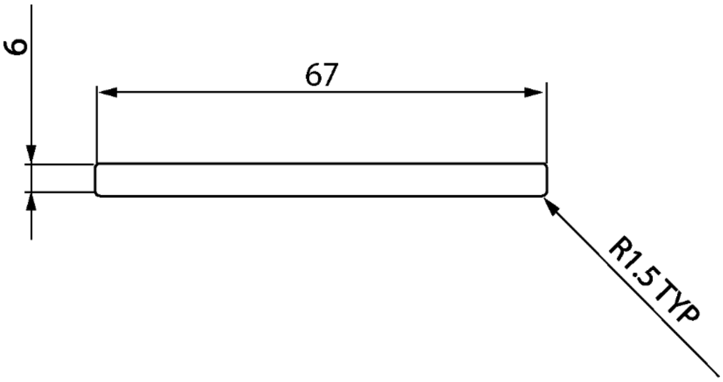

Figure 3.3. Schematic showing die dimension specifications of die used in EMPT experiments, all given numbers are in mm.

The as-received material after extrusion exhibited a recrystallized microstructure with equiaxed grains, although there was a thin peripheral coarse grain (PCG) structure in the surface as a result of hot extrusion, displayed in Figure 3.4.

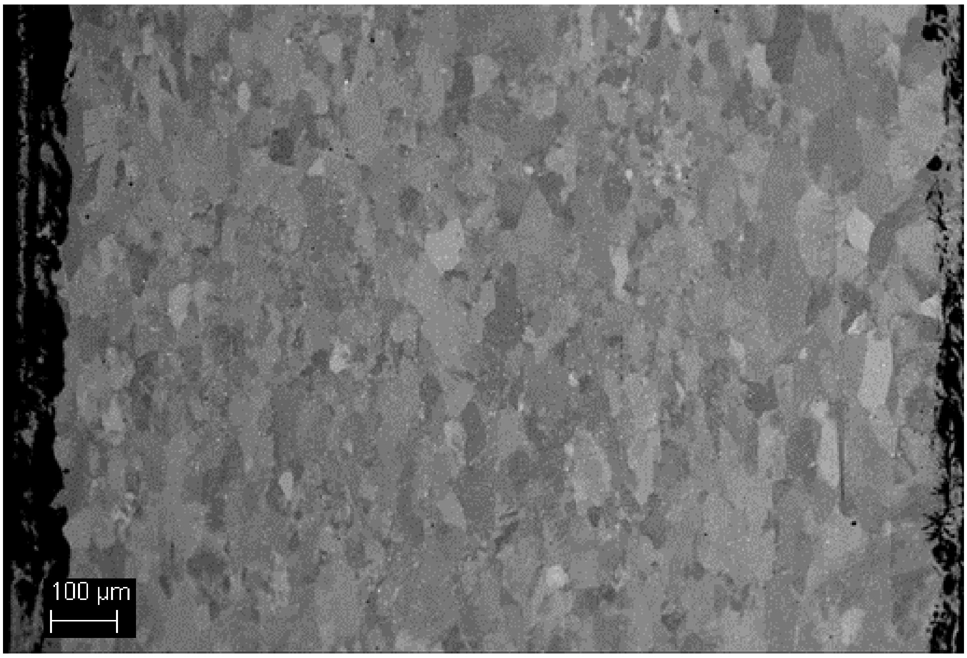

Figure 3.4. SEM Micrograph showing PCGs in the microstructure of an AA6xxx series aluminium alloy in the as extruded state.

3.1.3 Specimen Dimensions

When handling and processing the samples, it is important to define the specific directions in which the samples are loaded and tested as well as the direction the samples are mounted for analytical processing such as SEM & EBSD.

Upon extrusion and the application of different deformation modes, there were changes in the distribution of crystallographic orientations in the material, and consequently the formation of textures. Thus, there was a possibility of anisotropy in the material and the samples might display different properties in each orientation.

As shown in Fig. 3.5, 3 major sample directions are defined as Extrusion/Rolling Direction (ED/RD), Normal Direction (ND), and Transverse Direction (TD).

The ED/RD direction, otherwise known as the longitudinal direction, is the direction in which the material has been processed through either extrusion or rolling or any other similar deformation technique. The ND direction is also known as the thickness direction, and this is the direction that is perpendicular to the surface of the sample. The TD direction is perpendicular to both the ED/RD and the ND direction. It points parallel to the width of the sample.

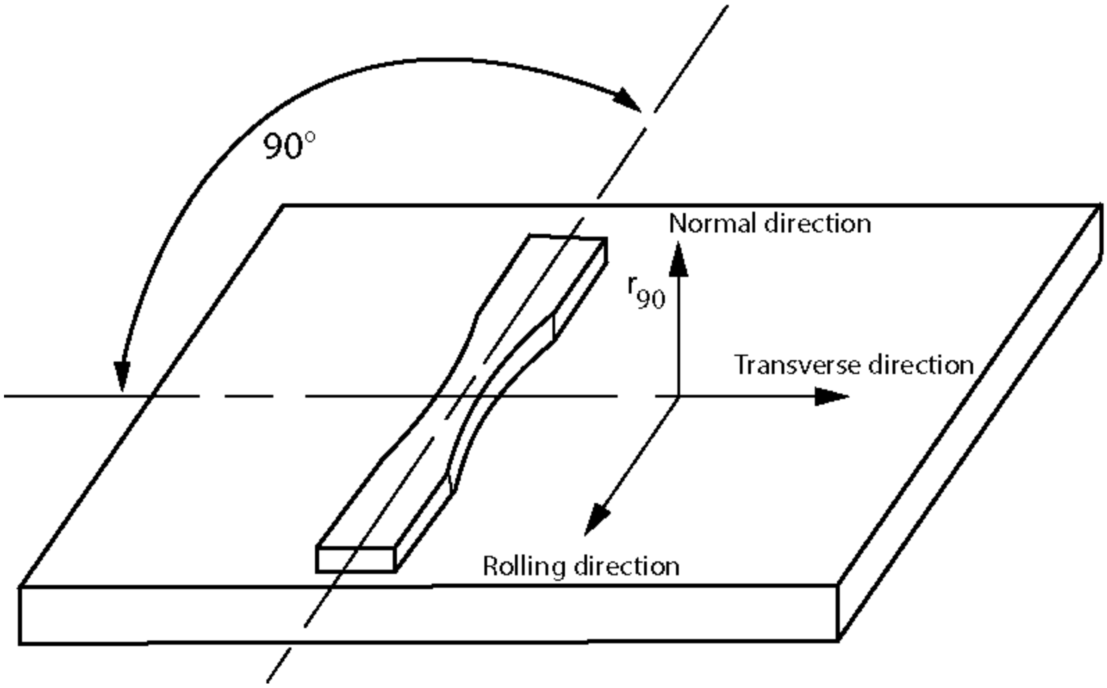

Figure 3.5. Tensile Sample Orientation.

3.2 Deformation

The methods of plastic deformation used in this investigation included stretching, rolling, the combination of stretching and rolling, and Electromagnetic pulse technology (EMPT). Sheet alloy samples were used for deformation methods with dimensions as described above.

3.2.1 Stretching

Stretching was applied using a tensile tester, the same tester used to test the final tensile properties of the material. The tensile tester used was an Instron 5569 tensile testing rig as shown in Figure 3.6.

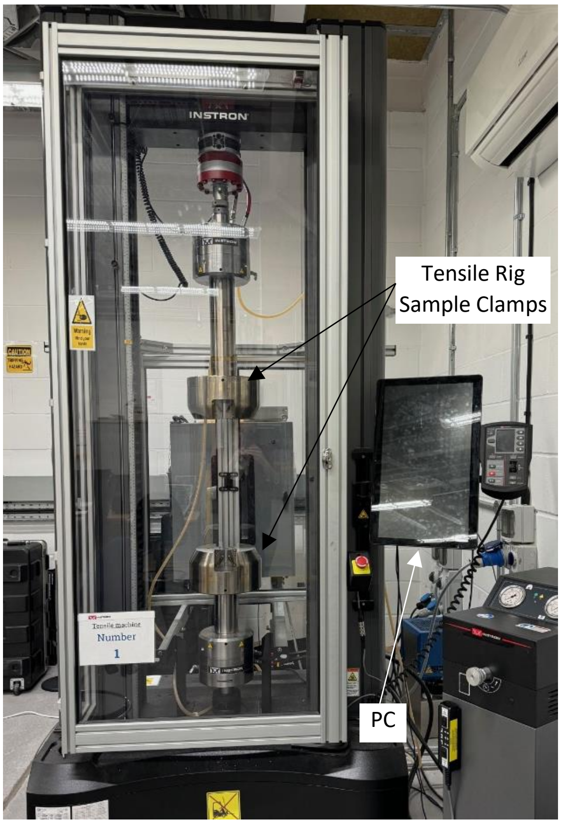

Figure 3.6. Instron 5569 Tensile Testing Rig.

The tester applies a force to the specimen and measures its response to the tensile force. Several parameters are contracted from the testing including proof stress, ultimate tensile strength and elongation which aid in choosing suitable materials for certain applications, although in the stretching test as a deformation method, the main concern was to apply a certain elongation to the sample.

In a stretching experiment, a 3mm alloy sheet sample was clamped to the jaws of the tensile tester and stretched along the extrusion direction. The samples were stretched until a 4% elongation of the material was achieved. In order to overcome the spring back effect, the material was actually stretched slightly past the expected elongation level to achieve the desired elongation level once the sample was de-loaded.

3.2.2 Rolling

Rolling deformation was applied to the 3mm sheets. The rolling reduction was achieved using a 300x150mm two-high Ford rolling mill, which was previously refurbished by Siemens. The sheets were rolled to achieve a 4% and 8% reduction, respectively. Plane strain conditions were assumed as there was a minimal reduction in the transverse direction relative to all other sample directions. Due to plane strain conditions, when the equivalent strain was calculated, it was shown that a 4% roll reduction was approximately equivalent to the 4% elongation achieved in the stretched material.

$$\varepsilon^{\circ} = \frac{\sqrt{2}}{3}\left[\left(\varepsilon_x-\varepsilon_y\right)^2+\left(\varepsilon_y-\varepsilon_z\right)^2+(\varepsilon_z-\varepsilon_x)^2+6\left(\varepsilon_{xy}\right)^2+6(\varepsilon_{xz})^2+6\left(\varepsilon_{yz}\right)^2\right]^{\frac{1}{2}} \qquad (3.1)$$

ε_x, ε_y, ε_z, ε_{xy}, ε_{yx} and ε_{yz} are strain tensor components

For the application of the rolling deformation, the thickness reduction was done in steps. The gap between the rollers of the rolling mill was incrementally reduced and all samples passed through at each width to ensure uniformity and accuracy between the rolling reduction of all the samples. After each pass, the thickness of each sample was measured and recorded using an RS Pro External micrometre. This process was repeated until all samples were at their intended thicknesses.

The roll reduction was calculated using this formula:

$$\mathbb{R} = \frac{t0-tf}{t0}\times 100 \qquad (3.2)$$

With $\mathbb{R}$ being the percentage rolling reduction, t0 being the sample initial thickness and tf being the final measured thickness.

3.2.3 Stretching and Rolling

For this combinational deformation mode. The material was first stretched using the method described above and then rolled, using the rolling method described above, immediately after. This mode was intended to imitate more complex deformation modes where both compressive and tensile strains are presented to the material through deformation. The four combinational conditions were: 4% stretching + 4% rolling (4s4r), 4% stretching + 8% rolling (4s8r), 8% stretching + 4% rolling (8s4r), and 8% stretching + 8% rolling (8s8r).

3.2.4 Electromagnetic Pulse Processing

Electromagnetic Pulse Technology (EMPT) was used as a deformation technique in this study. EMPT is a new forming technique which uses brief bursts of electromagnetic energy to plastically deform the sample. The pulses used are artificially formed by an electrically conductive using a coil in the chamber. When the coil is loaded with an alternating current, opposing current flow is generated. The generated current flows in the opposite direction to the current in the coil thus generating a repellent force. This discharge current is only switched on for no more than 25 microseconds. EMPT technology is known to be of low cost as well as having mechanical advantages such as a reduction in spring back and an increase in the formability of aluminium alloys.

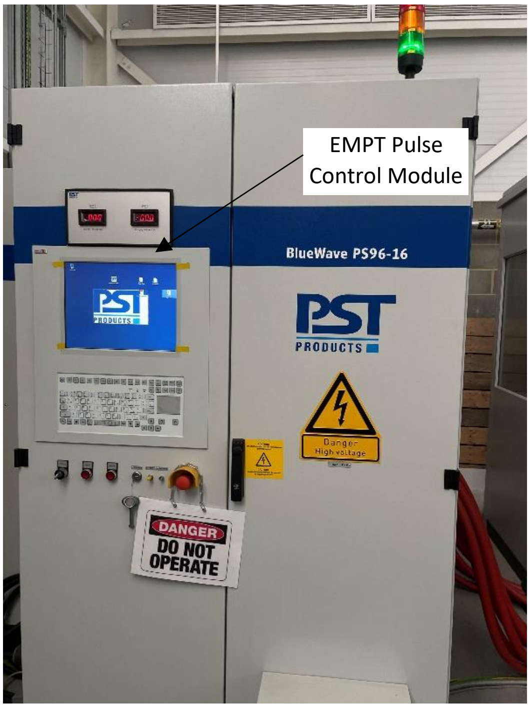

Figure 3.7. Bluewave PS96-16 Electromagnetic Pulse Technology Set Up

The electromagnetic waves were applied to 6mm sheets of the alloy. A die was placed above the sheet, and both were clamped down. Upon exposure to the electromagnetic wave, the sheet took the shape of the die. Thicker sheets were needed for this process as the dislocation spread in the thinner sheets were not as easily seen. The energies used to cause these deformations in the material were: 20kJ, 30kJ & 40kJ. The deformation presented like that expected in a bending sample, where there was an area of compressive deformations as well as an area of tensile deformations.

3.3 Thermomechanical Processing Scheme

Thermomechanical processing is a combination of plastic deformation and heat treatment of the workpiece in order to attain improved properties in the material. A range of thermomechanical conditions were investigated in this study.

A specific sequence of thermomechanical processing was applied in this investigation, coined the “aDA” process as described in Chapter 2. It consists of a short artificial pre-ageing step, followed by the deformation step which in this case ranged from uniaxial stretching, rolling, a combination of stretching & rolling, and EMPT. The artificial final ageing step succeeded this to produce the final material with the desired peak properties.

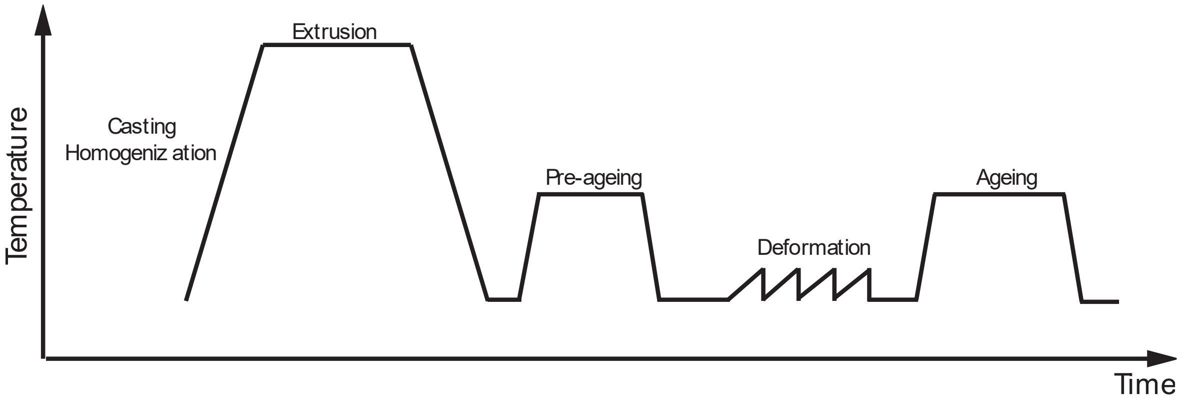

Figure 3.8. Schematic of the Thermomechanical Process

Figure 3.8 shows all the steps included in the aDA process. After extrusion, the material is defined as the “as-extruded” material. The extrusion was performed in such a way that the material was pre-heated at a temperature in the range for solid solution treatment to obtain a supersaturated solid solution state (SSSS), extruded at a temperature above precipitation, and quenched at a speed that prevented precipitation to occur. As a result, the as-extruded material was in the SSSS state. The material thus tended to naturally age from this point. In order to create a standard testing condition, prior to any further processing, the material was kept in a storage room and left at ambient temperature for 48hrs to allow them to floor age. This state was defined as T4. After this 48-hour period had passed the samples were immediately processed according to their desired states. This ensured that the starting material in all cases was kept constant.

3.3.1 T4 + Deformation

Plastic deformation by stretching and rolling was applied to the material in the T4 state. To perform this experiment, the material in T4 state was cut into lengths of 200mm and then subjected to the deformation modes selected.

Stretch was carried out using a tensile tester to apply strains of 4% and 8%. A rolling mill was used to apply reductions of 4% and 8%. The combination of stretching and rolling deformation was conducted sequentially, with stretching always coming first followed by rolling. The conditions for this combinational deformation mode were: 4% stretch + 4% roll (4s4r), 4% stretch + 8% roll (4s8r), 8% stretch + 4% roll (8s4r) & 8% stretch + 8% roll (8s8r).

3.3.2 T4 + Pre-ageing

As part of the aDA scheme, a pre-ageing step was applied to the material in the T4 state, under a range of combinations of temperature and duration: 150C/3h; 150C/8h; 150C/24h; 170C/2h & 170C/4h. These temperature and time combinations are lower than those normally used for peak hardening treatment and are employed to enhance the performance in the final peak ageing, and therefore called pre-ageing conditions.

3.3.3 T4 + Pre-ageing + Deformation

In the initial experiments, the pre-ageing condition was fixed to 170C/4h and the deformation mode was the independent variable. Further experiments were carried out with the deformation mode being kept constant at 8% stretch and the preaging condition as the independent variable.

To perform the experiments, the material was first prepared to the T4 status and then cut into 200mm lengths and then pre-aged as described in section 3.3.2 above. These pre-aged samples were then subjected to the same deformation modes as described in section 3.3.1.

3.3.4 T4 + Deformation + Final Ageing

This DA scheme was selected to particularly clarify the impact of pre-aging step in the aDA process. Experiments were carried out to test the mechanical properties of the material achievable without the pre-aging step. The material in the T4 state was deformed using the deformation modes described previously.

After deformation, the samples were then age-hardened at 150C and 170C for a time required to reach peak hardness. The time was achieved through a separate ageing kinetics experiment.

3.3.5 T4 + Pre-ageing + Deformation + Final Ageing

This was the complete aDA process. It was conducted to obtain the mechanical properties under the peak hardening conditions, which are modified to account for the impact of pre-ageing and deformation.

The material in the T4 state was pre-aged, and then plastically deformed followed by a final ageing to reach peak properties.

3.4 Heat Treatment

3.4.1 Artificial Ageing

An oil bath using conductive silicone oil as heating agent was used to carry out the ageing treatment of the material. The samples were submerged in the heat conductive silicone oil at the desired temperature and left there for a predetermined time to allow the correct ageing response. After this time had passed, the samples were removed from the oil and quenched in cold water.

The oil bath used was a Memmert One WNB 14 as shown in Figure 3.9 with a range of ageing temperatures of 70C-200C. An oil bath was used for ageing treatment due to its consistency and uniformity in the temperature it provides, and high reliability, compared to other heating agents.

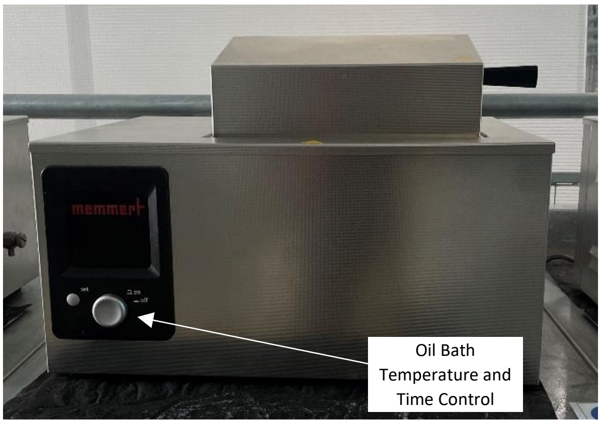

Figure 3.9. Memmert One WNB 14 Oil Bath

3.4.2 Experiment for Determining Ageing Conditions

An ageing kinetic experiment was carried out utilising an oil bath and hardness testing to find the ageing performance of the material. This preliminary ageing treatment was conducted at 170C for various times of up to 72h to determine the conditions for pre-aging, peak ageing, and final ageing. The times used for the kinetics measurement were 0.5h, 1h, 1.5h, 2h, 2.5h, 3h, 3.5h, 4h, 4.5h, 5h, 6h, 8h, 12h, 16h, 24h, 48h, 72h.

This time scheme was chosen to allow for all rapid changes in the mechanical properties in the initial stages of ageing to be recorded. The time interval after 5h was more spaced out as there were no longer noticeable changes in properties at 30-minute intervals.

3.5 Sample Preparation

3.5.1 Cutting

The material provided by Constellium was in the form of 1m long strips of the alloy. To prepare the material for the various processing, testing and analysis steps, the material had to be cut into proper lengths for the respective processes.

There were 2 main cutters used carry out this cutting. Namely the MetPrep QCut Brilliant 200 saw, and Prosaw Bomar ALU 400 shown in Figure 3.10.

The two cutters were used to cut the samples into proper lengths for processes like tensile stretching, rolling, bending and so on. The cutters were also used to cut the samples into smaller more uniform pieces for preparation for ESBD and TEM samples.

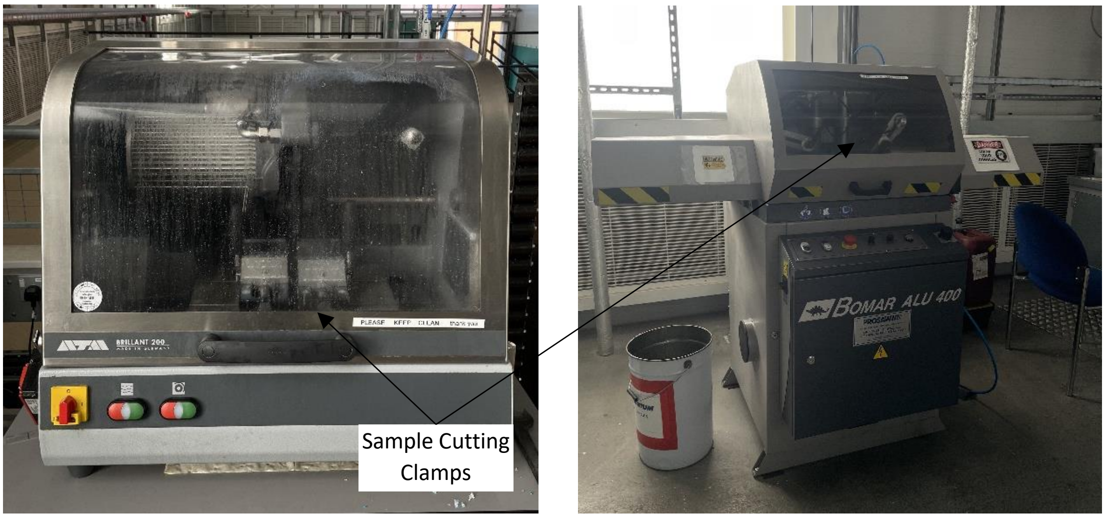

Figure 3.10. Sample Cutting Machinery. (a) MetPrep Qcut Brilliant 200 Saw (b) Prosaw BOMAR ALU 400.

3.5.2 Cold Mounting

The samples were cold mounted in a blue resin material provided by MetPrep. The resin was made up by mixing two parts of the acrylic powder and one part of the complementary liquid to form a warm blue solution which hardened over time. They were then mixed using a stirrer to ensure an even distribution and proper reaction of the entire solution. The samples were placed in circular moulds which had a diameter of 30mm, they were held by plastic stands to ensure the correct sample face would be displayed on the surface. The solution was then gently poured over the samples and allowed to harden. Once the acrylic cold mount had hardened, they were popped out of the moulds and polished.

Cold mounting was chosen over hot mounting as some of the samples were in the T4 condition and exposure to heat could have generated some sort of ageing response. This was kept constant across all samples.

3.5.3 Grinding & Polishing

After could mounting, the samples were ground using progressively finer Silicon Carbide abrasive papers, ranging from 80grit to 2400grit. The cold mounted samples were loaded onto the QATM Saphir 250 automatic polishing machine along with the grinding papers shown in Figure 3.11. The time, rotation speed and force were set appropriately to reach a surface finish presenting as few and shallow scratches as possible. After this, the samples were polished.

The polishing method was similar to the grinding process, using the same automatic polishing machine and similar settings. The grinding papers were swapped out for a Chemicloth M magnetic polishing pad as well as an oxide polishing suspension (OPS) solution. Immediately after polishing, the samples were cleaned with water and ethanol and then dried in order to prevent the formation of OPS crystals on the surface of the sample.

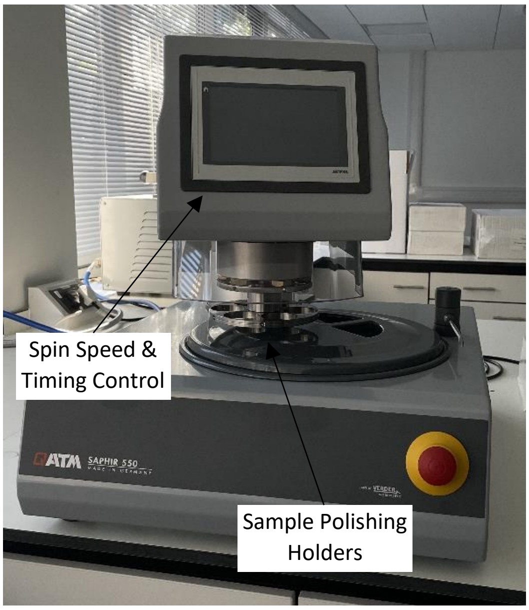

Figure 3.11. Metallurgical grinding and polishing machine, QATM Saphir 250.

3.5.4 Tensile Specimen Machining

The tensile samples were machined into the standard dog bone profiles by Constellium according to the ASTM E 8M standard using the QAM Saphir 250 as shown in Figure 3.12. The samples were cut into 200mm lengths and prepared through the required thermomechanical steps. A template was used to draw out the sample and the processing specifications of each sample was marked on the side using an engraving pen.

Figure 3.12. Metallurgical grinding and polishing machine, QATM Saphir 250.

3.6 Mechanical Testing

3.6.1 Hardness Tests

Hardness measurements were taken of the material to determine its strengthening behaviour. Vickers hardness was used as an easy mode of measuring the hardness of the material sample. The hardness of the material is measured using an indenter and a measurement look up book. The working principle is to measure the materials ability to resist the plastic deformation applied by the indenter at predetermined load forces. The harder the material, the greater it's resistance to the indenting force and thus the smaller the appearance of a dent on the sample surface.

Vickers's micro-hardness measurements were taken using the Wilson 432SVD Vickers Hardness Tester and the Zwick/Roell ZHV30. A load of 10N was used with a dwelling time of 10 seconds. Preparation of the samples for hardness testing included: Cold mounting of samples with the ND-ED exposed to allow hardness testing across the TD. The samples were cold mounted using a non-reactive acrylic resin, using the procedure described in section 3.5. For each sample, there were a total of 5 indents made. The size of the indent was measured automatically by the machine with the option for the user to correct any incorrectly measured values. The d1 and d2 values were then used to calculate the HV10 values using equation 3.3. The readings of these hardness values were averaged to obtain the average hardness for each given sample. The results were stored in a table on excel.

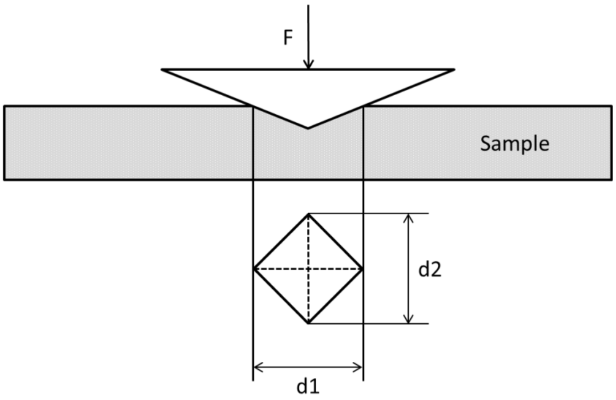

Figure 3.13. Vickers Hardness Indentation Measurement.

$$d = \frac{d1 + d2}{2} \quad HV = 0.1891 \times \frac{F}{d^2} \qquad (3.3)$$

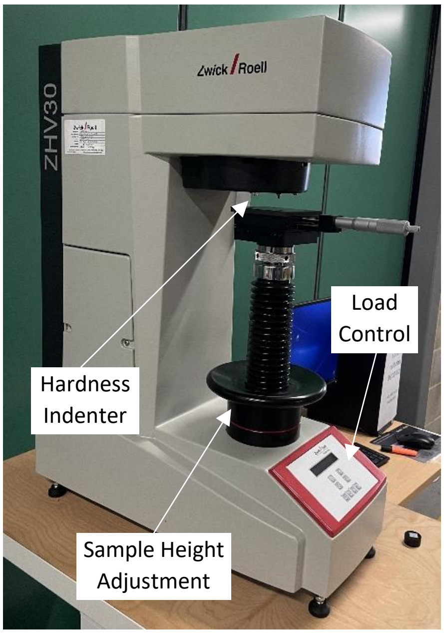

Figure 3.14. Zwick/Roell ZHV30 Vicker's Hardness Tester

Hardness mapping was performed on the EMPT samples using the Wilson VH3300. These were used to show the distribution of strain due to the applied deformation. There were many indents placed across a large representative region of the sample and the hardness at each locus was recorded, the varying hardness readings across the sample would give information on the effects of the deformation applied. For this the samples were cold mounted. The computer automatically converted this into a map that showed how the hardness of the material changed across the area. The step size used for the colour maps was 2.5 HV.

The maps were generally reliable and consistent but there were slight issues with the hardness readings around the edges of the sample as any measurements taken at the interface of the sample and the resin would give a faulty reading. For this reason, readings at the extremities were omitted. The machine's placement of the indents was slightly skewed also; thus, the generated maps did not exactly match up with the location it was placed on the sample.

Figure 3.15. Wilson VH3300 Automated Knoop/ Vickers Hardness Tester

3.6.2 Tensile Testing

Standard flat tensile specimens were cut and machined from the extruded sheets along the extrusion direction. The gauge length of the specimens was 50mm as shown in Figure 3.16 below.

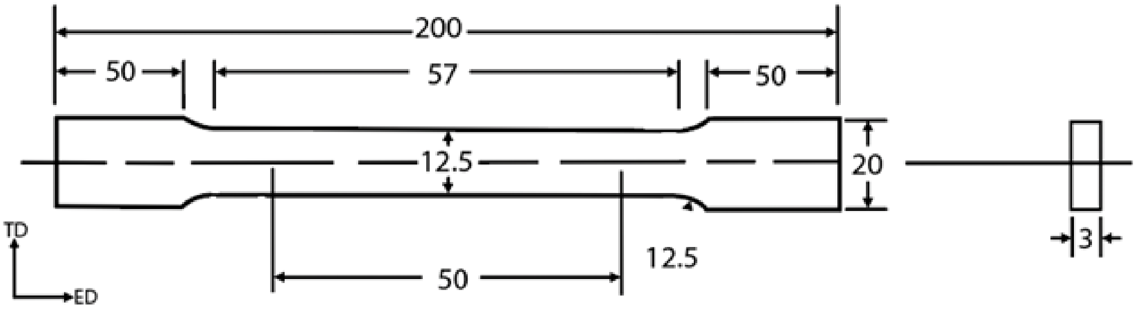

Figure 3.16. Tensile sample geometry. All given numbers are in mm.

The tensile specimens were all tested on an Instron 5569 Universal Electromechanical Tensile Tester at room temperature. The machine was set to an initial strain rate of 1.5%/min and then it ramped up to 24mm/min. A 50mm extensometer was attached to the middle of the sample which fed live information to the tensile rig about the progression of strain in the material. The rig collected this information as raw data to be used to compute the required mechanical properties. Three samples of each testing condition were made and tested to allow for an average to be calculated as well as a standard deviation.

The raw data from the tensile tester was saved and exported. Using this data, the flow charts were then created, displaying information on the mechanical properties such as the Young's Modulus, YS (Yield Strength), UTS (Ultimate Tensile Strength), Uniform Elongation, and Total Elongation.

3.7 Microstructural Characterisation

This section lays out the details of the visual and analytical methods used in the study to characterise the microstructures of the respective samples. The techniques were used in conjunction to get a better view and understanding of the structures found in and formed in the matrix through each step of the material processing. This in turn allowed for qualitative analysis and conclusions to be drawn.

3.7.1 Optical Microscopy

For optical microscopy, the samples were cut, mounted, ground and polished in the way described in 3.5. To more clearly reveal the microstructure of the alloy, chemical etchants were used. These etchants included Keller's Reagent, FeCl and NaOH. The etchant attacked grains of differing orientations to different degrees, and this allowed a contrast between grains to be formed, making it easier for individual phases and grains to be seen under the microscope.

The microstructures were examined using a Zeiss Axioscope 1 optical microscope. This microscope made use of visible light sources above and below the samples as well as a myriad of lenses to magnify images of small areas of the material samples with a digital camera. Several magnification levels, ranging from 20 – 1000 times were used in the microstructural examination under either bright-field or polarised mode.

The accompanying software aided in collecting measurements of average grain sizes and also displayed the distribution of intermetallic present in the matrix. The intercept method was used in the measurement of the grain sizes. Straight lines were drawn along the ED in different areas. 5 lines were used in each image to come up with the averages.

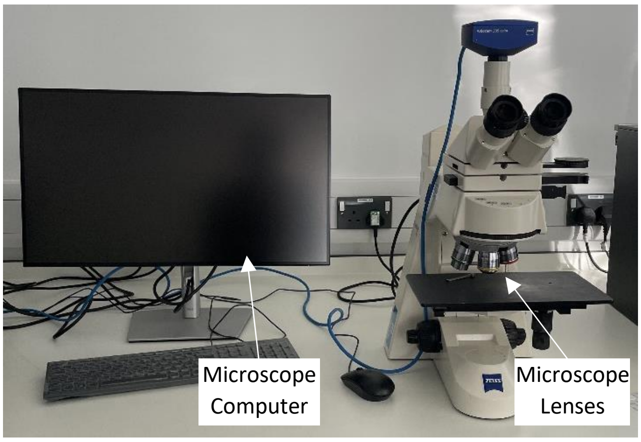

Figure 3.17. Zeiss Axioscope 1 Optical Microscope.

3.7.2 Scanning Electron Microscopy

Extensive microstructural examinations were carried out using SEM. Samples were cold mounted in the ED-ND plane to allow the TD direction to be analysed. They were then grinded, polished and unmounted followed by electropolishing to prepare the sample surface for observation. The samples were then observed using the Zeiss Supra 55-VP FEGSEM to obtain secondary or backscattered electron images. The system was able to create highly magnified images by using electron beams as opposed to light photons which were directed at the sample specimen. This beam of electron is generated at the top of the microscope by an electron gun. Electromagnetic fields and lenses are used to focus and direct the beam towards the sample. These electrons hit and interact with the sample. Detectors are present around the sample to collect the reflected x-rays, backscattered electrons, and secondary electrons. These electron signals carry information that allows the system to perform calculations and produce a final image on the screen.

This system used a tungsten thermal emission gun which allowed for the observation of solutes and intermetallic. The contrast also allowed the different adjacent grains to be imaged effectively. An accelerating voltage of 10kV was used at a working distance of 13mm.

This SEM system also allowed the operation of BSD imaging techniques as well as EDX all through the manipulation of the parameters such as operating voltages, working distances etc. Using the SEM to display the grain morphology as well as the presence of strain inside of said grains and how this strain was distributed across the bulk of the material.

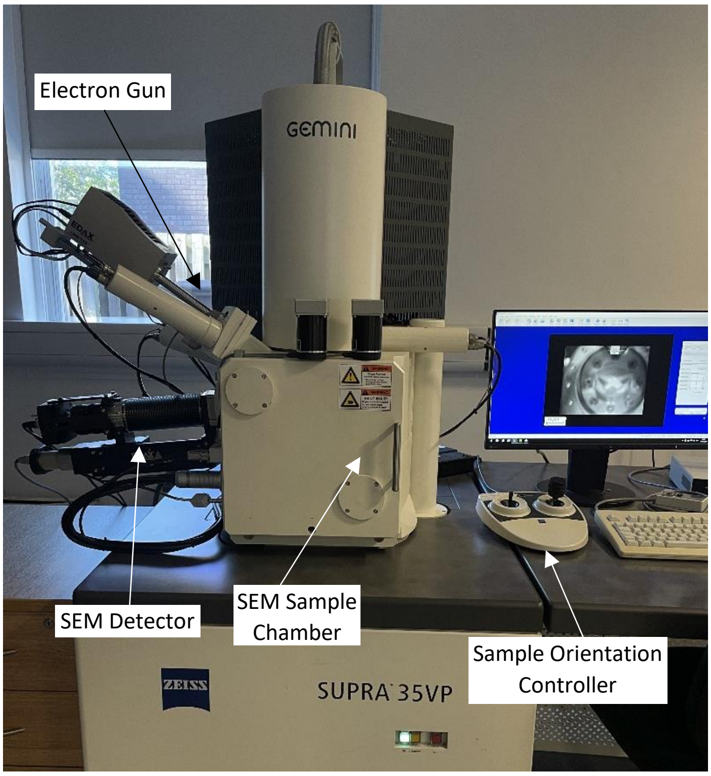

Figure 3.18. Zeiss Gemini Supra 35VP SEM Machine

Electron Backscattered Diffraction

Surface Preparation

EBSD specimens were cut from the different samples for analysis by EBSD. They were first cold mounted, grinded, and polished. Then they were unmounted to allow electropolishing which removed surface strains allowing dislocations in the material to be seen much more easily. The material was electropolished using a 30% nitric acid and methanol solution with a 12V potential difference between the terminals at a temperature of -30C for 60 seconds per sample. The samples were then washed with alcohol and dried quickly using an air drier to leave a clean surface without any streaks.

Data Collection

The EBSD microscope ran at 15KV, at an aperture of 120 and at a working distance of 13mm. The step size used to collect the maps was 0.13 at a magnification of between 750 and 1k times. The collector was set to identify only the α–Al phase. Microstructure observations were observed in the ED-ND (Transverse Direction) plane to reveal the effects of the deformations more clearly – although some data were obtained in the TD-ND plane to examine microstructural features. The data acquisition was done by the Zeiss CrossBeam 340 Focused

Ion Beam (FIB). Samples were loaded into the chamber at a 70-degree tilt in the direction of the detector to allow the best possible formation of the Kikuchi readings.

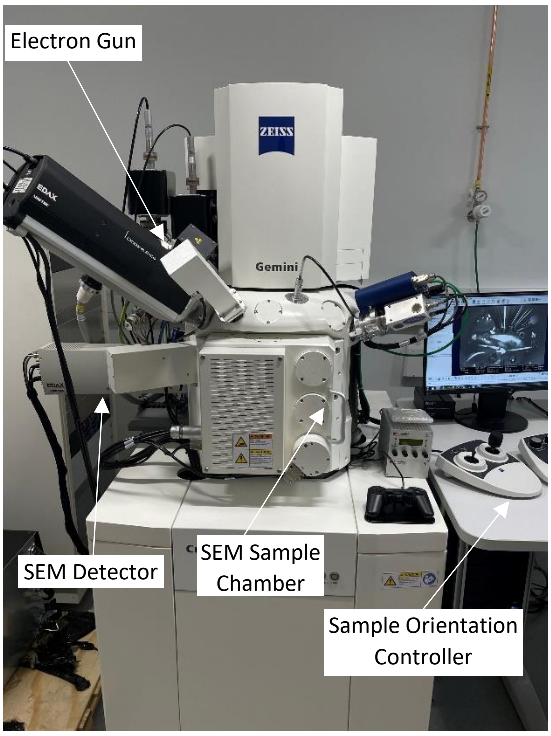

Figure 3.19. Zeiss Gemini Crossbeam 340 FIB.

OIM Software Analysis

The attained EBSD data were processed and analysed using the TSL-OIM software, version 8. Parameters such as Image Quality (IQ) maps, Inverse Pole Figure (IPF) maps, Kernal Average Misorientation (KAM) maps, Geometrically Necessary Dislocations (GND) maps and Orientation Distribution Function (ODF) maps were created and these helped in the characterisation of structures and factors such as grain size, dislocation density, and crystallographic texture.

IPF maps

IPF maps were created using the collected data from the EBSD indexing. These maps display crystallographic orientations of the points inside and at the grain boundaries of grains in a material. Individual grains can then be visualised with each colour representing a crystallographic direction defined by the IPF. The samples were mounted into the ED-ND plane and this information was inputted into the system to allow correct alignment of the directions. Low angle grain boundaries are indicted using a light grey colour and high angle grain boundaries were represented using a black line.

GND Maps

In GND maps, the data collected is used to evaluate the spatial distribution and density of dislocations in the crystalline material. The orientation of a measured point was compared to all the neighbouring points. The computer uses a mathematical calculation to calculate the misorientations that are caused by GNDs. By analysing the misorientation at each kernel, the GND needed to accommodate the misorientation is determined. The number and locality of neighbouring points used can be altered to change the resolution given. For the investigation, the second neighbour was used. Ranges of misorientations between 5-15 degrees were highlighted by light grey points and these were identified as low angle grain boundaries (LAGB's). High angle grain boundaries (HAGB's) were represented by black points in the EBSD maps and the range for these boundaries was between 15-62.5 degrees of misorientation.

KAM Maps

Similar to the GND maps, these maps were calculated using the average misorientation between the selected point and neighbouring kernels. The misorientations were then analysed in ranges. Misorientations less than 0.13 were seen as noise and were set to the blue colour and were classed as the matrix background. The next important range was between 5-15 degrees, these were identified as LAGB's, they were set to a light grey colour to be seen on the map. Another key range of misorientations were the 15–62.5-degree misorientations. These misorientations were classed as HAGBs and were marked with a black colour on the EBSD KAM maps. The maximum misorientation angle in an FCC crystal is 62.5, all misorientation angles above this can be represented by another equivalent angle. The final range of dislocations which were instrumental in viewing the dislocation densities of the samples was the 0.13-2-degree range. These were split into equally divided ranges of 0.13 degrees using the gradient function in the program. There were generally minimal readings in the 2–5-degree range of misorientations so the ranges for the dislocations were limited to 0.13-2 degrees to allow for better contrast in the map. The described ranges can be seen in the figure below.

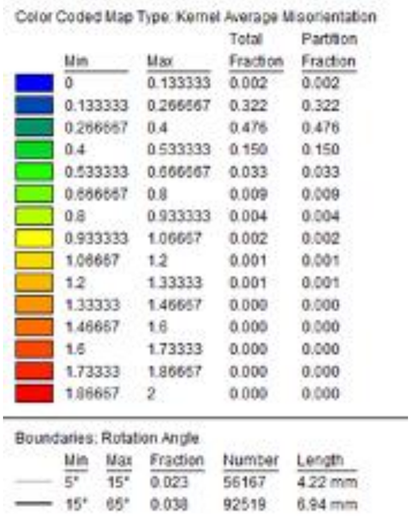

Color Coded Map Type: Kernel Average Misorientation

	Min	Max	Total Fraction	Partition Fraction
🟦	0	0.133333	0.002	0.002
🟦	0.133333	0.266667	0.322	0.322
🟩	0.266667	0.4	0.476	0.476
🟩	0.4	0.533333	0.150	0.150
🟩	0.533333	0.666667	0.033	0.033
🟩	0.666667	0.8	0.009	0.009
🟨	0.8	0.933333	0.004	0.004
🟨	0.933333	1.06667	0.002	0.002
🟨	1.06667	1.2	0.001	0.001
🟧	1.2	1.33333	0.001	0.001
🟧	1.33333	1.46667	0.000	0.000
🟧	1.46667	1.6	0.000	0.000
🟥	1.6	1.73333	0.000	0.000
🟥	1.73333	1.86667	0.000	0.000
🟥	1.86667	2	0.000	0.000

Boundaries: Rotation Angle

	Min	Max	Fraction	Number	Length
─	5°	15°	0.023	56167	4.22 mm
━	15°	65°	0.038	92519	6.94 mm

Figure 3.20. KAM Map Colour Key

ODF Data

ODF data are a function of the orientation space associated with each orientation the volume percentage of crystals in a specimen that are in a specific orientation and is used in acquiring textural information on the sample specimen. A random textured specimen would have and ODF constant of one. The values of the ODFs can then be measured as multiples of the random distribution. From this information, Pole Figures of the material texture can also be formed.

3.7.4 Transmission Electron Microscopy

TEM specimens were cut and prepared from sheets of the alloy. The specimens were cut into thin slices perpendicular to the extrusion direction to around 500 microns in thickness. These were then polished to a thickness of approximately 100 microns forming thin films. These thin films were then punched into round discs that were to be used for the TEM analysis. The films were then jet electropolished using a Streurs Tenu-Pol 5 electropolishing machine set up.

The solution used in the preparation was a 25% nitric acid in methanol electrolyte. The solution was kept at a temperature of below –25C, tethered with the addition of liquid nitrogen. The voltage of the set up was set to 15 volts and the flow rate of the jet was 28.

The TEM system used was the Jeol 2100F Transmission Electron Microscope. The operating accelerating voltage was 200kV and this was kept consistent between all images collected and across all sample conditions. The beam generator at the top of the system produced a highly focused concentrated beam of electrons using electromagnetic fields and lenses which were directed at the samples. After the interaction with the material, the electrons which were transmitted through the specimen were collected by a detector which then converted the diffraction pattern into an image on the computer screen.

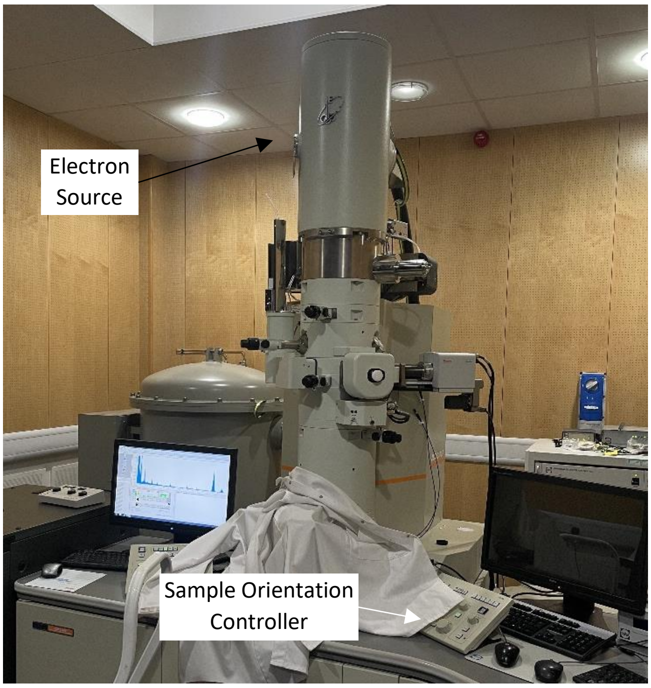

Figure 3.21. Jeol 2100F Transmission Electron Microscope.

3.8 Case Study

As the material was a crush alloy, tests were conducted to test the mechanical properties of the material in the fully thermomechanical processed test state.

These experiments consisted of crush tests with the aim of improving both the materials strength and crushability. The material was extruded into profiles resembling those in Figure 3.22 using the third die. All dimensions are displayed in the figure. Immediately after the extrusion the profiles were quenched and left to floor age for 48 hours.

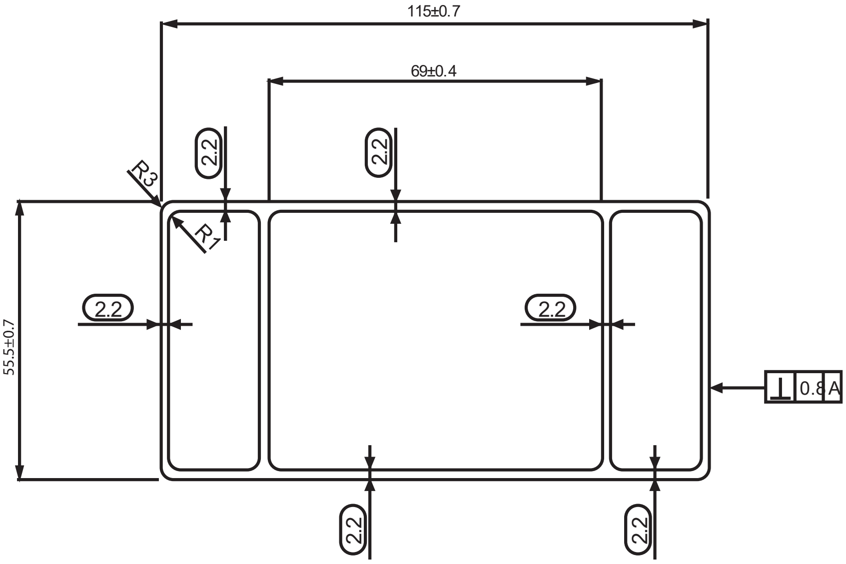

Figure 3.22. Schematic showing die dimension specifications of die used in stretching and crush test experiments, all given numbers are in mm.

Following this the samples were aged and deformed to the appropriate conditions as discovered in the TMA tests that yielded best final mechanical properties.

These prepped samples were then subjected to tensile, bending and crush tests. The tensile samples were cut out of the profile and tested as described in section 3.6.

Quasistatic crush tests were also performed on the profiles with loading speeds of 100mm/min to retrieve information of their crush index and the energy absorption. The samples were loaded onto the machine and the horizontal plate began to descend onto the sample. The plate continued to descend until the material failed by the formation of cracks or till it could no longer withstand the forced applied by the machine. As the specimens were strained, they formed the characteristic crimples that are commonly seen in crush samples.

Figure 3.23. Crush test performed on aluminium profile in the optimised TMA state.

Chapter 4. Results

This chapter describes the results of experimental work that was carried out with the selected AA6xxx series alloy. The material produced by Constellium was extruded at high temperatures using three dies, giving rise to three specimen types. The first specimen type was a flat 3mm thick strip used for the majority of the study. The thicker 6mm flat specimen was used for the EMPT studies and the final extruded profile was not a flat specimen and was used in the studies regarding the material's crush performance and properties.

The material was exposed to numerous thermomechanical processing steps and then mechanically tested as described in section 3. This chapter details the results from the mechanical tests, namely hardness testing, tensile testing, bend testing and crush testing. This will aid in the quantification of and analysis of the mechanical properties that the material presents as a result of the thermomechanical treatment.

Once these results were collected, the microstructure of each material, in each processing condition, was characterised using a wide range of apparatus and methods including, Optical Microscopy, Scanning Electron Microscopy, Electron Backscatter Diffraction and Transmission Electron Microscopy. With each, special and novel techniques were used in order to extract and analyse the differences in the type, number, morphology, and dispersion of components present in the microstructure of the material.

These results together would then help in drawing a link between the enhancements in the mechanical properties and the structures present that these enhancements could be attributed to.

4.1 Microstructure and Mechanical Properties of Starting Material (T4 and T4 + Preaging)

The starting 6xxx series alloy, after casting was homogenised and solution heat treated then extruded into long strips. In this state, the alloy was examined using optical microscopy (OM), scanning electron microscopy (SEM) and electron backscattered diffraction (EBSD) to understand the features of the as extruded prior to any mechanical processing, plastic deformation, and ageing treatment. The desired microstructure displays fairly homogeneous equiaxed grains of varying granular orientations. Extrusion effects may be seen in the material.

Understanding these features of the starting material will be pivotal in identifying structures formed as a result of ageing and deformation applied to the material through the thermomechanical processing route and forming a link to the enhancement of mechanical properties.

4.1.1 Starting Material Optical Microscope

Figure 4.1 presents an optical microscopy image of the starting material in the as-extruded state. This is the material without application of any stages of the thermomechanical processes. The contrast in the image was achieved with the use of Keller's Reagent as an etchant. It can be seen from the micrograph that the grains are characterized as recrystallized and equiaxed. Extensive optical microscopic and SEM examinations showed that the grain structure was generally homogeneous in size and morphology.

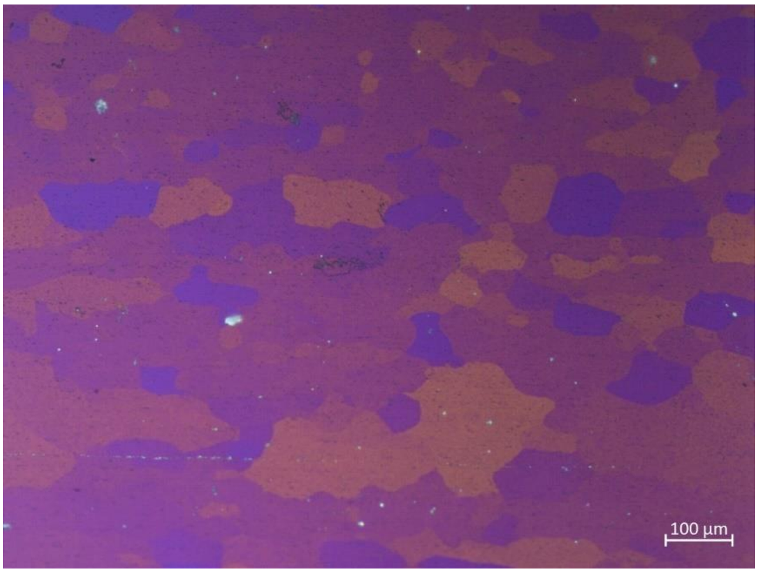

Figure 4.1. Optical micrograph showing the recrystalise grains in centre of an extruded AA6xxx series aluminium alloy in the as-extruded state.

4.1.2 Starting Material SEM

SEM images taken of the material, shown in Figure 4.2 display similar features to those seen in the optical micrograph. Here the images are captured at multiple magnifications. Figure 4.2 (a) displays the spread of grains as well as the homogeneity in morphology of the grains across the bulk area of the specimen.

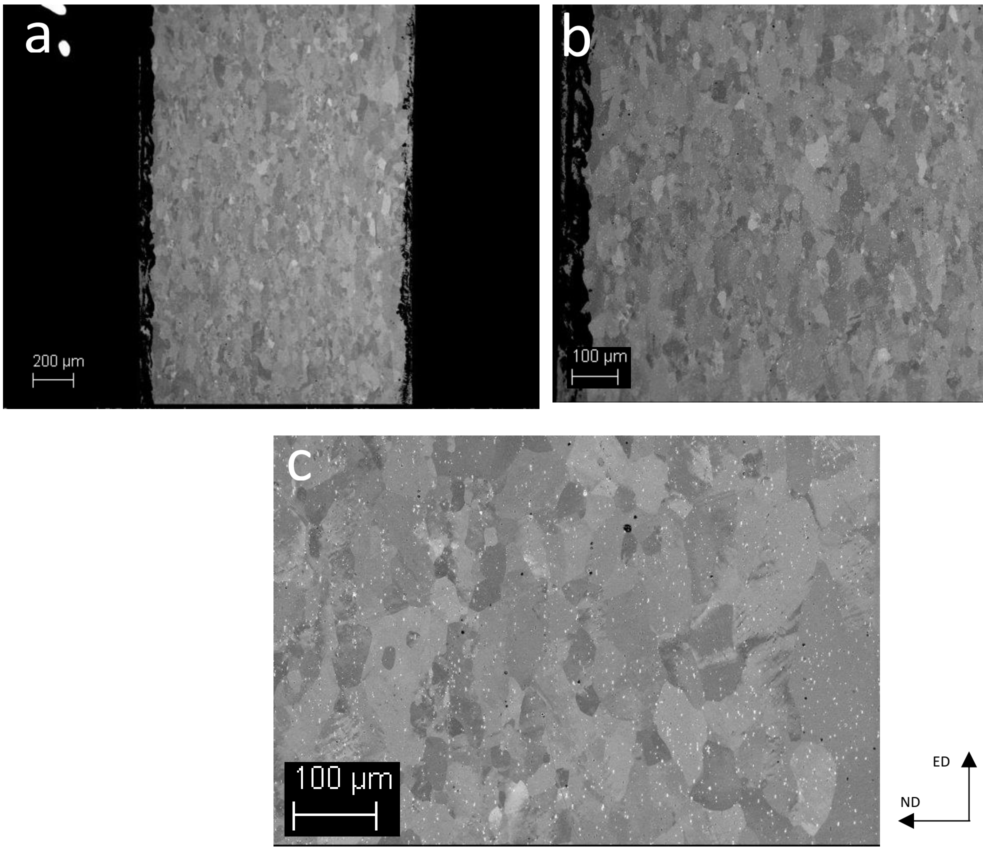

Figure 4.2. SEM micrographs showing the microstructure of the AA6xxx aluminium alloy in the as-extruded state. (a) 21x mag (b) 45x mag (c) 150x mag with SEM conditions of – 10kV Electron High Tension (EHT) and 10.9mm working distance, collected in BSD1 mode.

Peripheral coarse grains can be identified across of micrographs at all magnifications which were produced as a result of the heat and friction generated in the extrusion process. The difference in contrasts between the grains is due to the difference in crystallographic orientation in adjacent grains. The grain boundaries are easily visible.

4.1.3 Starting Material EDX

Particles visible in the SEM images of section 4.12 were chemically characterized using energy dispersive x-ray spectroscopy (EDX). X-rays released from the sample under the electron source gave a characteristic spectrum allowing compositional analysis of said particles. Figure 4.3 shows the area examined as well as the spots that were analysed.

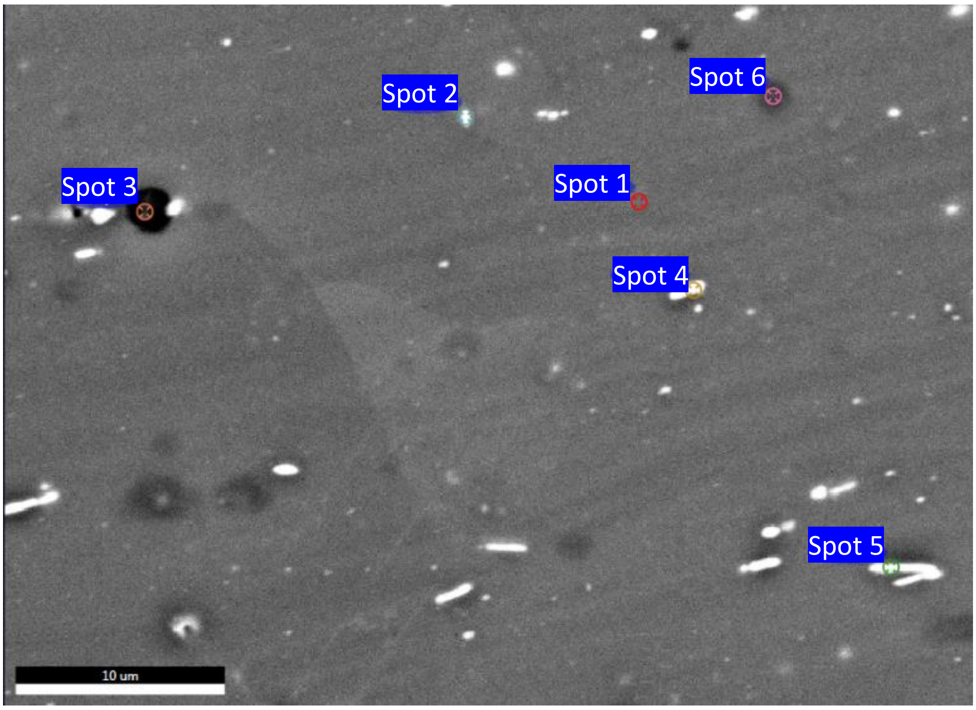

Figure 4.3. EDX analysis of an AA6xxx series aluminium alloy in the as-extruded state.

In Figure 4.3, 6 spots of interest are selected. EDX spot 1 is of the main alloy matrix, the spectrum of Figure 4.4 (a) shows a characteristic peak for aluminium, with a weight % of 97.45 with 2.31 of magnesium by weight %.

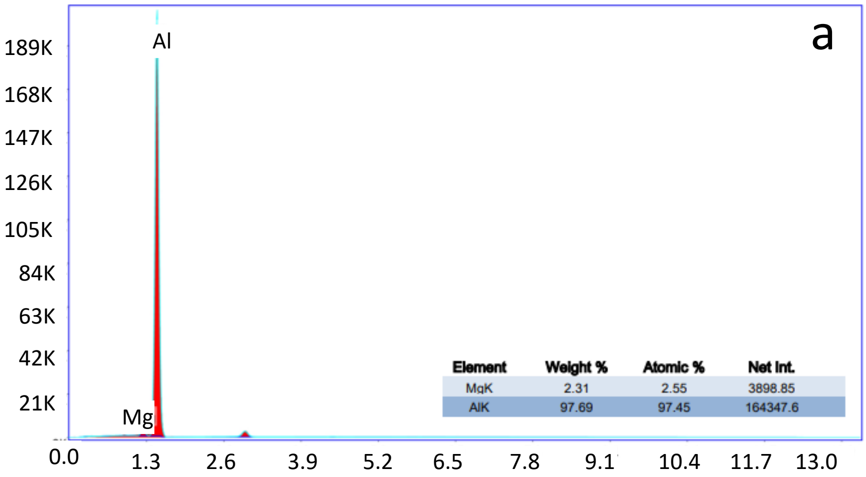

Element	Weight %	Atomic %	Net Int.
MgK	2.31	2.55	3898.85
AlK	97.69	97.45	164347.6

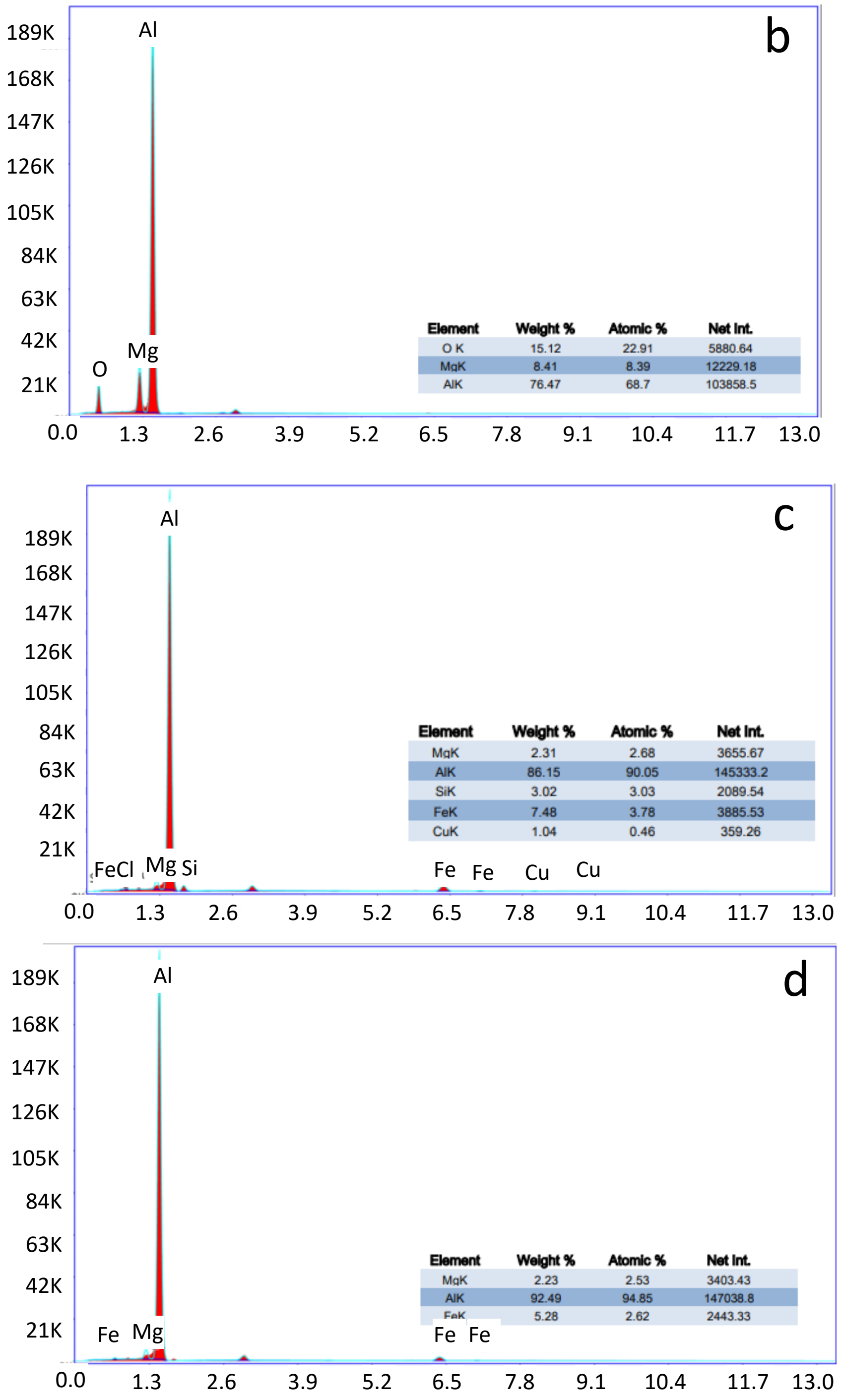

Element	Weight %	Atomic %	Net Int.
O K	15.12	22.91	5880.64
MgK	8.41	8.39	12229.18
AlK	76.47	68.7	103858.5

Element	Weight %	Atomic %	Net Int.
MgK	2.31	2.68	3655.67
AlK	86.15	90.05	145333.2
SiK	3.02	3.03	2089.54
FeK	7.48	3.78	3885.53
CuK	1.04	0.46	359.26

Element	Weight %	Atomic %	Net Int.
MgK	2.23	2.53	3403.43
AlK	92.49	94.85	147038.8
FeK	5.28	2.62	2443.33

Figure 4.4. EDX spectral analysis of an AA6xxx series aluminium allow in the as-extruded state. a) Spot 1 b) Spot 3 c) Spot 4 d) Spot 5.

Figure 4.4 (b) shows peaks for aluminium, magnesium and oxygen suggesting the presence of an aluminium magnesium oxide in the solution. In spot 4, a peak for iron impurities is identified, illustrated in Figure 4.4 (c), as well as peaks detecting aluminium, magnesium, silicon, and copper. This is likely an intermetallic phase of magnesium silicide or copper aluminium with contaminations of iron.

In Figure 4.4 (d), representing the bright spot 5, there are peaks for aluminium, magnesium and iron which possibly would be an Al3Fe or Mg2Fe intermetallic compound.

4.1.4 Starting Material EBSD

Figure 4.5 shows an inverse pole figure (IPF) map across a large area of the bulk region, displaying a vast number of equiaxed grains.

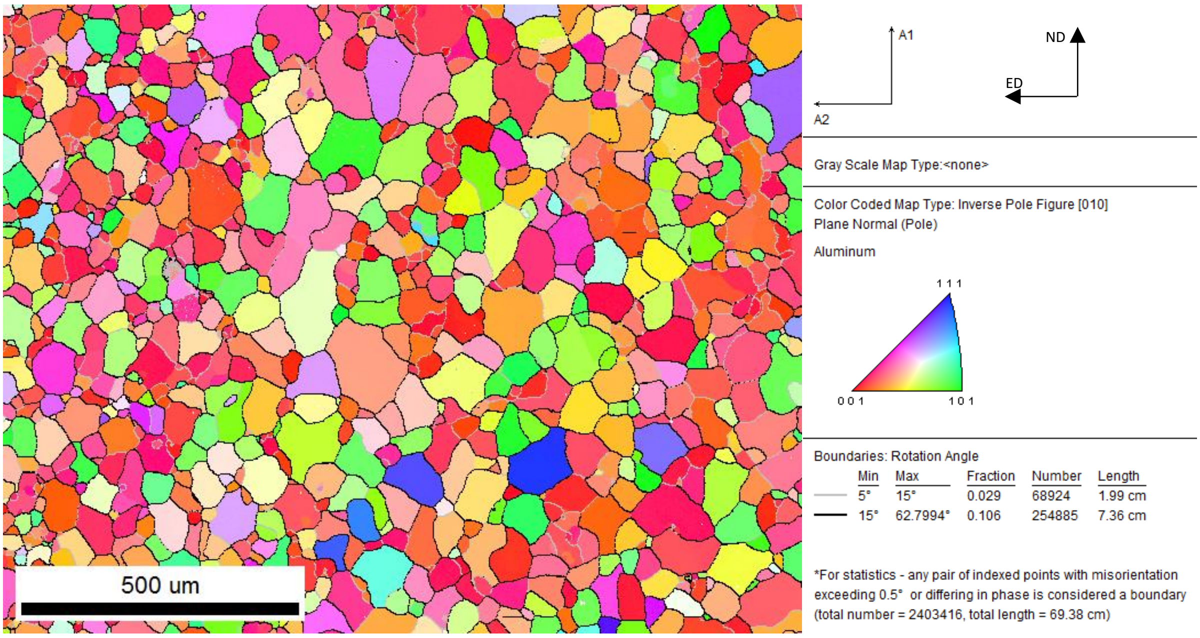

Figure 4.5. EBSD Inverse Pole Figure Map, showing a homogeneous equiaxed grain structure of the alloy in the as-extruded state.

There was no processing applied to the material at this state, thus, all material features present were as a result of the extrusion. It can be said that there is a strong cube texture which is confirmed by the inverse pole figure on the right-hand side of Figure 4.5. A substantial number of grains are highlighted in red in this EBSD IPF map corresponding to a 001 orientation as signified in the IPF key. Individually, the grains show uniform orientations in the crystals with no variations in hue indicating homogeneity in the crystals.

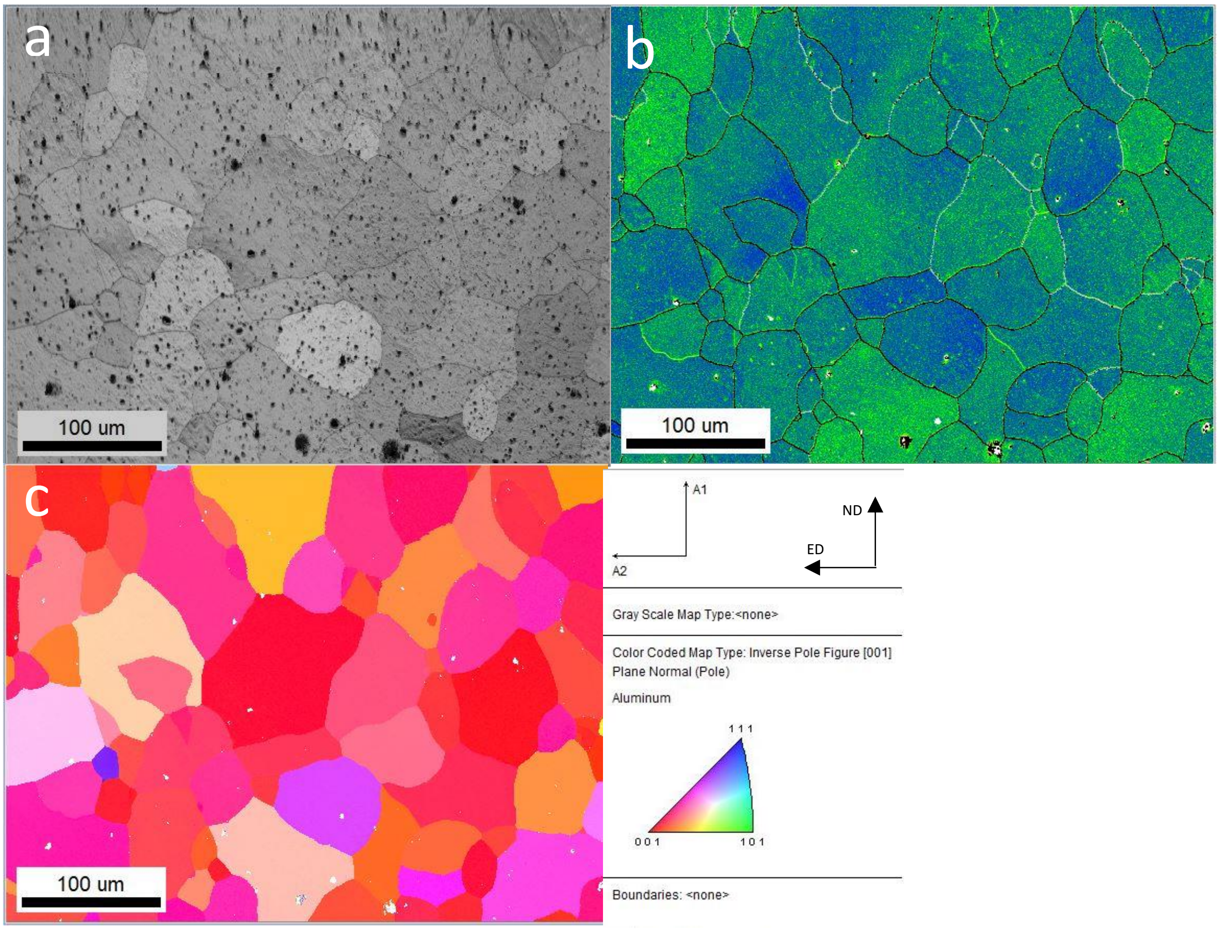

Figure 4.6. EBSD maps showing the detailed grain structure of the AA6xxx series aluminium alloy in the as extruded state: (a) Image Quality Map, (b) Kernel Average Misorientation Map, (c) Inverse Pole Figure Map.

In addition to a mapping of the general bulk area to identify more global features in the starting material, an investigation into a more concentrated representative region was conducted to clearly uncover more local and detailed microstructural features as shown in the EBSD maps in Figure 4.6, which was taken at a magnification of 250x at a step size of 0.13. Figure 4.6 (a) shows the image quality map in this region. The image is clear with strong pattern indexing throughout the map. Black dots can be seen distributed across all grains originating from intermetallic particles which are either falling out of the material during metallographic preparation or being poorly indexed by the system during data collection. Figure 4.6 (c) shows an IPF map that correlates with the information garnered in figure 4.5, with equiaxed, homogeneously orientated grains. The misorientation information shown in Figure 4.6 (b) crucially displays the lack of structured dislocations and other features, the random spots of low-level orientation variance are the typical randomly occurring dislocations as well as noise and interference associated with the collection method.

4.2 Deformation Structure

This section includes descriptions of the deformation response of the material in this as extruded state. Plastic deformation imparted on the alloy via different strain modes such as stretching and rolling and EMPT generate and multiply dislocations in the crystal structure.

Observing this behaviour of deformation in the as extruded state creates a base understanding of dislocation behaviour in this specific alloy. Once precipitate particles are introduced to the material through ageing treatments, alteration in features and structures present can be attributed to the mechanisms occurring.

4.2.1 T4 + Stretching

From backscattered electron micrographs gathered using SEM as shown in Figure 4.7, the region of a mechanically stretch deformed material is compared to the starting material. There are stark differences in the appearance of the grains even at the low strain level of 4% stretch. Visible variances in contrast inside of grains are present in Figure 4.7 (b), exhibiting the presence of dislocation structures and bands as a direct result of the plastic deformation. Grains also appear to be elongated along the extrusion direction in Figure 4.7 (b)

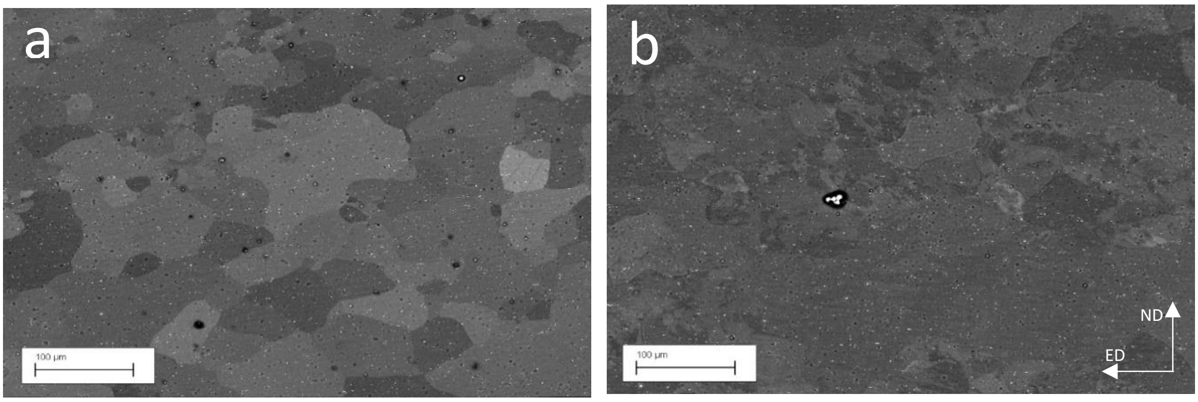

Figure 4.7. Back Scattered Electron micrographs: a) as extruded and b) 4% uniaxial stretching.

4.2.2 T4 + Rolling

A global and more localised backscattered images of a cold rolled deformed material in Figure 4.8 show that similar to the stretch deformed material, there is a slight visible elongation of the material along the extrusion/rolling direction with variances in the orientations inside of the grains, showing the presence of a density of dislocations.

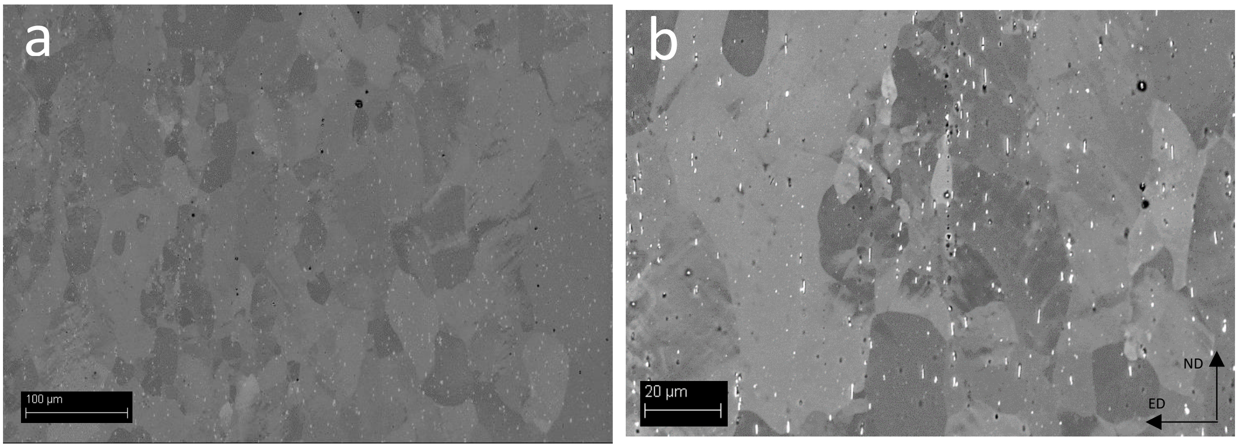

Figure 4.8. Back Scattered electron micrographs of an extruded AA6xxx series strip after 8% cold rolled deformation: a) 150x magnification and b) 500x magnification.

4.2.3 T4 + Combined Stretching and Rolling

Figure 4.9 shows the deformation structure of the sample that underwent a combined strain path, i.e. 8% uniaxial stretching in the extrusion direction immediately followed by 4% rolling along the same direction. As expected, the extent of deformation is more severe compared with the deformation structure after 4% stretching (Figure 4.8), the initial grain structure has been destructed (Figure 4.9 (a)), and microbands can be seen to have formed (Figure 4.9 (b)).

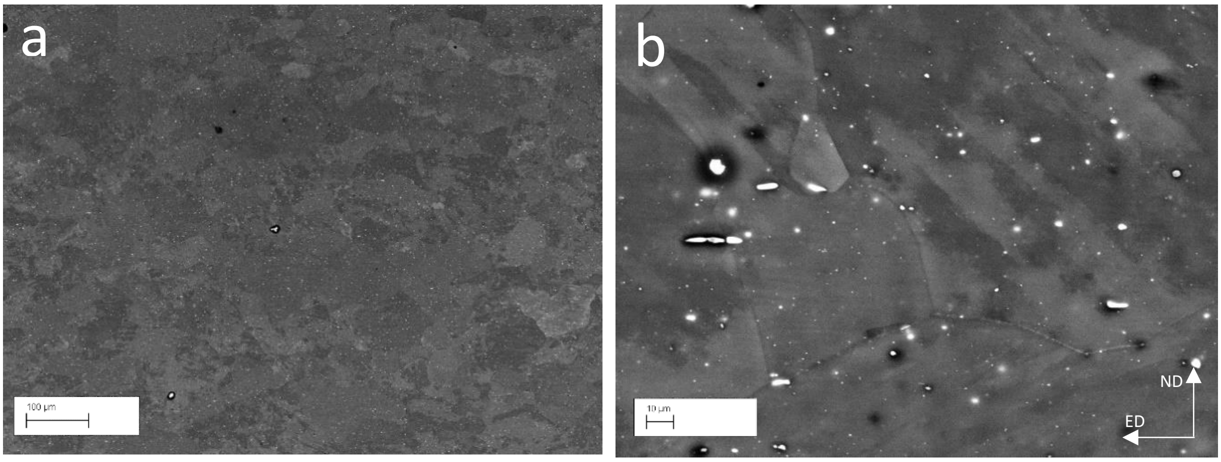

Figure 4.9. Back Scattered electron micrographs of an extruded AA6xxx series strip after 8% stretch and 4% cold rolling deformation: a) 150x magnification and b) 1kx magnification.

4.2.4 EMPT

Figures 4.10 and 4.11 display the microstructural information for an EMPT sample using both SEM and EBSD analysis. As the material was bent to the shape of a die, there is a region that experienced compressive forces and a region of tensile forces. There is also a transition in strain levels between these two distinct regions. The strain levels in these regions are far greater than those seen in the stretched and rolled samples. This is depicted in Figure 4.10 (a) where there are well defined dislocation bands inside of the grain on the right. Figure 4.10 (b) shows that this misorientation spread is common amongst various grains. this micrograph at 500 x magnification also shows the peripheral coarse grains present which are flattened and elongated in the direction in which the deformation was applied to the material.

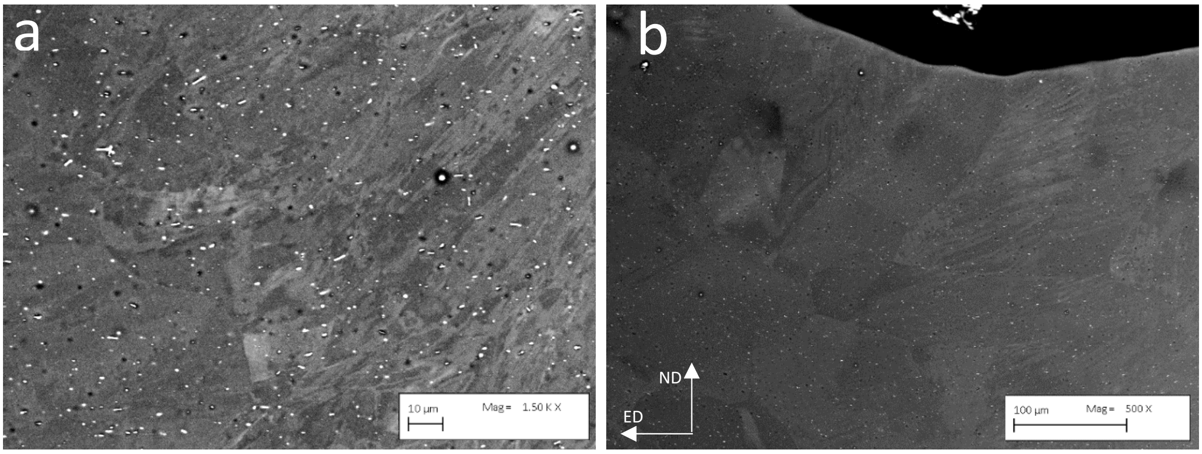

Figure 4.10. Backscattered electron micrographs of an extruded AA6xxx series strip after exposure to a 30kJ electromagnetic forming voltage to bend the sample to the die geometry: a) 1.5kx magnification and b) 500x magnification.

Figure 4.11. EBSD micrographs of an extruded AA6xxx series strip after exposure to a 30kJ electromagnetic forming voltage to bend the sample to the die geometry at 75x magnification.

The IPF map in Figure 4.11 shows the changes in the grain morphology and orientation across the thickness of the sample similarly to the SEM images, after the EMPT forming, the PCG's remain in the specimens, they are yet again elongated and display small variations in the orientation spread inside of the grains. Looking to the centre of the map, it can be seen that there is a strong deformation texture formed. The grains are mostly orientated to the 001 plane. There are significant changes in the grain morphology in this area; the grains elongate along forming direction. Inside of the grains there is a large amount of orientation changes depicted by the changes in colours. There are defined bands angled at approximately 45°. These changes in orientation inside of the grains were due to the presence of larger numbers of dislocations added to the crystal matrix affecting its uniformity and crystallinity. The greater the changes in misorientation found in a grain the larger the density of dislocations present in said grain.

4.3 Aging Selection

4.3.1 Preaging Kinetics

Experiments establishing the preaging and final ageing conditions using under aging, re-aging (post deformation) and hardness tests are conducted. The conditions for the thermomechanical process were decided iteratively using the results from ageing kinetic experiments. Subsequent to prolonged aging durations, Table 4.1 shows that for the different temperatures, the peak hardness was achieved at different times indicated in red text.

Table 4.1. Vickers Hardness Measurements used in determining the preaging conditions for the AA6xxx series aluminium alloy.

HRS	150C	170C	190C
0	79.96	79.96	79.96
1	80.86	86.14	**104**
2	85.42	101.96	121.08
4	91.04	**120.72**	**127.16**
8	**102.32**	130.06	123.08
16	115.08	**132.4**	118.66
24	120.96	130.9	116.42
48	129.82	128.76	112.56
72	**133.34**	124.62	108.84
120	130.88	124.54	102.96
240	127.66	115.36	_

*Red = Peak

** Blue = Halfway Hardening Point

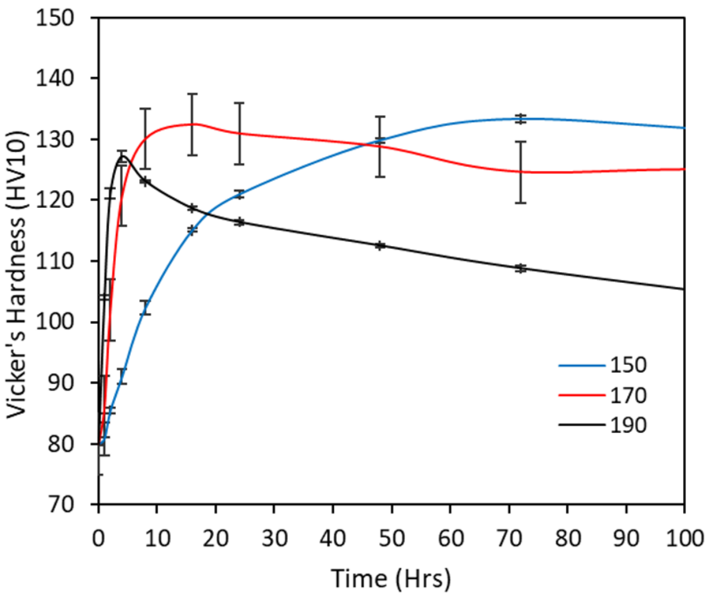

Figure 4.12. Vickers Hardness as function of time for determining preaging conditions of an AA6xxx series aluminium alloy.

For 170° C, the peak hardness was achieved at 16 hours of continual ageing. After this duration of time, the material reached the overaged status and resultant hardness began to decrease steadily, this is displayed in the chart on the right for all the different temperatures. This peak hardness state however was T6 and at this stage, the addition of any deformation would not be beneficial.

For the preaged condition, which is an underaged condition, the selection parameter for the time duration condition was the point when the hardness was about half of the hardening increase on the hardening curve. At the midpoint of the hardening increase, it was assumed that there is a sufficient number of clusters/precipitates in the matrix for the subsequent dislocations to interact with, but there is still solute remaining in solution to allow for the further hardening in the final ageing step post deformation. There is also a possibility that the dynamic interaction between clusters and precipitates developed in preaging and dislocations during subsequent deformation may result in certain extent of dissolution of the clusters and precipitates. At the hardness levels below this midpoint, the density of clusters/precipitates may be too low to provide a great deal of interactions with the dislocations that are to be added during deformation. For 170° C the preaging condition was selected as 4 hours with a hardness of 120.72 HV10.

4.3.2 170C Final Age Kinetics

For the 170° C preaging condition, the final ageing step was carried out at 170° C again. The duration for this final ageing condition was decided using ageing kinetics. The samples which had been subjected to a preaging and a deformation step were then heated at 170° C for varying amounts of time and the peak hardness was recorded. This was the final, fully processed condition. The peak values are displayed in Table 4.2 and 4.3, in red bold font.

Table 4.2. Vickers Hardness Measurements for the Final Age Kinetics in the Thermomechanical Process at 170C for stretching and rolling deformation modes.

HRS	4%s	8%s	4%r	8%r
0	126.2	134.3	120.8	126
1	132.8	135.2	126	129.8
2	135	138.8	129.2	135
4	137	**142.8**	130.2	**137**
6	**139.2**	141.4	**134.6**	132
8	136.8	139.6	127.6	130.6
16	138.2	136.8	127.4	128.4
24	136.34	132.6	124.2	125.8
48	129	129.6	123.6	123.4

*Red = Peak

Table 4.3. Vickers Hardness Measurements for the Final Age Kinetics in the Thermomechanical Process at 170C for combination deformation modes.

HRS	4%s4%r	8%s4%r	4%s8%r	8%s8%r
0	125	127.3	132.6	133
1	133.7	130.3	134	136.7
2	135	136.7	137	138.3
4	**138.7**	**142.7**	142.3	**143.7**
6	138.3	142.3	**145**	140.7
8	134.3	139	138.7	137.3

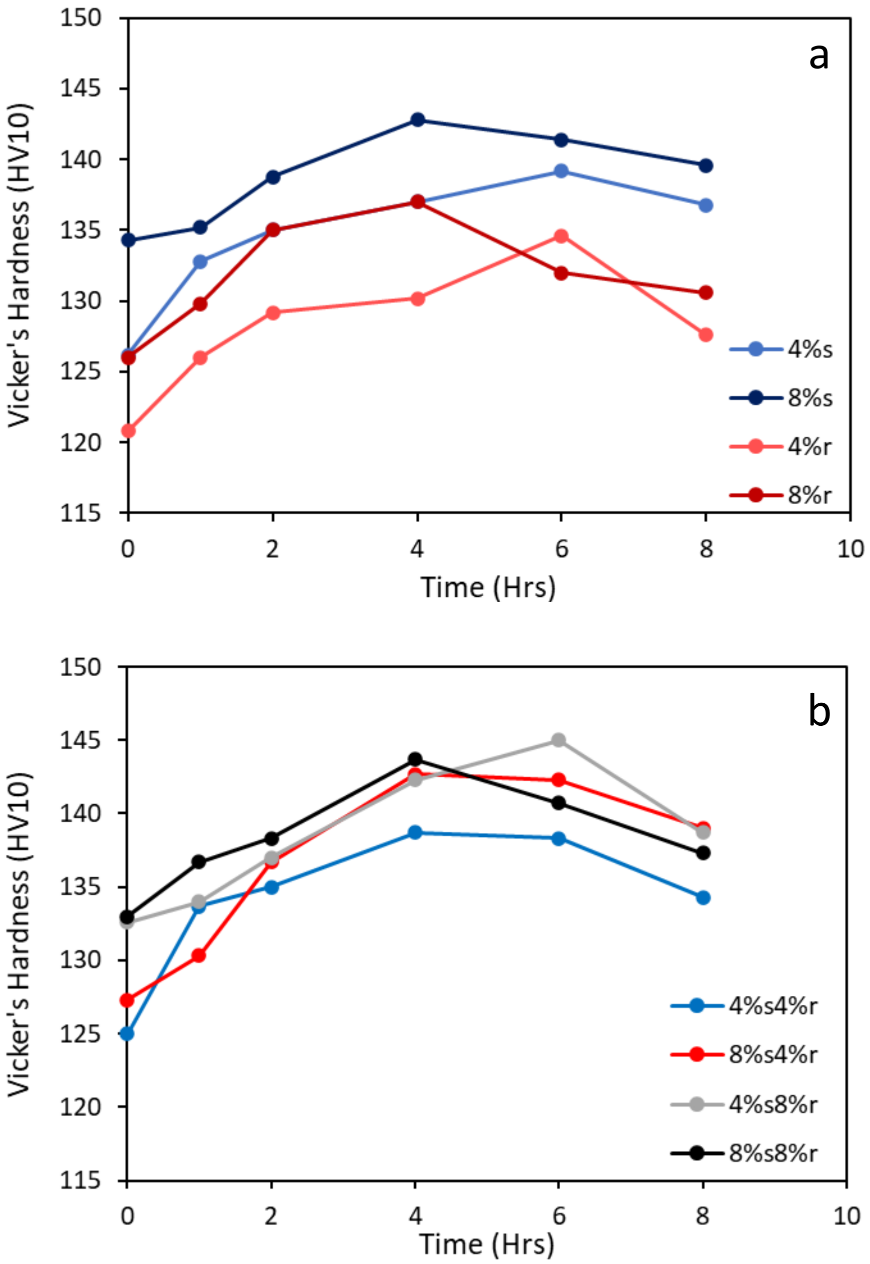

Figure 4.13. Vicker's Hardness as a function of thermomechanical conditions for a) stretching and rolling deformation modes and b) combination deformation modes.

For all conditions, the peak hardness was reached at a time period between 4-6 hrs depending on the level of strain applied to the material prior to the final ageing. After this stage of peak hardness, the hardness began to steadily decrease due to coarsening of the precipitates in the process of over ageing. This can be visualised in the graphs presented in Figure 4.13.

The hardness achieved in the combined deformation modes were higher than those of the singular deformation modes as a result of their relatively higher strain levels. This shows that although hardening response to the deformation was not that great in the previous step. The dislocations introduced in this stage acted and aided in the precipitation in the final ageing step.

4.3.3 190C Final Age Kinetics

For the preaging condition of 150° C/3h, the final ageing step was carried out at 190° C. To determine this final ageing duration, the samples were also made to undergo final ageing kinetics. The peak hardness values marked in red in Table 4.4 and 4.5 show these peak values. As the ageing temperature was much higher, there were smaller increments in times between the samples measured as a greater resolution was needed to find the exact point of the peak hardening.

Table 4.4. Vickers Hardness Measurements for the Final Age Kinetics in the Thermomechanical Process at 190C for stretching and rolling deformation modes.

HRS	**4%s**	**8%s**	**4%r**	**8%r**
0	96.3	96.3	96.3	96.3
0.25	107.3	110.7	107	108.7
0.5	115	116	110	116
1	118.7	123.7	118	120.3
1.5	**121.3**	**125.7**	121.3	**123.3**
2	120.7	121.7	**122**	120.7
2.5	118	120.3	117	118.7
3	117.3	117.7	116	116.7
3.5	116.3	114.7	113	115
4	114.3	113	112	113.7
4.5	113	112.3	111.7	111.7
5	113	112	111.3	111.3
6	112.3	111	110	110.7
7	111	110.3	109.3	109.7
8	106.7	108.3	105.3	107.7

***Red** = Peak

Table 4.5. Vickers Hardness Measurements for the Final Age Kinetics in the Thermomechanical Process at 190C for combination deformation modes.

HRS	**8%s4%r**	**4%s8%r**
0	96.3	96.3
0.25	112	112
0.5	119.3	121.3
1	124.3	123.7
1.5	**125.3**	**124.7**
2	125	123.3
2.5	122.3	119.3
3	121	117.3
3.5	117.7	116
4	114.3	114.3
4.5	113.7	112.3
5	112.3	111.7
6	111.7	111
7	110.7	109.3
8	106.7	106.3

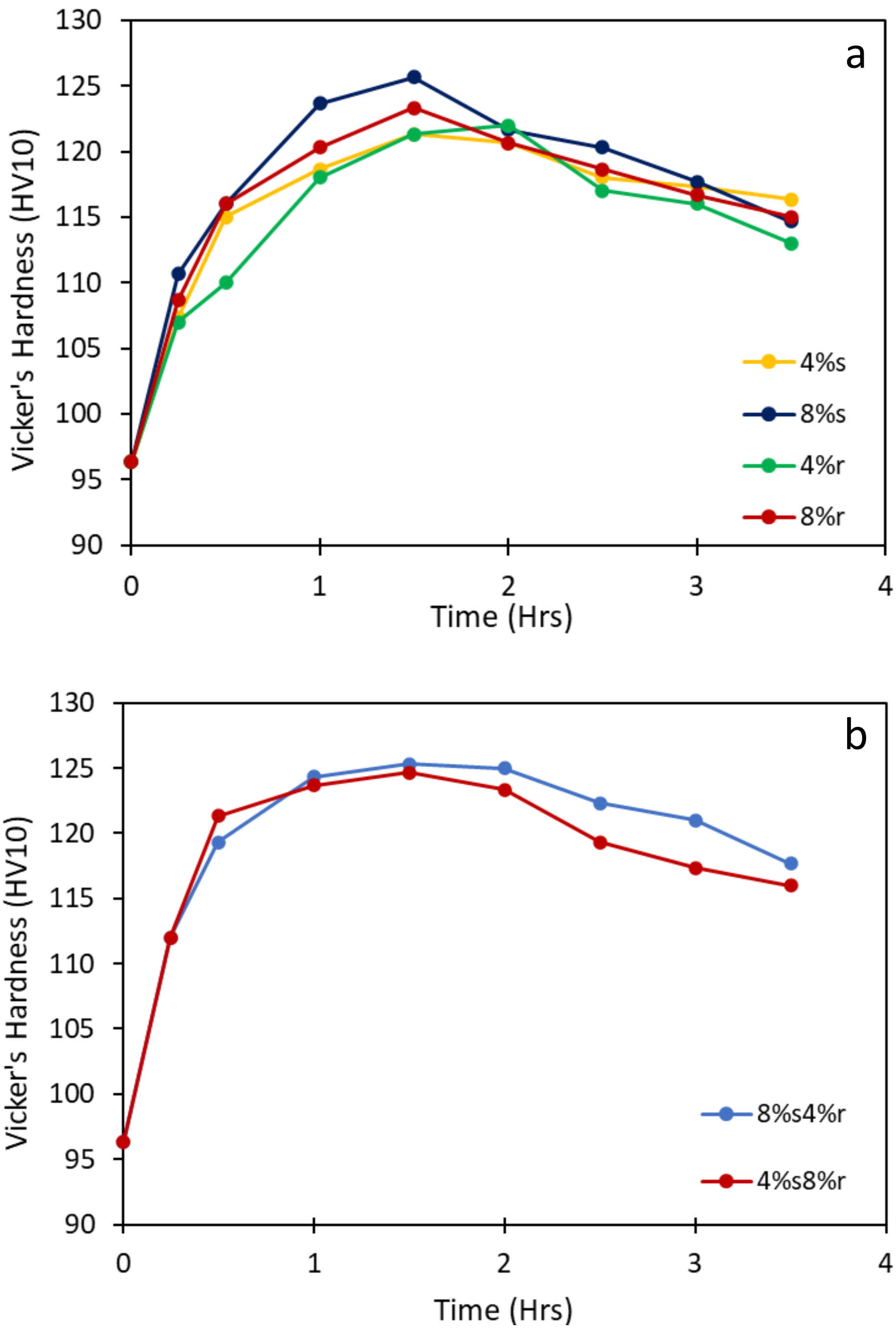

Figure 4.14. Vicker's Hardness as a function of thermomechanical conditions for a) stretching and rolling deformation modes and b) combination deformation modes.

For this final ageing temperature, the time required to reach this peak was much shorter. This shows the importance and dependency of the process on temperature. The final hardness condition in these samples were also lower than those in the earlier TMA recipe. The preaging and final ageing temperatures used largely determined the hardening achieved at the end of the processing.

4.4 Mechanical Performance

The different strengthening processes in this specific thermomechanical route, namely, grain boundary strengthening, strain hardening and precipitation strengthening all combine to give the overall strengthening of the final. It was expected that precipitation hardening would give rise to the greatest increase in mechanical properties out of all the strengthening mechanisms.

Measured properties of hardness and tensile strength are displayed to quantify and compare the varied stages of the thermomechanical process.

4.4.1 Hardness Testing

Each hardness sample was indented at 5 locations in the bulk region to obtain readings of the materials Vickers Hardness. Averages and the standard deviation of each state were calculated and tabulated.

Table 4.6. Vickers Hardness Measurements for Stretched Deformed Material in the T4 condition.

Temper	**Condition**	**1(HV10)**	**2(HV10)**	**3(HV10)**	**4(HV10)**	**5(HV10)**	**AVG(HV10)**	**StDev**
T4	As Extruded	63	64	64	64	65	64.0	0.707
T4	4% stretch	67	68	69	68	66	67.6	1.140
T4	8% stretch	73	68	74	75	73	72.6	2.702

Table 4.7. Vickers Hardness Measurements for Rolled Deformed Material in the T4 condition.

Temper	**Condition**	**1(HV10)**	**2(HV10)**	**3(HV10)**	**4(HV10)**	**5(HV10)**	**AVG(HV10)**	**StDev**
T4	As Extruded	63	64	64	64	65	64.0	0.707
T4	4% roll	68	68	67	68	67	67.6	0.650
T4	8% roll	72	73	73	73	73	72.8	0.386

Table 4.8. Vickers Hardness Measurements for Combined Stretched and Rolled Deformed Material in the T4 condition.

Temper	Condition	1(HV10)	2(HV10)	3(HV10)	4(HV10)	5(HV10)	AVG(HV10)	StDev
T4	As Extruded	63	64	64	64	65	64.0	0.707
T4	4%s + 4%r	80	78	79	80	80	79.2	0.804
T4	4%s + 8%r	82	81	78	80	80	80.1	1.537
T4	8%s + 4%r	85	84	85	84	85	84.5	0.583
T4	8%s + 8%r	87	87	87	90	89	88.0	1.532

The Vickers hardness measurements in the tables show the trend in the mechanical properties of the deformed specimens in the as-extruded condition. In both stretching and rolling, there was a positive correlation where, as the strain level was increased, the strength and hardness of the material also increased. Across all conditions, the T4 8%stretch + 8%roll sample reads the greatest hardening.

This can be seen more clearly in Figure 4.13 below.

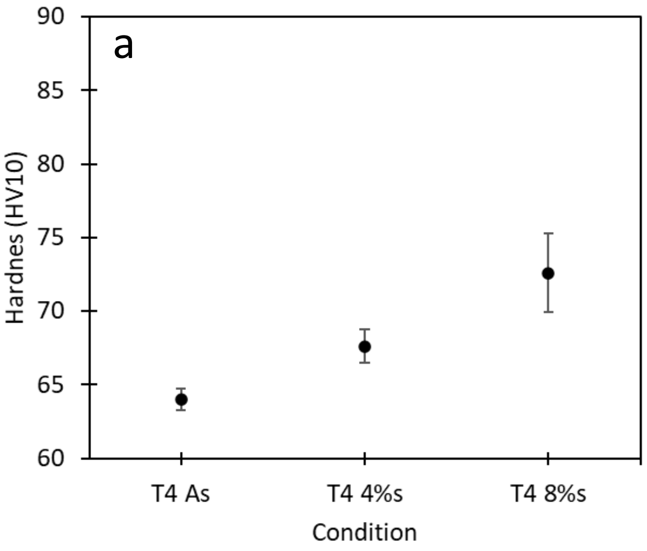

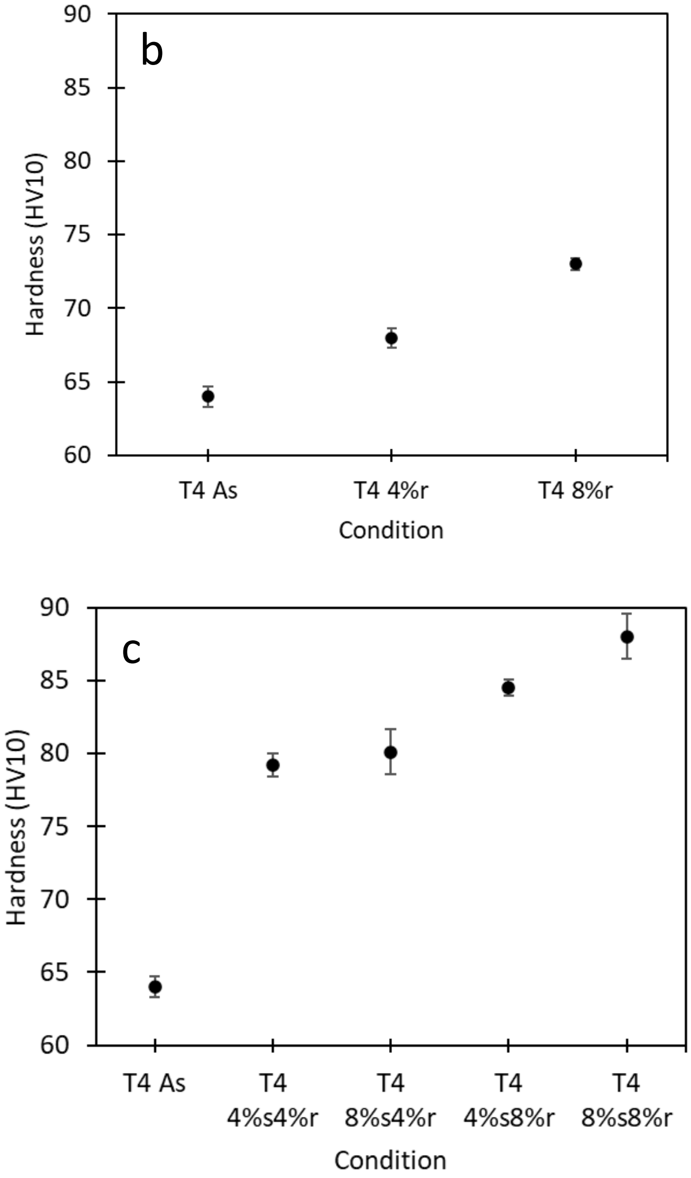

Figure 4.15. Vickers Hardness Measurements for Various Deformation Conditions in the T4 Temper a) stretch b) roll c) combinational.

Comparing the stretched samples and the rolled samples, there is virtually no difference between the hardness recordings at the same strain level. In most samples, the standard deviation is low, with the T4 8% stretch sample having the greatest variance in measurements across the 5 indents.

As for the combination conditions, where both stretching and rolling were applied to the specimens in the same direction, the equivalent strain can roughly be calculated by directly adding the stretch and roll strain levels. For example, the 4%stretch + 4%roll sample can be approximated to have a strain level of 8%. Just as in the stretched or rolled material, as the level of strain in the material is increased, so is the final hardness values. The primary strengthening mechanism at play here is work hardening.

Table 4.9. Vickers Hardness Measurements for Stretched Deformed Material in the PreAged condition 170C/4h.

Temper	Condition	1(HV10)	2(HV10)	3(HV10)	4(HV10)	5(HV10)	AVG(HV10)	StDev
PreAged	No Deformation	120.2	120.6	120.9	120.8	121.1	121	0.342
PreAged	4% stretch	124.9	127.4	124.5	127	127.2	126.2	1.384
PreAged	8% stretch	134.9	136.3	133.8	134.6	131.9	134.3	1.617

Table 4.10. Vickers Hardness Measurements for Rolled Deformed Material in the PreAged condition 170C/4h.

Temper	Condition	1(HV10)	2(HV10)	3(HV10)	4(HV10)	5(HV10)	AVG(HV10)	StDev
PreAged	No Deformation	120.2	120.6	120.9	120.8	121.1	121	0.342
PreAged	4% roll	119	122	121	120	122	120.8	1.303
PreAged	8% roll	127	127	126	124	126	126	1.095

Table 4.11. Vickers Hardness Measurements for Combined Stretched and Rolled Deformed Material in the PreAged condition 170C/4h.

Temper	Condition	1(HV10)	2(HV10)	3(HV10)	4(HV10)	5(HV10)	AVG(HV10)	StDev
PreAged	No Deformation	120.2	120.6	120.9	120.8	121.1	121	0.342
PreAged	4%s + 4%r	124	126	125	126	123	125	1.304
PreAged	4%s + 8%r	128	127	127	128	126	127.3	0.837
PreAged	8%s + 4%r	132	134	132	133	133	132.6	0.837
PreAged	8%s + 8%r	133	131	135	134	133	133	2

Initial investigations were carried out on the preaging condition of the 170^{o}C/4h. Similarly, to the T4 condition, the hardness of each sample was measured after the application of preaging and deformation. The trend seen in the T4 state is mirrored in the Preaged state. As the level of deformation is increased, so is the hardness achieved in the Vicker's hardness measurement. Unlike in the as-extruded state however, there is a difference in the hardness increments achieved in stretch and rolling. Comparing the 4% strain level for stretching and rolling, there was a greater increase in the hardening in the stretched than in rolled samples. The trend is also the same when comparing the 8% strain level for both stretch and roll. It appears that the dislocations introduced through the stretch deformation had a greater interaction with the clusters and dislocations introduced during the preaging step resulting in this better hardening response.

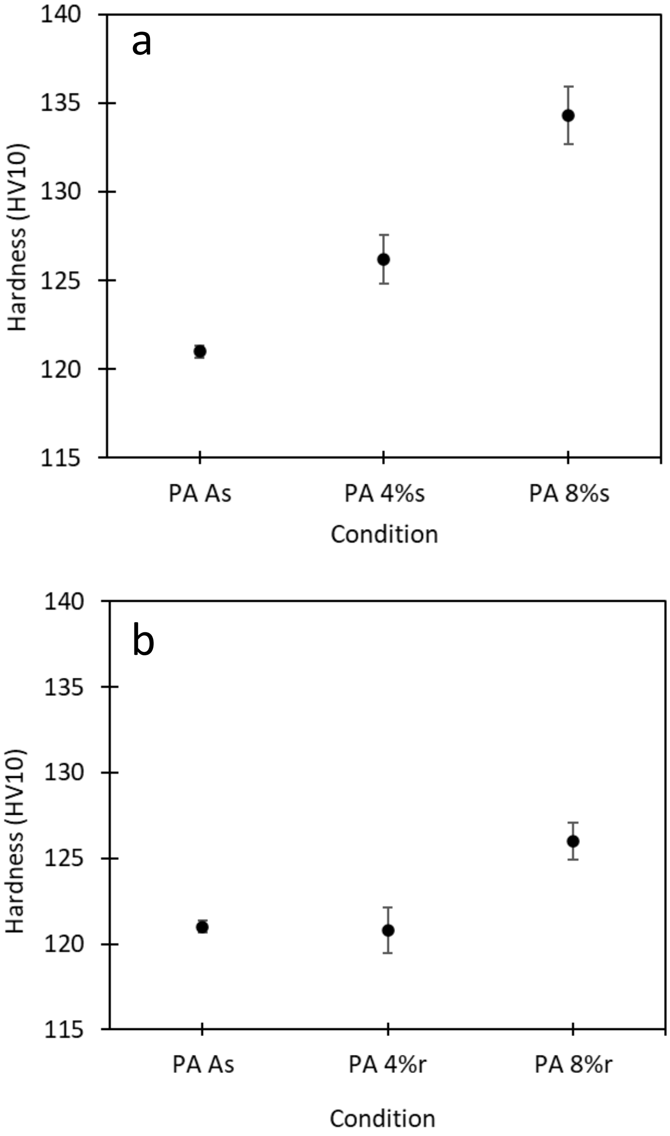

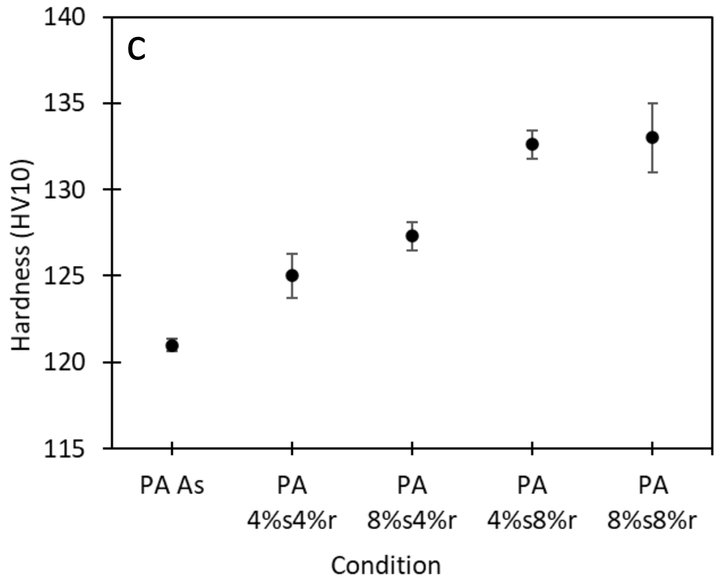

Figure 4.16. Graphs Displaying the Vickers Hardness Measurements for Various Deformation Conditions in the 170° C PA Temper a) stretch b) roll c) combinational.

There is again low deviation between the measurements of the indents. Table 4.9 shows the results for the combined deformation conditions. Just as with the as extruded samples, there is a positive increase in the hardness as the equivalent strain level increases. The 8%stretch + 8%roll sample shows the greatest hardening. The effect of rolling was seemingly less significant as the hardness reading of 4% stretch + 4% roll was only slightly greater that the hardness recorded for 4% stretch alone. The same is true for 8% strain level, where the average hardness value for the 8% stretch + 8% roll is similar to the average hardness of the 8% stretched alone sample. This may be due to the plane/direction in which the stretch and roll deformations are applied and the direction the hardness indents are measured compared to these.

Table 4.12. Vickers Hardness Measurements for Stretched Deformed Material in the PreAged condition 150C/3h.

Temper	Condition	1(HV10)	2(HV10)	3(HV10)	AVG(HV10)	StDev
PreAged	No Deformation	97	95	97	96.33	1
PreAged	4% stretch	108	108	106	107.33	1.528
PreAged	8% stretch	112	110	110	110.67	1.528

Table 4.13. Vickers Hardness Measurements for Rolled Deformed Material in the PreAged condition 150C/3h.

Temper	Condition	1(HV10)	2(HV10)	3(HV10)	AVG(HV10)	StDev
PreAged	No Deformation	97	95	97	96.33	1
PreAged	4% roll	106	107	108	107	0.577
PreAged	8% roll	109	109	108	108.67	1.528

Table 4.14. Vickers Hardness Measurements for Combined Stretched and Rolled Deformed Material in the PreAged condition 150C/3h.

Temper	Condition	1(HV10)	2(HV10)	3(HV10)	AVG(HV10)	StDev
PreAged	No Deformation	97	95	97	96.33	1
PreAged	4% + 8%	113	112	111	112	1.528
PreAged	8% + 4%	114	112	110	112	1.528

For the 150°C/3h preaging condition, the hardness increase achieved after being subjected to deformation was also recorded. A trend is similar to that in the earlier preaging condition at 170° C. The measured hardness of the ageing alone is higher in the 170° C than at 150° C, at 121 and 96.33 HV10 respectively. This suggests that the 150° C preaging state was in an earlier stage of the precipitation sequence, meaning in the matrix, there is the presence of smaller clusters and less formed precipitates. This is also verified in the preaging kinetics data of Figure 4.12, where the mid-point of hardening was at an ageing time of 24h – this aging time would be in theory comparable to the samples aged to the previous 170 ° C/4h preaged state.

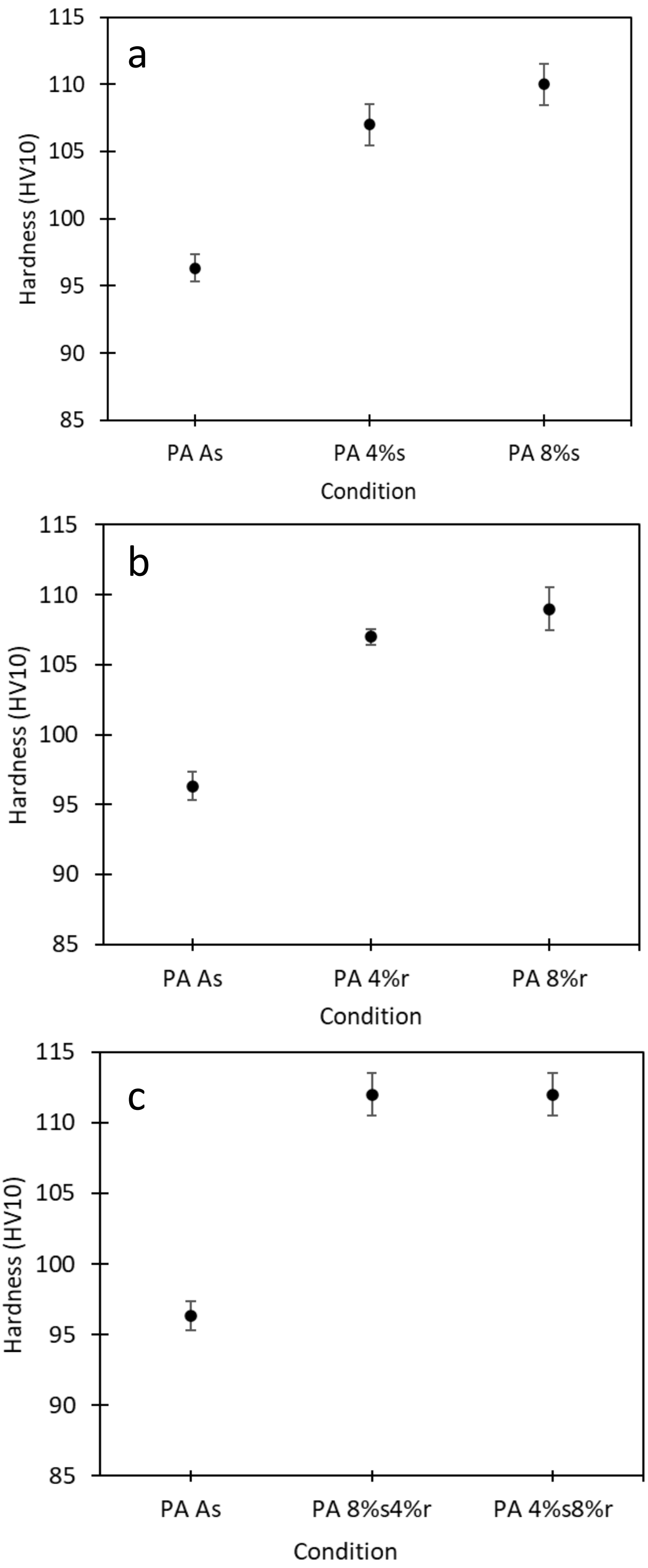

Figure 4.17. Graphs Displaying the Vickers Hardness Measurements for Various Deformation Conditions in the 150 ° C PA Temper a) stretch b) roll c) combinational.

Comparing the hardness figures of the stretched and rolled samples, as in the 170° C preaging condition, the stretch deformation gives a higher hardening response, but it is not as pronounced. This may be because the 150° C preaging condition is closer to the T4 state where the effect of both stretching and rolling were equal.

When comparing the combined deformation modes, the 4%stretch + 8%roll sample and the 8%stretch + 4%roll have the exact same hardness measurements. Just as in the T4 stage, as the combined equivalent strain is 12%, the hardness measurements for these samples were more than any measured for the stretch or roll only samples.

Generally, the hardness measured in the 150° C conditions are less than those measured in the 170° C condition. These lower recorded increases in hardness can be attributed to the samples being in the earlier stages of the ageing process.

Electromagnetic Pulse Technology (EMPT), was used as a more complex deformation mode to observe the effects on this high speed plastic deformation on the material performance. The effective strain path was completely different to those present in stretching and rolling. The lack of frictional forces in the procedure was also of interest. Strips of the aluminium alloy are contoured around a die using electromagnetic energy. This induced a current in the workpiece, creating a Lorentz force that causes a deformation.

Automatic hardness maps of the EMPT specimen illustrate the hardening spread across the specimen in response to the sophisticated pulse forming technique. A complex hardening consisting of tensile and compressive strains give rise to these colourful maps. Different stages of the processing route are mapped to allow comparison.

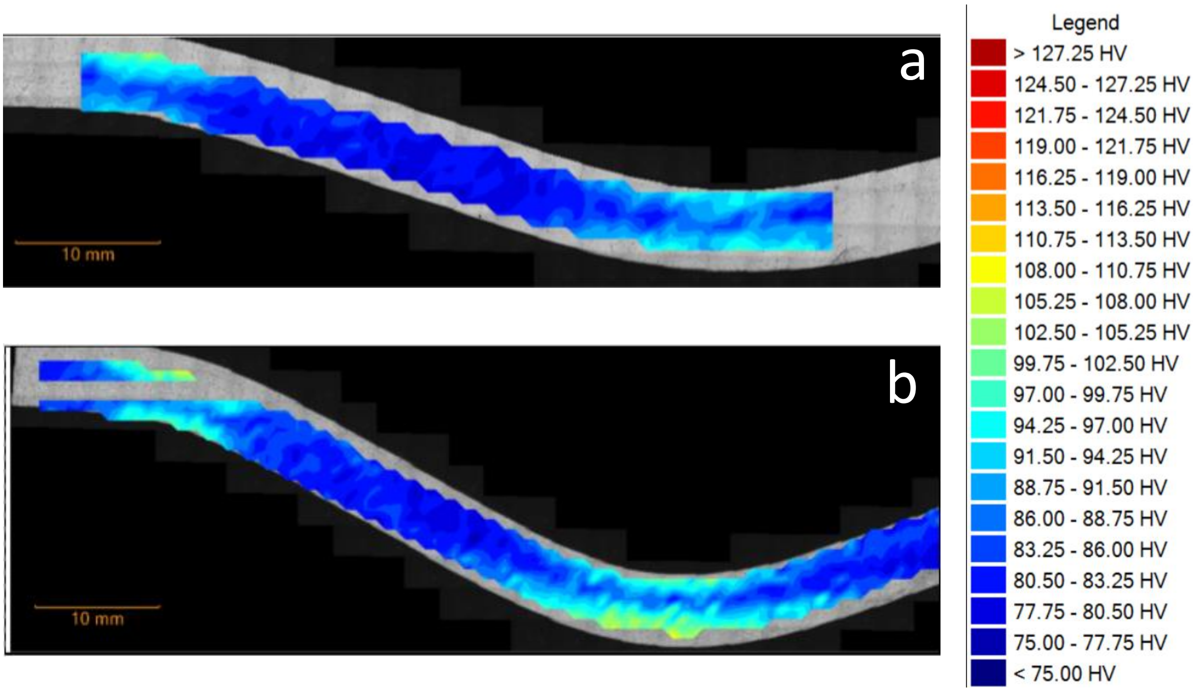

Figure 4.18. Hardness Spread Maps displaying the hardness distribution across the transverse plane of a specimen bent through EMPT forming in the T4 condition. Forming energies of (a) 30KJ and (b) 40KJ.

From Figure 4.18 the hardness distribution in the EMPT formed sample can be seen. Due to the relative low strength of the material in the T4 state, the sample is more formable and was able to, when compared to all other conditions, take the shape of the die more easily. The higher energy used consequently produced a specimen with a higher bend angle. There are localised areas of hardness in the specimen due to the stress fields created by the forming technique. The majority of the hardness increase was limited to the bent areas. This can be seen in Figure 4.18 in the middle of the bend as well as at the bend terminal. Compressive forces as well as tensile forces are responsible for the hardness increases in this material and are displayed in the image in a comparable manner to those in a normal bend sample. As this sample was in the T4 as-extruded condition, the comparable hardness seen were relatively low – using the key on the right-hand side, the hardness of the bulk material was approximately 77HV. This is a 13HV increase compared the measured hardness of the normal T4 material and so there is some hardness increase in the bulk area as a result of the forming. The hardness measured in the bent region of the sample however has a hardness ranging from 99-110 HV, which is a significant increase.

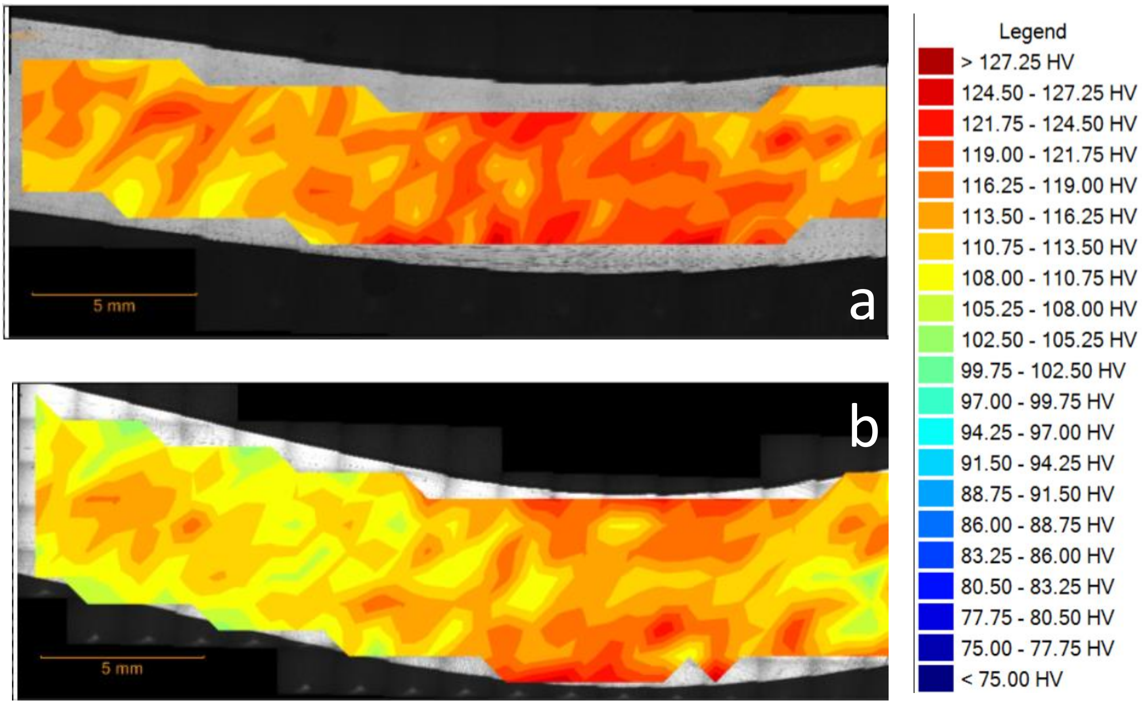

Figure 4.19. Hardness Spread Maps displaying the hardness distribution across the transverse plane of a specimen bent through EMPT forming in the Preaged condition. Forming energies of (a) 30KJ and (b) 40KJ.

In the preaged condition, the sample is far less formable, and this is illustrated by the lower bend angle in both samples compared to the T4 samples even at the same energy levels. Again, the hardness increase was mostly localised in the bent area, so this figure focused in on this area gives a higher resolution. From both samples, the highest recorded hardness is at the top and bottom of the bends, the hardness lessens towards the middle region. Compressive forces acted in the top of the material and tensile forces are present in the bottom section. The hardness measured in this bend area range from 110-121HV. There is a great variation in hardness localised to one small area of the sample.

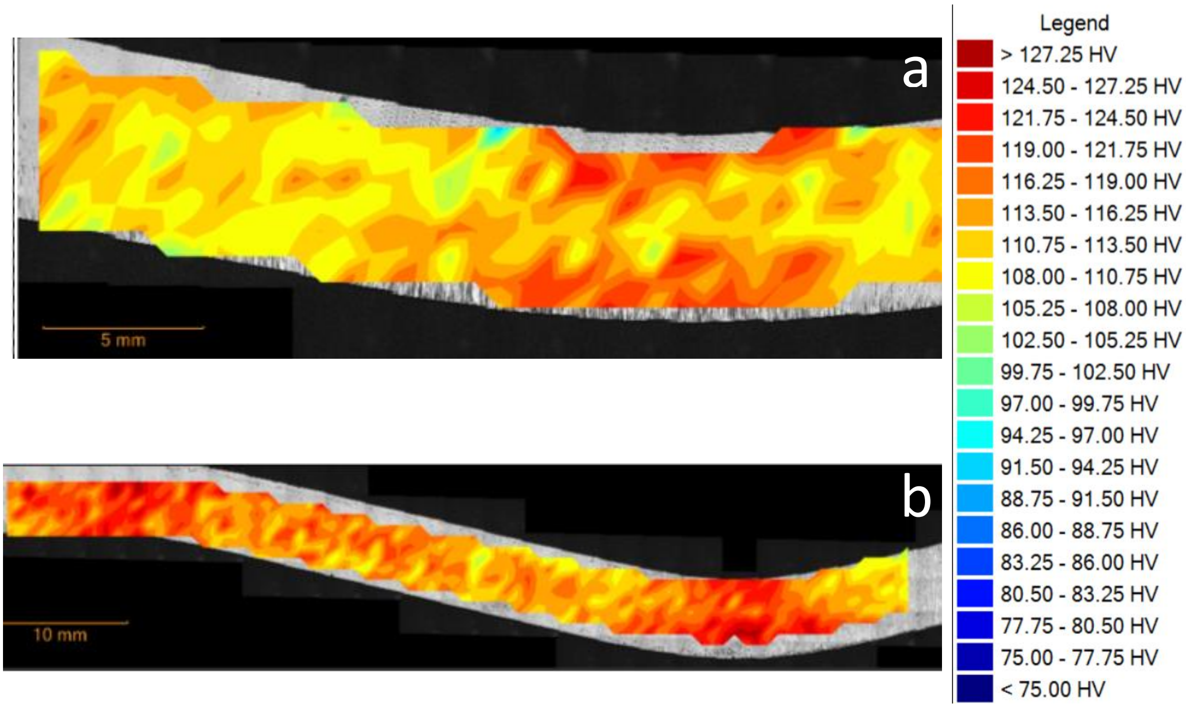

Figure 4.20. Hardness Spread Maps displaying the hardness distribution across the transverse plane of a specimen bent through EMPT forming in the Fully Processed condition. Forming energies of (a) 30KJ and (b) 40KJ.

In the fully processed material, the hardness throughout the material is generally much higher than in all other processing states. The localised hardness feature is again present in samples at both levels. The formability of samples in this condition is the least and so the bending in the region is less than the previous. The hardness readings in these samples range from 94-127HV. The peak hardness achieved is not that much greater than in the preaged condition. This is because of the high strain level of the EMPT forming method, the hardening achieved after just the Preaged + EMPT formed condition are very close to the best hardness of the material.

4.4.2 Tensile Response

Table 4.15 shows the results from the tensile mechanical testing of the material at the various stages of the thermomechanical process. From the aging kinetics performed in section 4.3.1, the recipe of a 170C temperature was a preaging time of 4 hours at 170C, followed by the required deformation and a final ageing of 170C for 4 hours. This preaging time was selected as the halfway hardening point.

Table 4.15. Tensile Test results for all thermomechanical conditions. Both Preaging and Final Ageing performed at 170C.

Temper	Strain Mode	Strain Level (%)	Hardness (HV10)	Yield Strength (MPa)	Tensile Strength (MPa)	Uniform Elongation (%)	Total Elongation (%)
As Extruded	None	0	64.0	88.0	211.2	17.3	18.9
Preaged*	None	0	120.72	249.1	307.3	10.6	14.6
T6**	None	0	132.4	309	334.4	8.2	12.7
TMA***	Stretch	4		323.5	342.1	6.6	11.9
T4	Stretch	4	67.6	173.9	251.7	16.6	18.7
T4	Stretch	8	72.6	186.2	254	10.8	15
T4	Roll	4	67.6	168.8	255.1	15.4	18.7
T4	Roll	8	72.8	178.0	253.4	12.7	16.1
T4	S+R****	4 + 4	79.2	196.2	248.7	10.8	15.1
T4	S+R	4 + 8	80.1	206.7	252.1	7.4	10.2
T4	S+R	8 + 4	84.5	206.6	250.9	8.9	10.1
T4	S+R	8 + 8	87.9	218.1	257.6	7.2	11.6
Preaged	Stretch	4	126.2	296.6	330.8	9.4	13
Preaged	Stretch	8	134.3	339.0	351.4	7.0	10.4
Preaged	Roll	4	120.8	282.2	323.9	7.7	12.5
Preaged	Roll	8	126	295.2	326.8	5.8	9.9
Preaged	S+R	4 + 4	125	329.6	375.9	11.4	16.6
Preaged	S+R	4 + 8	127.3	335.3	378	7.5	12.6
Preaged	S+R	8 + 4	132.6	349.8	379.7	4.9	10.9
Preaged	S+R	8 + 8	133	341.6	371.5	4.5	9.2
aDA*****	Stretch	4	141.8	337.9	349.3	6.1	11.1
aDA	Stretch	8	143	356.9	364.5	5.4	10.2
aDA	Roll	4	134.8	303.8	331.5	6.7	11.7
aDA	Roll	8	137	324.2	348	6.2	10.6
aDA	S+R	4 + 4	138.7	329.8	352.4	6.4	11.8
aDA	S+R	4 + 8	142.7	342.6	367.1	6	11.2
aDA	S+R	8 + 4	145	347.7	365.5	5	9.5
aDA	S+R	8 + 8	143.7	352.8	369.3	4.5	9.3

* Preaged Condition: 170C/4h
** T6 Condition: 170C/12h
*** TMA is the Thermomechanical Processing Condition: - 150/3h + 4%stretch + 190/4.5h
**** S+R is the Combination of Stretch + Roll
***** aDA is the Thermomechanical Process Condition: - 170/4h + D + 170/4h

Table 4.16. Tensile Test results for all thermomechanical conditions. Preaging temperature being 150C and Final Ageing performed at 190C.

Temper	Strain Mode	Strain Level (%)	Hardness (HV10)	Yield Strength (MPa)	Tensile Strength (MPa)	Uniform Elongation (%)	Total Elongation (%)
As Extruded	None	0		64.0	88.0	17.3	18.9
Preaged*	None	0		151.6	257.1	17.5	17.9
T6**	None	0		307	338	10.5	14.7
TMA***	Stretch	4		323.5	342.1	6.6	11.9
T4	Stretch	8		221.9	251.9	7.8	10.8
T4	Roll	8		214.8	263.15	8.8	13.8
Preaged	Stretch	4		232.9	284	12.8	18.2
Preaged	Stretch	8		270.4	298.9	8.7	13.8
Preaged	Roll	4		199.7	279.7	14	19.3
Preaged	Roll	8		243.3	292.1	9.5	14.6
aDA	Stretch	4		319	340.2	7.8	13.3
aDA	Stretch	8		335.1	350.9	6.4	11.5
aDA	Roll	4		301.4	334.8	7.5	12.65
aDA	Roll	8		317.7	346.9	6.3	11.4
aDA	S + R****	4+ 8		326.2	350.4	5.8	10.9
aDA	S + R	8 + 4		331.3	353.1	6	10.9

* Preaged Condition: 150C/3h
** T6 Condition: 150C/72h
*** TMA is the Thermomechanical Processing Condition: - 150/3h + 4%stretch + 190/4.5h
**** S+R is the Combination of Stretch + Roll
***** aDA is the Thermomechanical Process Condition: - 150/3h + D + 190/1.5h

In Table 4.16, the tensile properties of the material under the 150C recipe are displayed. Again, the aging kinetics of section 4.3.1 allowed for the choice of the processing conditions. The preaging time used here was retrieved from the Constellium optimised TMA process which was discovered to be an aging time of 3 hours. For the 150C recipe, following preaging and a deformation step, the final ageing condition was found to be and ageing time of 1.5 hours at a temperature of 190C. From the ageing kinetics, the 150C condition is in a slightly less developed stage of the precipitation sequence which explains the lower nominal mechanical properties. The 150C recipe as well as the 170C recipe would be useful in comparing the effects of preaging conditions of the final mechanical properties reached.

Tensile curves given as true stress-strain curves with the yield stress given as the 0.2 proof stress, tensile strength given as the highest obtained tensile strength before necking, uniform elongations are obtained at the point necking commences and total elongation is taken at the point of fracture.

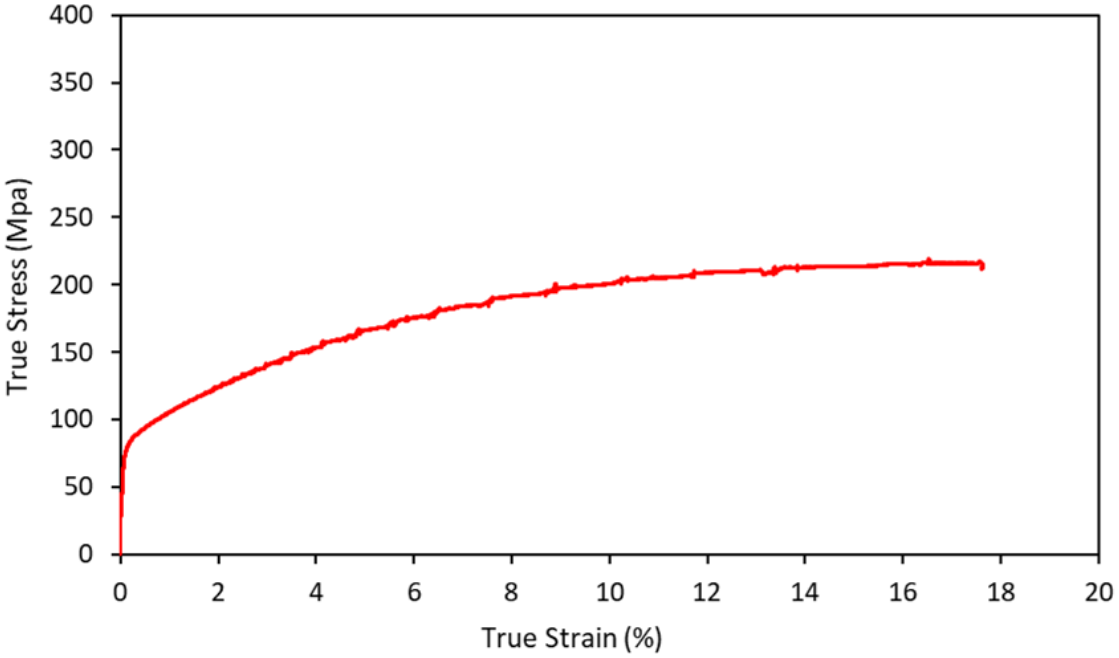

Figure 4.21. Tensile Flow curve depicting the tensile properties of the Aluminium alloy in the T4 state, as-extruded condition.

Figure 4.21 displays the starting material in the as-extruded condition. This state is critical and will aid in further comparison. Changes in mechanical properties that are realised will be highlighted and referenced back to this original flow curve and changes in the shape and characteristics of the curves will help in understanding the changes that have occurred in the material as a result of these thermomechanical processes. Fluctuation seen in the flow curve are as a result of vibration of the tensile testing system.

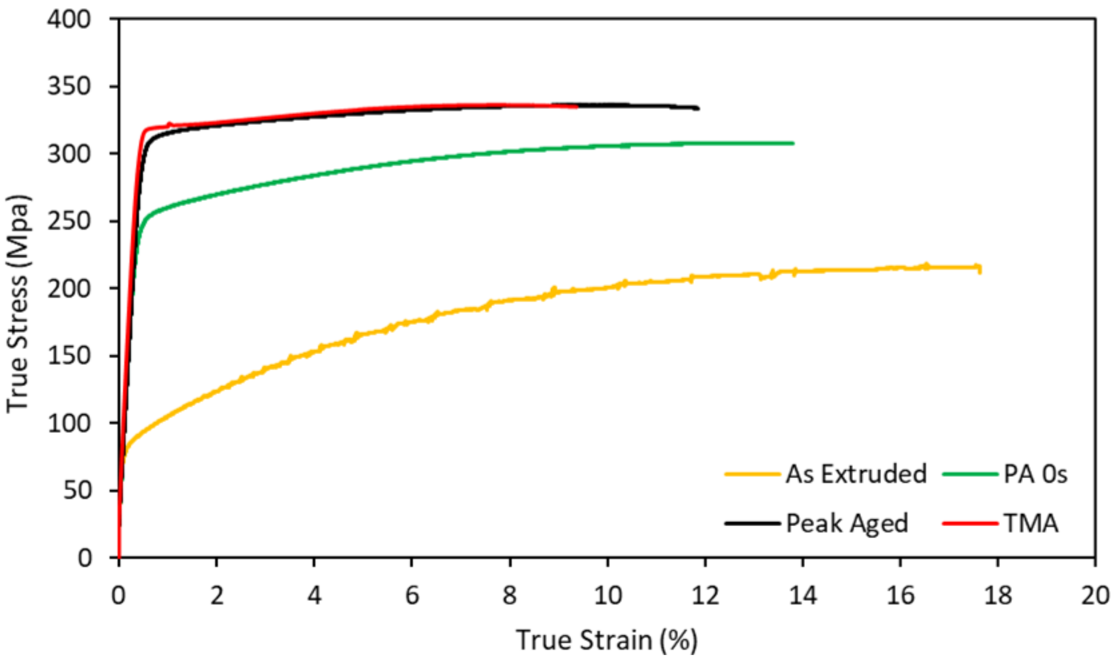

Figure 4.22. Tensile Flow curve depicting the tensile properties of the Aluminium alloy in the T4 state, as-extruded condition.

As seen in Figure 4.22, some of the tensile mechanical properties from key stages are compared. The as extruded, the preaged, the peak aged and TMA conditions are compared. The trend shows that as the material progresses along the thermomechanical process, the tensile properties are enhanced, this is in alignment with the results from the hardness tests in section 4.3.1. As the yield strength and the tensile strengths are increased though however, the uniform elongation of the material is reduced and thus the material becomes far less ductile. The ability of the material to work harden also decreases progressively as the material becomes increasingly processed.

The TMA condition, given by Constellium has the highest yield and tensile strengths. The peak aged (T6) condition is 170^{o} C has a similar yield and tensile strength, however. The Preaged sample is in an underaged condition and thus the underdeveloped precipitates present in the microstructure do not correlate to the optimal conditions for peak hardening.

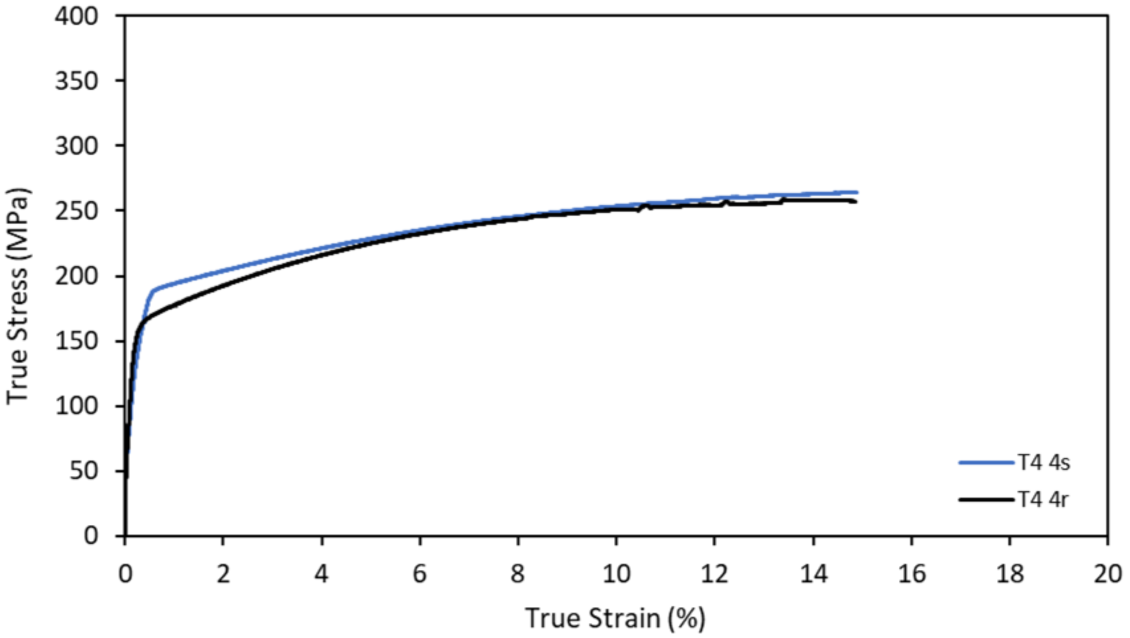

Figure 4.23. Tensile Flow curve depicting the tensile properties of the Aluminium alloy in the T4 state, at 4% strains for stretch and roll deformation, respectively.

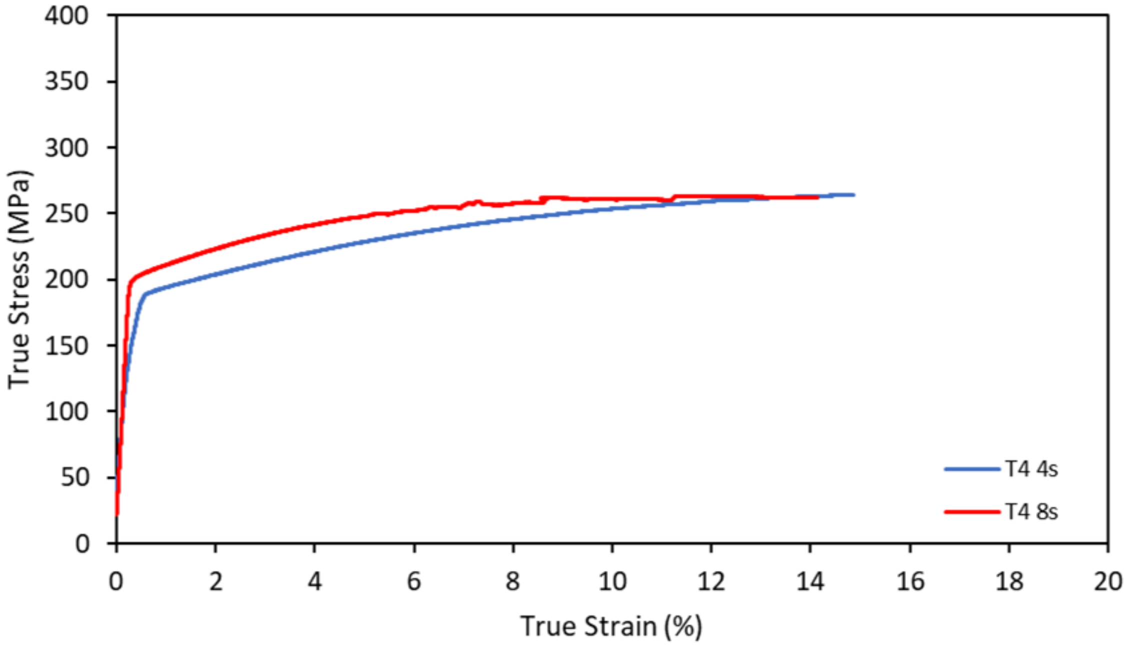

Figure 4.24. Tensile Flow curve depicting the tensile properties of the Aluminium alloy in the T4 state, at 4% and 8% strains for stretch deformation, respectively.

The two charts, Figure 4.23 and Figure 4.24 show the material's tensile response with exposure to deformation. The effects of work hardening alone are seen and thus when precipitates are introduced to the microstructure through ageing, the interactions occurring in the material can be inferred and understood.

From the charts, the strain level is important in deciding the final properties of the material. In both stretch and roll modes of deformation, the 8% strain level gives the highest final yield and tensile strengths. It can also be seen though that there is a compromise between strength and ductility. This is shown in Figure 4.24 where the 4% and 8% strain levels of stretch are compared. The 8% strain level has higher strength values, but the ductility is reduced.

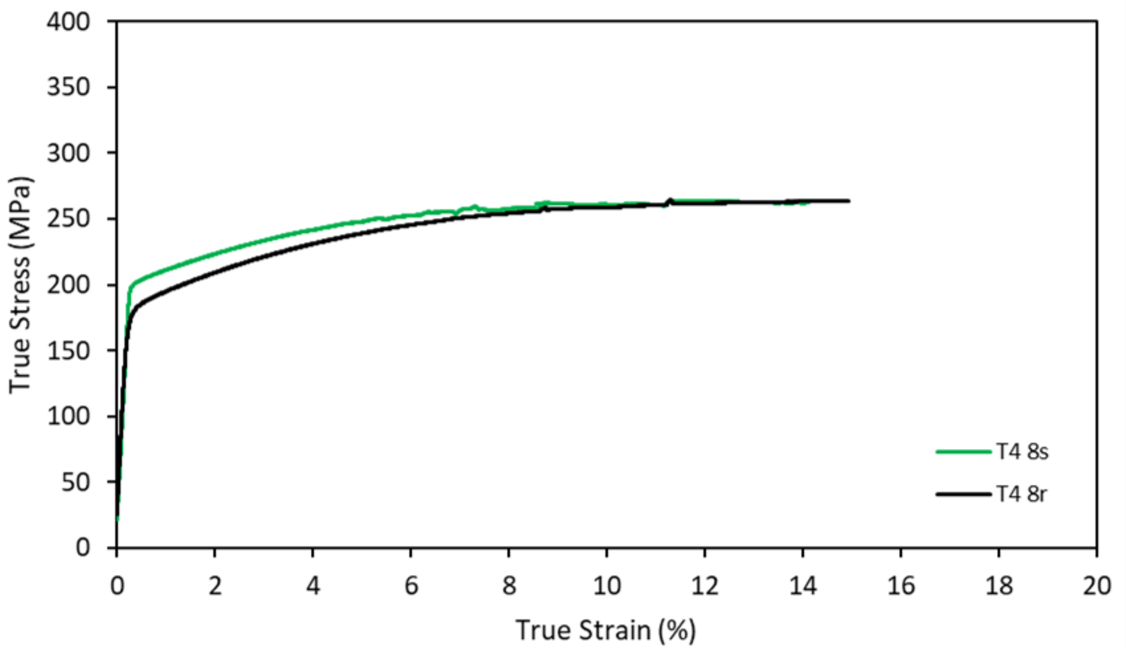

Figure 4.25. Tensile Flow curve depicting the tensile properties of the Aluminium alloy in the T4 state, at 8% strains for stretch and roll deformation, respectively.

Comparing the different deformation modes, in Figure 4.23 and in Figure 4.25 it can be seen that at both strain levels, stretch deformation gives a slightly higher strength advantage for the level of strain input in the material. The yield strength achieved by the 8% stretch strain level is 4.6% higher than that achieved by the rolled sample of the same strain level. The flow charts taper off and their ultimate tensile strengths and ductility are virtually identical.

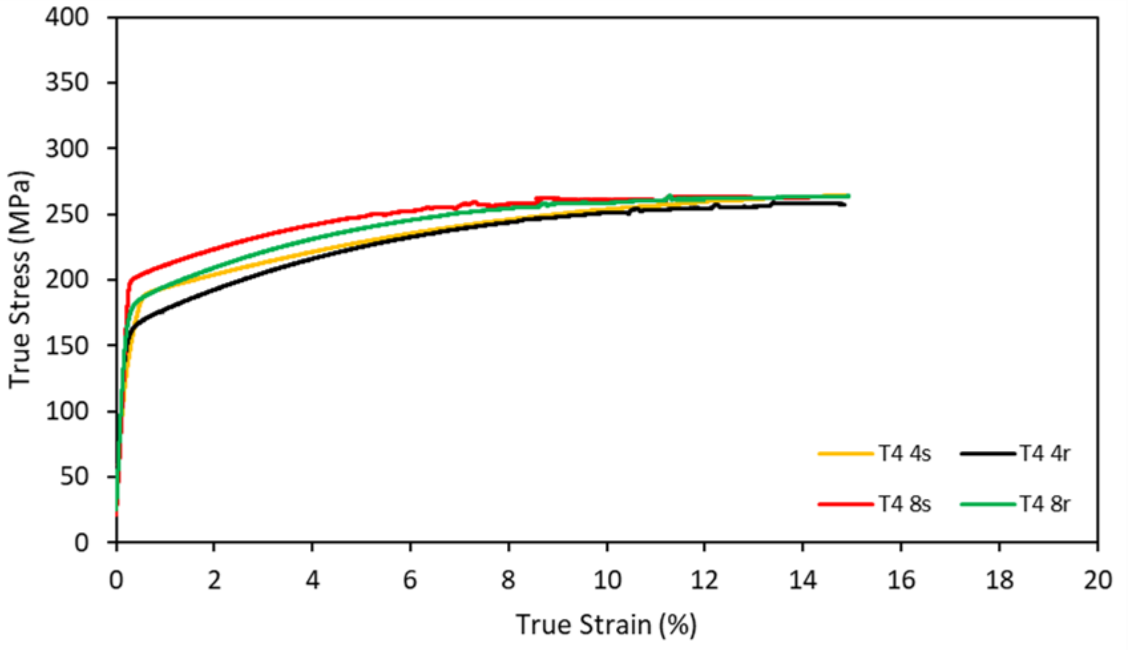

Figure 4.26. Tensile Flow curve depicting the tensile properties of the Aluminium alloy in the T4 state, at 4% and 8% strains for stretch and roll deformation, respectively.

Figure 4.26 displays the trends seen in the deformation processing more clearly. The 4 flow curves are joined in one graph.

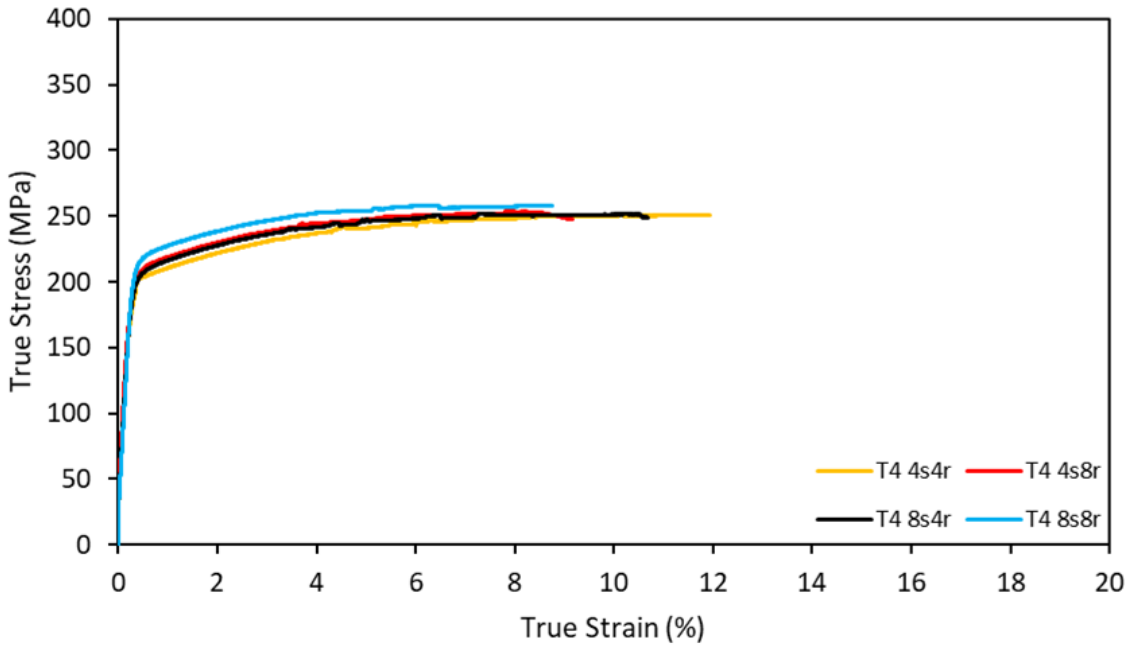

Figure 4.27: Tensile Flow curve depicting the tensile properties of the Aluminium alloy in the T4 state, showing varying degrees of stretch and roll deformation strains.

To imitate a more complex deformation mode, the two types of deformation were combined. This means the resultant material had a combination of tensile and compressive forces applied to it. The trend seen in these materials are similar to those seen in the simple deformation modes. As the degree of strain is increased, so is the strength of the material, but the ductility of the material reduces as a result. The stretch deformation was always performed before the roll deformation in processing. Comparing the 4s8r and the 8s4r conditions, where the equivalent strain levels are the same, the measured tensile parameter are very close in value, this is coherent with what was seen in the hardness testing of these conditions.

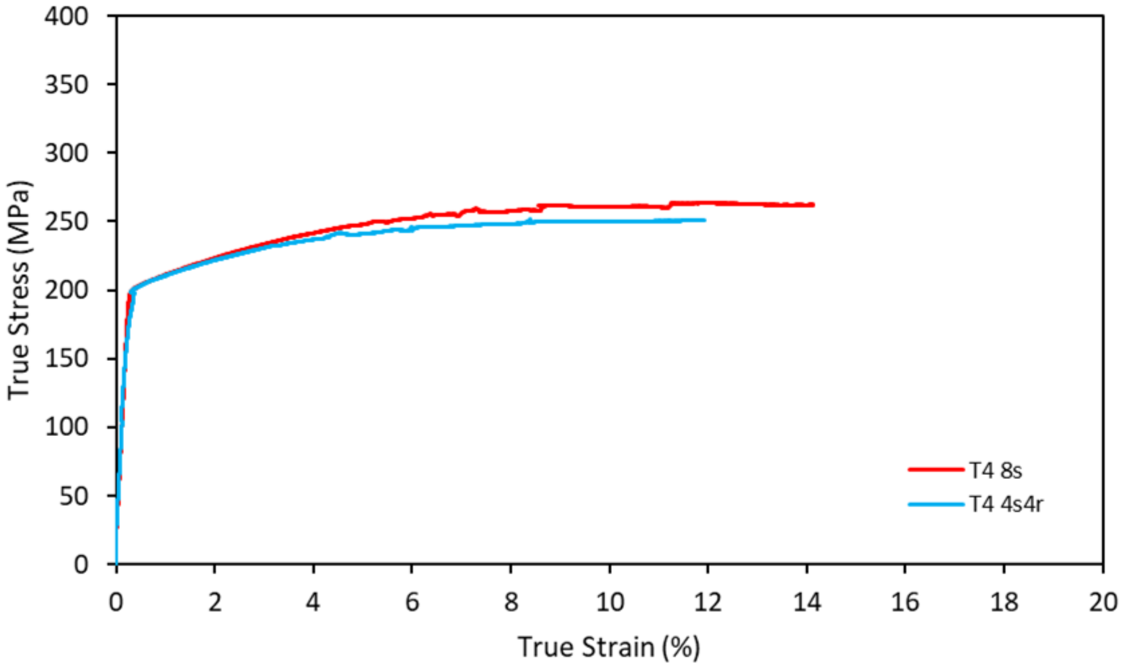

Figure 4.28. Tensile Flow curve depicting the tensile properties of the Aluminium alloy in the T4 state, at 8% stretch and 4% stretch + 4% roll strains.

Figure 4.28 compares the tensile flow curves of the 8% stretched condition and the 4%stretch+4%roll combined condition. These two states have the same calculated strain levels, but the figure displays a noticeable difference in the ultimate tensile strength and ductility of the two tested materials. The yield strengths of the two conditions are remarkably similar, however.

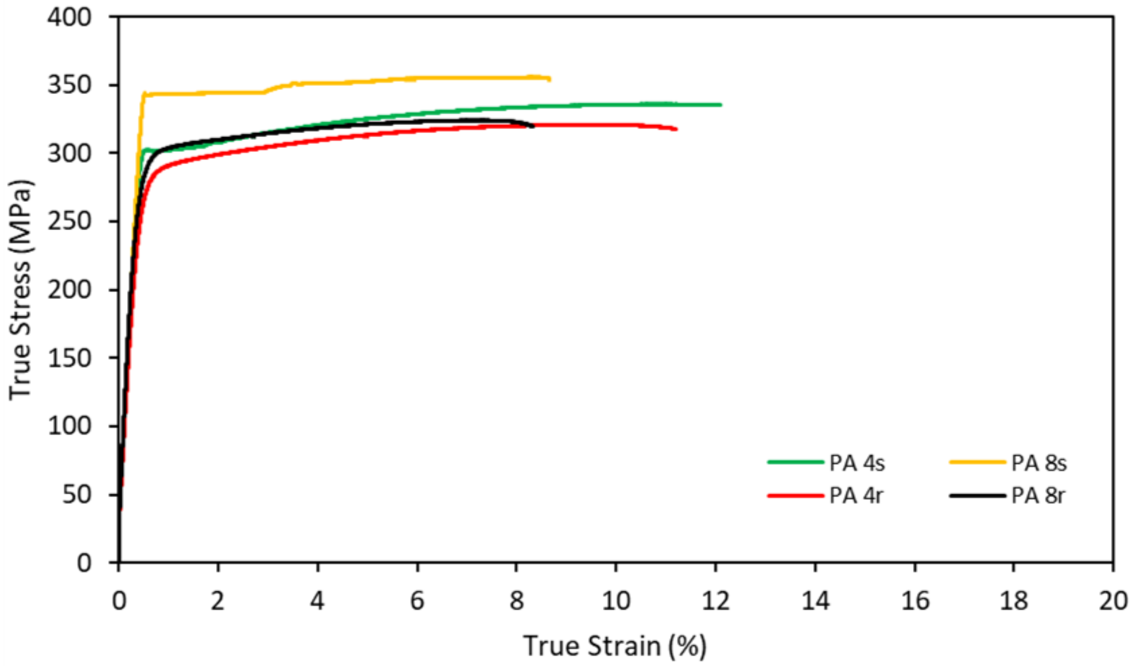

Figure 4.29. Tensile Flow curve depicting the tensile properties of the Aluminium alloy in the Preaged state, at 4% and 8% strains for stretch and roll deformation, respectively.

In the states where the material was preaged and then deformed, the general trends seen in the as-extruded hold true. Figure 4.29 shows the results for the material with the 170^o C/4h preaging condition. The higher strain levels yielded more strength and a lowered ductility. Stretch deformation also gave a greater effect in these mechanical properties as compared to roll deformation. There is a much larger effect in the stretch deformation samples than in the preaged condition that can be seen in the as-extruded condition. In the figure, the yield strength of 4% stretch is close in nominal value to that of 8% roll even though it has a 100% greater strain level than the stretched sample.

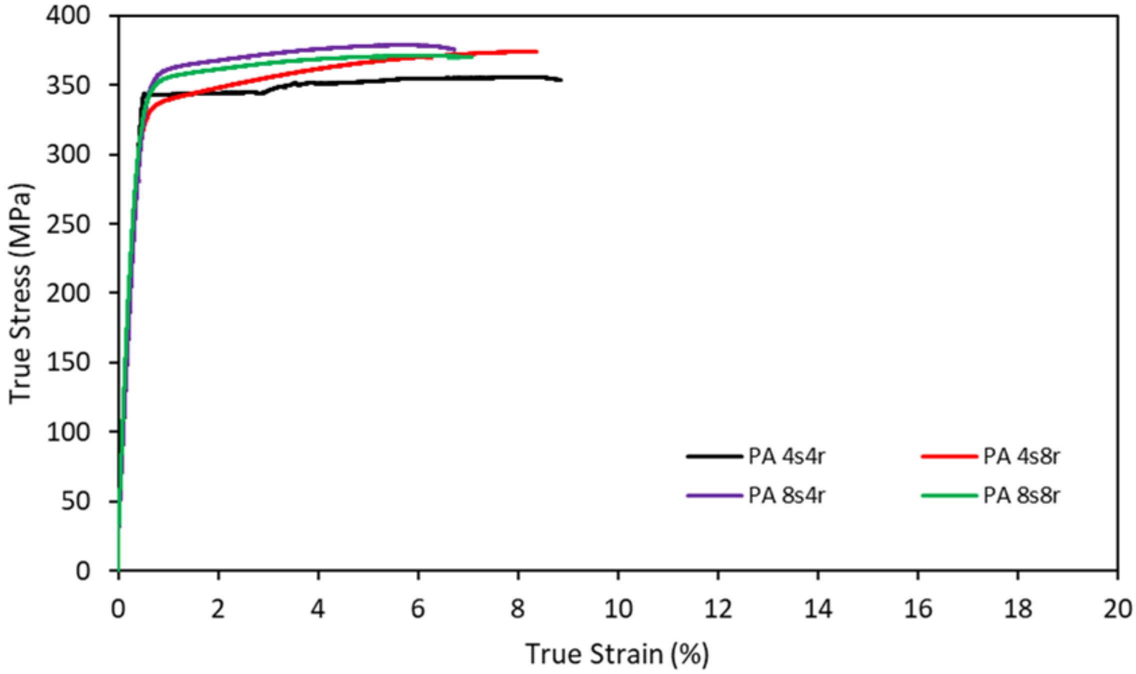

Figure 4.30. Tensile Flow curve depicting the tensile properties of the Aluminium alloy in the Preaged state, showing varying degrees of stretch and roll deformation strains.

The combined deformation results following preaging at 170^{o} C for 4 hours can be seen in Figure 4.30. Again, as the strain level is increased so are the strength parameters of the material and the ductility is also compromised similarly to as in the as-extruded state. However, in this condition, there is a slightly better mechanical performance in the 8% stretched + 4% rolled sample than the 8% stretched + 8% rolled.

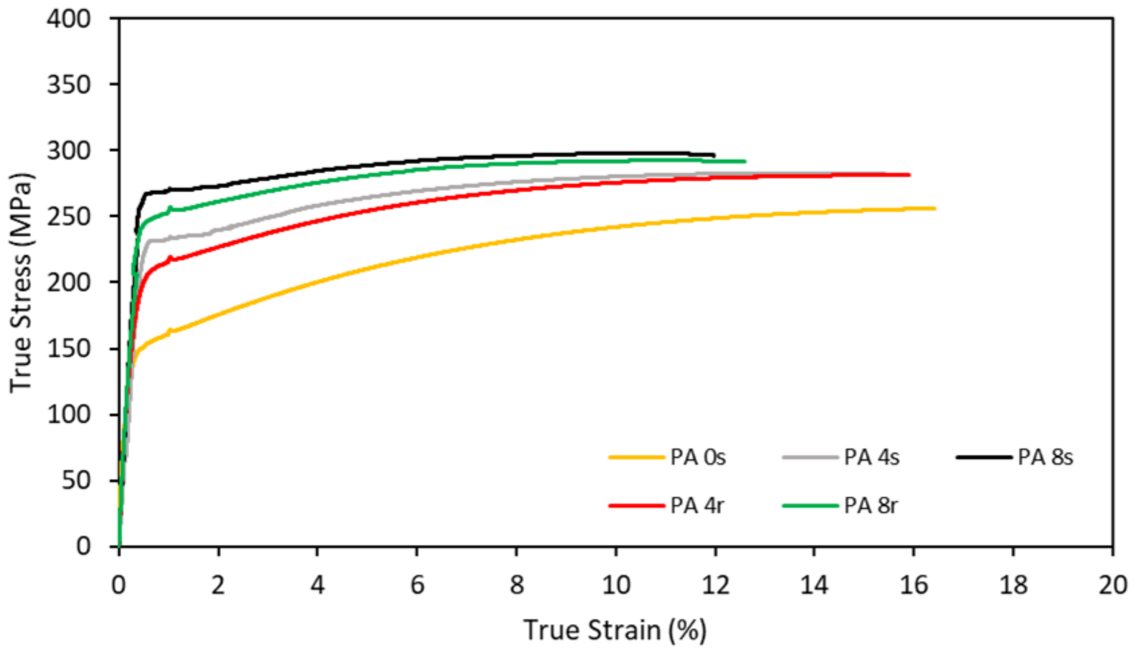

Figure 4.31. Tensile Flow curve depicting the tensile properties of the Aluminium alloy in the PreAged state, at 4% and 8% strains for stretch and roll deformation, respectively.

In the 150° C condition, displayed in Figure 4.31, the same trends seen in the 170° C/4h preage condition are upheld. The nominal values are lower however as the preaging does not develop more coarse precipitates. The material with the preaging + 8%stretch deformation displays the highest values for strength and the lowest ductility. As all the samples with the 150° C preaging are not as strong as the 170° C preaged samples, they also generally have a better ductility value.

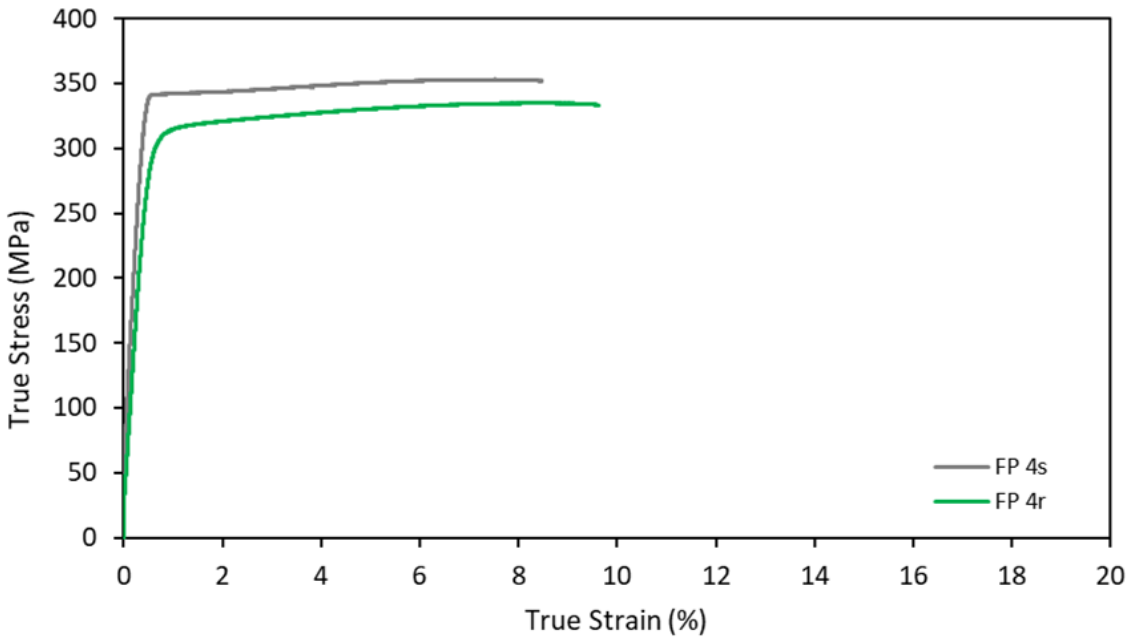

Figure 4.32. Tensile Flow curve depicting the tensile properties of the Aluminium alloy in the Fully Processed state, at 4% strains for stretch and roll deformation, respectively.

Tensile testing of the material was performed in the final stage of the thermomechanical process after following the 170^{o} C preaging and final ageing recipe. Figure 4.32 shows the flow curve of material with a 4% stretch and 4% roll deformation applied. As seen in all other previous states, the stretch deformation although at the same strain level shows a greater tensile property enhancement. The 4% stretch condition has a 34MPa greater yield strength than the 4% roll condition, this is a 11.2% better increase relative to the roll sample. The elongation of the stretch sample is less and thus a lesser ductility. (303.8,337.9)

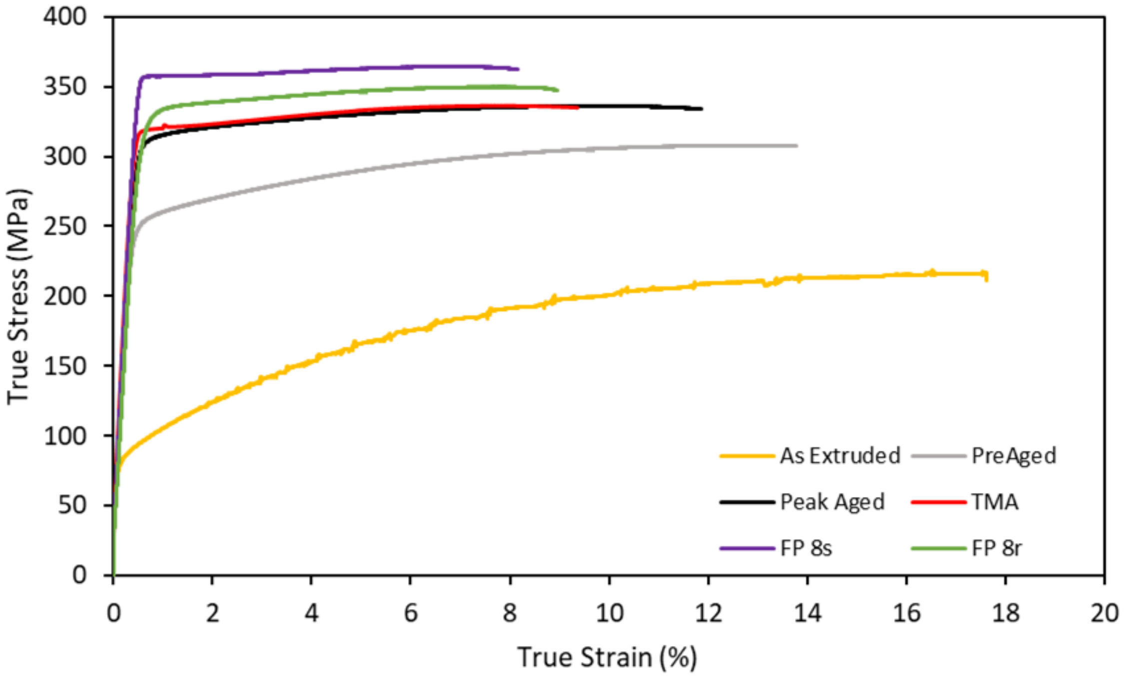

Figure 4.33 Tensile Flow curves showing the properties of an aluminium alloy in various steps of a thermomechanical process. As-extruded state, PreAged state (PA), Peak Aged state, fully processed with and 8% stretch strain state (FP 8s), Fully processed with and 8% roll strain state (FP 8r).

The chart in Figure 4.33 summarises and displays the critical investigated thermomechanical conditions from the study of the 170^{o} C recipe. The chart allows comparative analysis of the mechanical properties achieved in the various states. It is shown that the application of an 8% strain level via either stretch or roll deformation gave rise to an increase in strength compared to the peak aged state. These states even achieved better mechanical properties than the industry provided TMA condition with limited reduction in ductility at this increased strain level of 8%. The trend is supported where the stretched material reaps better results than the cold rolled material at the same strain level.

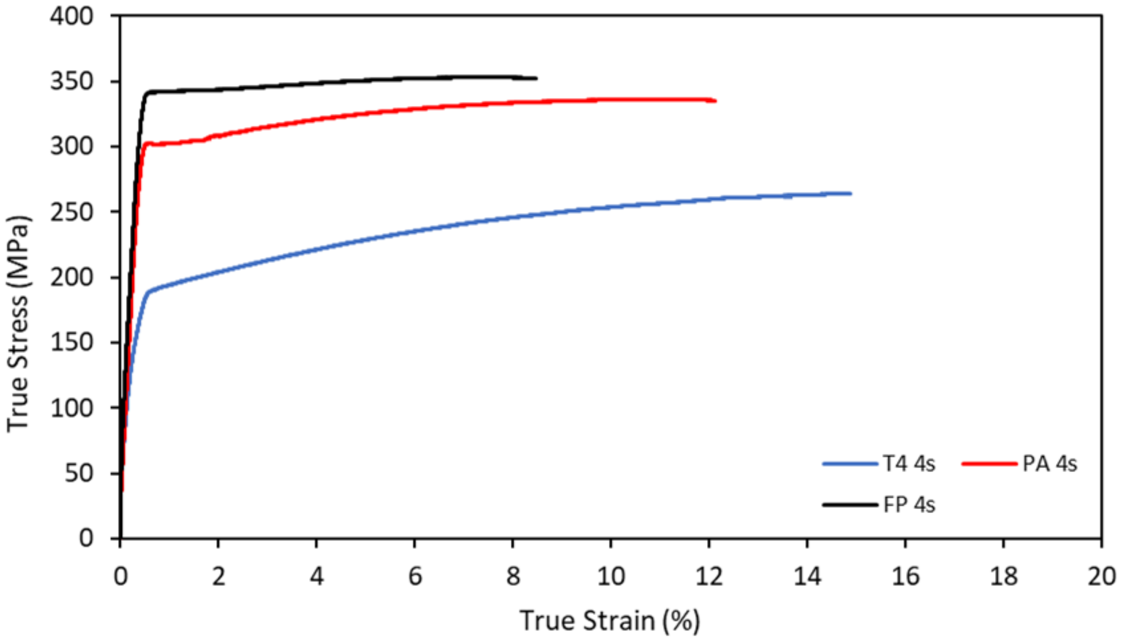

Figure 4.34. Tensile Flow curves comparing 4% stretch strain in varying stages of a thermomechanical process. T4, PreAged and Fully Processed.

Figure 4.34 shows the tensile flow curves for the material, maintaining the same strain level but at different stages of the thermomechanical process applying the 170º C recipe. As the sample becomes more developed, the strength is significantly increased, and the ductility of the material gradually reduces. The greatest increase in the material strength is when the preaging is introduced to the material as the presence of the precipitation is more critical than the rise in dislocation density attributed to cold working.

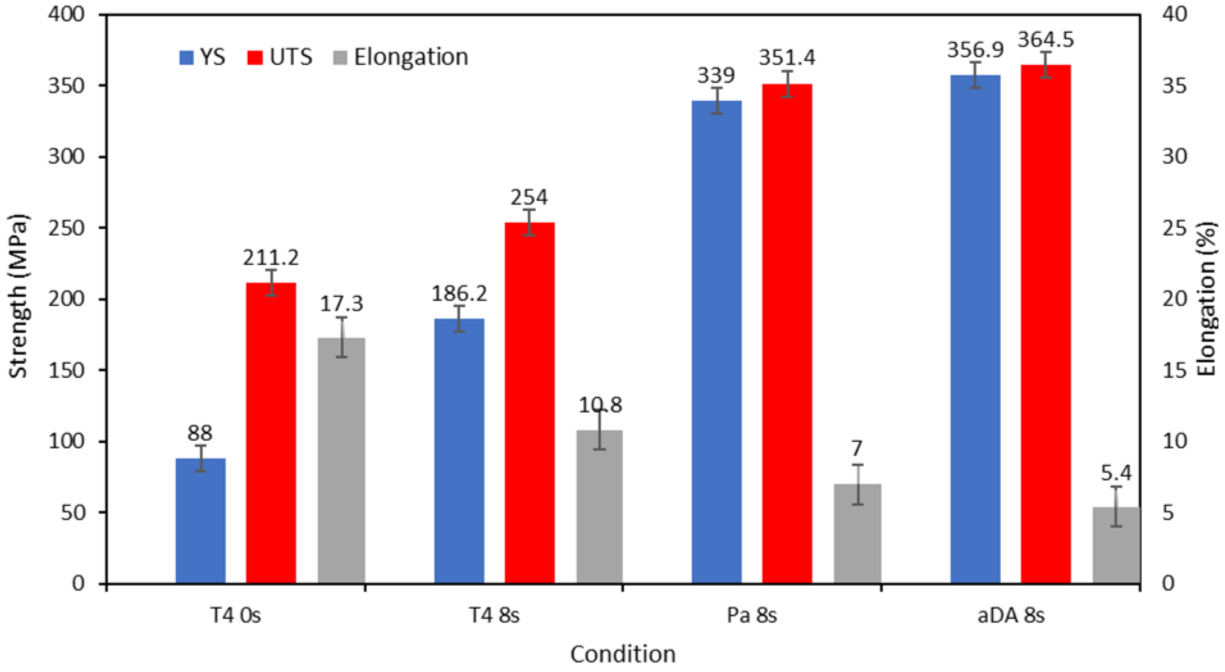

Figure 4.35. Charts displaying the trend seen in the tensile mechanical properties of the material deformed by an 8% stretch strain.

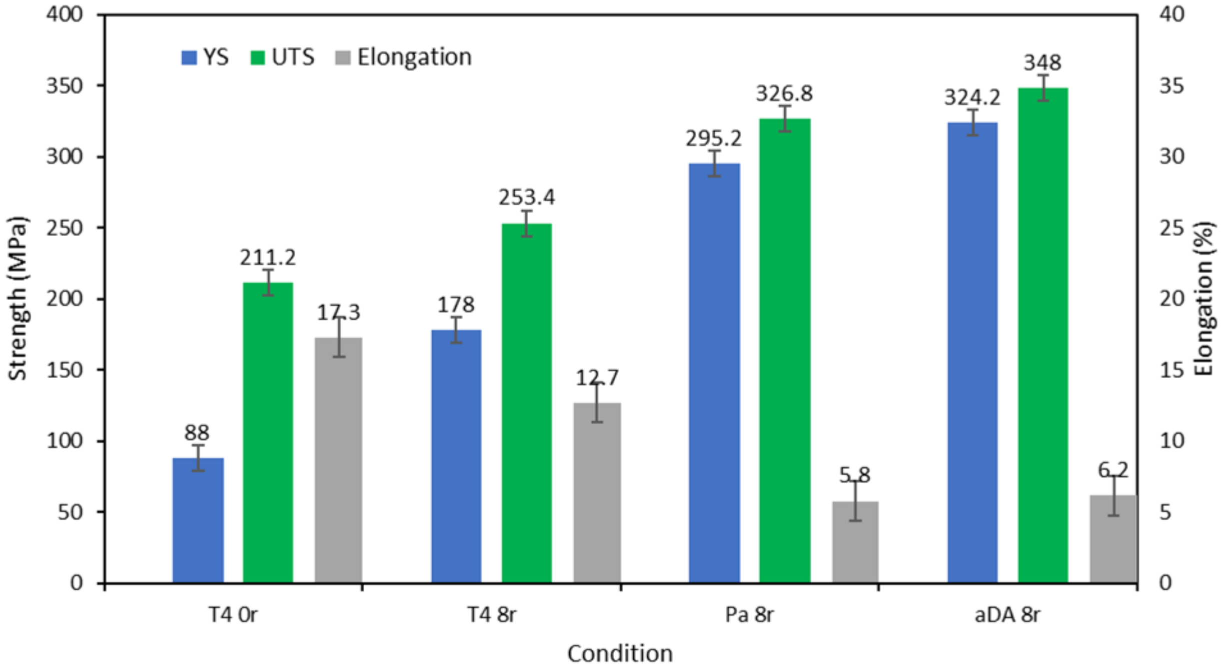

Figure 4.36. Charts displaying the trend seen in the tensile mechanical properties of the material deformed by an 8% roll strain.

The bar graphs in Figures 4.35 and 4.36 show the tensile results for the 8% strain level for stretch and roll deformation, respectively in the 170° C thermomechanical processing recipe. These two samples showed the greatest enhancement in mechanical properties in this recipe and are the critical samples to be investigated in microstructural analysis.

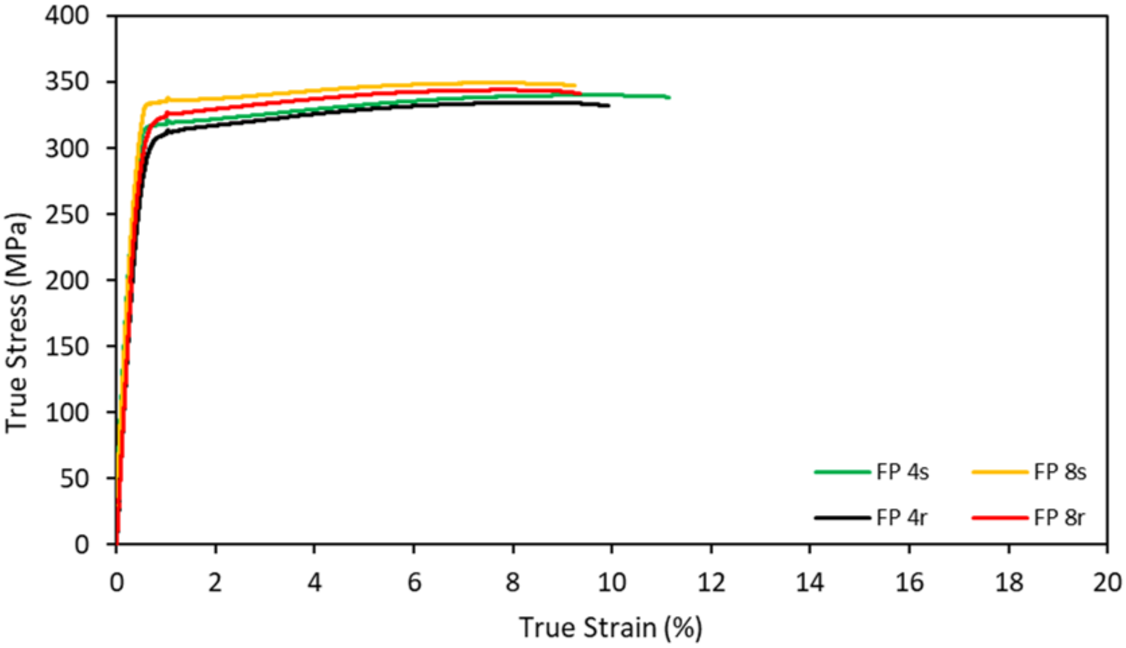

Figure 4.37. Tensile Flow curve depicting the tensile properties of the Aluminium alloy in the Fully Processed state, at 4% and 8% strains for stretch and roll deformation, respectively.

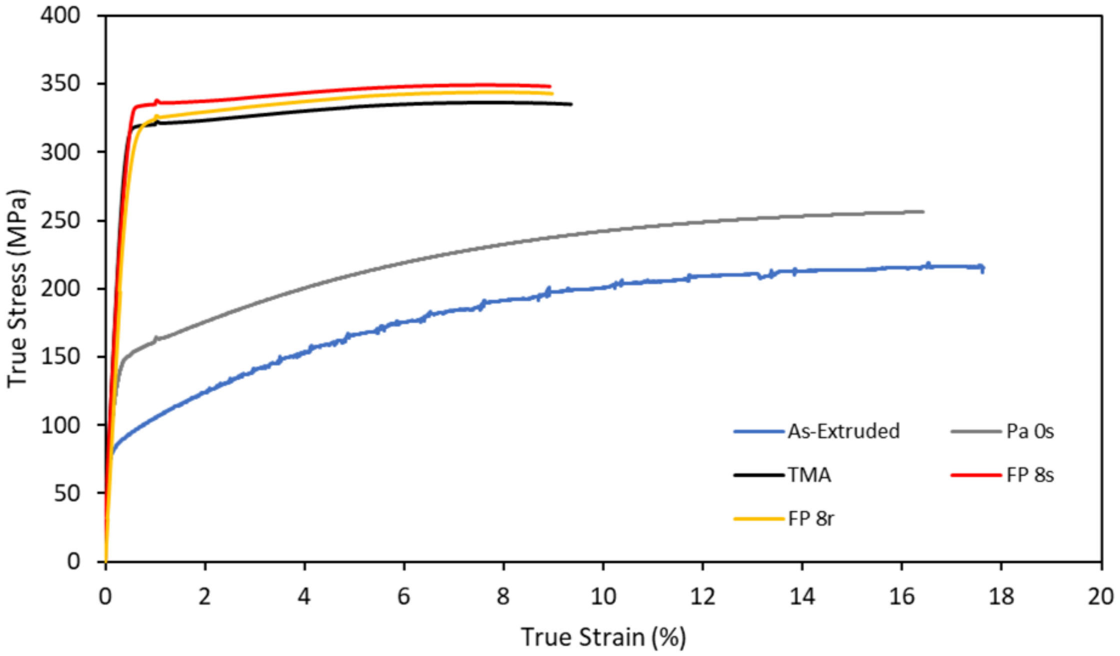

Figure 4.38. Tensile Flow curves showing the properties of an aluminium alloy in various steps of a thermomechanical process. As-extruded state, Preaged state (PA), Fully processed with and 8% stretch strain state (FP 8s), Fully processed with and 8% roll strain state (FP 8r).

For the recipe with the 150° C Preage + 190° C final age condition, there was the same trend seen in the 170° C Preage + 170° C final age condition. The application of the strain level of 8% by either the roll or stretch deformation mode achieved a greater strength when compared to the industry provided TMA condition. This increase in properties was far less than in the 170° C recipe, however. The 170° C recipe yields a far greater thermomechanical response than the 150° C recipe across the boards and thus it was selected for further investigation and characterisation. The reason for this lower final performance can be seen in Figure 4.38, the strengths achieved through preaging at this temperature are not much greater than the strengths measured in the sample in the T4. This does not promote the interactions that would be needed downstream in the full process to achieve greater tensile results.

Using the stress strain curves achieved through mechanical testing, the work hardening coefficients were calculated to understand the work hardenability of the material in various states of the thermomechanical process. This allowed information of the stress-strain relationships during plastic deformation to be extracted from the graphs. Understanding how the material hardens would aid in predicting behaviour through these deformation processes. The degree to which the hardening of the material is due to deformation and to what degree the precipitation hardening plays a role is also understood from this parameter. The calculation was based on the assumption that the stress-strain relationship follows a power-law relationship:

$$\sigma = K\varepsilon^n \qquad (4.1)$$

where σ is the flow stress, ε the strain, n the hardening coefficient, and K is a constant equal to the flow stress when $\varepsilon = 1$.

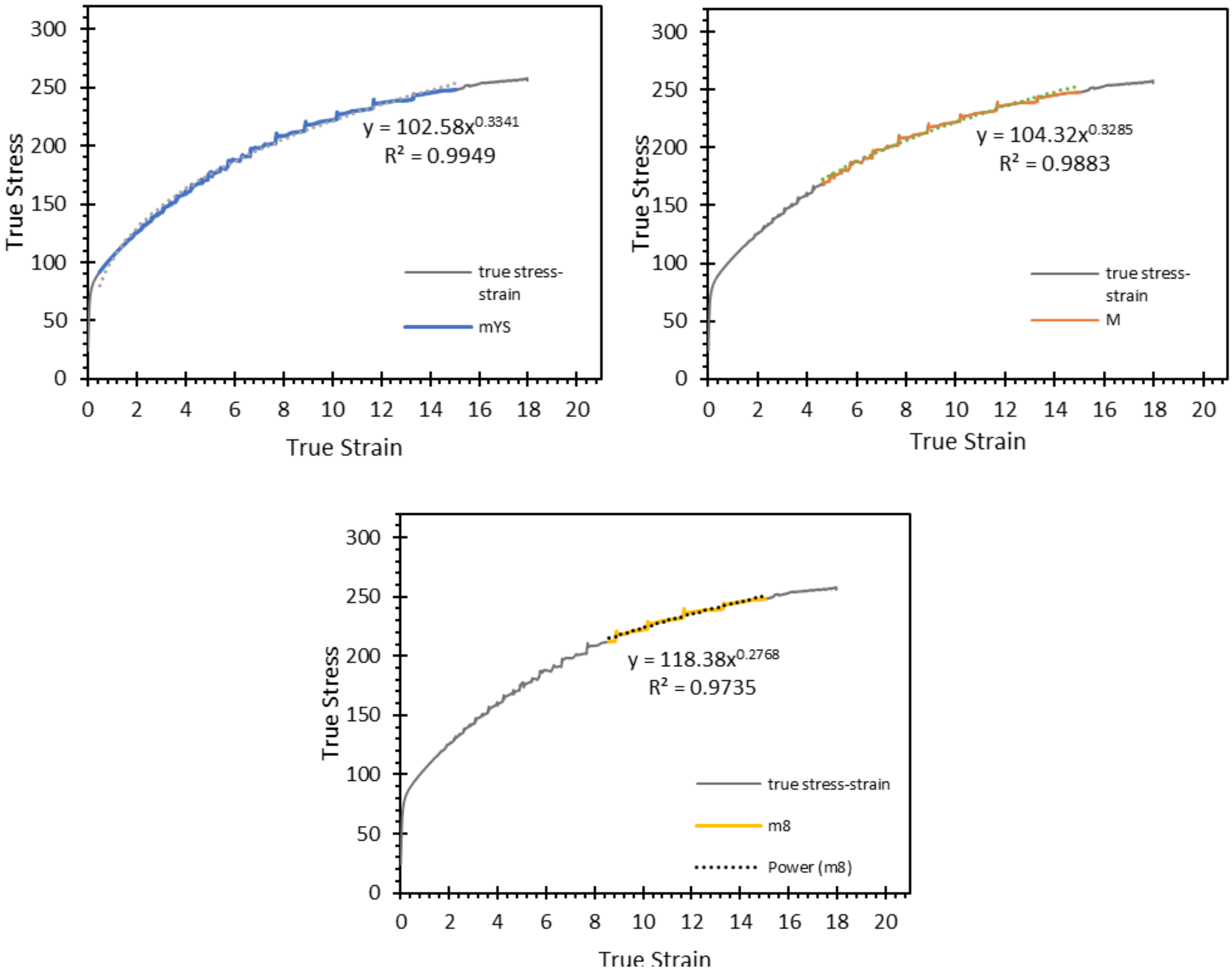

Figure 4.39. Tensile flow curve of the aluminium alloy in the as extruded condition. The power law used to calculate the work hardenability of the material at different stages of the curve. R^2 value shows the statistical reliability of the value.

Figure 4.39 shows 3 graphs of the T4 as-extruded state with the hardening coefficient measured at 3 different points of the flow curve. The hardening coefficient corresponding to the yielding point(mYS) gave a value of 0.3341 which is a medium-low work hardenability coefficient. This is the work hardenability of the starting, as-extruded material. The other two coefficients were taken relative to 4% strain level (m4) and 8% strain level (m8) and read as 0.3285 and 0.2768 respectively. These correspond to the strain rates that are applied to the material in the deformation step. This indicates that as the material is progressively strained, the work hardenability of the material decreases but not drastically. Meaning that the levels of strain applied to the material in the deformation step are relatively low, and the material has a great potential to harden following this step.

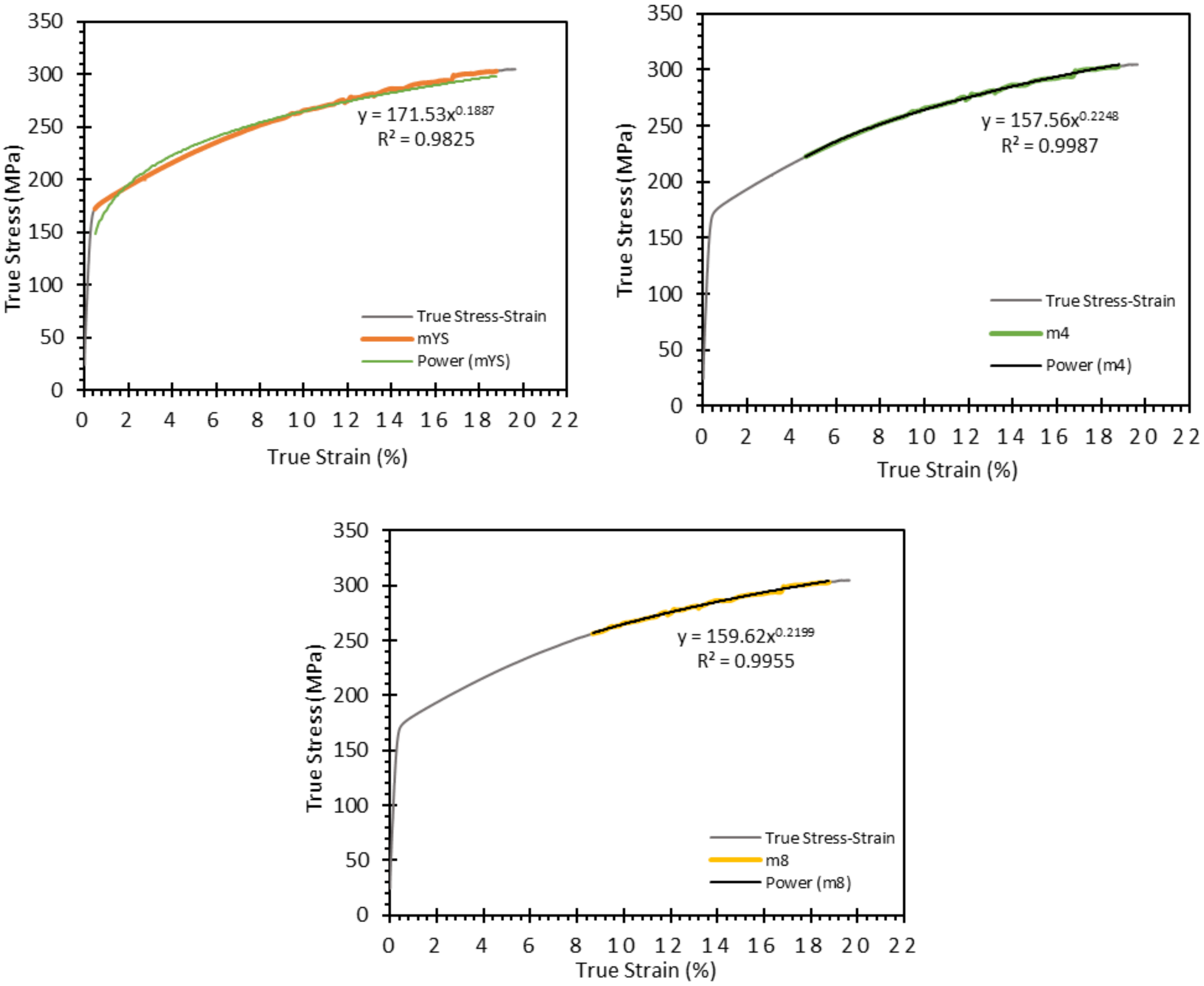

Figure 4.40. Tensile flow curve of the aluminium alloy in the as extruded condition with the addition of a 4% stretch strain. The power law used to calculate the work hardenability of the material at different stages of the curve. R^2 value shows the statistical reliability of the value.

The work hardening coefficient for the stretch deformed material was also analysed at the same 3 differing points of the flow curve. Figure 4.40 shows this for the 4% stretch strained material. As the yielding point on this curve would correspond approximately to the 4% strain level on the t4 as-extruded curve shown in Figure 4.39, changes in the work hardening coefficient would indicate that the material had hardened of softened in the period between the deformation being applied and the mechanical test being performed. The mYS for this curve was 0.1887. When compared to the m4 value of Figure 4.39 which was 0.3285 the value had significantly decreased, indicating the movement of dislocations, clusters/precipitate particles, or the interaction of both. This resulted in a material that had hardened and had a reduced capacity to further harden.

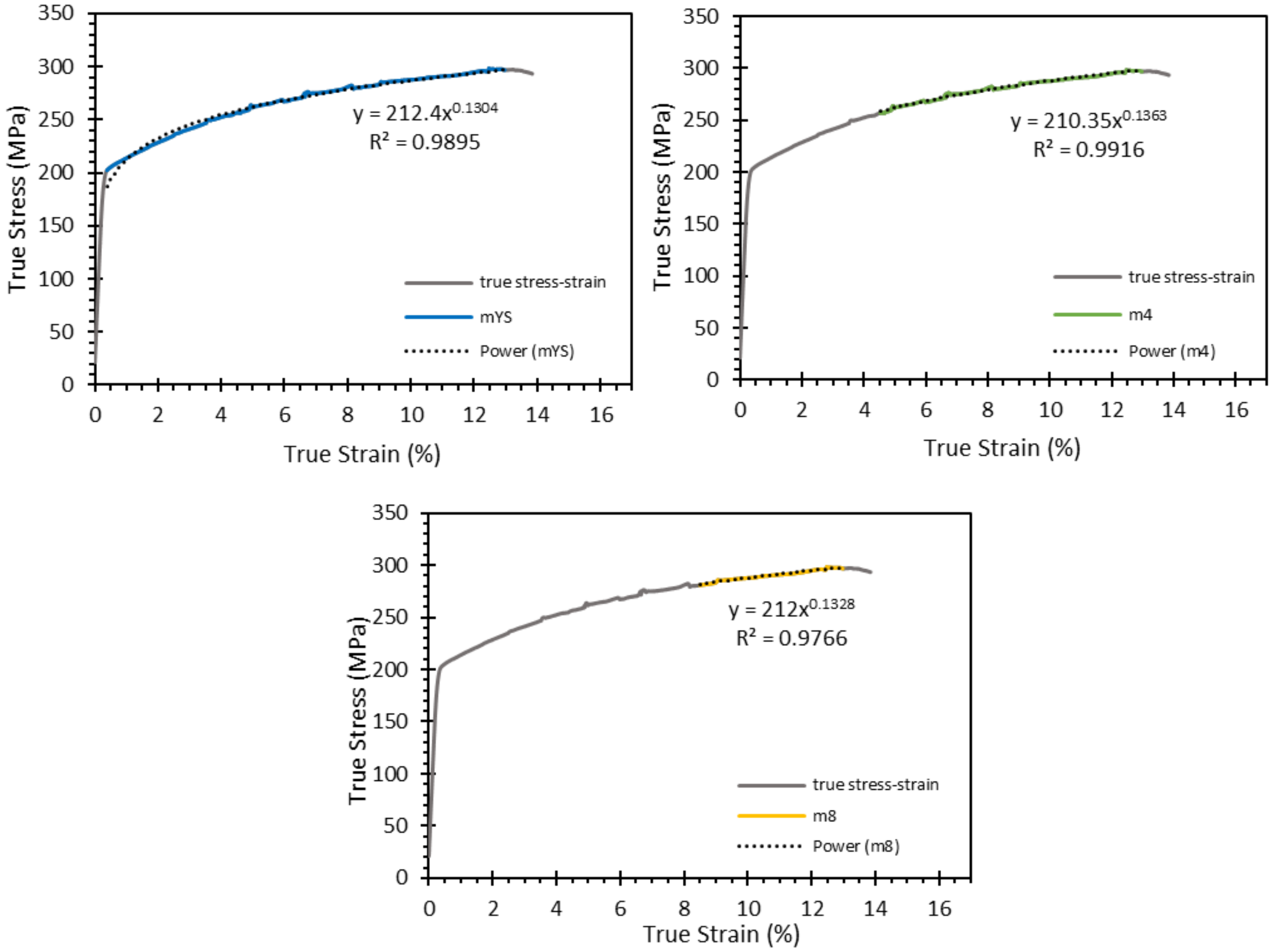

Figure 4.41. Tensile flow curve of the aluminium alloy in the as extruded condition with the addition of an 8% stretch strain. The power law used to calculate the work hardenability of the material at different stages of the curve. R^2 value shows the statistical reliability of the value.

In an 8% stretch deformed sample, the mYS value of the flow chart compares to the 8% strain level on the t4 as-extruded curve in Figure 4.39. As in the 4% stretched material, the work hardening coefficient reduced from 0.2768 to 0.1304. The value of the coefficient was more than halved meaning that the effect at this elevated strain level was even more pronounced than that seen in the 4% stretched material. There is hardening occurring in the material during the period between when the strain is applied and when the material is tensile tested. As the dislocation density in the more strained material is greater, there would be fair greater motion of solutes into the dislocation structures.

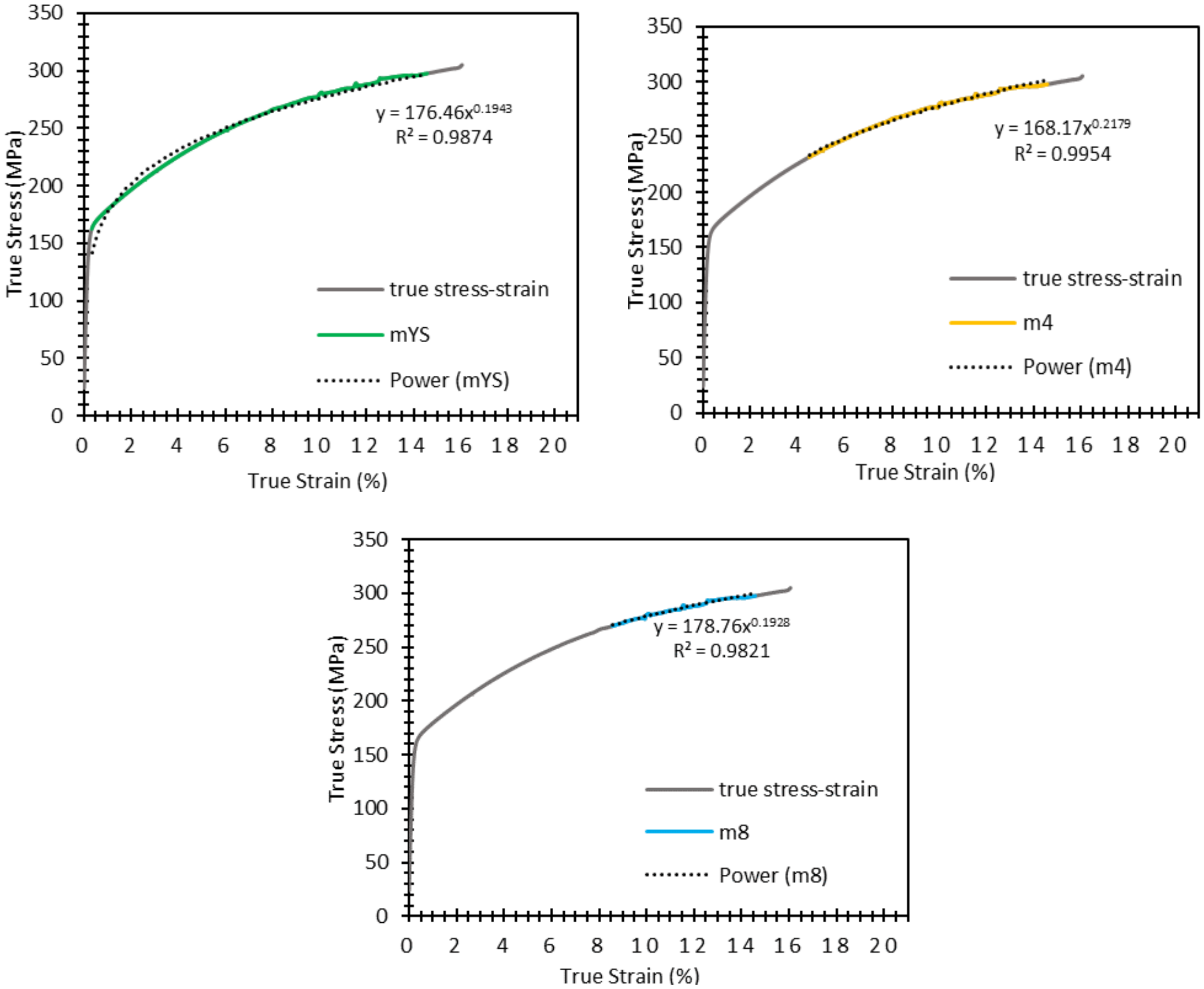

Figure 4.42. Tensile flow curve of the aluminium alloy in the as extruded condition with the addition of a 4% roll strain. The power law used to calculate the work hardenability of the material at different stages of the curve. R^2 value shows the statistical reliability of the value.

The working hardening coefficient was compared in the roll deformed samples also. From Figure 4.42, the measured mYS value of the 4% roll deformed material was 0.1943. comparing this to the m4 value of Figure 4.39 which was 0.3285 it is clear that similar to the stretch deformed material of the same strain level, the work hardenability of the material decreases, suggesting interactions between the structures in the material matrix. Comparing the work hardening coefficients relative to the yielding point of both the 4% stretched and the 4% rolled samples, the 4% stretched sample had a lower value of 0.1887 meaning that the material was slightly more hardened than the rolled samples. This correlates with the raw tensile strength data for the yield strength and ultimate tensile strength as the 4% stretch deformed sample has greater enhanced mechanical properties.

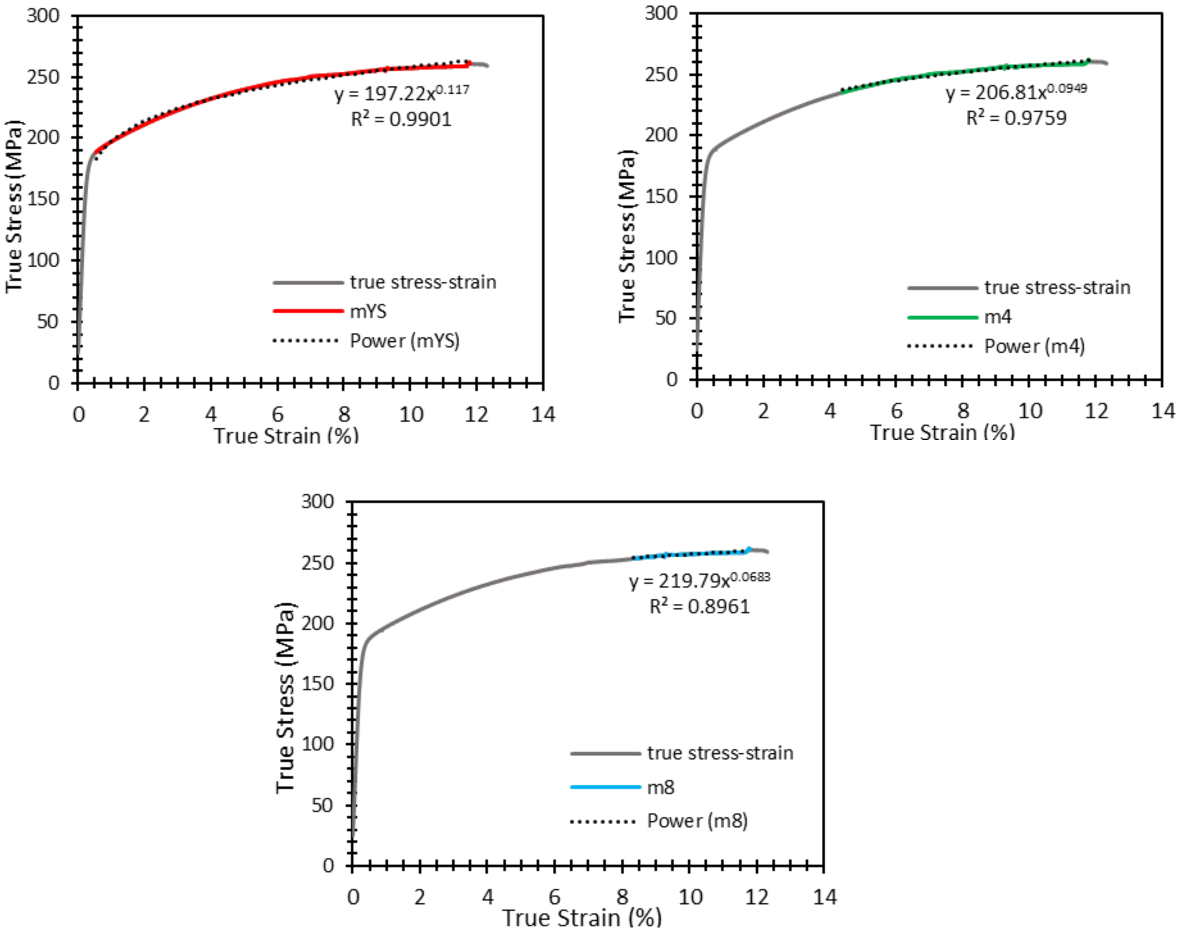

Figure 4.43. Tensile flow curve of the aluminium alloy in the as extruded condition with the addition of an 8% roll strain. The power law used to calculate the work hardenability of the material at different stages of the curve. R^2 value shows the statistical reliability of the value.

Figure 4.43 shows the relevant flow charts and calculated work hardening coefficients for the 8% roll deformed tensile samples. The work hardening coefficient is decreased to 0.117 from 0.2768, this is slightly over a 50% decrease. Comparing to the 8% stretch deformed sample, the trend is maintained where the hardening in the rolled samples are not as great as that in the stretched samples.

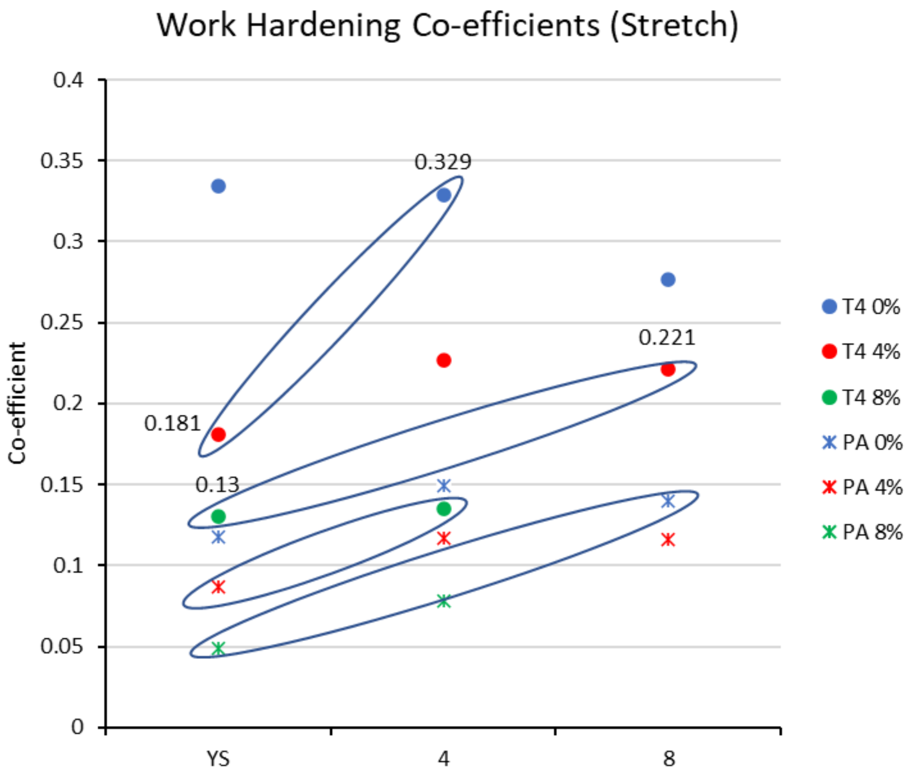

Figure 4.44. A chart displaying and comparing the work hardenability of an aluminium alloy in various conditions including a pre-ageing at 170C and a stretch strain of 4% and 8%.

Figure 4.44 compares the various work hardening coefficients of the stretch deformed samples at the various states of the thermomechanical process. The dot "•" points correlate to the materials deformed in the T4 as-extruded state, whilst the cross "×" points are representing the samples stretch deformed after a short preaging step. The vertical axis shows the calculated work hardening coefficient whilst the horizontal axis shows from which point the coefficient was measured relative to i.e. mYS, m4, m8. The rings show the comparable coefficients and more clearly shows the trend of the decrease in work hardenability as compared to the expected values from tensile testing.

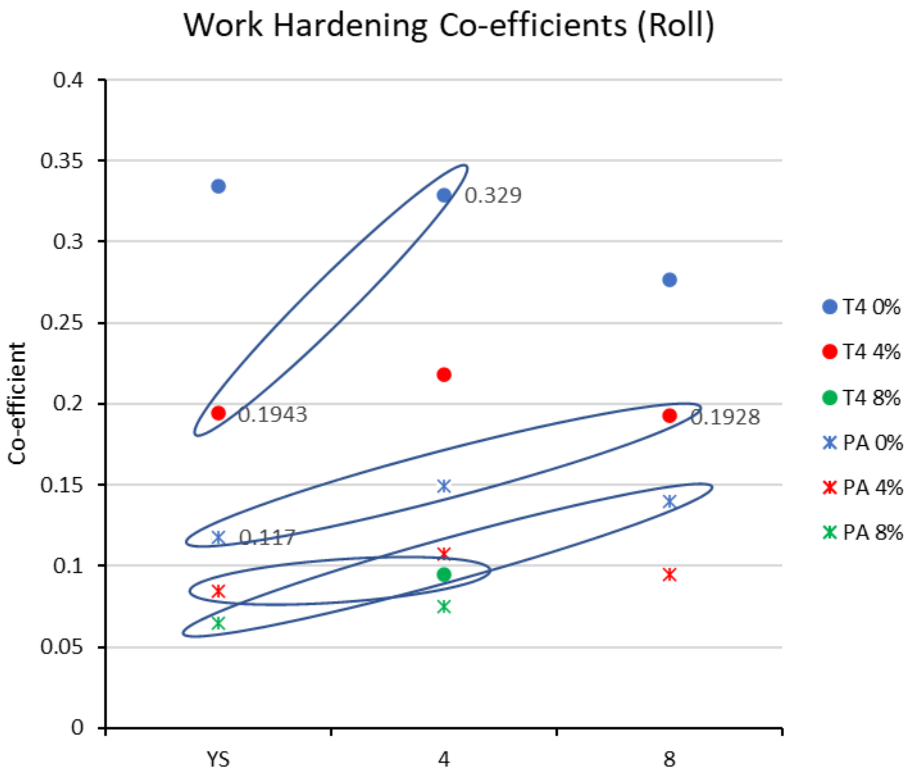

Figure 4.45. A chart displaying and comparing the work hardenability of an aluminium alloy in various conditions including a pre-ageing at 170C and a roll strain of 4% and 8%.

Figure 4.45 focuses on the rolled samples. The trend seen in the stretch samples is also shown in the rolled samples and can be seen clearly in the graph when comparing points. The relative comparable coefficients are illustrated by the rings in the chart.

4.5 Microstructural Characterisation

The great divergence in the hardness and tensile properties as a result of the material processing alludes to variance in effects caused by the different steps and stages of the thermomechanical process. Notably stretch strain invokes a different mechanical behaviour in the material to that of roll strain even for an equivalent strain applied to the material. The temperature used in the process of strengthening the material also has an observable effect on the final properties achieved.

Assumptions made from these trends can be reasoned and explained through microstructural analysis. EBSD as a technique was used to gain an in-depth analysis of these material alterations. IPF, KAM, GND as well as texture Pole Figures and ODF maps were used to reveal these changes. This would allow a link to be drawn between enhanced mechanical properties and examined changes in microstructural features.

4.5.1 Electron Backscatter Diffraction

Figure 4.44 displays the sample in the undeformed state. Using the same sample in the EBSD IPF map of Figure 4.3, the equiaxed grains can be seen to have limited levels of dislocations inside of the grains. Using the KAM map in Figure 4.44, the local misorientation that are present inside of the grains can be calculated. The KAM map can effectively show local plastic deformation quantitatively. The key on the right-hand side displays the misorientation degree as well as the volume fraction of the measured kernels that are measured to be in each range of misorientations. Red being higher degrees of misorientation and blue being lesser orders of misorientation. The misorientations in the material can be attributed to the presence of defects in the crystal matrix.

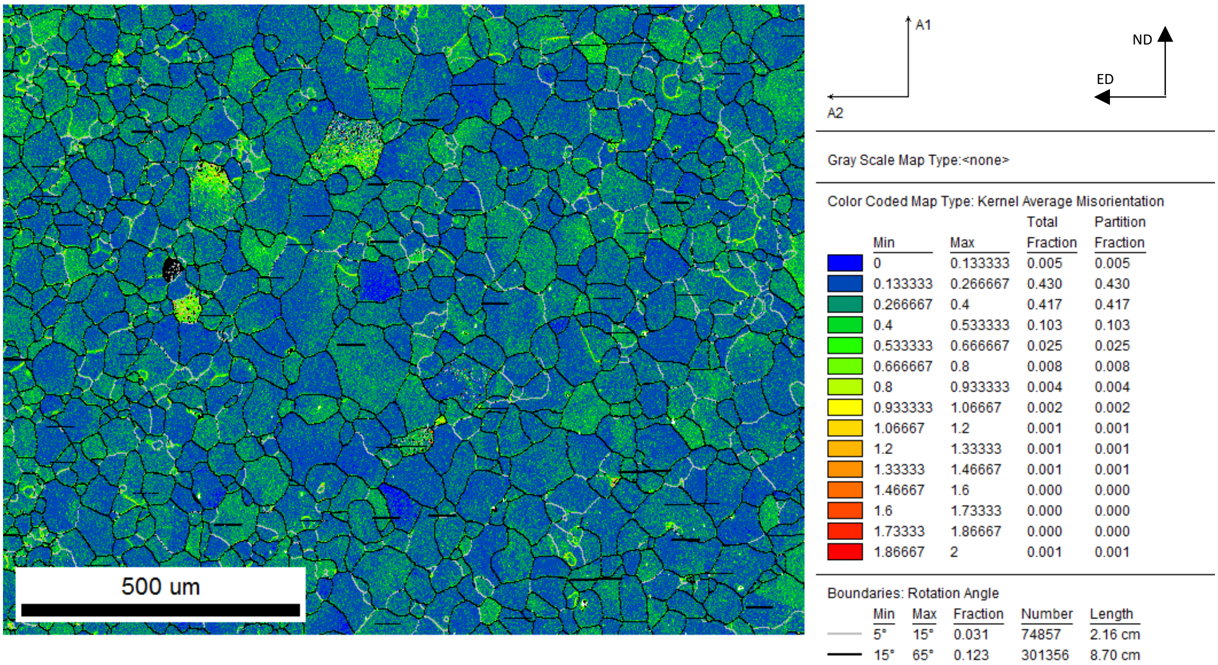

Gray Scale Map Type:<none>

Color Coded Map Type: Kernel Average Misorientation

	Min	Max	Total Fraction	Partition Fraction
🟦	0	0.133333	0.005	0.005
🟦	0.133333	0.266667	0.430	0.430
🟩	0.266667	0.4	0.417	0.417
🟩	0.4	0.533333	0.103	0.103
🟩	0.533333	0.666667	0.025	0.025
🟩	0.666667	0.8	0.008	0.008
🟩	0.8	0.933333	0.004	0.004
🟨	0.933333	1.06667	0.002	0.002
🟨	1.06667	1.2	0.001	0.001
🟧	1.2	1.33333	0.001	0.001
🟧	1.33333	1.46667	0.001	0.001
🟧	1.46667	1.6	0.000	0.000
🟥	1.6	1.73333	0.000	0.000
🟥	1.73333	1.86667	0.000	0.000
🟥	1.86667	2	0.001	0.001

Boundaries: Rotation Angle

	Min	Max	Fraction	Number	Length
—	5°	15°	0.031	74857	2.16 cm
—	15°	65°	0.123	301356	8.70 cm

Figure 4.46. EBSD Kernel Average Misorientation Map of an AA6xxx series alloy in the as-extruded state. 75x magnification, 0.5-micron step size.

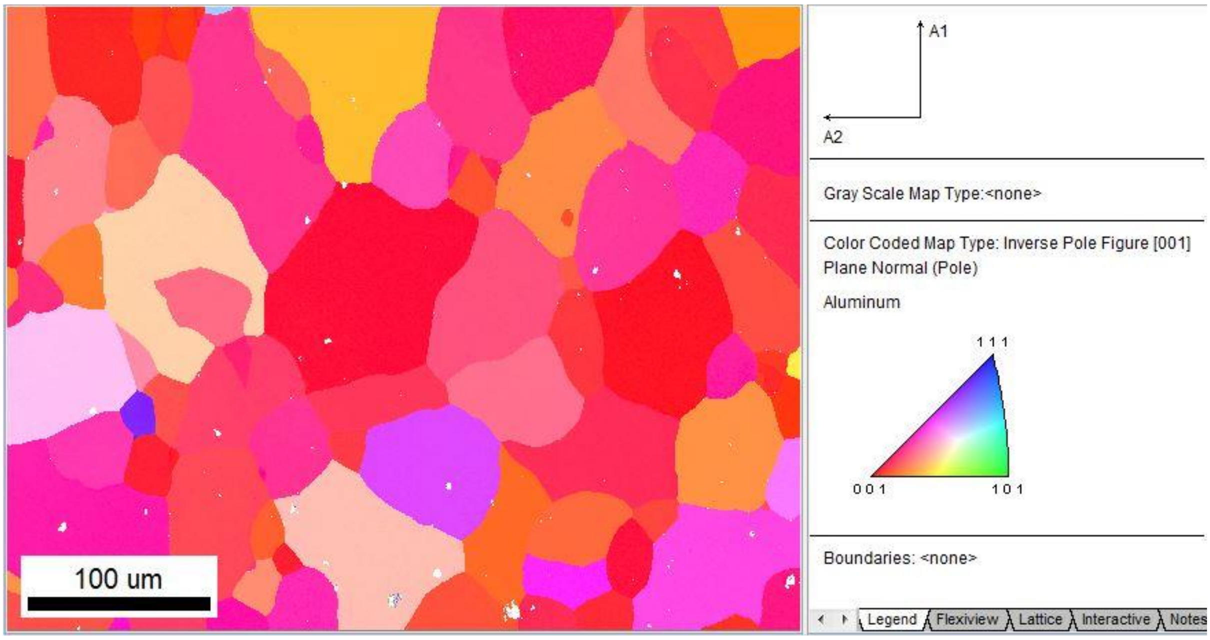

Gray Scale Map Type:<none>

Color Coded Map Type: Inverse Pole Figure [001]
Plane Normal (Pole)

Aluminum

Boundaries: <none>

Figure 4.47. EBSD Inverse Pole Figure Map of an AA6xxx series alloy in the as-extruded state. 250x magnification, 0.13-micron step size.

Figure 4.47 shows the IPF map of a smaller representative region of the sample bulk in the T4 as-extruded state at a smaller measurement step size, to obtain a greater resolution for dislocation density characterisation. This is the starting material state. The graph displays numerous equiaxed grains of varying orientations in the crystal. The grain boundaries are highlighted using a black line highlight and these grain boundaries are defined as points reading a misorientation in the range of 15-62.7994 degrees. LAGBs are displayed with a grey highlight and are described in the map as misorientation readings falling in the range of 5-15 degrees.

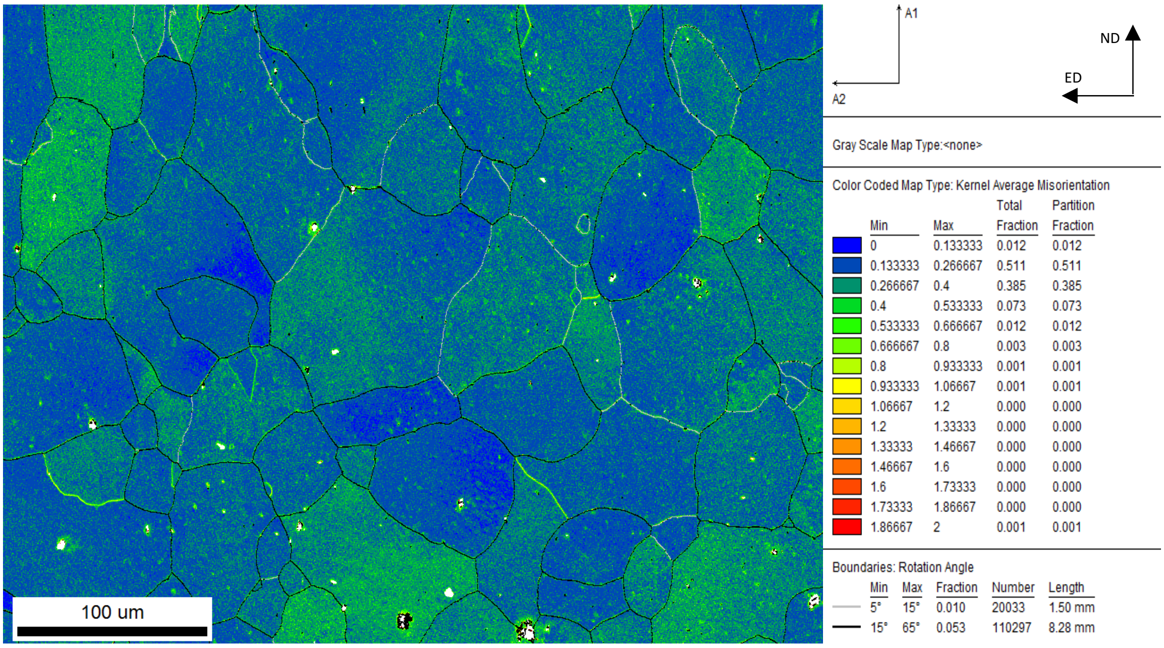

	Min	Max	Total Fraction	Partition Fraction
🟦	0	0.133333	0.012	0.012
🟦	0.133333	0.266667	0.511	0.511
🟩	0.266667	0.4	0.385	0.385
🟩	0.4	0.533333	0.073	0.073
🟩	0.533333	0.666667	0.012	0.012
🟩	0.666667	0.8	0.003	0.003
🟩	0.8	0.933333	0.001	0.001
🟨	0.933333	1.06667	0.001	0.001
🟨	1.06667	1.2	0.000	0.000
🟧	1.2	1.33333	0.000	0.000
🟧	1.33333	1.46667	0.000	0.000
🟧	1.46667	1.6	0.000	0.000
🟥	1.6	1.73333	0.000	0.000
🟥	1.73333	1.86667	0.000	0.000
🟥	1.86667	2	0.001	0.001

	Min	Max	Fraction	Number	Length
—	5°	15°	0.010	20033	1.50 mm
—	15°	65°	0.053	110297	8.28 mm

Figure 4.48. EBSD Kernel Average Misorientation Map of an AA6xxx series alloy in the as-extruded state. 250x magnification, 0.13-micron step size.

Figure 4.48 shows the material in the as extruded state again but at this higher magnification and greater resolution to attain more information on the dislocations present in this area. All following specimens are measured using to same parameters to allow effective comparison. The sample in the undeformed state has a relatively low level of misorientations, similar to Figure 4.46. There are no visible dislocation bands present inside the grains. from the key it can be seen that the majority, 0.523 by vol fraction, of the indexed points have a misorientation in the blue range, which is the crystal matrix without dislocations present. There is a level of misorientation in the material and these can be attributed to the random presence of dislocations that can be found in any crystal matrix. There are also some dislocations introduced into the material during the extrusion processing. Finally, a level of the misorientations in the grains can just be due to low level noise generated from the indexing process.

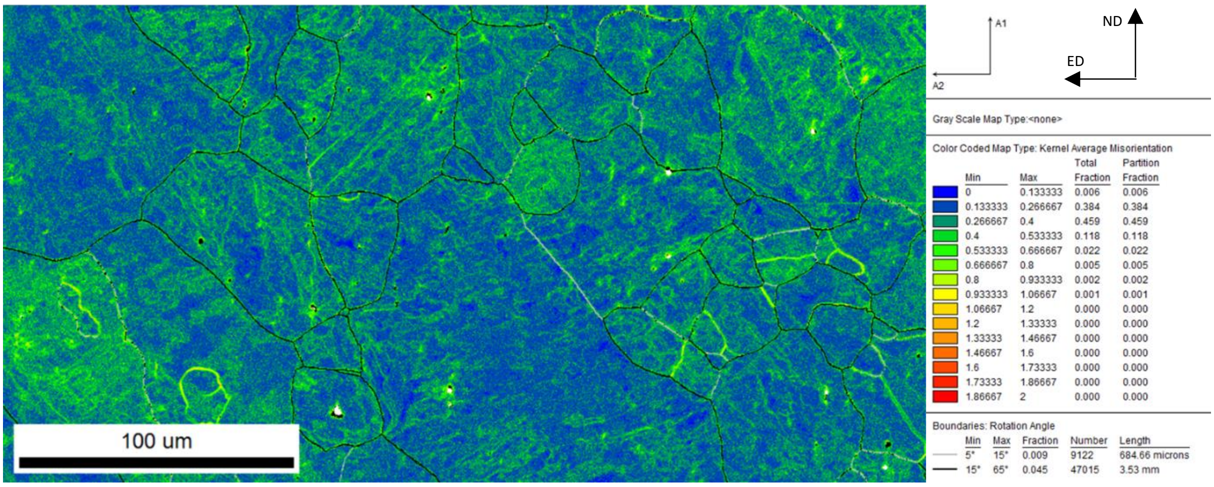

Gray Scale Map Type:<none>

Color Coded Map Type: Kernel Average Misorientation

	Min	Max	Total Fraction	Partition Fraction
🟦	0	0.133333	0.006	0.006
🟦	0.133333	0.266667	0.384	0.384
🟩	0.266667	0.4	0.459	0.459
🟩	0.4	0.533333	0.118	0.118
🟩	0.533333	0.666667	0.022	0.022
🟩	0.666667	0.8	0.005	0.005
🟨	0.8	0.933333	0.002	0.002
🟨	0.933333	1.06667	0.001	0.001
🟨	1.06667	1.2	0.000	0.000
🟧	1.2	1.33333	0.000	0.000
🟧	1.33333	1.46667	0.000	0.000
🟧	1.46667	1.6	0.000	0.000
🟥	1.6	1.73333	0.000	0.000
🟥	1.73333	1.86667	0.000	0.000
🟥	1.86667	2	0.000	0.000

Boundaries: Rotation Angle

	Min	Max	Fraction	Number	Length
—	5°	15°	0.009	9122	684.66 microns
—	15°	65°	0.045	47015	3.53 mm

Figure 4.49. EBSD Kernel Average Misorientation Map of an AA6xxx series alloy deformed under tension to a strain level of 4%. 250x magnification, 0.13-micron step size.

Figures 4.49 and 4.50 display the KAM maps of the samples after the application of strain with 4 and 8% strain levels, respectively. It can be seen that there is an evolution of the dislocations in the material. The levels of misorientation in both conditions are much higher than those measured in the starting material.

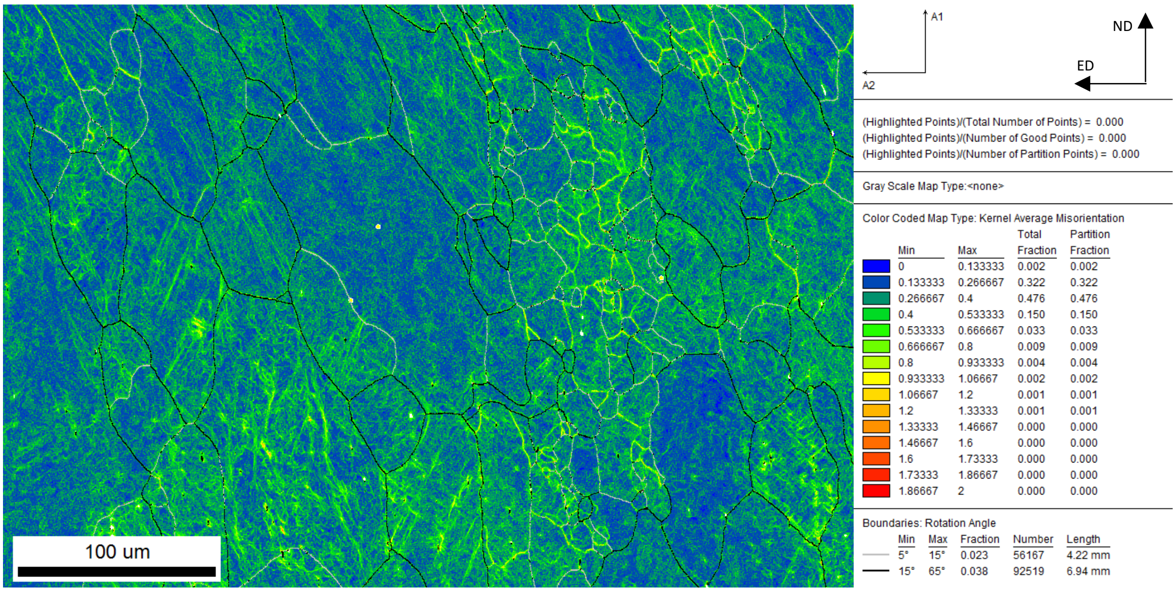

(Highlighted Points)/(Total Number of Points) = 0.000
(Highlighted Points)/(Number of Good Points) = 0.000
(Highlighted Points)/(Number of Partition Points) = 0.000

Gray Scale Map Type:<none>

Color Coded Map Type: Kernel Average Misorientation

	Min	Max	Total Fraction	Partition Fraction
🟦	0	0.133333	0.002	0.002
🟦	0.133333	0.266667	0.322	0.322
🟩	0.266667	0.4	0.476	0.476
🟩	0.4	0.533333	0.150	0.150
🟩	0.533333	0.666667	0.033	0.033
🟩	0.666667	0.8	0.009	0.009
🟨	0.8	0.933333	0.004	0.004
🟨	0.933333	1.06667	0.002	0.002
🟨	1.06667	1.2	0.001	0.001
🟧	1.2	1.33333	0.001	0.001
🟧	1.33333	1.46667	0.000	0.000
🟧	1.46667	1.6	0.000	0.000
🟥	1.6	1.73333	0.000	0.000
🟥	1.73333	1.86667	0.000	0.000
🟥	1.86667	2	0.000	0.000

Boundaries: Rotation Angle

	Min	Max	Fraction	Number	Length
—	5°	15°	0.023	56167	4.22 mm
—	15°	65°	0.038	92519	6.94 mm

Figure 4.50. EBSD Kernel Average Misorientation Map of an AA6xxx series alloy deformed under tension to a strain level of 8%. 250x magnification, 0.13-micron step size.

There are dislocation bands and structures present in the matrix. In the more heavily strained sample at 8% stretch, the level of misorientation is even greater, indicating the presence of even more dislocations in the microstructure. The volume fraction information shows that the crystal matrix that without misorientation is 0.390 and 0.324 in the 4% and 8% stretch strained materials, respectively. These volume fractions are far lower than those seen in the undeformed specimen.

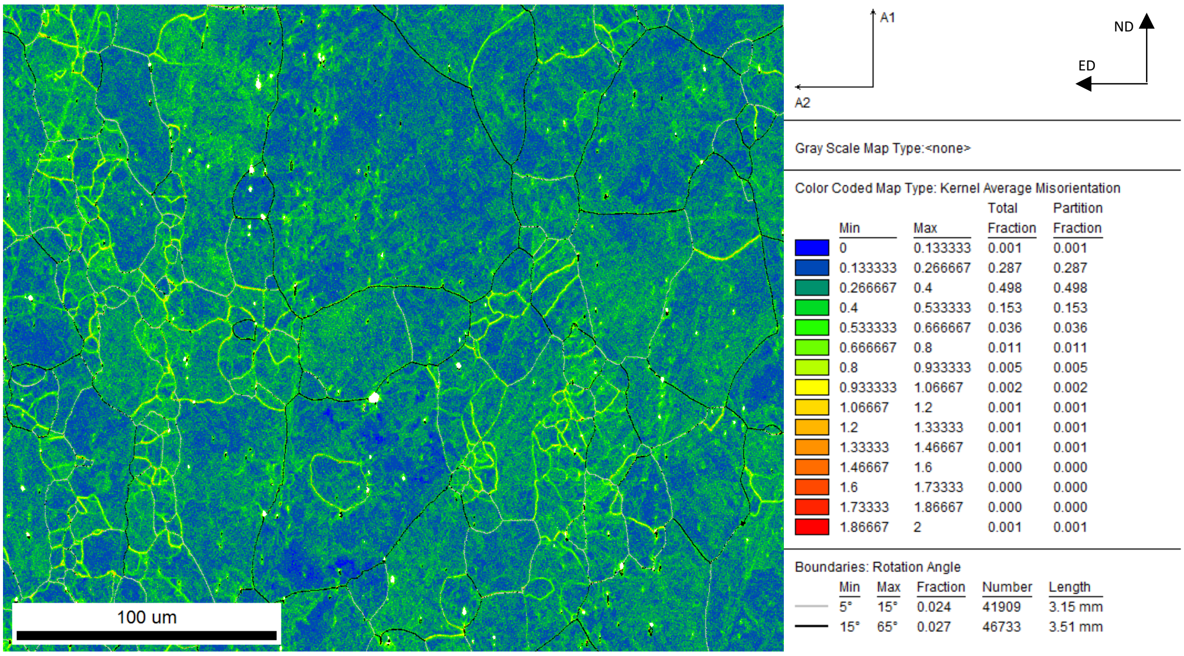

Gray Scale Map Type:<none>

Color Coded Map Type: Kernel Average Misorientation

	Min	Max	Total Fraction	Partition Fraction
🟦	0	0.133333	0.001	0.001
🟦	0.133333	0.266667	0.287	0.287
🟩	0.266667	0.4	0.498	0.498
🟩	0.4	0.533333	0.153	0.153
🟩	0.533333	0.666667	0.036	0.036
🟩	0.666667	0.8	0.011	0.011
🟨	0.8	0.933333	0.005	0.005
🟨	0.933333	1.06667	0.002	0.002
🟧	1.06667	1.2	0.001	0.001
🟧	1.2	1.33333	0.001	0.001
🟧	1.33333	1.46667	0.001	0.001
🟧	1.46667	1.6	0.000	0.000
🟥	1.6	1.73333	0.000	0.000
🟥	1.73333	1.86667	0.000	0.000
🟥	1.86667	2	0.001	0.001

Boundaries: Rotation Angle

	Min	Max	Fraction	Number	Length
—	5°	15°	0.024	41909	3.15 mm
—	15°	65°	0.027	46733	3.51 mm

Figure 4.51. EBSD Kernel Average Misorientation Map of an AA6xxx series alloy deformed through rolling to a strain level of 8%. 250x magnification, 0.13-micron step size.

The map in Figure 4.51 shows the material in the 8% roll deformed state. Just as in the two maps of the stretch deformation, the misorientation levels are far greater than that seen in the undeformed sample. Comparing the 8% stretched sample to the 8% rolled sample, the volume fractions are fairly similar, this is depicted in the graph below, comparing the two volume fractions. There is a slightly greater amount of misorientation in the roll sample, but this is not significant.

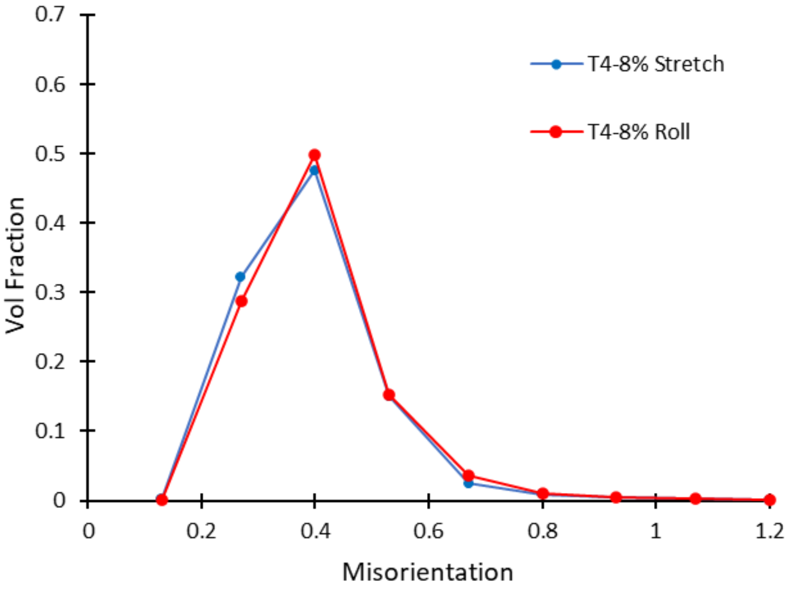

Figure 4.52. Graph showing the spread of misorientation from an EBSD KAM map of samples deformed to an 8% strain level through roll and stretch deformation.

The chart in Figure 4.52 shows the volume fractions of each range of misorientation ranges seen on the right-hand side of the KAM maps. The misorientation volume fraction spread in both the 8% stretch and 8% roll samples as calculated from their respective KAM maps. The two conditions display a very similar spread of misorientations, implying that the levels of dislocations in the crystals are at a similar level. The types of dislocations structures in present may differ, however.

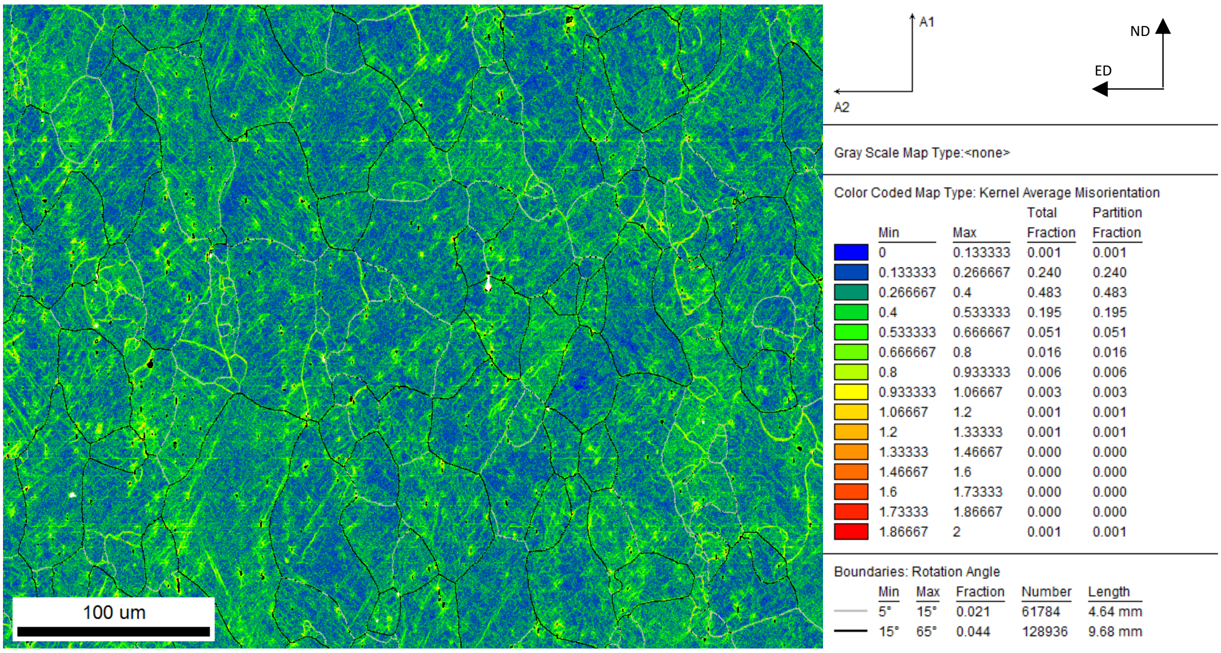

Gray Scale Map Type:<none>

Color Coded Map Type: Kernel Average Misorientation

	Min	Max	Total Fraction	Partition Fraction
🟦	0	0.133333	0.001	0.001
🟦	0.133333	0.266667	0.240	0.240
🟩	0.266667	0.4	0.483	0.483
🟩	0.4	0.533333	0.195	0.195
🟩	0.533333	0.666667	0.051	0.051
🟩	0.666667	0.8	0.016	0.016
🟨	0.8	0.933333	0.006	0.006
🟨	0.933333	1.06667	0.003	0.003
🟨	1.06667	1.2	0.001	0.001
🟧	1.2	1.33333	0.001	0.001
🟧	1.33333	1.46667	0.000	0.000
🟧	1.46667	1.6	0.000	0.000
🟥	1.6	1.73333	0.000	0.000
🟥	1.73333	1.86667	0.000	0.000
🟥	1.86667	2	0.001	0.001

Boundaries: Rotation Angle

	Min	Max	Fraction	Number	Length
―	5°	15°	0.021	61784	4.64 mm
―	15°	65°	0.044	128936	9.68 mm

Figure 4.53. EBSD Kernel Average Misorientation Map of an AA6xxx series alloy deformed using a combination of stretch and roll deformation to 8% and 4% strain levels, respectively. 250x magnification, 0.13-micron step size.

Figure 4.53 shows the KAM map of a sample deformed in the combined state. The material is first stretched to 8% stretch strain level and then 4% roll strain level. The appearance of the graph can be compared to that of the 8% stretch strain level map in Figure 4.50 and the 8% roll stretch strain level map in Figure 4.51. However, in the misorientation key on the right-hand side, the level of misorientation and thus the number of dislocations in the crystal matrix is greater and this follows the trend that, as the level of deformation is increased, so is the level of misorientation measured in the KAM map.

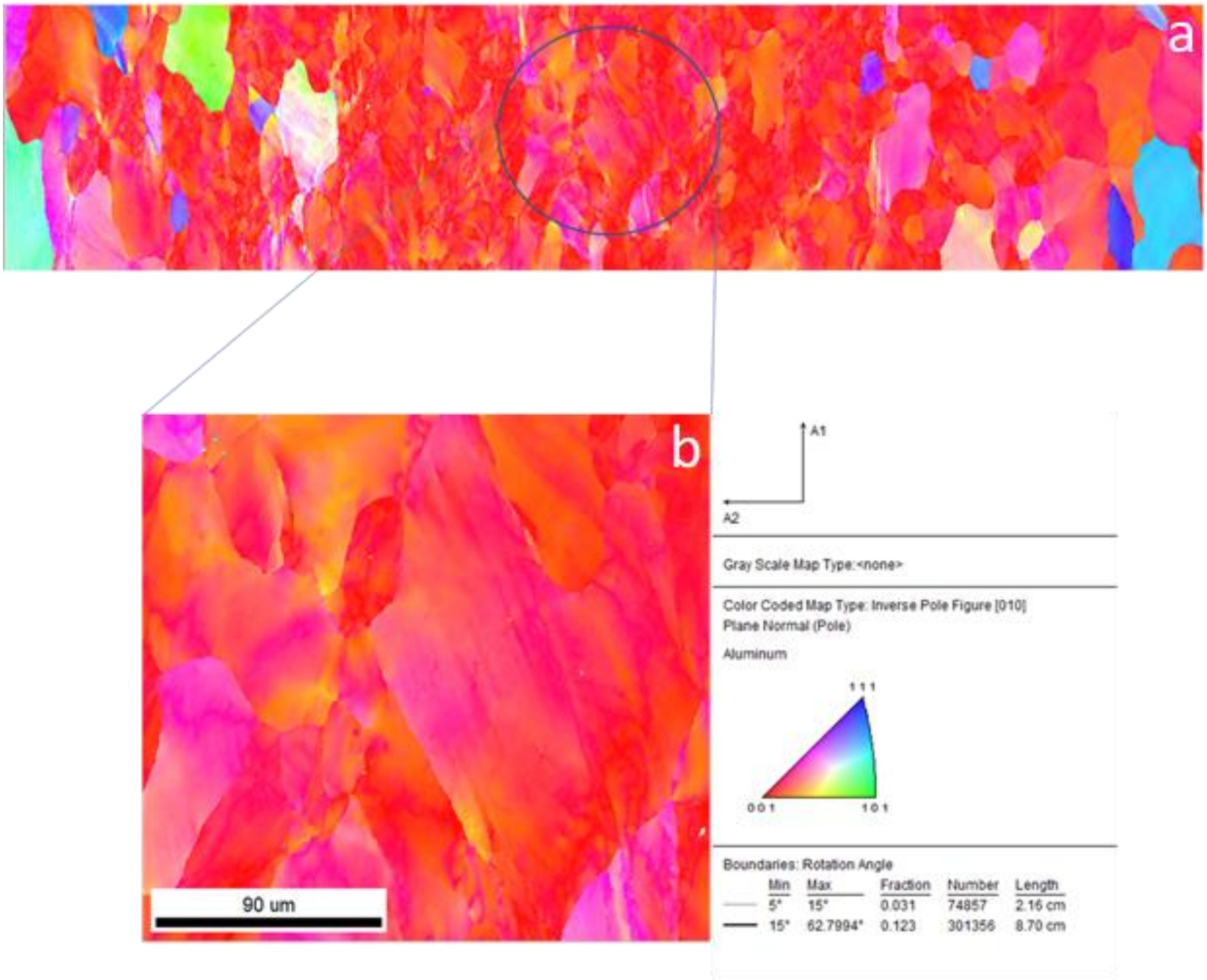

Figure 4.54. EBSD Inverse Pole Figure Map of an AA6xxx series alloy formed using EMPT at an energy of 30kj. 75x magnification, 0.5-micron step size.

Figure 4.54 (a) displays the IPF map of a section of the EMPT formed sample. Figure 4.54 (b) focuses in on the middle region for a higher resolution. Inside the grains, there are visible changes in the orientation readings, indicating the presence of some sort of complex dislocation network. A deformation texture can be seen as a result of this high-level deformation mode. In the centre region where the majority of the magnetic forces were acting, virtually all of the grains have a 001-plane orientation with small deviances from these poles due to the resultant dislocations. The grain morphologies in the area are fairly similar. They appear as slightly flattened and elongated along the extrusion direction.

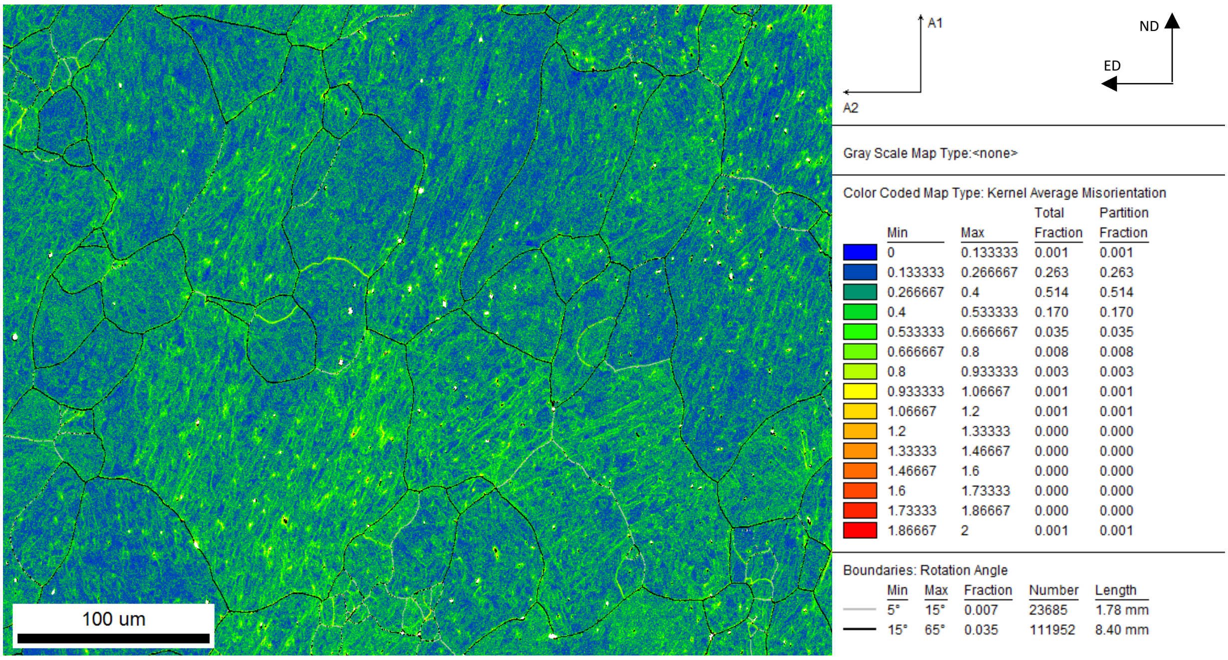

Color Coded Map Type: Kernel Average Misorientation

	Min	Max	Total Fraction	Partition Fraction
🟦	0	0.133333	0.001	0.001
🟦	0.133333	0.266667	0.263	0.263
🟩	0.266667	0.4	0.514	0.514
🟩	0.4	0.533333	0.170	0.170
🟩	0.533333	0.666667	0.035	0.035
🟩	0.666667	0.8	0.008	0.008
🟩	0.8	0.933333	0.003	0.003
🟨	0.933333	1.06667	0.001	0.001
🟨	1.06667	1.2	0.001	0.001
🟧	1.2	1.33333	0.000	0.000
🟧	1.33333	1.46667	0.000	0.000
🟧	1.46667	1.6	0.000	0.000
🟥	1.6	1.73333	0.000	0.000
🟥	1.73333	1.86667	0.000	0.000
🟥	1.86667	2	0.001	0.001

Boundaries: Rotation Angle

	Min	Max	Fraction	Number	Length
—	5°	15°	0.007	23685	1.78 mm
—	15°	65°	0.035	111952	8.40 mm

Figure 4.54. EBSD Kernel Average Misorientation Map of an AA6xxx series alloy Preaged and deformed through stretch to a strain level of 4%. 250x magnification, 0.13-micron step size.

The level of misorientation measured in the KAM map is significantly increased in the processing stage following a short preaging. There are more appearances of dislocation bands inside of the grain as compared to the sample deformed in the as extruded state. The magnitude of the misorientation in the sample is not starkly different to that in the as extruded state however, but the volume fraction of these misorientations is larger. Visually, there is still a lot of blue, undeformed space of the bulk crystal in the background overlayed by the bands of green representing the dislocations.

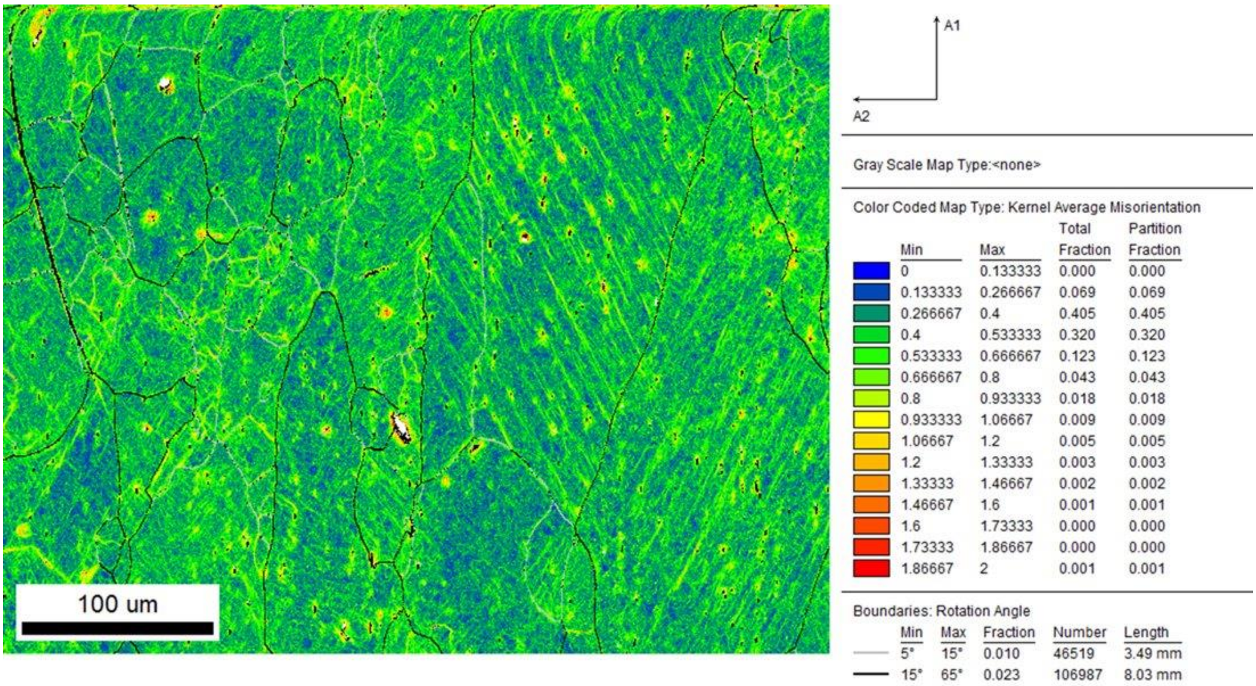

Gray Scale Map Type:<none>

Color Coded Map Type: Kernel Average Misorientation

	Min	Max	Total Fraction	Partition Fraction
🟦	0	0.133333	0.000	0.000
🟦	0.133333	0.266667	0.069	0.069
🟩	0.266667	0.4	0.405	0.405
🟩	0.4	0.533333	0.320	0.320
🟩	0.533333	0.666667	0.123	0.123
🟩	0.666667	0.8	0.043	0.043
🟨	0.8	0.933333	0.018	0.018
🟨	0.933333	1.06667	0.009	0.009
🟨	1.06667	1.2	0.005	0.005
🟧	1.2	1.33333	0.003	0.003
🟧	1.33333	1.46667	0.002	0.002
🟧	1.46667	1.6	0.001	0.001
🟥	1.6	1.73333	0.000	0.000
🟥	1.73333	1.86667	0.000	0.000
🟥	1.86667	2	0.001	0.001

Boundaries: Rotation Angle

	Min	Max	Fraction	Number	Length
—	5°	15°	0.010	46519	3.49 mm
—	15°	65°	0.023	106987	8.03 mm

Figure 4.56. EBSD Kernel Average Misorientation Map of an AA6xxx series alloy Preaged and deformed through stretch to a strain level of 8%. 250x magnification, 0.13-micron step size.

In the material where the strain level of the stretch was 8%, there is a far greater response. Visually, there is greater volume of space occupied by the green highlight. This shows the much greater density of dislocations. Comparing this to the as extruded and deformed state, there is more significant banding structures inside of the grains. There is also, to a small degree, a larger volume of higher misorientated points, measured, the yellow and red spots in the micrograph map areas where there are much higher orders of misorientations and thus a far greater dislocation density. There appears to be some interaction between the clusters or early-stage precipitates formed in the material through the short preaging step and the dislocation which are introduced following the deformation step.

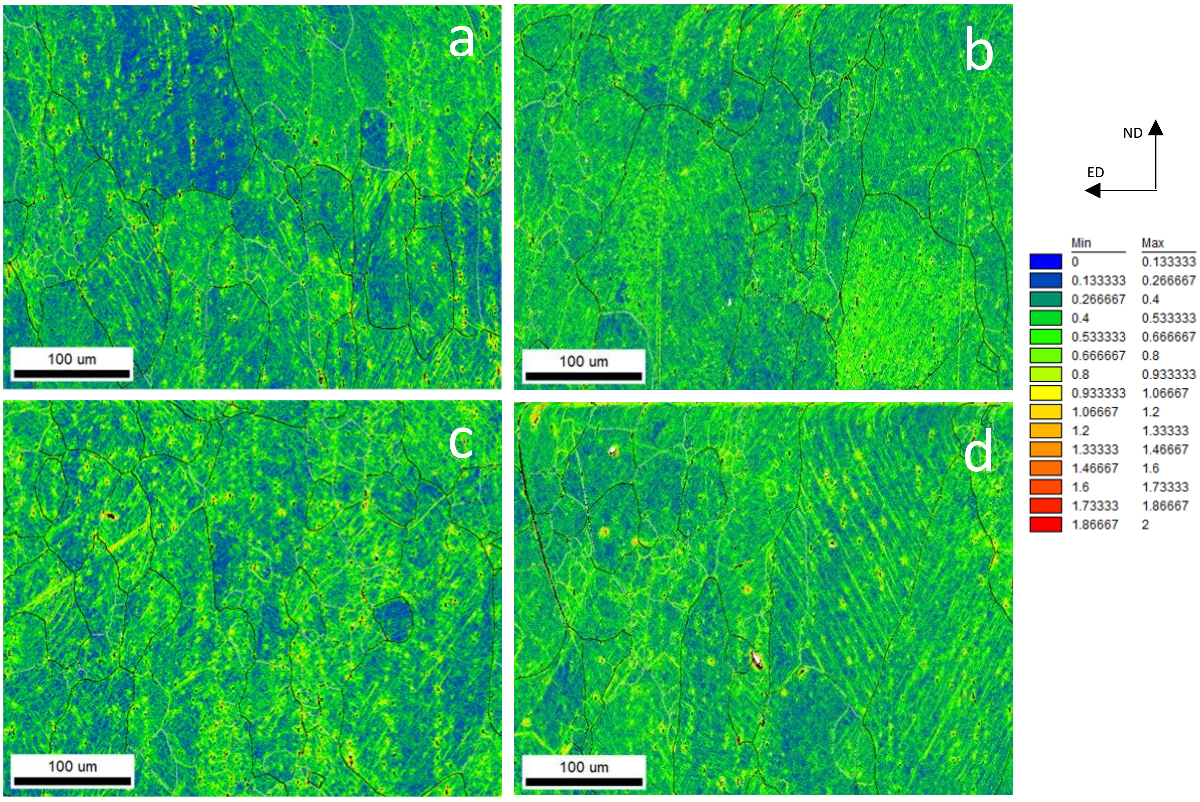

Figure 4.57. EBSD Kernel Average Misorientation Maps of an AA6xxx series alloy Preaged to different stages followed by a deformation using stretch to a strain level of 8%. 250x magnification, 0.13-micron step size. (a) 150C/8h + 8s; (b) 150C/24h + 8s; (c) 170C/2h + 8s; (d) 170C/4h + 8s.

The effect of varying the pre-ageing step can be seen in Figure 4.57. As a whole, it can be seen that the effect of increasing the dislocation density is maintained across all conditions regardless of the ageing recipe used. The interactions between the precipitates and dislocations are preserved. The structures formed differ slightly and the spread of the volume fractions are quite different. The volume fractions are graphed in the graph below.

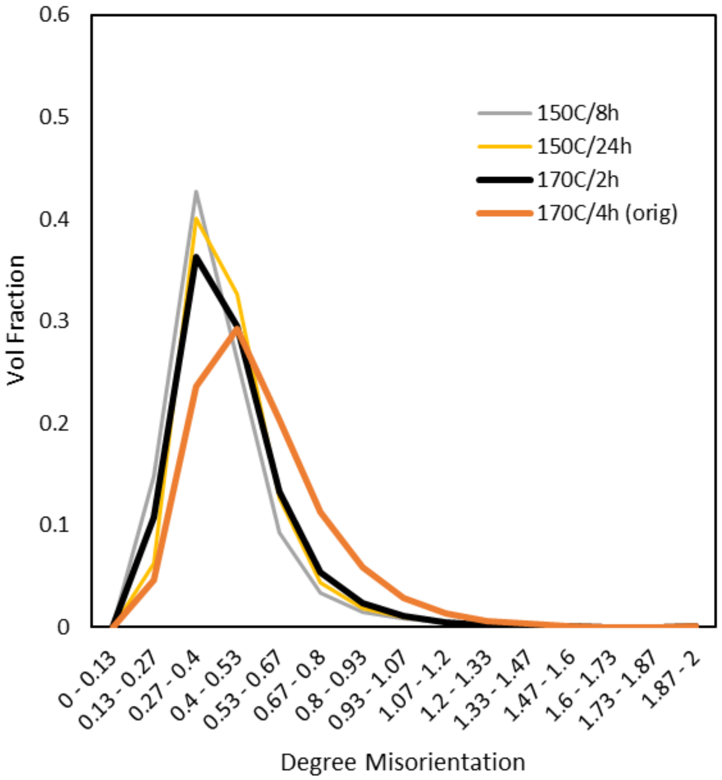

Figure 4.58. Graph showing the spread of misorientation volume fraction from an EBSD KAM map of samples aged to varying times and then deformed to an 8% strain level through stretch deformation.

From the graph in Figure 4.58, the ageing condition that gave rise to the highest levels of misorientation was the recipe with the 170C/4h preaging step + 8% stretch strain, depicted in Figure 4.57(d). In this graph, the line is skewed more to the right-hand side represent a greater level of misorientation in the sample specimen. The 170C/4h + 8% stretch strain condition had more measurements with even higher levels of misorientation than the other states. The two samples aged at the 150C temperature, the level of misorientations found in the samples are reasonably less than those seen in the 170C samples. This seems to say that the 170C temperature was more effective at producing this effect. Potentially the precipitation sequence is slightly altered/different at this temperature and so the precipitate/cluster complex present interacts differently with the dislocations introduced through the deformation stage.

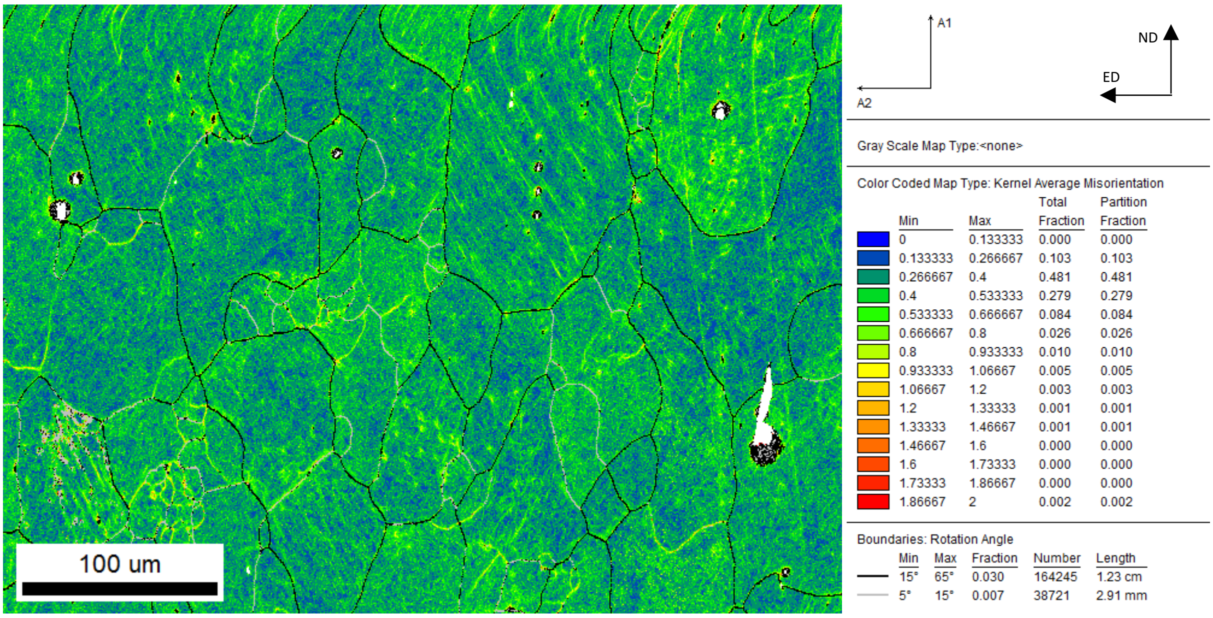

Gray Scale Map Type:<none>

Color Coded Map Type: Kernel Average Misorientation

	Min	Max	Total Fraction	Partition Fraction
🟦	0	0.133333	0.000	0.000
🟦	0.133333	0.266667	0.103	0.103
🟩	0.266667	0.4	0.481	0.481
🟩	0.4	0.533333	0.279	0.279
🟩	0.533333	0.666667	0.084	0.084
🟩	0.666667	0.8	0.026	0.026
🟩	0.8	0.933333	0.010	0.010
🟨	0.933333	1.06667	0.005	0.005
🟨	1.06667	1.2	0.003	0.003
🟧	1.2	1.33333	0.001	0.001
🟧	1.33333	1.46667	0.001	0.001
🟧	1.46667	1.6	0.000	0.000
🟥	1.6	1.73333	0.000	0.000
🟥	1.73333	1.86667	0.000	0.000
🟥	1.86667	2	0.002	0.002

Boundaries: Rotation Angle

	Min	Max	Fraction	Number	Length
—	15°	65°	0.030	164245	1.23 cm
—	5°	15°	0.007	38721	2.91 mm

Figure 4.59. EBSD Inverse Pole Figure Map of a AA6xxx series alloy fully processed using the thermomechanical recipe, including a stretch deformation of 8% strain. 250x magnification, 0.13-micron step size.

The KAM map shown in Figure 4.59 corresponds to a fully processed sample. The material follows the 170C recipe with an 8% stretch strain deformation applied in-between the aging steps. The levels of misorientation in the material is greater than that seen in the starting as-extruded material, however, when compared to the material after preaging and deformation without the final ageing step applied, the degree of misorientation is lowered. This is due to the slight recovery of dislocations that takes place at the slightly elevated temperatures of the final aging step.

4.6 Summary

From the results accumulated and presented in this study, a few interesting trends and findings have been revealed and concluded.

a) The effect of the TMA process in strengthening the heat treatable Al-Mg-Si-Cu alloy is greatly dependant on the various steps taken which attain strengthening through a mixture of strengthening mechanisms. Variations in these parameters lead to noticeable changes in the final presented material behaviour and in turn the microstructure of the crystals.

   Quantitative mechanical behaviour analysis through hardness and tensile test illustrate that there is a significant difference in the strengthening capabilities of stretching and rolling as a strain mode. From the data, stretch deformation had a greater efficacy in hardening the material in all states of the thermomechanical process and even across ageing temperatures.

b) The premise of combining stretch and strain deformation was to observe the complimentary effect of applying stretch and roll deformation to material and if this had any advantageous effects on the final mechanical properties. In the T4 state, the higher strain levels meant that there was a stark increase in strength as compared to the other lower strain levels as there was a greater capacity for hardening. Once the material was aged however and the work hardenability of the material had been greatly decreased, there was no evident benefit to administering this combinational strain mode as compared to the lower strain levels. The ductility was also compromised as a result of these higher strain levels.

c) A short Preaging step as a part of the thermomechanical processing of the material evoked a great enhancement in the final properties of the material with the greatest enhancement achieved with the material subjected to the following thermomechanical recipe: 170^{o} C/4h + 8% stretch + 170^{o} C/4h. This resulted in a final yield strength of 356.9MPa, an ultimate tensile strength of 364.5MPa and a uniform elongation of 5.4%. It was proven that as a result of this preaging, there was a high density of precipitates formed in the crystal matrix that interacted with the dislocations introduced due to the plastic deformation applied. These precipitates pinned the dislocations forming a complex that would affect the final re-aging step. There were many interactions between the dislocations and precipitates and the dislocations even acted as nucleation sites for the precipitates formed which would all coalesce to attain the enhanced mechanical properties observed in the mechanical tests.

d) There was a noticed difference in the way that the dislocations interacted with the precipitates of different samples which was seen in the EBSD KAM maps. The 150C samples aged to 8 hours and 24 hours were at different stages of the precipitation sequence. Resultantly, the network of precipitates presented in the crystal matrixes differed. This meant that when the deformation was applied, the dislocation-precipitate interactions that occurred were different and to different degrees in the two conditions, as illustrated in Figures 4.67 and 4.69 with the different apparent dislocation densities. It was then deducted that the stage of the precipitation sequence in the preaging step was of key importance in the enhancement of mechanical properties. A more developed precipitate group yielded higher strength, but lower ductility and a slightly less developed state gave a better strength ductility compromise.

e) There was a difference in the mechanical properties of the 150 C and 170 C ageing conditions. The 170C recipes yielded a greater mechanical response than the 150C.

Chapter 5. Discussion

The discussion chapter analyses and evaluates comprehensively, the experimental results and findings of the study, showing the effects of the various thermomechanical processing routes on the mechanical behaviour of the AA6xxx series alloy as laid out in chapter 4. This chapter consists of four main sections. The first delves into the methodological aspects of the preaging step. The precipitation hardening kinetics and selection of preaging conditions are analysed as well as the premise for the half-peak ageing conditions which are compared to similar works in literature. The effects of this preaging are then discussed as well as the tailored microstructure it produced. Links to these features of the microstructure and the mechanical properties obtained are drawn and explained.

The next section deals with the deformation induced changes in mechanical performance. The mechanical response to strain via the varied strain modes and paths: stretching, rolling, combination of stretching and rolling, and EMPT are discussed at length, comparing their differences in measured properties and the evolution of their microstructures through analytical imaging and diffraction methods. The textures of these specimen through ODF maps are reviewed, further explaining these noted differences. Following this characterisation of the processing induced features, the next section outlines the interaction schemes occurring between these defects that ultimately lead to the enhanced property development.

Data from different stages of the thermomechanical processing are compared. The interplay between temperature, timing and deformation are highlighted and a focus is placed on how these factors influence the materials microstructural evolution.

Finally, the optimal aDA condition is discussed, and a heuristic assessment of the selected processing route is given, offering valuable insights into the hardening mechanism.

5.1 Preaging

The thermomechanical process used in this study was a 3-step manufacturing, strengthening process consisting of two heat treatment stages with a deformation stage in between these ageing steps. Prior to this specific processing however, the recrystalised material was subjected to solution heat treatment (SHT) at approximately 550C and rapidly cooled through water quenching to obtain a supersaturated solid solution. In literature, SHT of 6xxx series alloys is commonly done at temperature ranges of 500-560^{o} C for times of between 5-180 minutes(Esmaeili, 2003)(Shen, 2007)(Chen, 2019)(Friedman, 2002).

Preaging is ubiquitously used in the heat treatable 6xxx series aluminium alloys in the automotive industry to prevent the negative effects of natural ageing. Preaging brings about stabilisation of the material during the processing and as well as at room temperature storage (Birol, 2005). Numerous studies have investigated the effect of preaging on these automotive alloys (Liu, 2005)(Tian, 2010)(Miller, 2000), giving insights into how the process can be used as part of the manufacturing process.

Critically, preaging had been found to significantly improve the final ageing kinetics and the precipitation strengthening effect when it is combines with deformation, normally at a low strain level. In the current study, the preaging was employed as a step of the novel thermomechanical scheme aDA.

5.1.1 Age Hardening Kinetics of the Material

The nanoscale second-phase particles formed in supersaturated 6xxx series aluminium alloys through ageing are responsible for the mechanism of precipitation hardening. These extremely small, uniformly dispersed particles can precipitate out of the matrix either through natural or artificial age hardening treatment, leading to typically different mechanical behaviours such as material strength (Liu, 2007).

Post extrusion and quenching, the natural ageing process begins in material at room temperature, forming clusters of Mg and Si atoms and in turn GP zones (Banhart, 2011)(Werinos, 2016). This process is inevitable and thus to maintain a control between all samples in this study, the material was rested to age at room temperature for 48 hours before any processing was carried out. The material at this state was more stable and although natural ageing was still occurring, the rate of this was significantly slowed and thus all samples were considered virtually at the same starting point. To further minimise the effect of the natural ageing of the material behaviour in the following thermomechanical processing, after this 48 hour resting period, the material was placed in a freezer kept at -20C which, based on experimental data obtained by the industrial sponsor, was shown to significantly slow down precipitation and vacancy diffusion.

In the present study, the effect of this natural ageing process can be seen in Figure 5.1

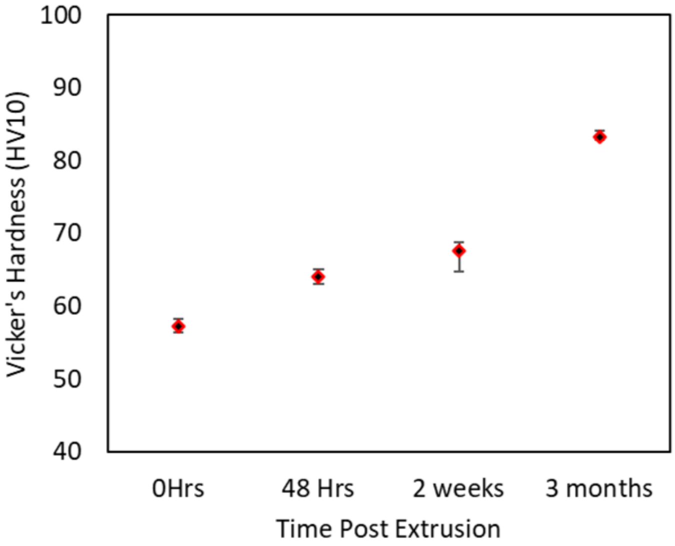

Figure 5.1. Vickers Hardness versus Natural ageing duration.

Immediately after extrusion, the average measured hardness of the material was 57.2 HV10. After the material was allowed to rest for 48 hours, the measured hardness had increased to 64 HV10 as per the age hardening kinetics described above. The sample aged at room temperature for 2 weeks increased its hardness much more slowly to 67.6 HV10 and finally, the sample allowed to rest for 3 months at room temperature in a storage room reached a hardness of 83.3 HV10. The effects of natural ageing were apparent and the need to hold a control was critical.

In the current study, Preaging referred to the intentional artificial ageing of the material through specific heat treatments otherwise known as artificial ageing. The ageing conditions, temperature, and duration selected largely affected the mechanical properties measured. Preaging performance at 150° C, 170° C, and 190° C was investigated at various time intervals to determine distinctly critical periods in the hardening development of the material. One key period was T6 or peak hardening, the condition of achieving the highest hardness in the material. This temper was highly dependent on the aging time and temperature used (Chen, 2019). Figure 4.12 shows the ageing kinetics results from varying ageing conditions. From the graph, 3 peak hardening points are registered for the 3 ageing temperatures, and these are: 150° C for 72 hours, 170° C for 16 hours, and 190° C for 4 hours with peak measured hardnesses of 133.34, 132.4 and 127.16 HV10 respectively. There is a trend that in hardness kinetic experiments, a lower temperature leads to a higher hardness than ageing at higher temperatures, but the trade-off is a longer ageing period also supported in a previous study (Yang, 2021).

Peak ageing tensile properties were also measured, displayed in Tables 4.15 and 4.16. The ageing condition of: 150° C for 72 hours attained a yield strength of 307MPa and an ultimate tensile strength of 338MPa, the uniform elongation measured was 10.5%. Tensile results from the: 170° C for 16 hours condition gave very similar tensile properties, with a yield strength of 309MPa, an ultimate tensile strength of 334.4MPa and a uniform elongation of 8.2%. unlike in the hardness tests, there was virtually no difference in the strength of the material under these two conditions.

Peak aging carried out on similar Al-Mg-Si alloys in studies showed similar hardening behaviours at similar conditions. Typical temperatures mostly ranged from 170-185° C, however, some studies operated temperatures as high as 220° C and some as low as 100° C.

A study by Jiang et al investigated the effect of ageing on the mechanical properties of thin-walled Al-Mg-Si-Cu alloy profiles. The profiles were treated to aging at 215° C for 60,120 and 300 minutes. Their results showed that with increasing ageing time came a reduction in the number density of precipitate particles as well as coarsening in the size of these particles, the precipitate type was also generally transformed from β'' to β' which resulted in a reduction of microhardness and strength, corroborating the results of the ageing kinetics graph in Figure 4.12. The artificial ageing condition of 215° C for 120 minutes gained a yield strength of 280MPa.

Cai et al altered ageing temperatures at a constant time of 2hrs, using times of 210, 215, and 220° C. The recorded yield strength of 271Mpa for the ageing condition of 220° C for 2 hrs gave optimal recorded mechanical properties. Mirzakhani et al 2015, found using ageing times of 180 and 200° C that the peak ageing was achieved at 8 and 4 hours respectively.

Lower temperature ageing on the same alloying system was conducted by Yang et al in a 2020 study. An ageing condition of 180° C for 3 hours, was used to attain and underaged status and an artificial ageing of 180° C for 6 hours was applied to the material to achieve a peak aged status. Mechanical properties for these ageing states were a yield strength of 258.6±5.2 MPa for the underaged state and 273.3±1.3 MPa for the peak aged state.

5.1.2 Selection of Preaging Conditions

As discussed above, preaging heat treatment of the material is routine practice in the automotive industry to stabilise it kinematically (Birol, 2005) leading to more predictable behaviours by the material. The adverse effects of natural ageing are supressed resulting in more favourable mechanical performance of the material(Hodžić, 2023). Saga, 1996 et al found that the temperature used for preaging is required to be above 70° C in order to garner the effective preaging stabilisation effect. It is shown extensively in the literature that the effect is enhanced by reaching a higher preaging hardness or strength (Birol, 2005)(Yang, 2019)(Takaki, 2014). Thus, the selection of these preaging conditions can be done scrupulously in order to tailor the desired properties of the material.

The upper range of peak aging temperatures discussed in section 5.1.1 and the minimum temperatures to effectively activate these preaging effects were considered in selection of the ageing temperatures. The duration of ageing determined the degree to which the material was hardened.

Ageing of 6xxx series elicits phase transformation in the crystal system that occur in specific sequences summarised as SSSS -> Atomic Clusters -> GP Zones -> β'' -> β' -> β (Burger, 1995) with other possible phases forming depending on other alloying elements (Chrominski, 2020). Peak ageing is achieved at a specific stage of this sequence where the highest number fraction of β'' precipitates are present in the material as they are considered the most effective phase at strengthening in the 6xxx alloy series. Before this stage the material is termed under-aged with more numbers of these less developed precipitate particles (Uan, 2006).

Preaging often is practiced as a 2-stage heat treatment cycle where it is commonly followed up by a longer, more extensive ageing process to achieve the final desired mechanical properties. It is well known by now that preaging can be advantageous in this way and can affect numerous material parameters such as formability and the final age hardening response (Liu, 2005)(Tian, 2010)(Ryen, 2015). Preaging application is also common as part of thermomechanical process. Many severe plastic deformation techniques including cryogenic rolling, high pressure torsion (HPT), and equal channel angular pressing (ECAP) are used in combination with the ageing process to attain significantly enhanced strength in Al alloys (Sabirov, 2013)(Estrin, 2013). However, these forms of thermomechanical processing were not directly applicable to the automotive or practical settings due to their complex and excessive procedures. (Wang, 2014).

In the current study, the aim of the preaging precipitation process was to initiate a uniform dispersion of these second phase particles that would have meaningful interactions with the dislocations generated through the following low strain plastic deformation in the material. A study by Yang et al showed through modelling and experimental work that the contribution of the β'' and β' precipitate phases to strengthening could be quantified in Al-Mg-Si aluminium alloys. In their work, two samples were aged to different stages, one to underaged status and the other to peak aged. The reason for these differences in contributions were understood to be as a result of their respective lattice strains with the β'' precipitates being found to be associated with a smaller lattice strain with respect to the crystal matrix.

Experiments by Wang in a 2014 study investigated the effect of a preaging step in a thermomechanical process. It was found that a preaging condition of 180^o C held for 2hours developed improved strength and ductility in an Al-Mg-Si-Cu alloy pronouncedly when compared to conventional peak aged aluminium sheets.

From the ageing kinetics experiments in this study, different points of the hardening sequence were investigated. The halfway peak and a lower preage state at different temperatures in order to access the effectiveness of these preaging states on the final properties and mechanical behaviour of the material following the full thermomechanical processing. It is an important consideration in the selection of the preaging condition to prevent the alloy from being aged too close to the precipitation peak as to not fully precipitate out the solutes in the matrix. This would resultantly limit the potential for hardening in the final ageing step of the thermomechanical process. There would be limited hardening as the precipitation driving force is exhausted. Hence, the halfway hardening point of the precipitation kinetics curve was of particular interest in this study, where there is a balance of precipitates formed in the matrix, with enough available for hardening in the final ageing step.

5.1.3 Precipitation Behaviour During Preaging

During the preaging of the material the precipitation that occurs is in the early stages where there are generally only atomic clusters and GP zones. In terms of nucleation and growth mechanisms, these are classified as the homogeneous category of precipitates, as well as the β’’ phase (Porter, 2009)(Liu, 2015)(Edwards, 1998). These nucleate uniformly across the whole volume of the supersaturated aluminium matrix and are mostly coherent with the matrix, exhibiting relatively low interfacial energy(Marioara, 2005)(Holmestad, 2010).

The main hardening precipitates β’’ nucleate and are metastable at temperatures ranging from 100^{o} C to temperatures well below 200^{o} C (Osuch, 2018) while their nucleation rate varies and are highly dependent on temperature, showing a positive correlation. Precipitation induced solute atoms often occurs on various defects present in the material such as vacancies, dislocations, and grain boundaries (Derlet, 2002).

Figure 5.2 shows the time-temperature-transformation(TTT) curves of an aluminium 6xxx series alloy explaining the general nucleation of these precipitate phases in relation to ageing time and temperature.

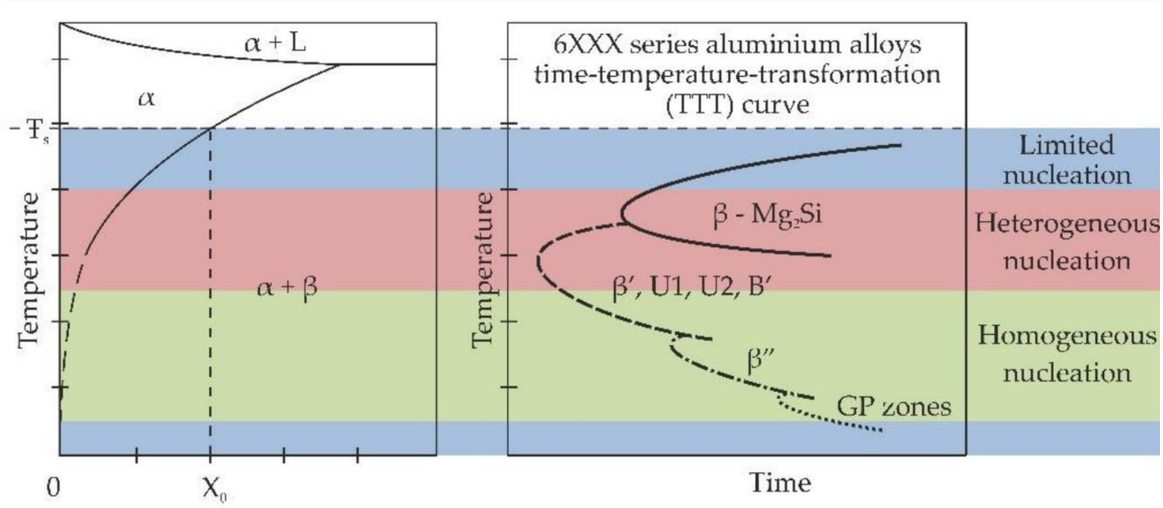

Figure 5.2. Schematic of the precipitation kinetics in 6xxx series alloys. (Osuch, 2018)

Analysis of the alloy after preaging was conducted with the TEM technique. These results are displayed in Figure 5.3

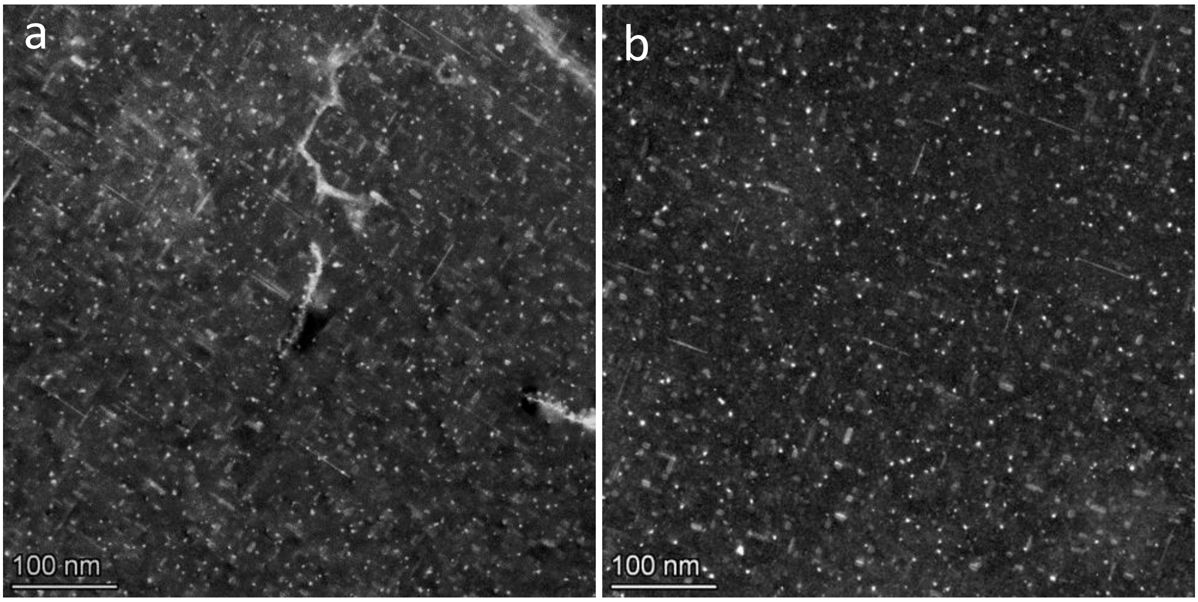

Figure 5.3. LAADF - STEM images showing the presence of precipitates at two preaging states of an aluminium 6xxx series alloy a) 150° C for 8hours b) 150° C for 24hours.

At 150° C, the two preaging conditions considered were aged for times of 8 and 24 hours. From the micrographs, there were a high density of fine homogeneously dispersed precipitates throughout the matrix. These precipitates that were formed were the early-stage clusters and GP zones. There are a number of rod-shaped precipitates, but their number densities are much lower as the material is in a relatively low stage of the precipitation sequence. Seemingly there is no great visible difference in the precipitation of the two preaging states as the precipitation densities appear similar. Measured precipitate densities are indeed very similar in both conditions. It was expected that the number densities in these two conditions would be different, but this was not the case. Referring to the mechanical property results, it can be assumed that the precipitation between the two conditions in Figure 5.3 differ. If the measurement is true and genuine, and there is no substantial differences between the precipitate densities in these two states, it would suggest that the particles not seen such as clusters and GP zones play a critical role in strengthening and dislocation storage in the material. It is unclear how GP zone development as a function of time occurred, leaving open questions for further investigation.

The later stage of preaging precipitation did prove advantageous in strengthening the material. The interactions between these preaging induced particles and the dislocations introduced in the deformation step would play a key role in governing the kinetics of the final ageing precipitation.

5.2 Deformation Induced Mechanical Property Enhancement

Material behaviour changes observed as a result of applied deformation can be seen in section 4.4. This mechanical property improvement can be attributed to the strengthening mechanism of strain hardening where the dislocation density in the material increased as a result of the geometrical changes in the material. Because of the absence of strong pinning agents, the work hardening was considered to be dominated by dislocation-dislocation interactions (Cahn, 1996).

Sole Deformation yielded apparent strength increases in the material but relative to the preaging conditions, these measured increments were not as stark. Therefore, precipitation hardening played a greater role of strengthening in this alloy system. Following the applied age treatments to the material, the samples were again deformed to introduce strain hardening. The behaviour of the material in these aged conditions differed largely to the behaviour in the as-extruded state.

As plastic deformation on the material was increased, the work hardening capacity of the material decreased. This was evaluated using the power law (equation 4.1).

5.2.1 The Effect of Strain

Table 4.6 shows the results from the stretch strain mode. From these results, the starting measured hardness of the material was calculated and averaged to be 64 HV10. When the material was plastically deformed to a strain level of 4% there was a slight increase in the material hardness measured, yielding a 5.6% increase to 67.6. At a strain level of 8% stretch, this hardness was increased to 72.6, a 13.4% increase as compared to the as-extruded state. This clearly indicated that as the applied strain level was increased, the resultant mechanical hardness was also proportionally increased.

The same trend held true in the roll deformed samples as laid out in Table 4.7 which achieved a 5.6% and a 13.8% increase for 4% and 8% strain levels. Obviously, as the strain level was increased in this as extruded state so was the measured Vickers hardness.

Tensile testing also reflected this trend. In Table 4.15, the gain in 0.2 yield strength compared to the starting material that was achieved from 4 and 8% strain levels was 97.6% and the 111.6% respectively. As expected, a greater strain hardening meant a decrease in the material’s ductility. There was minimal effect on the ultimate tensile strength of the material across all strain levels. This can be seen in Figure 5.4

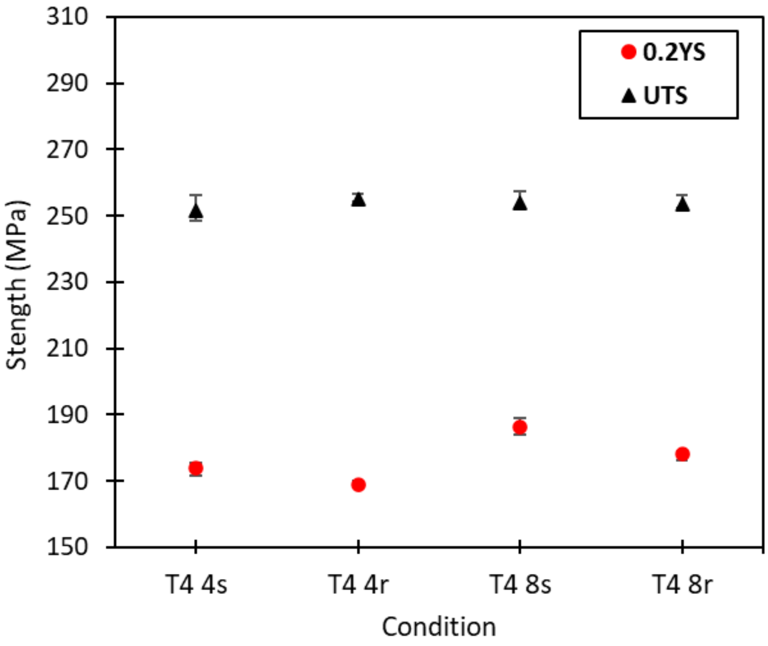

Figure 5.4. Tensile strength result of a strain hardened 6xxx series aluminium alloy.

SEM Electron Backscattered Diffraction (EBSD) technology coupled with the OIM 8 software was used to reveal the dislocation densities in these various material samples. It was shown using Kernel Average Misorientation (KAM) Maps that the dislocation densities varied depending on the strain level.

There was a clear trend that as the strain level applied to the material in the deformation step increased, so did the degree of and density of dislocation in the material matrix, visually and quantitatively measured. This correlates that as the density of dislocations in the material matrix increased, there is a resultant increase in the mechanical properties which is congruent with the words written in F,J,Humphrey's book and is also observed in the works of Cho in a 2021 paper.

In this technique, the dislocation densities were measured indirectly. The rotations and elastic strain fields caused in the local area of these dislocations resulted in misorientations that were picked up and calculated by the detector and OIM software on the computer. The presence and degree of these measured misorientations were then put through a mathematical algorithm to infer the dislocations present in the material that caused them.

The dislocations that were measured and are responsible for these misorientations in the material are the geometrically necessary dislocations (GNDs) which are produced during the deformation stage of the thermomechanical processing through plastic deformation. GNDs are generated to accommodate the internal strain orientation gradient fields in the crystal of the material. This accommodation is necessary to allow the lattice to maintain its continuity. GNDs were first proposed by Nye and then further developed by the work of Ashby. In Nye's dislocation density tensor, aij represents the density of dislocations present in the crystal with "i" being the Burgers Vector and "j" the dislocation line vector. The dislocations that do not contribute to the dislocation density tensor (aij) are known as statistically stored dislocations (SSDs); they are randomly formed through dislocation multiplication. An example of these are dislocation dipoles. Both GNDs and SSDs are present in the lattice of a deformed material. As SSDs cancel out, any non-zero dislocation density tensor components containing lattice curvature and can be measured by spatial orientation changed. SSDs therefore do not show up in the KAM and GND maps formed in the OIM software, as there is no registered misorientation as a result of their presence. There is a strong link between the GND and SSD densities in a crystal lattice, and thus it is possible to relate the dislocation density tensor to the dislocations present in the neighbourhood.

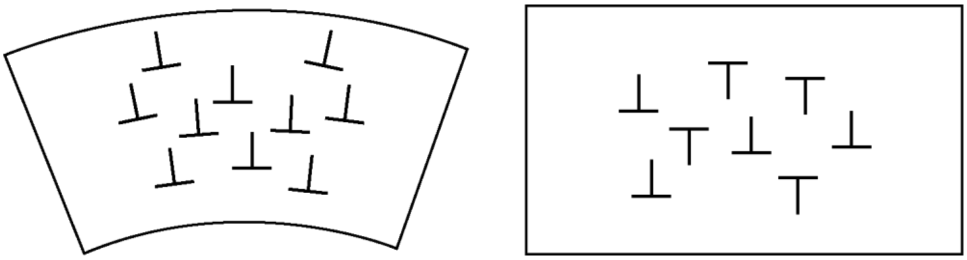

Figure 5.5: Formation of Geometrically Necessary Dislocations (GNDs) compared to Statistically Stored Dislocations (SSDs).

These misorientations in the KAM Maps were set to a range of 0-5 degrees, as these are the ranges that the curvatures caused by these GNDs fall into (Choundraj, 2022). Misorientations higher than these are attributed to low angle grain boundaries (LAGBs). These lattice curvatures caused by the GND dislocations do present misorientations of lower than 2 degrees but there is also a lot of orientation noise signals present in this range. These artefact readings would corrupt the actual dislocation densities due to the sensitivity of Euler angle derived misorientation readings and thus all readings in this range were omitted.

The use of a very small step size gives a high-resolution KAM map – to attain these maps, a small representative area was mapped. The data acquisition was at a magnification of 250x with a step size of 0.13, kept standard across all investigations. This resulted in an acquisition time of 72 hours to collect these highly detailed mappings. The step size used for measuring this density was critical. When the measured step size is doubled, the derived dislocation density is altered significantly (Jiang, 2013) this results from the kernel at which the measurements were taken from, meaning the relative misorientation to the location and its neighbouring kernels would be varied significantly. In preliminary studies, it was found that as the step size was progressively decreased, the average misorientation and thus dislocation density calculated was increased. At this very fine step size, a greater number of dislocations are discernible and contribute to a greater GND volume fraction. Contrastingly, at a coarser step size, groups of dislocations and clusters will be defined as SSDs as their burger's vectors oppose one another and thus cancel out meaning no net/measured lattice rotation at that kernel. Jiang, 2013 summarises this as, the measured density variations are due to the changes in the cut-off point between the identification of GNDs and SSDs.

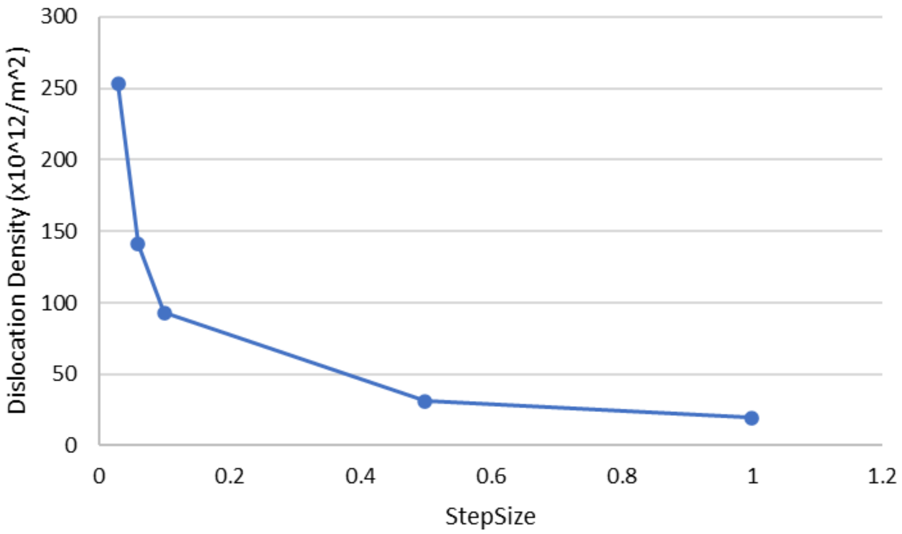

Figure 5.6. Step size effect on average dislocation density in a 6xxx series aluminium alloy.

Alternate dislocation density measuring techniques exist, each having their own are limitations and uncertainties says Gallet in a 2023 publication. Namely: XRD, TEM/ECCI & HR-EBSD. However, these methods vary in the way they measure dislocation density as well as the types of dislocations they are able to characterise.

XRD for instance enables the measurement of dislocations within crystallites and the disorientation that this causes. Dislocations in the grain boundaries and dislocation cells are not picked up when this density of dislocations are calculated. These dislocations are the main sources of GNDs in the alloy's lattice microstructure (Gallet, 2023). The crystallites have a low disorientation in the area; these can be either inside dislocation cells or inside of the grain, meaning dislocation cells will also be seen as grains in this method.

Using the TEM/ECCI technique measures solely isolated dislocations in the grains. Although all grains can theoretically be seen, there is a degree of difficulty in determining and identifying dislocations at or near the grain boundaries as the conditions required for observing dislocations change rather quickly. Dislocations in cell walls that overlap one another present a level of uncertainty rendering any calculation of their densities inaccurate.

In comparison, the dislocation densities measured through the varying techniques would be different because of the methodology employed. The EBSD technique would be able to identify dislocations found in clusters whilst the XRD and TEM/ECCI methods do would not. Consequently, the dislocation densities in EBSD measurements would be generally higher in comparison especially in deformed samples. The EBSD route is incapable of detecting densities of SSDs in the crystal. As TEM/ECCI detects isolated dislocation lines, although both GNDs and SSDs could be identified, mainly SSD densities would be inferred.

Gallet, 2023 found that after deformation, the GND densities increased more rapidly than the SSD densities especially for the material at the 10% strain level. Ideally, utilising a combination of these techniques to characterise both GND and SSD densities in the same region would be optimal but tracking the changes of the GND dislocation population is seemingly more indicative of the microstructural changes occurring during these stages where the material is strained.

Hence GND volume fractions measured in the respective maps were appropriate for characterising dislocation evolution. Figure 5.7 shows the measured GND density in the T4-8% stretched sample generated using the GND function of the OIM 8 software. The misorientations measured pertaining to dislocation presence measured in the KAM maps of Figure 4.50 are charted in a graph in Figure 5.8.

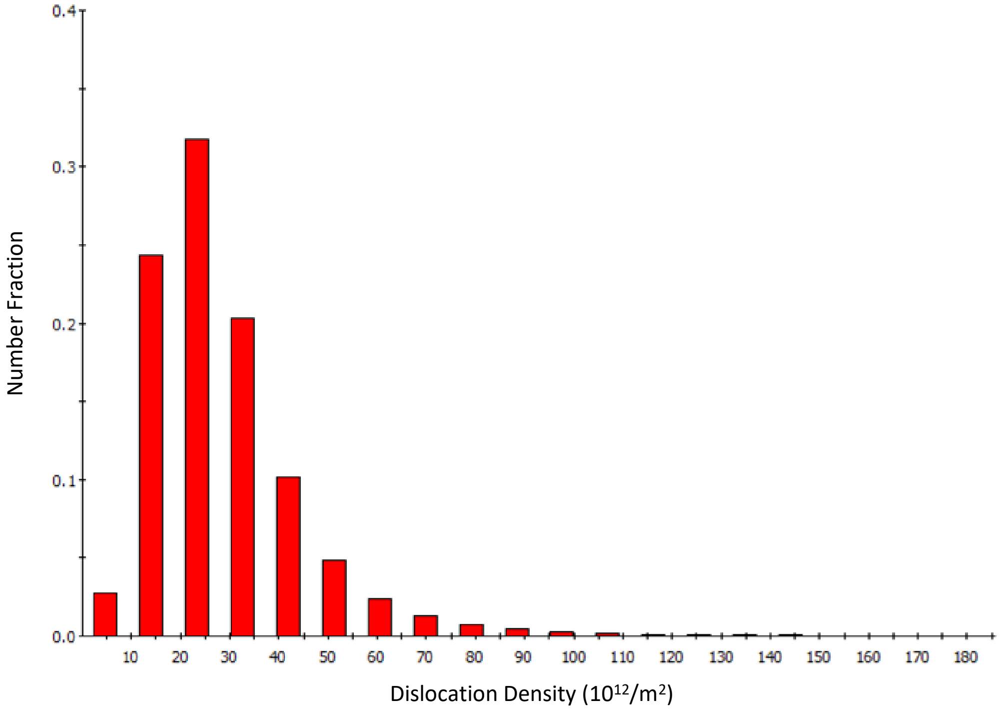

Figure 5.7. Dislocation density number fractions measured in a 6xxx series aluminium alloy plastically deformed through stretching by 8%.

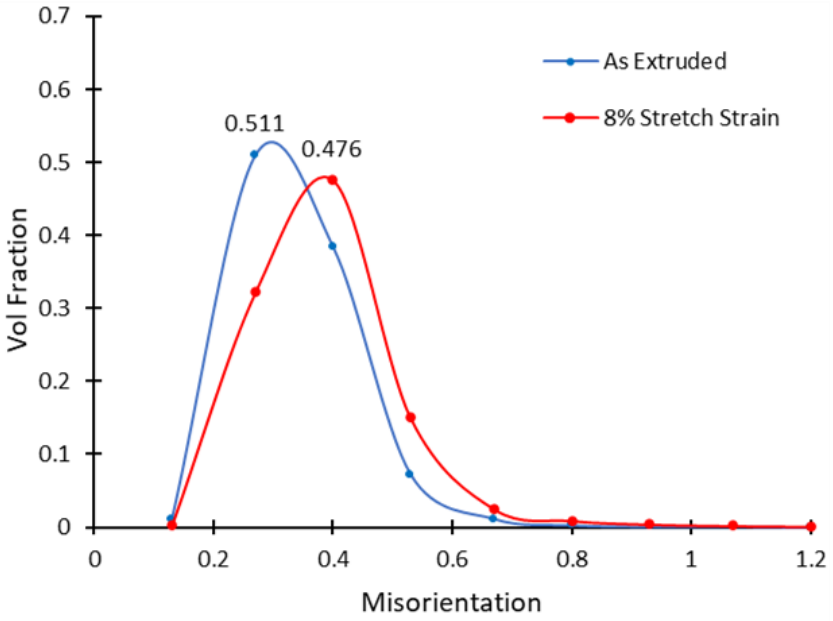

Figure 5.8. Misorientation Spread from an EBSD KAM Map of a 6xxx series aluminium alloy deformed to an 8% strain level through stretching.

The charts in Figures 5.7 and 5.8 show that the dislocation densities can accurately be inferred from the misorientation volume fractions characterized by the KAM map. In Figure 5.8, the kernel misorientations measured in the as extruded sample is compared to that of the 8% stretch strained sampled. Obviously, due to the plastic deformation applied an increase in the recorded misorientation can be seen. The peak is shifted to the right, illustrating a higher volume fraction of higher misorientation due to these aggregations of dislocations within the various crystallites. The average dislocation density in the T4 8% stretch strained sample was given as $28.7x10^{12}$ /m^2.

5.2.2 The Effect of Strain Mode

Through quantitative mechanical behavioural analysis of the Al-Mg-Si-Cu alloy, there was found a noticeable difference in the strengthening capabilities of stretching and rolling as strain modes. The properties achieved in the hardness and tensile tests clearly illustrate these differences, which are apparent across all variations of the thermomechanical processing and even across ageing temperatures. The reasoning for this is not fully clear but these differences in mechanical properties can be explained through microstructural analysis and supported by studies in literature.

From the data it became evident that the strain hardening achieved through stretching was significantly more than that of rolling seen in Tables 4.6, 4.7 and 4.15 as well as Figures 4.25 and 5.2. The deformation applied to these extruded strip samples in both rolling and stretching were essentially in plane strain and the calculated equivalent strain in both cases were equal, with an error of 0.04% for 4% strain and 0.07% for 8% strain.

A major difference in the two modalities is the means of this application of strain. During rolling, the applied stress acts only within the volume of material that is between the rolls and propagates along the sample, affecting the material in stages. However, in stretching, the deformation flow acts on the whole work piece simultaneously. This stress force in stretching is therefore distributed along the whole sample whilst the forces acting on the material in rolling are all applied to said region between the rolls at any given moment.

This distinction between the two strain modes is likely to have an effect on the grains becoming activated as a result of the critically resolved shear stress (CRSS). Grain rotation and grain boundary sliding occurring in the material during the two deformation modes will also be different, resulting in anisotropic hardening in the material. It is likely that this causes some of the strengthening achieved in the rolling samples to act in other directions than that tested through tensile testing in the extrusion direction. The rotated grains would align specific slip systems with the extrusion direction as well as grain boundaries in other directions also which would influence the mobility and multiplication of dislocations in the crystals. Another difference in the application of these two strain modes is the effect of friction on the surface of the sample which occurs during rolling but not in stretching.

These differences manifest as changes in crystallographic texture (rolling texture) (stretching texture) (show changes in the extrusion texture). The local and global homogeneity of deformation induced dislocation structures may also be altered. Reviewing the EBSD data, the texture of the stretch and rolled samples is characterised. Pole Figure Contour, Orientation, and Orientation Distribution Function (ODF) maps were used to identify the texture fibres formed and presented under differing processing conditions.

Post extrusion texture was a notable variable that contributed to the behaviour of the material and there was an evident cube texture presented in the material after this processing. The pole figures in Figure 5.5 display texture components as viewed from {001}, {110} and {111} of this Al-Mg-Si-Cu alloy in the as-extruded state.

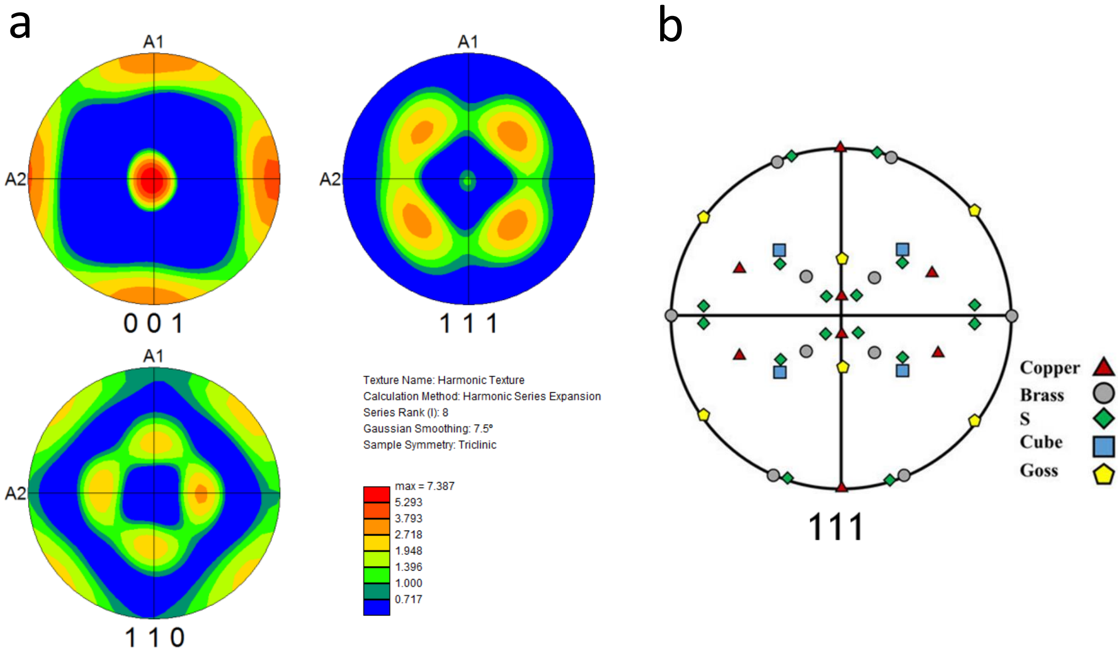

Figure 5.9. EBSD Pole Figure Map of an AA6xxx series alloy in the as-extruded state a) showing {001}, {110} and {111} b) the typical {111} texture for a rolled FCC material. (Hirsch, 1988)

Referring to the Figure 5.9 b) which describes the typical texture components for a rolled FCC material as they appear in {111} pole figures as well as 5 commonly found textures in this system all being defined by crystallographic orientation, obviously from the {111} pole figure is Figure 5.9 a), there is a strong cube {001}<100> texture component present in the specimen. Slight deviations from these grain orientations are present, illustrated as tailing and lower intensity of these textures around this ideal crystallographic orientation. The presence of other weaker textures fibres are registered in the mapping. The calculated 7.387 times random figure shows that there is a strong texture with preferred orientation of these grains relative to the sample reference frame.

Figure 5.10 shows an orientation map generated with the EBSD data illustrating grain orientations relative to the global specimen orientation. Volume fractions of the aforementioned typical texture components were calculated. In support of the pole figure description, a significant volume fraction, 0.274 of cube textured grains which are homogeneously distributed are visualised with small presence of other texture components.

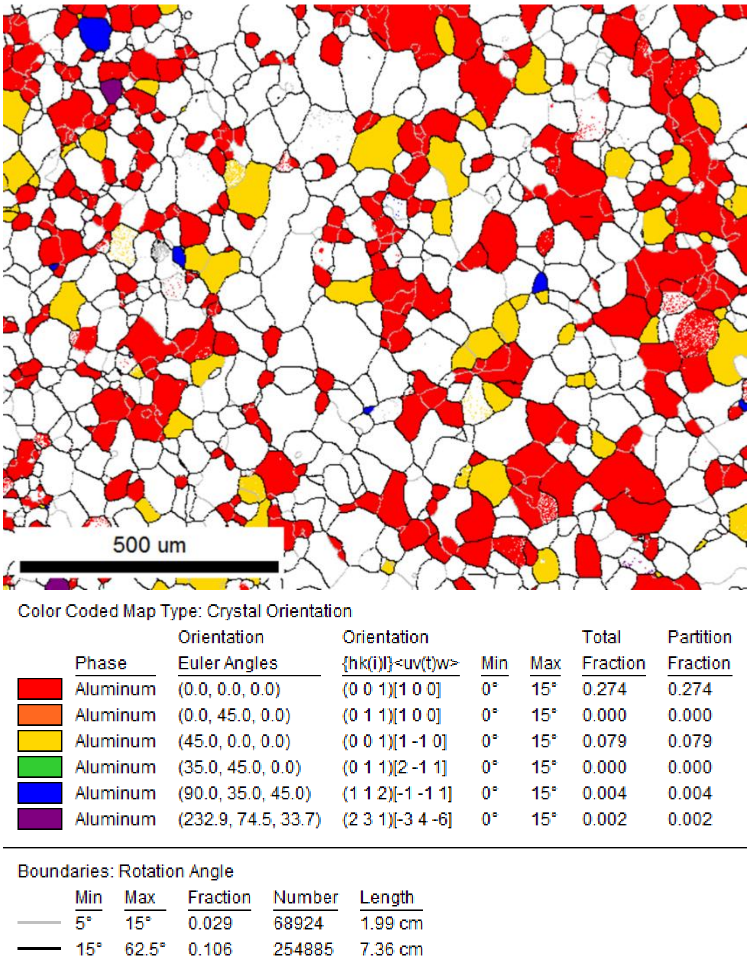

Color Coded Map Type: Crystal Orientation

	Phase	Orientation Euler Angles	Orientation {hk(i)l}<uv(t)w>	Min	Max	Total Fraction	Partition Fraction
🟥	Aluminum	(0.0, 0.0, 0.0)	(0 0 1)[1 0 0]	0°	15°	0.274	0.274
🟧	Aluminum	(0.0, 45.0, 0.0)	(0 1 1)[1 0 0]	0°	15°	0.000	0.000
🟨	Aluminum	(45.0, 0.0, 0.0)	(0 0 1)[1 -1 0]	0°	15°	0.079	0.079
🟩	Aluminum	(35.0, 45.0, 0.0)	(0 1 1)[2 -1 1]	0°	15°	0.000	0.000
🟦	Aluminum	(90.0, 35.0, 45.0)	(1 1 2)[-1 -1 1]	0°	15°	0.004	0.004
🟪	Aluminum	(232.9, 74.5, 33.7)	(2 3 1)[-3 4 -6]	0°	15°	0.002	0.002

Boundaries: Rotation Angle

	Min	Max	Fraction	Number	Length
—	5°	15°	0.029	68924	1.99 cm
—	15°	62.5°	0.106	254885	7.36 cm

Figure 5.10. EBSD Orientation Map of an AA6xxx series alloy in the as-extruded state.

Figure 5.11 gives the orientation distribution of the alloy in the as-extruded state as contour maps representations. They each square shows the different sections of the ϕ$_2$ angle of the Euler space between 0-90^o at 15^o step increments. Such maps containing more information than can be extracted from the previous maps alone. Maxima at specific regions of the orientation space correspond to peak-type components and complete or incomplete fibre components (Ray, 1986). As in the pole figure and orientation mappings, the main texture composition is cubic {001}<100>.

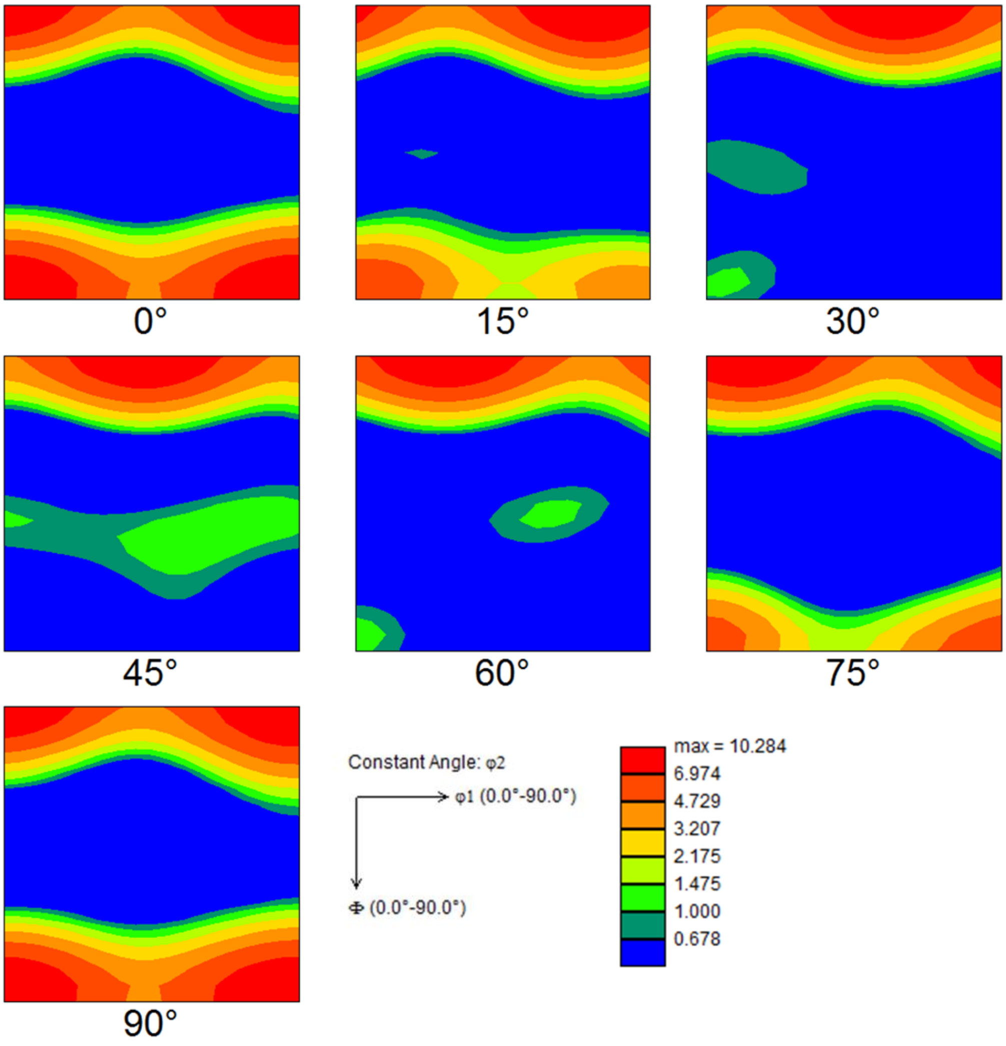

Figure 5.11. Crystallographic Orientation Distribution Map of an AA6xxx series alloy in the as-extruded state.

Changes in the strain hardening behaviour of the material in the T4 state can be attributed to changes in the texture's components upon application of these rolling and stretching deformation modes. Both strain modes seemed to produce anisotropic properties, acting in different preferred orientations.

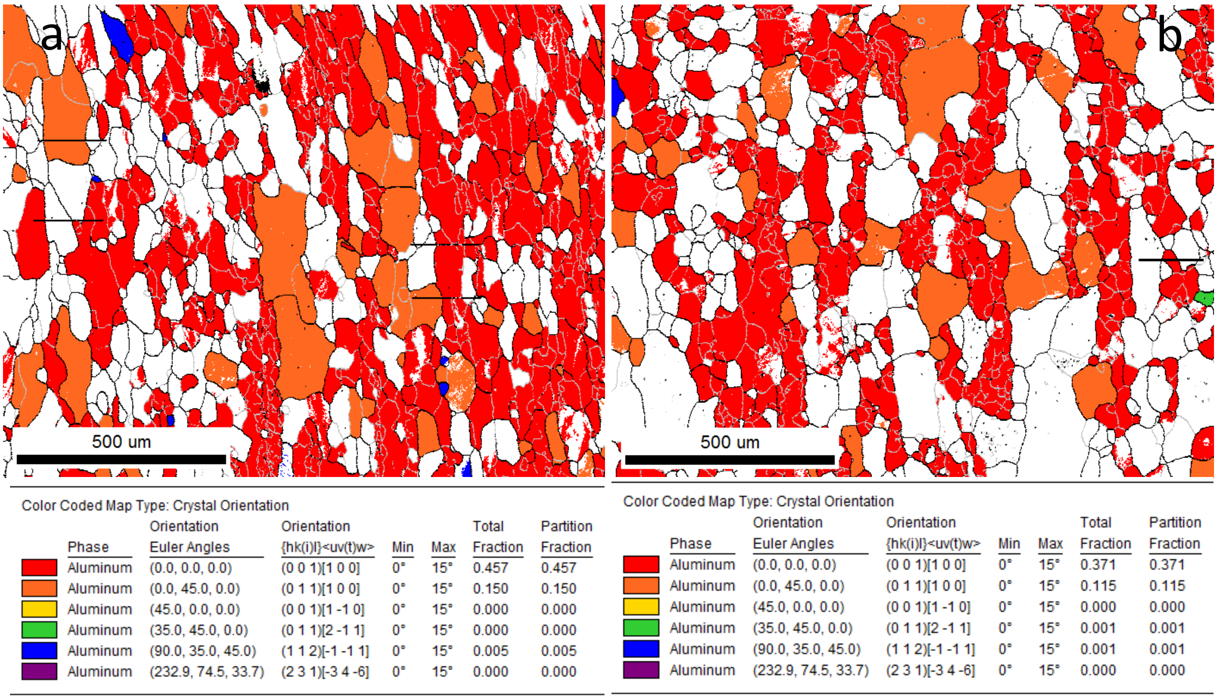

Color Coded Map Type: Crystal Orientation

	Phase	Orientation Euler Angles	Orientation {hk(i)l}<uv(t)w>	Min	Max	Total Fraction	Partition Fraction
🟥	Aluminum	(0.0, 0.0, 0.0)	(0 0 1)[1 0 0]	0°	15°	0.457	0.457
🟧	Aluminum	(0.0, 45.0, 0.0)	(0 1 1)[1 0 0]	0°	15°	0.150	0.150
🟨	Aluminum	(45.0, 0.0, 0.0)	(0 0 1)[1 -1 0]	0°	15°	0.000	0.000
🟩	Aluminum	(35.0, 45.0, 0.0)	(0 1 1)[2 -1 1]	0°	15°	0.000	0.000
🟦	Aluminum	(90.0, 35.0, 45.0)	(1 1 2)[-1 -1 1]	0°	15°	0.005	0.005
🟪	Aluminum	(232.9, 74.5, 33.7)	(2 3 1)[-3 4 -6]	0°	15°	0.000	0.000

Color Coded Map Type: Crystal Orientation

	Phase	Orientation Euler Angles	Orientation {hk(i)l}<uv(t)w>	Min	Max	Total Fraction	Partition Fraction
🟥	Aluminum	(0.0, 0.0, 0.0)	(0 0 1)[1 0 0]	0°	15°	0.371	0.371
🟧	Aluminum	(0.0, 45.0, 0.0)	(0 1 1)[1 0 0]	0°	15°	0.115	0.115
🟨	Aluminum	(45.0, 0.0, 0.0)	(0 0 1)[1 -1 0]	0°	15°	0.000	0.000
🟩	Aluminum	(35.0, 45.0, 0.0)	(0 1 1)[2 -1 1]	0°	15°	0.001	0.001
🟦	Aluminum	(90.0, 35.0, 45.0)	(1 1 2)[-1 -1 1]	0°	15°	0.001	0.001
🟪	Aluminum	(232.9, 74.5, 33.7)	(2 3 1)[-3 4 -6]	0°	15°	0.000	0.000

Figure 5.12. EBSD Orientation Map of an AA6xxx series alloy at 75x magnification a) after 8% stretch strain and b) 8% roll strain.

As illustrated in the misorientation maps in Figure 5.12 a) and b) the volume fraction of the cube {001}<100> texture component is significantly increased upon the straining of the material through both deformation modes as compared to the as-extruded state. From a measured volume fraction of 0.274 in the extruded state, these volume fractions are increased significantly to 0.457 and 0.371 in the stretch and roll samples respectively. The measured volume fraction of this cube {001}<100> texture is notably more enhanced in the material as a result to strain hardening by stretch deformation suggesting the cube texture enhanced hardening more in the material specimen.

In regard to the goss{110}<001> texture component which was also increased in volume fraction in both deformation modes suggesting it could also be a contributing factor to the strengthening achieved in the material through strain hardening. In the as extruded texture state, there was no recorded volume fractions of this texture orientation component, but this volume fraction is stated as 0.150 in the 8% stretch strained sample and 0.115 in the 8% roll strained sample. Again, there is a greater increase in the volume fraction of the 8% stretched strained sample indicating the specific anisotropy achieved by the stretch strain differing from that achieved through the roll strain of the same level, suggesting that this global texture had a greater efficacy in contributing to the overall hardening of the material.

Chakraborty et al in a 2020 study investigated the texture evolution of these common components and how they affected strengthening behaviours in FCC metals under plane strain deformation. It was found that with increasing deformation, the cube texture accumulated dislocation density faster than all other texture components which is also corroborated by the works of (Rajmohan, 2000) and (Kallend, 1984). This increased storage of dislocation density played a role during the strain hardening and in turn translated into being advantageous when tested mechanically through tensile testing.

Electromagnetic pulse technology (EMPT), a high-speed forming technique was used as an alternative strain mode through which the material specimen was plastically deformed, differing greatly, relative to the stretching and rolling strain modes which were considered simpler deformation modes. Through the use of an electromagnetic field, a Lorenz force was generated, which acted on the material (Li, 2014). As the material was formed through this force alone and at a much higher strain rate, there was no mechanical contact applied to the material and thus no frictional forces were present throughout the forming process (Jiang, 2014) . The associated generated force deformed the sample into the shape of a placed die, resulting in the desired final specimen profile. The microstructural evolution of the cross section as a result of this plastic deformation, which is rarely reported, showed significant differences to those formed through other techniques.

Due to this forming, a complicated deformation structure was created with a mixture of tensile and compressive strains apparent in the material in different regions. The majority of the forming took place at the two bending regions as can be seen in Figure 4.18, meaning that there were two mainly tensile regions and two mainly compressive regions. On the inside of the bends, there were more compressive forces acting on the material through forming and on the outside, there were tensile forces present. Across the thickness of the material, the forces acting on the sample varied greatly with shear and a mixture of compressive and tensile forces acting on the material. The major strengthening in the material was achieved locally concentrated in the compressive and tensile zones of the specimen as illustrated in Figures 4.18 – 4.20, suggesting that the forming forces acted preferentially in these areas. This differed greatly to the hardening behaviour of the rolling and stretching material which displayed uniformly distributed hardening across the bulk of the material.

There were noticeable differences in the strengthening capabilities of this strain mode as compared to the stretching and rolling modes. The properties achieved in hardness tests can be compared to those attained through the other deformation modes, with EMPT formed samples showing much greater hardening in the T4 states. This is a result of the much higher strain level applied through the samples, resulting in a greater strain hardening response due to elevated dislocation storage. This same trend was also illustrated by (Jin et al) in a 2021 study of Electromagnetic forming, where they found that as the effective strain of the EMF increased, the dislocation density and stored energy were resultantly increased. The dislocation structures formed also differed, being more developed, as dislocation bands, evidenced in Figure 4.10 and 4.11.

There were 2 forming energies used, 30kj and 40kj and as revealed in the hardness results of 4.18, the expected trend of, the greater the forming energy the greater the deformation achieved in the material, and also the higher the hardness of the final produced specimen. In the T4 state deformed using a 30kJ energy, at the bent region of the samples, the peak hardness achieved in the tensile zone was 106.12 and a peak hardness reading of 102.06 measured in the compressive region. In the T4 40kJ sample, the hardening achieved was greater, with a maximum hardness of 111.10 in the tensile zone and 108.57 in the compressive zone. Comparing this to the strengthening achieved in the other modes of plastic deformation, the highest hardness value achieved was at T4 with a strain of 8% roll which resulted in an averaged hardness reading of 72.8. As stated above, the deformation level in the EMPT samples were significantly higher, justifying this huge difference in strengthening achieved.

To investigate the preaging step of the TMA process with this complex strain mode, a preaging was applied to the material and the samples were subjected to the EMPT straining. The hardnesses achieved in the material were not reflective of the increased hardening seen in the simpler deformation modes. When looking at the sample strained with the 30kJ pulse energy after the preaging, the peak hardness reached in the tensile zone was 127.38 and 125.85 in the compressive area. This was increased in comparison to the T4 state but comparing this to the result achieved through the simpler modes where a strain of 8% stretch after the same preaging condition achieved a hardness of 134.3. This value in the stretched material was also still higher than the hardness achieved at the 40kJ EMPT straining energy which achieved a hardness of 128.59 and 127.45 in the tensile and compressive regions respectively.

Reasoning for this poor strengthening performance were that once the material was aged, it was stronger, meaning that the pre-described straining energies were no longer sufficient to cause the necessary full forming of the material to the die meaning that the effective strain achieved was far less in these cases and even less in the T6 state. ultimately, the degree of strain hardening was far less, with potentially lower dislocation storage than in the simpler straining modes.

Microstructural analysis from Figure 4.10 showed that in the specimen deformed at a forming voltage of 30kJ, the volume fraction of equiaxed grains was significantly decreased with grains being elongated along the extrusion direction, with a majority of these grains rotating to align with the 001 crystallographic direction after the applied strain. EBSD analysis of the EMPT formed specimen was conducted and shown in Figure 4.54, giving a more intuitive display of the effect of the strain mode on the AA6008 alloy across different regions along the thickness of the sample.

5.2.3 The Effect of Strain Path

Although the combinational strain modes of 4% stretch and 4% roll deformation level had an equivalent strain level of 8%, however, when compared to the 8% stretch strain level and the 8% roll strain level, the measured hardening in the combinational strain mode was higher, a 23.8% increment was recorded in this state. Quite unusual as the equivalent strain level of the combinational strain mode was the same as the strain mode of the stretch strain mode. Upon repeating the experiment, the same results held true.

This potentially suggests that the dislocations introduced through the differing strain modes exhibited some beneficial interactions that aided in the hardening of the specimen in a way that was not present in the simple singular deformation modes.

Another reasoning could be that there are mechanisms at play in the period between when the material is first deformed via stretching and then roll deformed. Potentially, natural ageing could be occurring in this period, especially with dislocations acting as nucleation sites for these small clusters. In turn, when the material is further deformed, the interactions and pinning of these dislocations would cause a greater storage of dislocations in the material leading to this enhanced tensile testing performance.

This mechanical behaviour was reversed in the material after the preaging step of the thermomechanical process was applied, when the effect of the cluster formation due to natural ageing was negated. As when the material is preaged, it is kinematically stabilised meaning that no or limited precipitation occurs when the material is laid at rest (Zhong, 2017)(Birol, 2005). Finer and more dispersed particles are then present in the material altering the response in the material. Comparing the tensile performance of the 8% stretch strain level to the combinational strain mode of 4% stretch and 4% roll level, the yield strength achieved in the latter was slightly lower, 9.4MPa, than the measured value of the former. Interestingly however, the Ultimate tensile strength achieved by this strain mode was higher, recorded at 375.9MPa as compared to 351.4MPa in the 8% stretch strained sample. This change in the behaviour proved that there was no advantageous effect of applying the combinational strain mode to the thermomechanical process to attain enhanced mechanical performance. In the same state however, the combinational strain mode of 8% stretch and 4% roll displayed the greatest hardening with a Yield strength of 349.8MPa and an ultimate tensile strength of 379.7MPa.

It is important to note that the highest combinational strain mode 8% stretch and 8% roll had an equivalent strain level of 16% which is 2 times higher than the highest strain level of the simpler singular strain modes and thus there can be no direct comparison between the strain hardening behaviours of the material.

In the final results where the entire thermomechanical process was applied and the combinational strain mode was used for the deformation step, the variance in the equivalent strain levels was further increased, further proving the ineffectiveness of the combinational strain mode in the process. The 8% stretch strain mode had an 8.2% greater yield strength than the combinational strain mode of 4% stretch and 4% roll.

There was no investigation where the roll deformation was applied before the stretch deformation. This strain path would have been of great interest and given insight into the effect of these strain modes on one another. The work in section 5.2.2 describes the differing textures generated through the different strain modes and thus the interplay between the strain modes and how they in turn affected the final texture formed could have resulted in an alternate strengthening performance in the material once the thermomechanical process as effected.

5.2.4 Hardening Behaviour

The Power-law stress strain relationship derives a metric that can be used to effectively describe the hardening behaviour of a material. The Hollomon equation given in equation 4.1 is used to calculate n, the work hardening coefficient/exponent. As the coefficient indicates the stress-strain relationship during uniform plastic deformation, the work hardening rate during plastic deformation can be assessed. The exponent is assessed from the yield strength and extends to the tensile strength. Work hardening coefficient values for metals fall in the range of 0.1-0.5, in an unprocessed state (Schaeffler, 2023).

Calculating the hardening exponent of the as-extruded material using its stress-strain flow chart gives a hardening exponent of 0.3341 from the yielding point of the curve. The work hardening exponent can be assessed from different parts of the curve to understand the variation in work hardening throughout the entirety of the tensile deformation. Key points on the graph to observe were the work hardening exponent from the 4% true strain point and the work hardening exponent from the 8% true strain point. These two points should in theory equate to work hardening coefficient of the strained materials as if they were de-loaded at this point, and reloaded, they would be expected to have been deformed to the same strain level. The strain hardening exponent measured at these points in the as extruded material were 0.3285 and 0.2768 for the 4% and 8% true strain level points respectively.

When compared to the hardening coefficients from the yield point of the 4% stretch strained material and the 8% stretch strained material, there is a great discrepancy in calculated values. For the 4% stretch strained material, the work hardening exponent value was recorded as 0.1887, whilst an exponent value of 0.1304 was given for the 8% stretch strained material. These values differed to those measured in the mechanical tensile test suggesting that there were some kinematical changes occurring in the material after the plastic deformation was applied in the t4 as extruded state. these changes can be attributed to the solute clusters formed during the natural ageing of the material discussed in section 5.1.1. These clusters interact with the dislocations applied through plastic straining either through stretching or rolling and increase the strength of the material, consequently reducing it's work hardenability. The presence of these dislocations promotes the precipitation of these solutes out of solution as the dislocations and vacancies introduced act as sites of nucleation for these solute particles. The indication of these parameters from these calculated exponent values are pivotal in identifying the phenomena at play, suggesting the role of these interactions between the defects in the matrix as opposed to the additive hardening or stacking of the different strengthening mechanisms.

These values of the hardening exponent are largely dependent on the microstructure of the alloy strip, including factors such as the grain sizes, second phase particles and dislocation densities (Tian, 2019). Obviously, as the processing of the material is increased, the work hardenability or the ability of the material to work harden decreases as the material becomes strengthened and its capacity for strengthening decreases. For this reason, the work hardening exponents in the preaged samples are significantly lower than those seen at T4.

From Figure 4.44 and 4.45 it can be seen that the m4 value which corresponded to the hardening exponent calculated from the 4% true strain level was generally higher than the value of the of the exponent calculated from the yielding point. These same effects were observed in the works of (Song, 2006)(Yan, 2006) where the n value for Al-Mg-Si-Cu sheets initially increased and then decreased under increasing strains in T4 states.

5.3 Preaging Enhanced Dislocation Density

The thermomechanical process comprised of heat treatments and applied mechanical plastic deformation gave rise to advantageous changes in the mechanical properties of the aluminium alloy. These mechanical enhancements were largely resultant from the interplay between dislocations and precipitates in-matrix. Changes in dislocation densities and precipitate morphology and dispersion as a result of plastic deformation and the preaging treatments highlighted and explained these changes in the material mechanical performance.

Preaging conditions played a significant role in the final ageing precipitation kinetics meaning meticulous modifications to these conditions achieved varying final results. The preaging conditions discussed in section 5.1.2, varying in temperature and time gave varying responses aiding in the characterisation of these microstructural effects.

5.3.1 Dislocation Structure in Stretching without Preaging

In the starting, as-extruded alloy, the treatment of age hardening alone produced a significantly larger increase in mechanical properties than that produced through the cold working techniques alone. This can be described as a result of the low strain levels of 4 and 8% rolling and stretching that were applied to the material. The alloy material used also had a relatively low work hardening response.

Deformation induced dislocation structures were found present in the material through EBSD analysis as a result of these low mechanical strains. Presenting as measured misorientations between kernels and their local neighbours in the regions where dislocation densities were increased, these structures could be identified.

As discussed, the low strain levels meant that dislocation structure evolution was not as significant as seen in heavily cold rolled and other highly deformed material through various other techniques. Structures such as dislocation cells, sub-grains and forests were not evident in the matrix through the EBSD analytical technique. Primarily dislocation tangles were found in the deformed material with their number fractions being increased with increasing strain levels.

Calculated dislocation densities in the current study were found to be in of the orders of magnitudes of x10^{12}/m^2 whereas in other heavily deformed materials these densities could fall in ranges as high as between x10^{14} - x10^{15}/m^2 seen in the works of Wang et al.

In the state where the material was strain without preaging treatment, there were less precipitates present in the matrix as well as these precipitates being far less developed. The main precipitates formed were atomic clusters through the natural ageing of the material at room temperature, controlled by the driving forced introduced by the super saturated solid solution status. These atomic clusters aided in the storage of dislocations throughout the straining of the material but the degree to which this occurred was not overwhelming in comparison to the preaged and deformed material. The dislocation densities present in the as-extruded material were relatively low with an average number of 14.52 x10^{12}/m^2. With increasing strain, these dislocations densities were noticeably increased with differences being shown between the deformation modes. These density changes are illustrated in Fig 5.13.

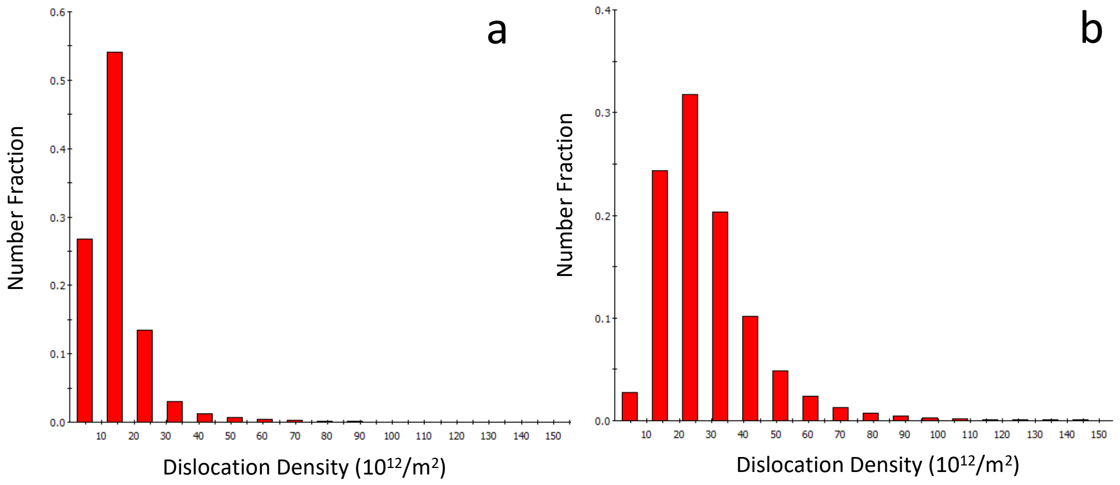

Figure 5.13. measured dislocation density vs volume fraction in a 6xxx series aluminium alloy in the a) as extruded state and b) 8% stretch strained.

Dislocation densities in the T4 – as extruded sample showed generally lower densities of dislocations whilst in the T4 and 8% stretch deformed sample, dislocation densities were higher and more spread in regard to volume fractions. The average dislocation density measured in this deformed sample was 28.67 x10^{12}/m^2 which is double that measured in the as-extruded state.

Dislocation density calculations in KAM maps garnered information about dislocation presence in different deformed areas with levels of low misorientations (0-1 degrees). GND densities could then be derived using equation 5.1.

$$\rho = \frac{\delta\theta}{Db} \qquad (5.1)$$

Where δ is a material constant of 3.0 for grain boundaries of varied characteristics, θ is the average calculated KAM value, D is the step size used in acquisition of the EBSD KAM map and b is the burgers vector.

The stored strain energy per unit volume can also be computed using the following equation.

$$E = \frac{1}{2}G\rho b^2$$

Where G is the shear modulus of aluminium (26.1 GPa), p is the dislocation density obtained in equation 5.1, and b is the burgers vector.

As seen in the KAM maps of Figures 4.48, 4.49 and 4.50 corresponding to the as extruded, 4% stretching and 8% stretching respectively, there are stark variations in the arrangements and distributions of these dislocations. No apparent structures appear to be formed in the grains of the as extruded sample. There are misorientations present however that are characterised as being caused by naturally occurring dislocations in polycrystals as well as some generated through the extrusion processing into alloy strips. These dislocations are fairly homogeneously distributed across the grains and no distinctive substructures can be observed.

In the 4% stretch strained material where the density of dislocations is significantly increased, to maintain strain compatibility across the variously orientated grains (Muransky, 2019)(Ashby, 1970), these geometrically necessary dislocations are heterogeneously spread throughout the microstructure. These arrangements of the GNDs are the most energetically favourable configurations in the system (Kuhlmann-Wilsdorf, 1989,1991). GND boundaries and deformation bands are thus generated inside of the grains as can be identified in the KAM maps of Figure 4.49. These deformation bands appear as green lines spread across the grains, typically generating, and terminating at the terminals of the grains. As a result of the CRSS associated with slip, these bands are orientated at around 45 degrees relative to the extrusion direction.

Similar structures are presented in the KAM maps of the 8% stretch deformed material with these GNDs also piling up to form deformation bands non uniformly across the crystals seen in Figure 4.50. The misorientation level in this sample is far higher as a result of the increased dislocation density. Bands formed are again orientated at around 45 degrees. Due to the pile up of a greater number fraction of dislocations, these bands appear to be more defined lines with some grains displaying a greater number of deformation lines than in the lower strained material.

Structures formed in strained material where ε_p = 7.8% and 13.9% were uncovered using EBSD corroborate this with the presence of GND boundaries formed which are stored in a heterogeneous arrangement (Muransky, 2019). These boundaries are found in alloys with high stacking fault energies with cellular dislocation structures being formed, displaying regions with relatively lower dislocations densities surrounded by these dislocation walls (Bay, 1992)(Morri, 1985). It is also evident that the dislocation accumulation is approximately proportional to the level of imparted strain, showing intergranular variations in density and distribution (Fleck, 2002)(Zecevic, 2105).

5.3.2 Dislocation Structure in Stretching with Preaging

As well as individually causing strengthening in the material, there was a significant degree of interactions between the dislocations and precipitates present in the material matrix that led to the overall increase in mechanical properties as well as the storage of dislocations.

In the as-extruded condition, the material subjected to a short pre-ageing, either at 150C or 170C, displayed significant microstructural changes as discussed in section 5.1. Changes in precipitation meant that upon cold working, significantly more barriers to motion for the dislocations were introduced. In comparison to the T4 state, where only a few dislocations were present, introduced through extrusion of the alloy sheets and mainly atomic clusters nucleating out of the solution, in the preaged state the majority of the solutes were precipitated out into the matrix as GP zones and β'' phases. These obviously would interact with the dislocations in a different manner.

As the atomic clusters formed through natural ageing were quite fine, it is assumed that they would be sheared easily by the dislocations gliding past them (Keyhani, 2018). They are less capable of trapping dislocations and thus a majority of these dislocations would pass into the grain boundaries where they are annihilated. The clusters however do contribute to slowing the motion of these dislocations hence why there is a noticeable increase in the storage of these dislocations in the T4 state.

To a greater extent, the spherical GP zones and β'' precipitates formed, which are the main constituents of the precipitation sequence present in the preaging step, create great disturbances to the motion of these dislocation. A greater number of dislocations are believed to be trapped by these early-stage precipitates of the artificial ageing (Yang, 2021). The storage of these dislocations causes perpetually more barriers to dislocation motion and may very well act as Frank-Read sources, further multiplying and generating dislocations in the bulk of the grains (Dieter, 1988). This type of dislocation generation consequently means the number fractions of dislocations stored after the deformation is concluded are significantly greater resulting in largely increased measured dislocation densities in these preaged samples.

Overall, 5 ageing conditions were considered to investigate this effect of preaging on the average dislocation density measured and to justify its efficacy in strengthening in the specific alloy system through the involvement of a preaging step in the thermomechanical set up.

For the 150^{o} C preaging temperature the three durations considered were at 3 hours, 8 hours, and 24 hours, which corresponded to different stages of the ageing process and thus the precipitation levels at each were different. At the 150^{o} C/3h state, the material was only aged to a considerably low ageing condition reflected in the low mechanical properties measured in tensile testing. The 150^{o} C/8h condition was still considered to be fairly underaged but at a more developed stage of the precipitation sequence. The final ageing condition was the 150^{o} C/24h condition which discovered as the half-peak preaging condition discussed in section 5.1. The effect of each of these stages of precipitation were considered in regard to their interactions with and effect on the storage of dislocations introduced in the deformation step of the thermomechanical process.

EBSD analysis on the 150° C preaging conditions highlighted key differences in the multiplication of dislocation number fractions in the material. KAM maps seen in Figure 4.57 a) and b) illustrate these differences clearly. As compared to the T4 sample deformed to 8% stretching the dislocation density in these samples are considerably higher across all preaging conditions.

The dislocation densities, calculated in the same way as the T4 samples are charted in Figure 5.14

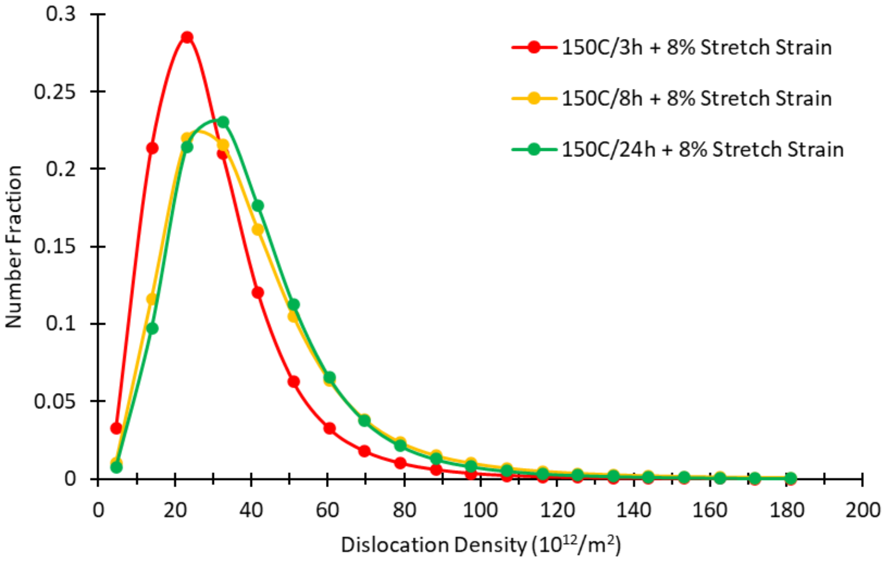

Figure 5.14. Dislocation density versus Number fraction chart from EBSD GND of a 6xxx series aluminium alloy.

The density number fractions of each of these preaging conditions can be compared. The dislocation density stored in the material at the halfway aged condition are the highest of all the conditions. The average dislocation density for this 150° C/24h condition was 40.35 $x10^{12}/m^2$ which is almost a 3-fold increase as compared to the starting condition and a 41% increase compared to the T4 and 8% stretched deformed sample, directly showing the effect of the presence of these precipitates present at this half peak condition.

The average dislocation densities calculated for the 150° C/3h and 150° C/8h preaging conditions were 30.44 $x10^{12}/m^2$ and 39.59 $x10^{12}/m^2$ respectively. Comparing the dislocation densities for the 150° C/8h and 150° C/24h preaging conditions, there was a slight difference in the dislocations densities meaning that the point at which the material is preaged is not extremely critical above certain time, as in the 150° C/3h preaging condition, the storage of dislocations is not significantly increased as compared to the T4 and 8% stretch deformed sample, 30.44 $x10^{12}/m^2$ and 28.67 $x10^{12}/m^2$. From GND analysis however, the dislocation structures formed at each of these stages show apparent differences in arrangement. After 3 hours of artificial ageing at 150° C, there are primarily GP zones and a lower number fraction of other more developed precipitates as compared to the other more aged conditions, this suggests that the microstructure in this earlier stage of precipitation is more alike to the T4 naturally aged condition. These early-stage precipitation does not have the same effect of storing dislocations as they are smaller and or less frequently distributed across the crystals. Hence there is a critical range for the observed effects of increased dislocation storage in the matrix.

The same effect can be seen in the two 170° C preaging conditions selected, where there is a slight change in this increase in dislocation density, however the half peak point shows a slightly greater response. A similar difference in the dislocation structures formed in the two states can also be seen in the KAM maps generated.

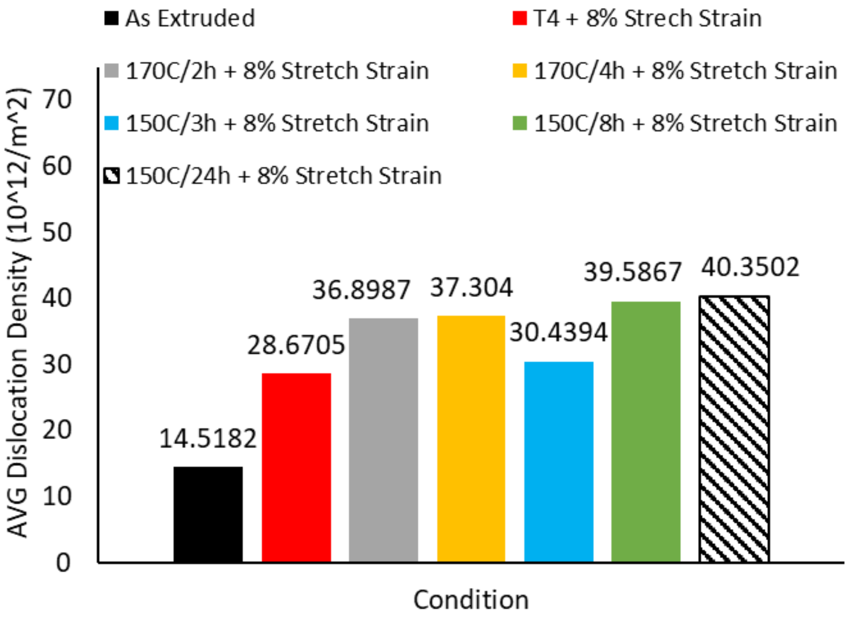

Figure 5.15. Average dislocation density for varied thermomechanical processing conditions.

In Figure 5.15, the 170° C/4h preaging condition which corresponds to the half peak point at 170° C gives an average dislocation density of 37.30 x10^{12}/m^2 whilst the 170° C/2h condition gives an average density of 36.90 x10^{12}/m^2. This ageing at 170° C for 2 hours corresponds to the ageing state of the 150° C/8h preaging condition which is close to the half peak condition but has experienced considerable ageing. Interestingly, the 150° C conditions exhibit a greater storing capacity of dislocations than the 170° C preaging conditions.

Although the densities of dislocations between the preaging conditions of each temperature are virtually the same, i.e. 150° C/8h and 150° C/24h having very similar number fractions of dislocations, the structures of dislocations seem to differ slightly. The appearance of dislocation bands in Figure 4.57 illustrates these slight differences. In Figure 4.57 (a), the dislocation bands appear to be straighter lines at 45-degree angles to the extrusion direction. Meanwhile the deformation structures in Figure 4.57 (b), correlating to the 150° C/24h + 8% stretch strain present as curved and more interlaced.

5.3.3 Interaction between Precipitates and Dislocations During Stretching

Major differences in the material behaviour and microstructure were identified when the pre-ageing was added to the thermomechanical sequence. The combination of pre-ageing and deformation produced apparent positive impact on the mechanical properties after final ageing, in particular at the strain level of 8% by stretching. With 8% stretching after pre-ageing, an increase in the yield strength from 309 MPa to 357MPa was observed (Table 4.15), which is a striking increase. This may be explained by the pre-ageing enhanced dislocation density during deformation as shown in Figure 5.15, which could promote heterogeneous nucleation and possibly increase the number density of precipitates in the final ageing treatment. It is reasonable to assume that the interactions between dislocations and the solute clusters and GP zones formed in the pre-ageing may play a strong role in dislocation multiplication and pinning during deformation.

An investigation by Li et al in 2021 into the effect of pre-stretch on the precipitation behaviour of an aluminium alloy found that pre-stretching the material to strains of 0%, 5%, 10% and 15% before ageing caused an increase in the material yield strength, with the peak YS values seen at 10% pre-strain. Interestingly, this study found that the 150^{o} C ageing temperature attained a higher yield strength than the 170^{o} C temperature with recorded values of 387.5 MPa and 376.8 MPa respectively, whilst the undeformed and aged sample had a yield strength value of 319.2 MPa. It was found using differential scanning calorimetry (DSC) and TEM that the high densities of dislocations generated through the deformation contributed to the acceleration of the precipitation in the alloy and the precipitation of GP zones and other phases are shifted to lower temperatures.

From the analysis of the TEM micrographs, it was discovered that the precipitate phases preferentially nucleated on the dislocations, meanwhile the high deformation energy created by the stretching aided in decreasing nucleation barriers (Gable, 2001). This suggests that in the final ageing, the increased dislocation density formed through the first ageing and deformation step encourage and stimulate further development of precipitation that endues the increase in the mechanical response of material in the fully processed material.

Experiments were conducted on the effect of stretching and final ageing with the preaging step removed. It was found that the mechanical properties were increased compared to the T6 aged material, but the strengths reached were not as high as those achieved with the preaging included. It was concluded that the presence of this preaging step in the thermomechanical process significantly enhanced the mechanical properties of the alloy. The nucleation sites, vacancies, and dislocations, generated by the preaging step enhanced precipitation in the final ageing.

Transmission electron microscopy was conducted in selected pre-ageing and deformation conditions with the assistance of Drs Raluca Negrea and Chamini Mendis to determine the, structure, size and distribution of precipitates and dislocation structures in the aluminium matrix following pre ageing and subsequent deformation for 2 different pre ageing conditions.

These investigations done with the electron beam parallel to <001> direction of aluminium along with the dislocation structures using Low angle annular dark field imaging technique. This specific orientation of the grains allowed a clear view of the relevant fine scaled details such as the precipitates and dislocations within the microstructure.

The acquired selected area electron diffraction (SAED) patterns aided in analysis by revealing the reflections arising from the aluminium matrix. Consequently, very weak diffraction features were detected (marked with a xxx circle in the image), signifying the presence of small precipitates which were formed in the preaging step of the thermomechanical process.

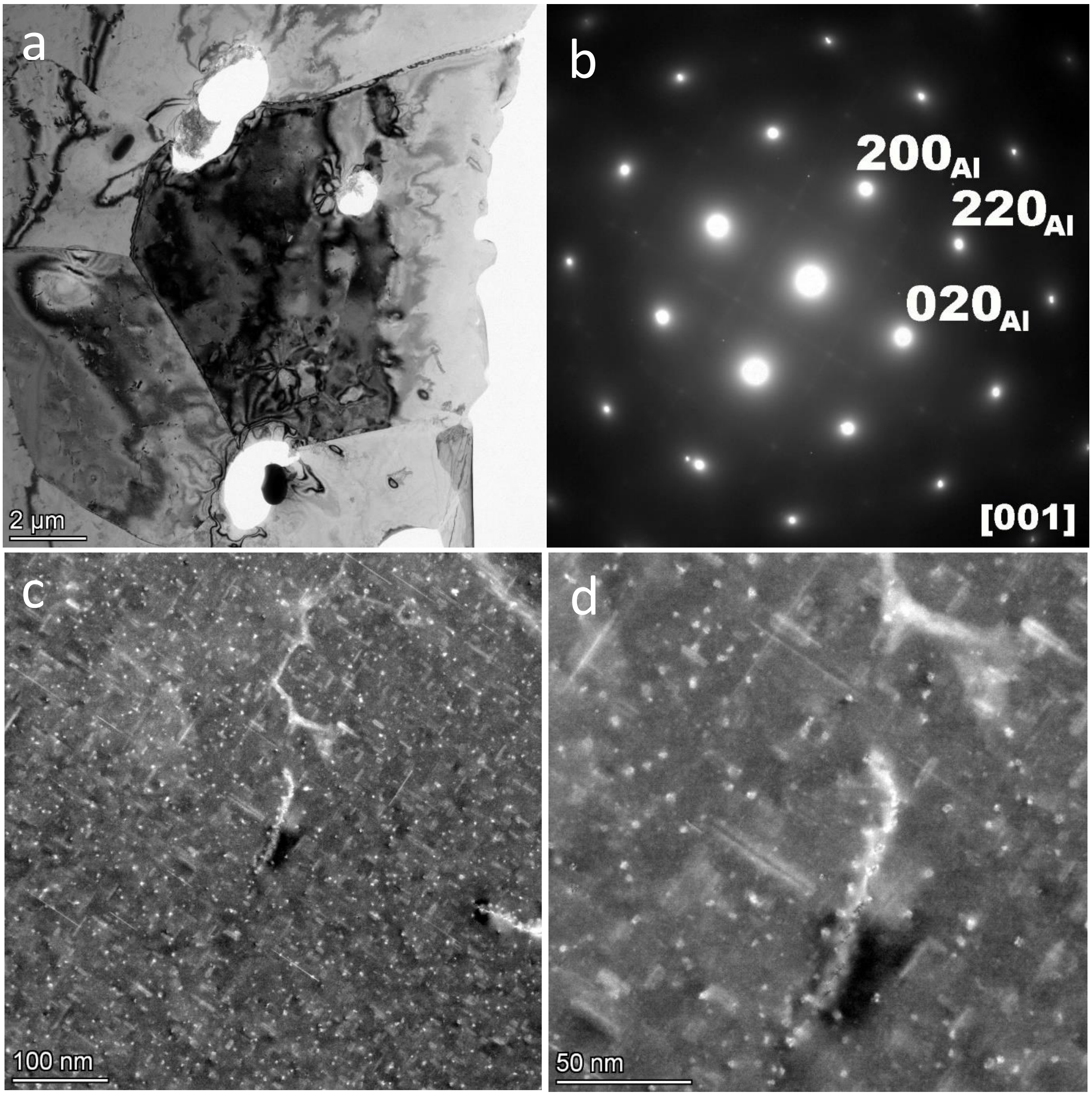

Figure 5.16. (a) BF – TEM image of the sample 150^{o}C/8h showing the grain tilted in [100] zone axis to study the precipitates inside Al matrix; (b) the SAED pattern acquired on the dark grain from the image (a) showing the main reflections corresponding to Al matrix and fade

reflections originate from the small and long precipitates; (c) and (d) LAADF – STEM images at different magnifications showing the presence of precipitates and dislocations in the Al matrix.

From Figure 5.16 (c), there is a large density of very fine scaled precipitates distributed uniformly, it is likely that the precipitates formed in these stages cause pinning and storage of the dislocations applied in the deformation stage that increases the dislocation density and presents the multiplication effect. The precipitates are expected to be early-stage precipitates and are likely to be GP zones and needle like precipitates, a few rod-like precipitates are also seen in the matrix. There is no plastic deformation applied to the material at this stage, as expected there are a very few dislocations presenting in the crystals left over from extrusion. Interesting to note, in Figure 5.16 (d), there are precipitates nucleating on the dislocation showing that these dislocations are acting as preferential nucleating sites for the particles during ageing.

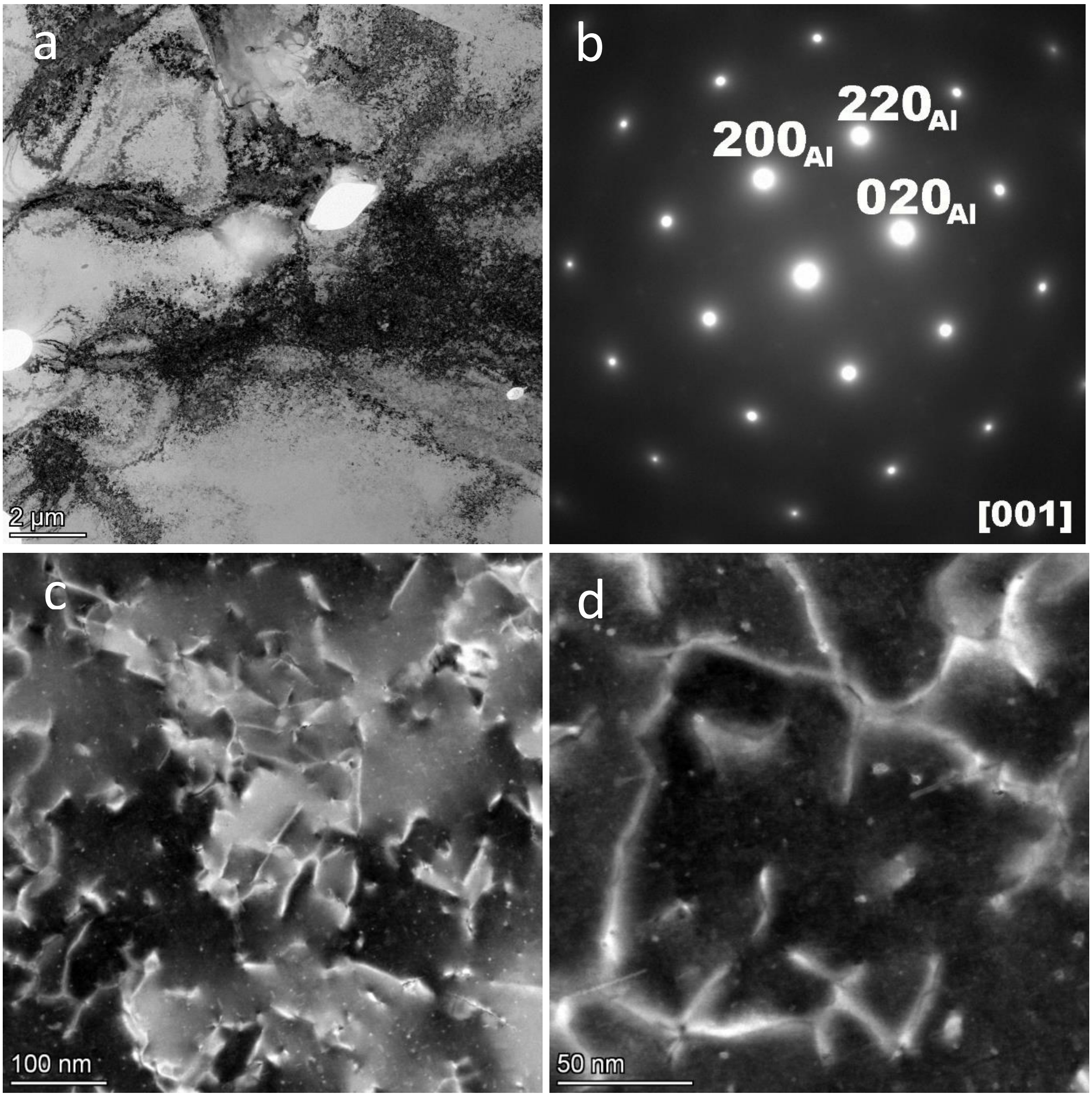

Figure 5.17. (a) BF – TEM image of the sample 150^{o}C/8h – 8% showing the grain tilted in [100] zone axis to study the precipitates inside Al matrix; (b) the SAED pattern acquired on the dark grain from the image (a) showing the main reflections corresponding to Al matrix and fade reflections originate from the small precipitates; (c) and (d) LAADF - STEM images at different magnifications showing the presence of precipitates and dislocations in the Al matrix.

Following the application of stretch deformation to a strain level of 8%, there is a stark increase in the number of dislocations identified in the material, Figure 5.17 (c). This conforms with the information as seen in the EBSD KAM map of Figure 4.57, the dislocation density is considerably increased.

The volume fraction of precipitate particles in the matrix has decreased significantly when compared to the samples subjected only to preaging. This is likely to be a result of the mobile dislocations, destroying or cutting some of the smaller and larger precipitates that were present in the solely preaged stage. Dislocations appear to be pinned by the remaining precipitates, forming dislocation-precipitate complexes, Figure 5.17 (d) also shows the entanglement of dislocations. The interactions between these complexes and the precipitates formed in the final aging step would likely cause the advantageous change in the final material properties.

Another two conditions were of samples which had the preage treatment of 150^o C/24h applied and condition that was stretched to a strain level of 8% after the ageing step. As this sample was aged to a different stage of the precipitation sequence, the interactions between the microstructural features are described and compared with those of the previous preaging condition.

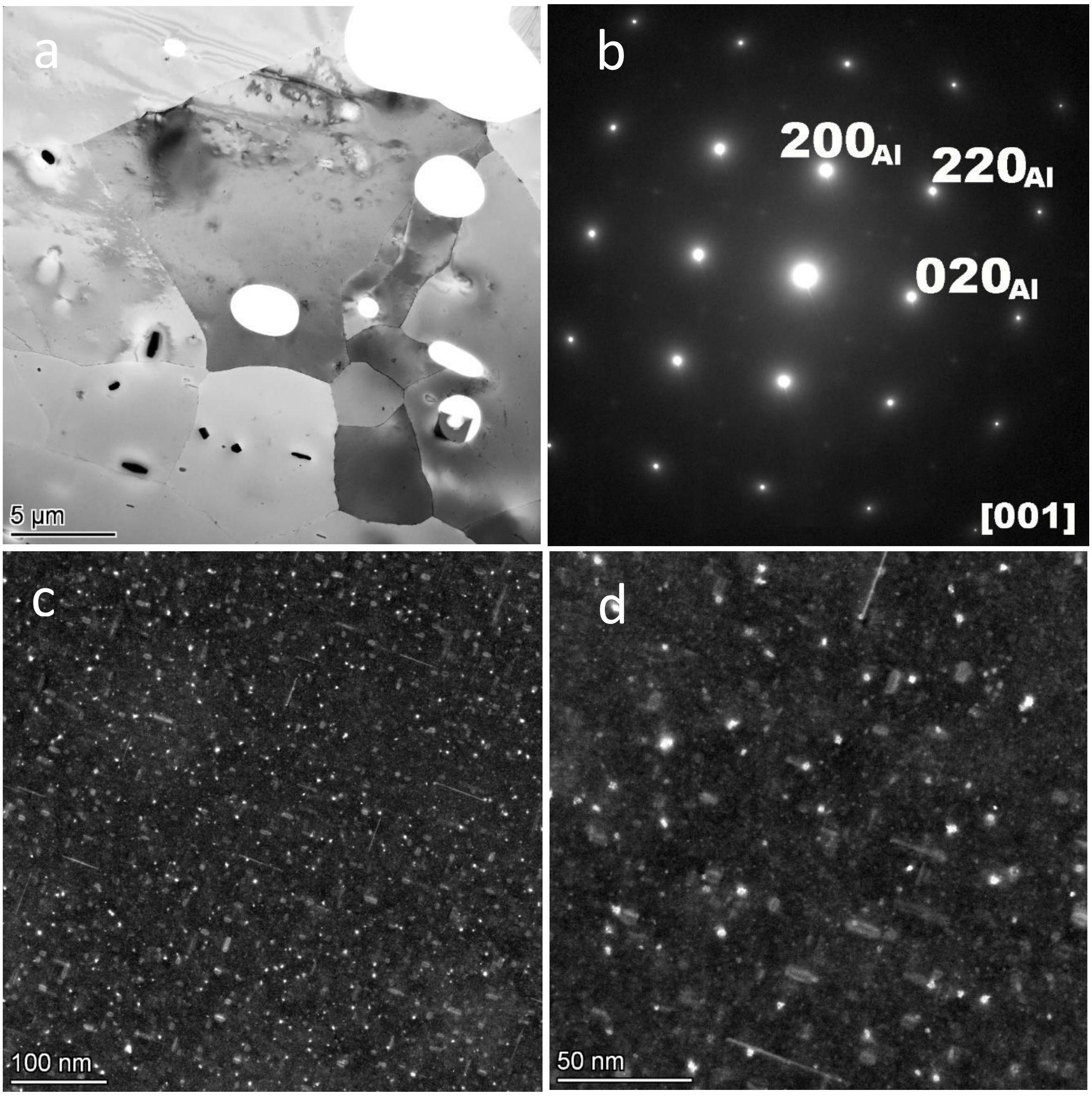

Figure 5.18. (a) BF – TEM image of the sample 150°C/24h showing the grain tilted in [100] zone axis to study the precipitates inside Al matrix; (b) the SAED pattern acquired on the dark grain from the image (a) showing the main reflections corresponding to Al matrix and fade reflections originate from the small precipitates; (c) and (d) LAADF - STEM images at different magnifications showing the presence of precipitates and dislocations in the Al matrix.

After a preaging of 150° C for 24 hours, the material was in a further stage of hardening as confirmed by the hardness data of the Table 4.1. Since precipitation hardening was the main strengthening mechanism of this preaged sample, it can be also assumed that the precipitates were either greater in number or further along the precipitation sequence. From Figure 5.18 (c) the precipitation density is not significantly greater than that seen in the lesser aged state of 150° C for 8 hours seen in Figure 5.16 (c), this implies and leads to the belief that the precipitate particles seen in this sample are more developed than those seen in Figure 5.16 meaning there are likely relatively more needles and rod like precipitate particles as a volume fraction and less of GP zones. There are more defined spots in the SAED pattern resulting from the small precipitates visible in Figure 5.18 (d).

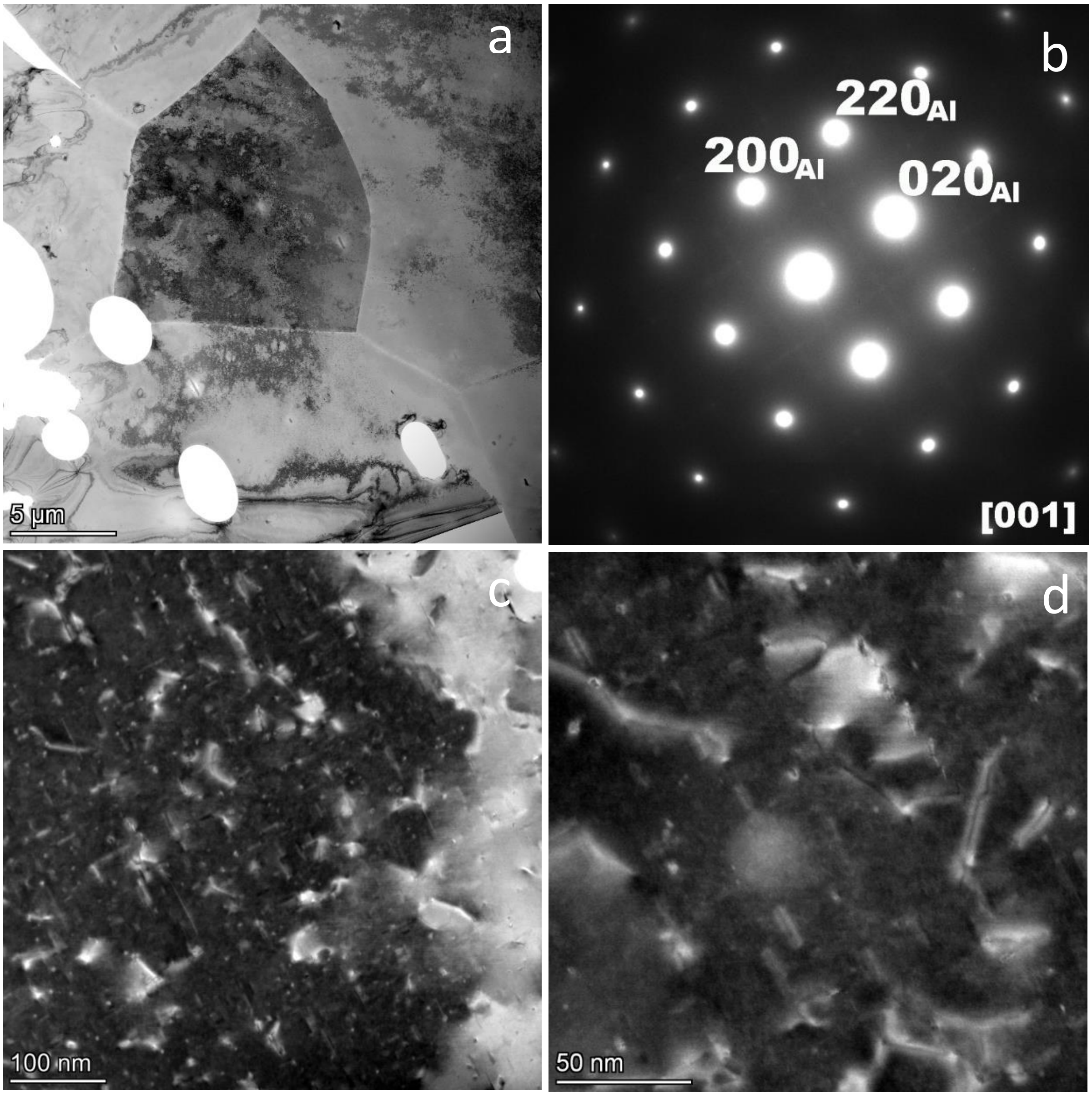

Figure 5.19. (a) BF – TEM image of the sample 150^{o}C/24h – 8% showing the grain tilted in [100] zone axis to study the precipitates inside Al matrix; (b) the SAED pattern acquired on the dark grain from the image (a) showing the main reflections corresponding to Al matrix and fade reflections originate from the small precipitates; (c) and (d) LAADF - STEM images at different magnifications showing the presence of precipitates and dislocations in the Al matrix.

Once the stretch strain is applied to the material in this preaged state, there is again a large increase in the dislocation number density, Figure 5.19 (d). These dislocations are different in appearance to those seen in Figure 5.17 which coincides with the results from the EBSD KAM analysis. It appears that the precipitates structures and arrangement in the two preaging conditions are different and this results in the interactions between these precipitates and applied dislocations also being different. As a result, the dislocation-precipitate complexes formed in this state differ to those seen in the alternate state.

The volume fraction of precipitates seen in Figure 5.19 (c) decreased relative to Figure 5.18, before the application of strain but this decrease is not as much as seen in the previous, lower preaging state. This could have a significant effect on the precipitation evolution in the final aging step leading to the differing property response.

Looking at the ageing kinetics, the 150C/8h is not yet at the halfway hardening point which yielded the enhanced hardening results. However, from the curve in Figure 4.12 there is still considerable hardening of the material and thus is it apparent that it is quite far along the precipitation sequence. As a result, there is a significant number of precipitates formed at this stage of preaging. When compared to the other ageing condition of 150/24h which is at the halfway hardening point described in section 4.3.1. There is also a high density of dislocations in the crystal matrix but as the material is still in the underaged state the majority of precipitates are fine and round as well as needle like precipitates. The precipitate assortment in the two conditions is different, however.

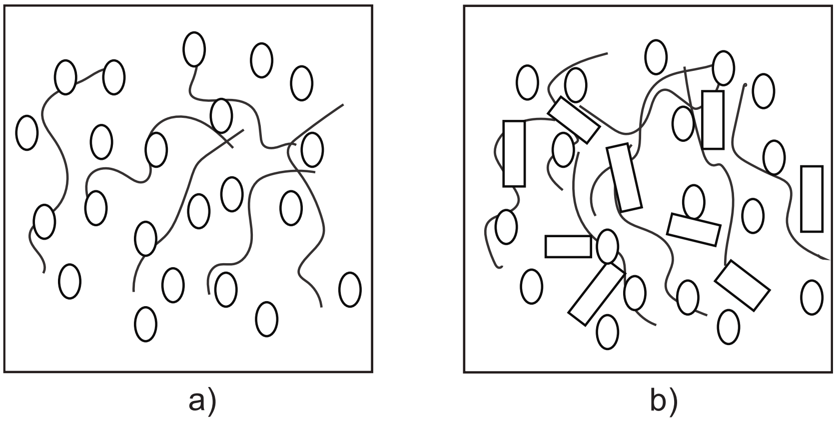

Figure 5.20. Schematic illustrating precipitate and dislocation structures present in thermomechanically processed aluminium alloys with spherical particles representing finer precipitates, rectangular particles representing rod like precipitates and curved lines representing dislocation lines. (a) 150^{o}C/8h condition (b) 150^{o}C/24h condition.

Following the application of the stretch deformation, in the material that had been aged at 150C for 8h prior, there is a significant number of dislocations. The precipitates formed in the preaging stage slow down dislocation slip as well as pinning and immobilising them. Cross referencing this back to the KAM maps in Figure 4.57, it is evident that the dislocation structures formed in the earlier ageing stages differ from those formed in the latter stages and this has a consequential effect of altering the kinetics of the final ageing step and resultantly the final mechanical properties achieved. In these KAM maps of Figure 4.57, the density and structures of dislocations formed in the different preaging stages are noticeably different and would raise different material behaviour in the re-aging step. From the mechanical properties given by tensile testing, it is apparent that a lower preaging condition gives a better strength-ductility trade off whilst a higher preaging state gives better strengthening in the final product.

In a lower preaging state, mostly finer, less developed precipitate particles are present in the microstructure. These precipitates are more easily cut by the passing dislocations but act as enough of a barrier to dislocation motion to store them as sessile dislocations in the matrix. The lack of these precipitates in the T4 state means that the dislocations move far more freely and are annihilated at the grain boundaries explaining the lower density of dislocations in the EBSD KAM maps of these states. These stored dislocations form structures and features in the microstructure that are complex. When they are aged, these structures interact with the final ageing precipitates, some of which are nucleating along the dislocation lines, this interaction with these specific structures causes there to be an improved ductility in the material.

In the higher preaging state, a mixture of finer particles and coarser/developed precipitates are nucleated. This is made evident by the similar density of precipitate particles discovered in the matrix at both stages of the preaging step, but the different mechanical properties. Some of these precipitates are efficient at trapping and storing these dislocations in the grains of the crystals, whilst the more developed precipitates may interact with the dislocations in a different way, some potentially forming Orowan loops. When the final ageing is applied, the final ageing precipitates formed are more developed and optimal for the enhanced properties. The precipitate-dislocation structures formed act prior act as Frank-Read sources to generate and multiply the dislocations, accommodating further slip.

It is possible that the enhanced hardness achieved is not at the point of fully peak aged, as due to the final ageing, the dislocation density is largely reduced or too much coarsening of the preaging precipitates is occurring. Thus, a compromise/ equilibrium is reached. Final ageing also regains some of the materials ductility.

5.4 Optimal aDA Conditions

Enhanced mechanical behaviour through a range of low strain thermomechanical procedures displayed interesting changes in the material response. Variations in final mechanical properties clearly illustrated the importance of parameter control throughout processing (Mortsell, 2019). Microstructural alterations throughout the preaging, deformation and final ageing steps could be potentially carefully selected to achieve optimal strength increases in the fully processed alloy (aDA).

Ageing temperature utilised in the 3-step thermomechanical process either in the preaging or final ageing elicited different precipitation kinematics which is corroborated in the works of (Zi, 2019). Ageing temperatures of 150° C and 170° C were used for ageing experiments. Significant increases in mechanical properties can be observed utilising condition relative to the T6 state. Application of the thermomechanical process also significantly reduced the heating times which would, in and industrial manufacturing setting, reduce costs if aDA were incorporated as part of the production process.

The preaging step proved pivotal in boosting dislocation generation in the deformation step. These complexes formed through precipitation-dislocation interactions when measured through tensile testing promoted notable increases in strength relative to the preaged and T6 measured mechanical yield and ultimate strength values.

In the final step where the material was aged again till peak hardness, the precipitate-dislocation complexes in the material microstructure played a crucial part in furthering the strength increase of the material. In the current study it was found that upon application of this further ageing step, increases in mechanical strength were achieved, far surpassing that of the material in the T6 state. from the work of Murayama, it is understood that these complexes formed in the initial stages helped in the final ageing precipitation nucleation. From the results of the study, it would seem that these spherical GP zones and dislocations as well as the vacancies associated with these defects formed in the preaging served as nucleation sites for the β'' precipitates which would develop in the subsequent artificial ageing where the material was aged at 175° C for 10 hours.

These particles formed in the preaging step vary to those formed in the natural ageing step, explaining the lack of the phenomenon in material aged at room temperature. Using a 3DAP atom probe, to investigate these particles displayed clear differences in the particles formed at different ageing conditions (Murayama, 1999). The effects of natural ageing in the material produced a reduction in the number density of β'' precipitates, whereas artificial ageing at 70° C caused an increase in the number fraction of these particles, this suggests the co clusters generated through natural ageing were of detriment to the generation of the most effective strengthening β'' phase in the alloy system where as the preaging promoted it.

Work conducted by Lai et al, 2020 showed the structures of dislocation induced precipitates formed in al-mg-si alloys. it was found that the precipitation of artificial ageing following deformation heterogeneously distributed across the crystal, forming sophisticated precipitation microstructure. It was found that the dislocation induced complex precipitates were short ranged ordered relative to polycrystalline precipitates and multiphase composite precipitates, suggesting formation of these precipitate-dislocation complexes are mainly formed due to a high nucleation rate and rapid growth parallel to the dislocation lines.

Comparing the achieved properties of fully processed conditions in the current study, it was found that a preaging at 170° C/ for 4h + 8% stretch strain and a final ageing of 170° C for 4 hours yielded optimal mechanical properties. From Table 4.15, the following mechanical properties were measured.

Yield Strength: 356.9MPa

Ultimate Tensile Strength: 364.5MPa

Uniform Elongation: 5.4%

Total Elongation: 10.2%

A significant increase in the mechanical properties of the alloy was also observed in the material under the same ageing conditions but deformed to a lower stretch strain level of 4%. Depending on the manufacturing application, whether a higher or lower degree of forming were to be applied, the deformation induced enhancements are still observed. 8% stretch gave the greatest response in this study and thus were preferentially utilised for further analysis in EBSD and TEM.

In the prescribed TMA processing condition of 150^{o} C/3h + 4% stretch + 190^{o} C/4.5h, the measured yield and ultimate tensile strengths were 323.5 and 342.1 MPa. The aDA processing of 170^{o} C/4h + 4% stretch + 170^{o} C/4h, there were significant increases in strength even at the same stretch strain level. The measured yield and ultimate tensile strength parameters were 337.9 and 349.3 MPa. Differences in the material response can be attributed to the preaging states described in section 5.3.2. in the first condition, the preaging was carried out to a far lower stage of the precipitation state which led to a lower storage of dislocations in the matrix as illustrated in the dislocation density measurements of Figure 5.15. Consequently, far less nucleation sites and precipitate-dislocation complexes were presented in the final ageing resulting in less-than-optimal precipitation in this step, the preaging had an obvious knock-on effect in the processing sequence of the alloy. In the second condition at 170^{o} C for 4 hours, the material was preaged to the half peak point described above. This half peak status gave a greater dislocation storage and a resultant enhanced final ageing precipitation.

Preaging conditions of 170^{o} C differed slightly to preaging at 150^{o} C comparatively in mechanical properties. In preaging, there was a greater strengthening achieved in the 150^{o} C conditions, however in the final aged material, the strengthening seen overall was superior in the samples aged at the 170^{o} C conditions.

Chapter 6. Conclusions and Further Work

6.1 Conclusions

From the current study, deformation induced enhancements to a 6xxx series aluminium alloy was achieved through development of a novel thermomechanical process comprised of a preaging, plastic deformation and final ageing step. The alloy displayed high strength and ductility as well as excellent extrudability. Significant strengthening of the Al-Mg-Si-Cu alloy present potential for advantageous industrial manufacturing applications in sheet part forming with great performance and economical benefit. Mechanical properties accumulated, and analytical data collected and presented in this study highlight interesting trends and findings concluded.

The age hardenable wrought aluminium alloy was DC cast and homogenised. Solution heat treatment at 550C for 30 minutes followed by immediate cold-water quenching was performed to maintain the super saturated solid solution state. Following this, the material was hot extruded into strips of dimensions: 200 x 50 x 3mm. Floor ageing post extrusion at room temperature for 48hrs was carried out to stabilise the material as well as providing a means of control. Natural ageing of the extruded material took place in this time.

This more stabilised state was termed the as-extruded state. Characterisation of the material in this state was performed to understand starting material properties, serving as a basis to identify material property enhancements henceforth. Hardness and tensile testing of the material averaged through 3 measurements each gave starting mechanical properties of 64 HV10, 88MPa Yield Strength, 211Mpa Ultimate Tensile Strength and a Uniform Elongation of 18.9%. Imaging and diffraction based analytical techniques revealed microstructural features of this starting state material showing recrystalised equiaxed grains which were homogeneous in morphology giving an average measured grain size of 85 microns.

In order to understand the deformation response of the alloy used in this study, plastic deformation of the material through various strain paths was performed in this as-extruded state. Stretching, rolling, a combination of stretching and rolling and Electromagnetic Pulse forming were used as main deformation modes in the study. Deformation evolution and structures formed varied between these strain paths, which were analysed using SEM EBSD techniques, highlighting key differences in dislocation densities generated between these strain modalities. Key mechanical property differences observed between stretching and rolling deformations modes were explained using orientation maps showing differences in the development in of texture components, namely cube and goss texture components. Combinational deformation modes of stretching and rolling did not display beneficial property enhancements.

Work hardening behaviour of the material in numerous conditions was determined using the power law relationship. A work hardening coefficient was calculated using the stress-strain curves achieved through tensile testing to form this analysis. Information of the stress strain relationship during plastic deformation helped in predicting material behaviour through the deformation processes.

EMPT formed samples deformed through the generated Lorentz forces from the electromagnetic energy presented a more complex deformation mode. Forming energies of 30KJ and 40KJ were studied. Automatic hardness maps were formed from a matrix of hardness measurements taken at regular spatial intervals across the bulk of the material. The colourful maps illustrated the complex deformation taking place in the sophisticated forming technique. The hardening was localised in specific regions experiencing tensile and compressive forces concentrated majorly in the bent regions of the sample. Hardening in other regions was not as pronounced.

Preaging kinetics performed at 150C, 170C and 190C aided in selecting preaging conditions. Hardness measurements were taken at intervals of 0.5h, 1h, 1.5h, 2h, 2.5h, 3h, 3.5h, 4h, 4.5h, 5h, 6h, 8h, 12h, 16h, 24h, 48h, 72h and charted, illustrating the hardening development of the material throughout artical ageing. Four main ageing conditions were found and investigated: 150^o C/ 8h, 150^o C/ 24h, 170^o C/ 2h, and 170^o C/ 4h. The half peak aged condition was described as the point of the ageing process at which the material was at half of the total hardness increase. Half peak was of particular interest due to the development of precipitation sequence which would have meaningful interactions with the dislocations introduced in the plastic deformation step of the thermomechanical treatment as well as retaining enough solute in solution to allow further effective precipitation in the final ageing step of the process. The 2 half peak conditions investigated in this study were 150^o C/ 24h, and 170^o C/ 4h. The remaining preaging conditions were in a lower aged state.

Precipitation development varied through the different preaging conditions including phase particles of atomic clusters, Guinier-Preston Zones and β'' particles altering defect interactions upon plastic deformation. Preaging induced precipitation increased the storage of dislocations cross all preaging conditions. Half peak conditions displayed a noticeably greater storage of dislocations structures in the crystals.

Final ageing of the material concluded the thermomechanical treatment achieving enhanced material property enhancements. Precipitate-dislocation complexes formed in the previous stages aided in beneficial precipitation nucleation and growth resulting in significantly improved mechanical properties.

A case study as an extension was conducted, displaying the effects of the achieved mechanical properties through the thermomechanical treatment. Mechanical properties investigated included crushability, bend performance and energy absorption, all parameters pertinent to engineering applications such as automotive bumper beams.

The overall conclusions gathered from this study are as given below.

1. A thermomechanical process comprised of a preaging step followed by low strain deformation and a final ageing was developed in a 6xxx series Al-Mg-Si-Cu alloy, leading to the achievement of considerable enhancement in the mechanical properties of the material.

2. Through mechanical testing it was discovered that stretching deformation at both strain levels tested demonstrated a greater efficacy in hardening the material than rolling deformation across all states of the thermomechanical process, including different pre-ageing conditions. The combinational strain deformation mode of both stretching and rolling did not display a significant advantage as part of the thermomechanical processing as compared to the other more simpler strain modes.

3. Microstructural development was strongly dependant on the parameters of the thermomechanical processing. The effects of these parameters such as preaging condition, strain path and strain level, on the structures formed in the heat treatable Al-Mg-Si-Cu alloy through the various steps determined the overall strengthening in the material through a mixture of strengthening mechanisms; precipitation strengthening and work hardening as well as interactions forming precipitate-dislocation complexes. Aforementioned microstructural changes lead to heterogenous nucleation and growth of second phase particles formed in the final ageing. The coalescence of these intragranular structures increased impedance of dislocation motion during mechanical testing.

4. Texture evolution varied noticeably between stretching and rolling deformation, explaining mechanical performance differences observed. In both deformation modes at both 4% and 8% strain levels there was a stark increase in the volume fraction of the cube {001}<100> texture component. However, the increase of this texture component is more pronounced in the stretching deformation mode across all strain levels. The volume fraction of the goss {110}<001> texture component is also noticeably greater in the stretching deformed samples also. Presentation of these texture components are dependent on the strain level applied, however.

5. A short preaging step as part of the thermomechanical processing, in combination with a low strain deformation step evoked a greater enhancement in the final properties as compared to a conventional thermomechanical process. The half-peak hardening point of the ageing kinetics was found to lead to the greatest preaging response with development of a significant number density of Guinier-Preston zones and the β'' main hardening phase.

6. Enhancement in preaging induced dislocation storage after deformation was observed and characterised by EBSD and TEM. The features of interactions between precipitation and dislocations and the formation of precipitation-dislocation complexes were dependent on the preaging conditions applied. Preaging sequence status achieved through different preaging durations lead to different formations of dislocation structures in the matrix with more developed precipitate particles in the material preaged to the half-peak point. The network of dislocation lines presented as being more bowed at the half-peak point as compared to the more underaged preaging status.

7. Preaging temperature differences were observed between 150^o C and 170^o C ageing conditions. Recipes constituting the 170^o C temperature attained a greater mechanical response. 170^o C/4h + 8% stretch + 170^o C/4h proved to be the peak thermomechanical condition, attaining a final yield strength of 356.9MPa, an ultimate tensile strength of 364.5MPa and a uniform elongation of 5.4%. Achieving considerable property improvements compared to similar alloys processed conventionally.

6.2 Further Work

Despite some short comings, the current work presents key findings, that are thought provoking and create opportunities for additional works to be carried out building upon said findings. The following chapter outlines relevant questions arising from the findings and explains further works that could be conducted to address them.

6.2.1 More Extensive Study of Preaging Kinetics

Due to time constraints, work in this study considered only a few preaging conditions. Although interesting findings were discovered, these were limited to these temperatures and times considered. Investigations into a greater range of conditions selected for preaging would be beneficial. Analysis of the preaging kinetics as well as characterising in depth the precipitation evolution would aid in a better, more informed understanding of finding an optimal thermomechanical treatment.

6.2.2 Interactions of Precipitates and Dislocations During Deformation

Some interactions between aging induced precipitations and dislocations introduced through plastic deformation were characterized in this study through EBSD and TEM techniques. Increases in dislocation storage were observed in samples preaged and deformed as well as differences in formed dislocation structures inside grains. More extensive study into these interactions causing these changes in dislocation storages would uncover the mechanisms of the evolution of these defects.

6.2.3 Precipitate Phase Characterisation

The current study considers the development of precipitate particles as related to the ageing kinetics and the widely known precipitation sequence. Interactions between these precipitates and dislocations formed in the crystals are identified using many analytical techniques. However, further TEM analysis of the precipitate phases formed throughout the crystal in the preaging step, including number densities and morphology can further uncover these interactions responsible for improved mechanical properties, aiding a greater understanding.

6.2.4 In-situ TEM Analysis of Final Ageing Precipitation

Although in this study, the preaging precipitation has been characterised in depth and its role in mechanical properties enhancements have been highlighted, final ageing phase particles and precipitation development are not as clearly understood. Dynamic development of precipitation in the final ageing step, especially morphology, nucleation and growth can be analysed through the use in-situ TEM to inform on the understanding of the material properties.

6.2.5 Manufacturing Specific Forming Processes

The current study works to understand the fundamental changes in material mechanical response as well as local and global microstructural changes in the material as a result of the applied thermomechanical process, specifically at low strain levels. However, in a manufacturing setting, very rarely are rolling and stretching used in the forming of automotive parts. Roll-bending, stretch-bending, press bending, and rotary stretch forming are more ubiquitously found in this area.

Developing and understanding of how these existing forming processes can be deployed as part of the process for attaining advantageous manufacturing induced properties is of great benefit for future engineering applications in the automotive industry.

6.2.6 Varied Alloy Systems Including 7xxx Series Aluminium Alloys

The improved mechanical performance obtained in this work, promoted by application of a novel thermomechanical process to the specific 6xxx series alloy achieved through microstructural development demonstrated significant potential for application in manufacturing forming processes with careful modifications to processing parameters.

The observed phenomena can be investigated in other 6xxx series alloy systems, notably AA6060 and AA6082 which are ubiquitously used in the automotive industry as well as other 7xxx series alloys in order to optimise and discover new, more superior mechanical performances of these alloys.

References

Abbass,R., et al, 2015. “Effect Of Precipitation Hardening on Mechanical Properties of Dissimilar Friction Stir Welded AA2024-T3 To AA7075-T73 Aluminium Alloys” 10.13140/RG

Abbott,T., et al, 2014. “Design With Magnesium- Alloys, Properties and Casting Processes”. Handbook Mech All Des Pg487-538

Andersen,S,J., et al, 1998. “The crystal structure of the B’’ phase in Al-Mg-Si alloys” Acta Mat. Vol46 Issue 9 Pg 3283-3298

Andersen,S,J., et al, 2007. “The crystal structure of the B’ phase in Al-Mg-Si alloys” Acta Mat 55, 3815-3823

Armstrong,R.W. 2016. “Hall-Petch Relationship: Use in Characterizing Properties of Aluminium and Aluminium Alloys*” Eng Mat Sci

Asgari,S., et al 1997. “Strain Hardening regimes and microstructural evolution during large strain compression of low stacking fault energy FCC alloys that form deformation twins” Met Mat Trans Vol28 Pg1781-1795

Ashby,M,F., 1970. “The deformation of plastically non-homogeneous materials” Phil Mag Vol21 Iss170 Pg399-424

Ashby,M,F., 2003. “The role of geometrically necessary dislocations in giving material strengthening” Scri Mat 48 (2003) 179-183

Askeland,D., et al, 2006 “The Science and engineering of materials – Sixth Edition” ISBN 0-495-29602-3

Awan.I., 2017. “Precipitates From Solid Solution” Jour Chem Soc Pak Vol39 Iss3 Pg319-336

Babu,S., 2022. “Thermo-Mechanical Processing”. Encyclopaedia of Materials: Metal and Alloys Vol.3 Pg 27-38

Banhart,j., et al 2011. “Kinetics of natural aging in Al-Mg-Si alloys studied by positron annihilation lifetime spectroscopy” Phys Rev B Vol83 014101

Bay,B., et al 1992. “Overview no. 96 evolution of F.C.C. deformation structures in poly-slip” Act Met Ma Vol 40 Iss2 Pg 205-219

Benedyk,J., 2010. “International Temper Designation Systems for Wrought Aluminium Alloys: Part II – Thermally Treated (T Temper) Aluminium Alloys”. Light Met Age Pg16-22

Bidin,N. 2012. “8 Arf Excimer Laser Annealing of Polycrystalline Silicon Thin Film”. 10.5772/52458.

Birol,Y., 2005. “Pre-aging to improve bake hardening in a twin-roll cast Al–Mg–Si alloy” Mat Sci Eng A Vol391 Pg175-180

Botha,J. 2016. “Extrusion Press Optimization”. Ind Sys Eng Vol438 Pg49-72 2263/62865

Burger,G,B., et al 1995. “Microstructural control of aluminium sheet used in automotive applications” Mat Char Vol35 Iss1 Pg23-39

Cahn,R,W., et al 1996. “Physical Metallurgy” ISBN 0 444 898751

Cai,Y,H., et al. 2013. “Microstructural Characteristics and Aging Response of Zn-containing Al-Mg-Si-cu Alloys”. Int J Miner Metall Mater 20, 659-664

Cai,Y,H., et al 2023. “Microstructure evolution and comprehensive properties of the extruded AA6008 crash-box profiles aged at 210 °C–220 °C” Jour Mat Res Tech Vol28 Pg3376-3384

Caillard., et al 2003. “Thermally activated mechanisms in crystal plasticity”. Vol 8 Pg3-433

Callister,W,D., 2007. “Materials Science and Engineering: An Introduction”. Book ISBN-13: 978-0-471-73696-7

Chen,X,M., et al. 2017. “Texture Evolution of 01570 Aluminium Alloy Sheet”. Mater Sci Eng. 170 012013

Chen,L., et al 2019. “Influence of aging treatment on the microstructure, mechanical properties and anisotropy of hot extruded Al-Mg-Si plate” Mat Des Vol182 107999

Chi,S. et al. 2020. “Influence Of Minor Zn Addition on Precipitation Behaviour and Intergranular Corrosion Properties of Al-Mg-Si Alloy”. Materials 2020, 13(3), 650

Chrominski,W., et al 2020. “Influence of dislocation structures on precipitation phenomena in rolled Al–Mg–Si alloy” Mat Sci Eng A Vol793 139903

Cho,C,H., 2021. “Effect of dislocation characteristics on electrical conductivity and mechanical properties of AA 6201 wires” Mat Sci Eng A Vol809 140811

Choundraj, J., et al. 2022. “Influence of misorientation angle and local dislocation density on B phase distribution in al 5xxx alloys” Sci Rep 12, 1817

Davoudi,K. 2018. “Plastic Deformation in Crystalline Materials” Acta Mat Vol1

Davoudi,K,M., et al 2018. “Dislocation evolution during plastic deformation: discrete dislocation dynamics study”. Jour Appl Phys Vol 123 Iss8

Derlet,P,M., et al 2002. “A first-principles study of the β” phase in Al-Mg-Si alloys” J Phys Cond Mat Vol14 Pg4011-4024

Diehl,J., et al 1956. “Tensile Deformation of Copper Single Crystals: I. Solidification Curves and Surface Appearances” Int Jour Mat Res Vol 47 Iss5 Pg331

Dieter,G,E., 1988. “Mechanical Metallurgy” McGrawHull, 3rd Ed ISBN 07-016890-3

Dillamore,I,L., et al, 1974. “The Mechanisms of Recrystallization in Cubic Metals with Particular Reference to Their Orientation-Dependence” Met Sc Vol 8 Iss1 Pg73-73

Djukanovic,G. 2018. “Latest Trends for Aluminium Demand in Automotive Industry” Auto Fab Treat Vol1 Pg19-25.

Djukanovic,G. 2019. “Aluminium Alloys in the Automotive Industry: A Handy Guide” Alu Pros Tech Vol1 pg3-6.

Doherty,R,D., et al 1998. “Current issues in recrystallization: a review”. Mat Sci Eng A Vol238 Iss2 Pg219-274

Edwards,G,A., Stiller,K., Dunlop,G,L., Couper,M,J., 1998. “The Precipitation Sequence in Al-Mg-Si Alloys”. Act Mat Vol.46 Issue 11, Pg.3893-3904

Esmaeili,S., et al 2003. “On the precipitation-hardening behaviour of the Al− Mg− Si− Cu alloy AA6111” Met Mat Trans A Vol34 Iss13 Pg 751-763

Estrin,Y., et al 2014. “Extreme grain refinement by severe plastic deformation: A wealth of challenging science” Act Mat Vol61 Iss3 Pg782-817

Fang,X., Song,M., Li,K., Du,Y., 2010. “Precipitation Sequence of an Aged Al-Mg-Si Alloy”. Journal Of Mining and Metallurgy Section B Metallurgy 46 (2)

Ferdynus,M., et al. 2019. “Numerical Crush Analysis of Thin-Walled Aluminium Columns with Square Cross-Section and a Partial Foam Filling”. Adv Sci Tech. Vol 13(3) pg 144-151

Fleck,N,A., 2002. “The role of geometrically necessary dislocations in giving material strengthening” Scr Mat Vol 48 Iss2 Pg 179-183

Field,D,P., 2005. “Analysis of Local Orientation Gradients in Deformed Single Crystals” Ultramicrosc. 103 (2005) 33-39

Friedman,P,A., et al 2002. “Failure of Al-Mg-Si alloys in bending” Pract Fail Ana Vol2 Iss1 Pg33-42

Gable,B,M., et al 2001. “The role of plastic deformation on the competitive microstructural evolution and mechanical properties of a novel Al–Li–Cu–X alloy” Li Met Vol1 Pg1-14

Gallet,J., et al. 2023. “Experimental measurement of dislocations density in metallic materials; A quantitative comparison between measurement techniques (XRD, R-ECCI, HR-EBSD, TEM)”. Mt Char Vol 199. 112842

Galindo-Nava,E,I., et al 2012. “Dislocation annihilation in plastic deformation: II. Kocks-Mecking Analysis” Act Mat Vol60 Iss6-7 Pg2615-2624

Gonostyrev,Y. 2015. “Misfit Stabilized Embedded Particles in Metallic Alloys”. Phsy. Chem Chem. Phys., 17,27249-27257.

Haynes 2020. “Welding and Fabrication – Effect of cold work on hardness applicable to high temperature alloys” Hay. Int. Inc. Vol1 Iss1 Pg8-9

Helmenstine, A. 2019. “Aluminium or Aluminium Alloys”. Alloying: Understanding the basics. Pg351-416

Hirsch,J., et al 1988. “Overview No. 76: Mechanism of deformation and development of rolling textures in polycrystalline FCC metals — I. Description of rolling texture development in homogeneous Cu-Zn alloys” Act Mat Vol36 Iss11 Pg2863-2882

Hodžić,E., et al 2023. “Influence of natural aging on the formability of Al-Mg-Si alloy blanks” Jour Man Pros Vol94 Pg228-239

Hollomon,J,H., 1945. “Tensile Deformation” Trans Met Soc AIME Vol162 Pg268-290

Holmestad,R., et al 2010. “Precipitation in 6xxx Aluminium Alloys” Jap Ins Lig Met Pg30-39

Hu,R., et al, 2010. “Dispersoid formation and recrystallization behaviour in an Al-Mg-Si-Mn alloy”. Journal of Materials Science & Technology 26 (3), 237–243

Hull and Bacon 2011. “Introduction to dislocations” Pg229-236

Humphreys,F,J., et al 2001. “Orientation Averaging of Electron Backscattered Diffraction Data” J. Microsc. 201 (2001) 50

Humphreys,F,J., 2004. “Recrystallization and related annealing phenomena” Sec Ed Vol1

Jackson,A.G. 2019. “Slip Systems. In: Handbook Of Crystallography” Pg83-88

Jiang,H,W., et al, 2014. “Deformation behaviour and microstructure evolution of pure Cu subjected to electromagnetic bulging” Mat Sci Eng A Vol593 Pg127-135

Jiang,G,D., et al 2022. “Effect of over-aging on the microstructure, mechanical properties and crashing performance of thin-walled Al–Mg–Si–Cu alloy profiles” Jour Mat Res Tech Vol21 Pg3074-3085

Jin,Y., et al, 2021. “Enhanced formability and hardness of AA2195-T6 during electromagnetic forming”. Jour All Comp 890 161891

Kallend,j., et al 1984 “Orientation dependence of stored energy of cold work in 50% cold rolled copper” Met Sci Vol18 Iss7 Pg381-386

Keyhani,A., et al 2018. “Dislocation-precipitate interaction map” Comp Mat Sci Vol141 Pg153-161

Kocks,U,F,. et al 1976. ”Laws for work hardening and low temperature creep” Jour Eng Mat Tech Vol98 Iss1 Pg76-85

Kocks,U,F,. et al 2003. “Physics and phenomenology of strain hardening: the FCC case” Prog Mat Sci Vol48 Pg171-273

Kohar,C,P., et al 2015. “Effects of elastic-plastic behaviour on the axial crush response of square tubes” Thi Wall Str Vol93 Pg64-87

Kopeliovich,D. 2012. “Plastic Deformation – Slip mechanism of plastic deformation” Sub-tech Pla. Def. Pg 1 Fig1

Kuhjmann-Wilsdorf,D., et al 1989. “Theory of plastic deformation: - properties of low energy dislocation structures” Mat Sci Eng A Vol113 Pg1-41

Kuhjmann-Wilsdorf,D., et al 1991. “Geometrically necessary, incidental and sub grain boundaries” Met Mat Vol25 Iss7 Pg1557-1562

Lai,Y,X., et al 2020. “Structures and formation mechanisms of dislocation-induced precipitates in relation to the age-hardening responses of Al-Mg-Si alloys” Jour Mat Sci Tech Vol41 Pg127-138

Landau,P., et al 2009. “Evolution of dislocation patterns in FCC metals”. IOP Conf Ser Mater Sci Eng 3 012004

Langford,G., et al 1969. “Strain hardening of iron by severe plastic deformation” ASM Trans Quart Vol62 Iss3 Pg623-638

Lausch,J., et al. 2020. “Crush Testing Approach for Flat-Plate Fibrous Materials”. Comp Part B Eng. Vol 200(1). 108333

Les,P., et al 1997. “Hardening and strain rate sensitivity in stage IV of deformation in F.C.C. and B.C.C. metals” Mat Sci Eng A Vol234-236 Pg453-455

Li,G,A., et al, 2021. “Effect of Pre-Stretch on the Precipitation Behaviour and the Mechanical Properties of 2219 Al Alloy” Mat Vol14 Iss9

Li,S 2018. “Introduction To Micromechanics and Nano Mechanics (2nd Edition)”. ISBN 978-981-281-413-5

Li, Y., Bushby,A,J., Dunstan,D,J., 2016. “The Hall-Petch Effect as a Manifestation of The General Size Effect”. Proc Math Phys Eng Sci Vol.472, Issue.2190, 20150890

Li,Z,G., et al, 2014. “Deformation texture evolution of pure aluminium sheet under electromagnetic bulging” Jour All Comp Vol589 Pg164-173

Liu,H., et al, 2005. “Pre-aging and microstructures properties on 6000 series aluminium alloys for automotive body sheets” Chin Non-fer Met Vol15 Pg270-276

Liu,H., 2007. “Effects of Different Tempers on Precipitation Hardening of 6000 Series Aluminium Alloys” Trans. Non-fer Met Soc China 17 (2007) 122-127.

Liu,M., et al 2015. “Early stages of solute clustering in an Al–Mg–Si alloy” Act Mat Vol91 Pg355-364

Maipal,S. 2017. “Solidification Mechanisms and Phase diagrams – stages of solidification process” Man Ac Hig Edu Pg12 Fig1

Maghami,S,A., et al 2013. “Effect of corner bluntness on energy absorbing capability of non circular metallic tubes subjected to axial impact” Int Jour Eng Trans B App Vol26(8) Pg 875-884

Mamalis,A,G., et al 2008. “Static axial collapse of foam-filled steel thin walled rectangular tubes: experimental and numerical simulation” Int Jour Cras Vol13(2) Pg 117-126

Marioara,C,D., et al 2005. “The influence of alloy composition on precipitates of the Al-Mg-Si system” Met Mat Trans A Vol36 Pg691-702

Mathers,G. 2020. “Heat Treatment of Welded Joints Part 4- Precipitation or Age Hardening” Figure 1

Miller,W,S., et al 2000. “Recent development in aluminium alloys for the automotive industry” Mat Sci Eng A Vol280 Pg37-49

Mirzakhani,B., et al 2015, “Combination of sever plastic deformation and precipitation hardening processes affecting the mechanical properties in Al–Mg–Si alloy’ Mat Des Vol68 Pg127-133

Morii,K., et al 1985. “Development of shear bands in F.C.C. single crystals” Act Met Vol33 Iss3 Pg379-386

Motra,B., et al, 2014. “Assessment of strain measurement techniques to characterise mechanical properties of structural steel”. Eng Sci and Tech Int Jrnl Vol 17(4) Pg260-269

Mortsell,E,A., 2019. “The Effect of Elastic Strain and Small Plastic Deformation on Tensile Strength of a Lean Al-Mg-Si Alloy” Metals (2019), 9(12), 1276.

Muransky,O., et al 2019 “On the measurement of dislocations and dislocation substructures using EBSD and HRSD techniques” Act Mat Vol175 Pg297-313

Murayama,M., et al 1999. “Pre-precipitate clusters and precipitation processes in Al–Mg–Si alloys” Act Mat Vol47 Iss5 Pg1537-1548

Nabarro,F,R,N., et al 1964. “The plasticity of pure single crystals” Adv Phys Vol13 Iss50 Pg193-323

Nakashima,P,N,H., et al, 2018. "The Crystallography of Aluminium and Its Alloys" Encyclopaedia of Aluminium and Its Alloys Pg488 – 586

Nasiruddin,M,S., et al 2017. “A Review of energy absorption of automotive bumper beam” Int Jour App Eng Res ISSN 0973-4562 Vol12(2) Pg 238-245

Nelson,S. 2015. “Deformation – Stress and Strain: Tensional, Compressional and Shear Stress” Phys. Geo. Pg1 Fig3

Nye,J,F., 1953. “Some geometrical relations in dislocated crystals”. Act Met Vol1 Iss2 Pg15-162 iSSN 00016160

Osten,J. 2019. “Development Of Precipitation Hardening Parameters for High Strength Alloy Aa7068”. Materials 2020, 13(4), 918

Osuch,P., et al 2018. “Impact of the Direct Ageing Procedure on the Age Hardening Response of Al-Mg-Si 6101 Alloy” Mat Vol11 Iss7 1239

Phaniraj,C. 2017. “Strengthening Mechanism or Precipitation Hardening – Orowan Bowing and Particle Cutting” Ind. Gan. Cent. Ato. Res. Pg3 Fig1

Polmear 1995. “Light Alloys: Metallurgy of the Light Metals (Metallurgy and Materials Science)”. ISBN 10: 0340632070

Porter,D,A., et al 2009. “Phase Transformations in Metals and Alloys, 3rd ed” CRC Press: Boca Raton ISBN: 9780423112256

Power,N 2017. “Aluminium Alloys – Characteristics and Uses” Azo Mat Pg1 Fig 2

Raabe,D 2020. “Aluminium Alloys – Historical facts about Aluminium and its alloys” Pro & Pow Vol7 Iss2 Pg103-119

Rajmohan,N., et al, 2000 “A new model for recrystallization of heavily cold-rolled aluminium using orientation-dependent stored energy” Act Mat Vol48 Iss13 Pg3327-3340

Rao,C. 2015. “Influence Of Tool Pin Profile on Microstructure and Corrosion Behaviour of AA2219 Al-cu Alloy Friction Stir Weld Nuggets”. Defence Technology Vol. 11, Issue 3, Pg. 197-208

Rappaz,M 2010. “Deformation Of Solids”. Numerical Modelling in Materials Science and Engineering, Pp. 287-364

Ray,R,K., 1986. “Orientation distribution function analysis of texture in a dual-phase steel” Mat Sci Eng Vol77 Pg169-174

Reed,R,P,. 1972. “Aluminium 2. A review of the deformation properties of high purity aluminium and dilute aluminium alloys” Cryo Gui Pg259-291

Reiso,O., 2004. “Extrusion of Al-Mg-Si alloys”. Materials Forum. Vol. 28. Citeseer, pp. 32–46

Rezvanian,O., et al 2007. “Statistically stored, geometrically necessary and grain boundary dislocation densities: microstructural representation an modelling” Pro R Soc A 463 2833-2853

Rivera-Diaz-del-Castillo,P,E,J., et al 2012. “Dislocation annihilation in plastic deformation: I. Multiscale irreversible thermodynamics” Act Mat Vol60 Iss6-7 Pg2606-2614

Rochet,C. et al. 2020. “Influence Of Equal-channel Angular Pressing on the Microstructure and Corrosion Behaviour of A 6xxx Aluminium Allot for Automotive Conductors”. Corr Sci Vol. 166, 108453

Rollet,A,D., et al 1988. “Strain Hardening at large strains in aluminium alloys” ISBN 8727455

Rupert,T. 2010. “Enhanced Solid Solution Effects on the Strength of Nanocrystalline Alloys”. Acta Mat, 59, 1619-1631

Ryen,O., etg al 2006. “Strengthening mechanisms in solid solution aluminium alloys” Met Mat Trans A Vol37 Pg1999-206

Ryen,O., 2015. “Precipitation, Strength and Work Hardening of Age Hardened Aluminium Alloys” Mat Sci and Eng 89 (2015) 012013.

Sabirov,I., et al 2013. “Nanostructured aluminium alloys produced by severe plastic deformation: New horizons in development” Mat Sci Eng A Vol560 Pg1-24

Saito,B. et al. 2014. ““HAADF-STEM And DFT Investigations of the Zn-containing’’ Phase in Al-Mg-Si Alloys””. Acta Mat Vol. 78, Pg. 245-253

Saga,M., et al 1996. “Effect of Pre-Aging Temperature on the Behavior in the Early Stage of Aging at High Temperature for Al-Mg-Si Alloy” Mat Sci For Vol217-222 Pg 821-826

Sathiyamoorthi,P. 2017. “Hardness As a Function of Grain Size Depicting the Hall-Petch Equation”. Materials And Design 134

Scamans,G. 2020. “Aluminium Automotive Sheet” Sur Int Ana Vol45 Iss10 Pg1430-1434

Schaeffler,D 2023. “Metal Properties: Strain-Hardening Exponent (n-Value)” Pre-Met Form Assos Vol92 2169018800

Sekine,K,. et al 1981. “The transition of torsional deformation textures in FCC metals” Proc 6th Int Conf Text Mat Pg396-407

Seumer,V., et al 1993. “Cold working in stages IV and V of FCC metals – I. Experiments and Interpretation” Act Met Mat Vol41 Iss2 Pg577-588

Shen,C,H., et al 2007. “Effect of pre-straining on the natural ageing and artificial ageing of an Al-Mg-Si alloy AA6022” Can Met Quart Vol46 Iss1 Pg65-74

Sheppard,T. 1999. “Extrusion Of Aluminium Alloys”. ISBN 978-1-4419-4728-4

Smallman,R.E. 2007. “Physical Metallurgy and Advance Materials”. Elsevier. ISBN 978-0-7506-6906-1

Song,Y,Q., et al 2006. “Theoretical and experimental standardization of strain hardening index in tensile deformation” Act Met Vol42 Pg673-680

Sparks,D., 2015. “Types of solids – lattice planes in cubic structure”. Cav o’ Chem Pg1 Fig4

Starink,M,J., et al. 2003 “A model for the yield strength of overaged Al-Zn-Mg-Cu alloys”. Act Mat Vol 51 Issue 17 Pg 5131-5150

Starke,E,A., Staley,J,T., 1996. “Application of modern aluminium alloys to aircraft”. Prog Aero Sci Vol 32(2–3) Pg131-172 ISSN 0376-0421

Takaki,Y., et al 2014. “Effects of Natural Aging on Bake Hardening Behaviour of AlMgSi Alloys with Multi-Step Aging Process” Mat Trans Vol55 Iss8 Pg1257-1265

Tanwir,A. et al. 2017. “Review On Aluminium and Its Alloys”. International Journal of Advanced Technology in Engineering and Science, pg. 278-294

Tian,N., et al 2010. “Pre-ageing treatment of Al-Mg-Si aluminium alloy sheet for automotive panels in T4 temper” J Mat Met Vol9 Pg137-142

Tian,N., et al 2019. “Prediction of the Work-Hardening Exponent for 3104 Aluminum Sheets with Different Grain Sizes” Mat Bas Vol12 Iss15 Pg2368

Uan,J,Y., et al 2006. “Precipitate evolution in underaged Al–Mg–Si alloy during thermal cycling between 25 °C and 65 °C” Mat Sci Eng A Vol419 Iss1-2 Pg98-104

Verlinden,B., Cahn,R.W., 2007. “Thermo-Mechanical Processing of Metallic Materials”. Pergamon, London. ISBN: 9780080444970

Wang,Q. 2018. “Coherent precipitate strengthening in compositionally complex alloys: a review”. Entropy, 20(11): 878

Wang,X. 2019. “Relationship among grain size, texture and mechanical properties of aluminums with different particle distributions”. Mat Sci and Eng A Vol.753 Pg. 122-134

Wang,Z., et al 2014. “Improving the strength and ductility of Al–Mg–Si–Cu alloys by a novel thermo-mechanical treatment” Mat Sci Eng A Vol607 Pg313-317

Wearing,D 2018. “The difference between hot rolled and cold rolled steel” Ste Lim Str Ste Fab Pg2 Fig1

Werinos,M., et al 2016. “Hardening of Al–Mg–Si alloys: Effect of trace elements and prolonged natural aging” Mat Des Vol107 Pg257-268

Wilm,A., 1911. “Beginnings of Duralumin” Metallurgie, 8 225–227

Yan,W., 2006. “Theoretical investigation of wear-resistance mechanism of superelastic shape memory alloy NiTi” Mat Sci Eng A Vol427 Iss1-2 Pg348-355

Yang,M et al 2020. “Quantified contribution of β” and β′ precipitates to the strengthening of an aged Al–Mg–Si alloy” Mat Sci Eng A Vol774 138776

Yang,Z., et al 2019. “Effect of pre-ageing on natural secondary ageing and paint bake hardening in Al–Mg–Si alloys” Mat Vol7 100413

Yang,Z., et al 2021. “Natural and artificial ageing in aluminium alloys – the role of excess vacancies” Act Mat Vol215 117014

Yoshida,K., et al 2007. “The effects of texture on formability of aluminum alloy sheets” Act Mat Vol55 Iss13 Pg 4499-4506

Yu,Q., et al 2013. “The effect of size on dislocation cell formation and strain hardening in aluminium” Phi Mag Vol94 Iss18

Zecevic,M., et al 2015. “A dislocation density based elasto-plastic self-consistent model for the prediction of cyclic deformation: Application to AA6022-T4” Int Jour Plas Vol72 Pg200-217

Zehetbauer,M., 1993. “Cold working in stages IV and V of FCC metals – II. Model fits and physical results” Act Met Mat Vol41 Iss2 Pg589-599

Zhao,Q. 2013. “The effect of silicon on the strengthening and work hardening of aluminium at room temperature”. Mat Sci and Eng A Vol 563 Pg. 147-151

Zhi-Xiu,W. et al. 2012. “Effect of Cu content on microstructures and properties of Al- Mg-Si-Cu alloys” Phys Eng Met Mat Pg143-151

Zhong,H., et al, 2017. “Influence of pre-ageing on the stretch formability of Al-Mg-Si automotive sheet alloys” Mat Sci Eng A Vol697 Pg79-85

Zhu,C., et al, 2016. "Determination of geometrically necessary dislocations in large shear strain localization in aluminium". Act Mat Vol 118 Pg383-394 ISBN 13596454

Zi,Y., et al. 2019. “Effect of pre-ageing on natural secondary ageing and paint bake hardening in Al–Mg–Si alloys” Mat Vol7 100413

Appendix

Case Study

As an extension, a case study was conducted to observe the effects of the enhanced mechanical properties achieved through the aDA thermomechanical processing. The main objecting of the study was to attain improvement in the mechanical behaviour of the crush alloy for applications in automotive bumper beam performance. Parameters such as crushability, bend performance and energy absorption were analysed to understand the strength to ductility compromise.

There were 3 conditions that were tested, and they were described using the following nomenclature: TMA1, TMA2 and TMA3. The conditions for each are displayed below.

TMA1: 150° C/3h + 8% stretch + 190° C/1.5h

TMA2: 150° C/3h + 10% stretch + 190° C/4.5h

TMA3: 170° C/4h + 4% stretch + 170° C/4h

Tensile Testing

Table A shows the average result for the varying conditions. The condition with the lowest performance was TMA2. The final yield and ultimate strengths achieved were the lowest as well as having the least ductility of all the samples measured. The recipe corresponded to the best ageing recipe achieved for the 150° C temperature, but the deformation level was increased to observe it's effect. No increase in strength was seen as a result of the increased strain level and it actually proved detrimental in the ductility of the material when compared to the other TMA conditions tested.

Table A. Tensile Test results show for all thermomechanical conditions.

Temper	Strain Mode	Strain Level (%)	Yield Strength (MPa)	Tensile Strength (MPa)	Uniform Elongation (%)	Total Elongation (%)
TMA1	Stretch	8	333.3	347.3	7.9	12.1
TMA2	Stretch	10	325.4	338.4	7.1	11.0
TMA3	Stretch	4	338.3	352.2	7.9	11.6

TMA1 and TMA 3 used the same ageing and deformation recipes described before. Cross examining the final results measured with those in Tables 4.13 and 4.14, the readings for strength and ductility fall within an acceptable range.

The strain level used in TMA 3 was 4% as compared to the 8% used in TMA1 yet the final strengths achieved are comparable. The preaging condition of 170^{o} C gave a better preaging effect and did not require as large of a strain level to achieve comparable mechanical properties.

Crush Testing

Using the die displayed in section 3.8, crush samples were extruded to test the crush index of the material. The specimen, tested through a crushing test were then analysed visually and the energy absorbed was derived from the raw data.

Figure A. Crush profile of an AA6xxx series alloy following a thermomechanical treatment of 150^{o} C/3h + 8% stretch + 190^{o} C/1.5h.

Figure A show the sample following the crush test. The material tends to fold into 3-4 central folds with numerous crumples to the side of the sample. The characteristic folds and crumples formed give information about the nature of the crush performance of the material. From visual analysis, the sample has only 3 minor cracks on the right-hand side with a quite uniform and symmetrical crumpling across the entire sample. The smooth profile formed indicates a ductile response in the material.

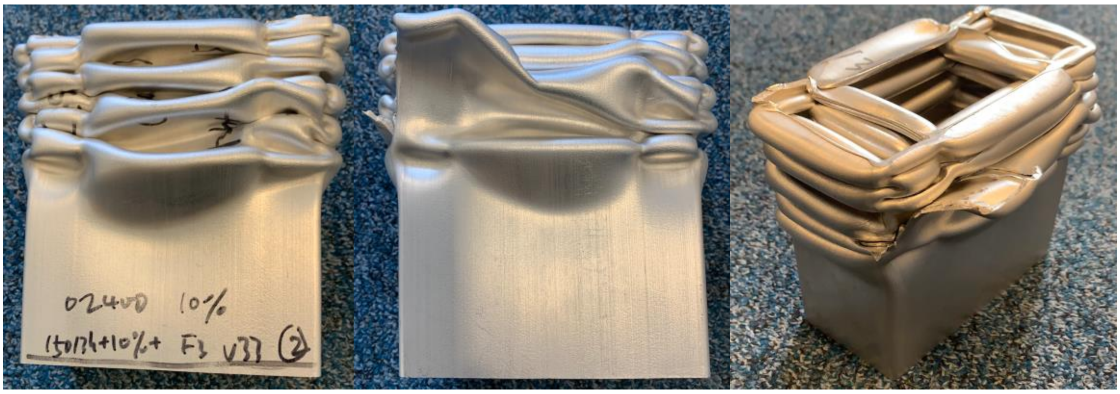

Figure B. Crush profile of an AA6xxx series alloy following a thermomechanical treatment of 150° C/3h + 10% stretch + 190° C/4.5h.

The crushing failure in the samples of the TMA2 condition differs to that seen in Figure A. there is a significant edge split on the back left side of the specimen. A total of 8 minor cracks are also be identified along the surface of the specimen. This failure corresponds to the decreased ductility seen in the tensile results of Table A.

Figure C. Crush profile of an AA6xxx series alloy following a thermomechanical treatment of 170° C/4h + 4% stretch + 170° C/4h.

Similarly, to the TMA1 condition, there is a uniform crumpling in the specimen of TMA3, with no major cracks. There are, however, visually more minor cracks on the sample surface. The crumpling zone is also not as symmetrical as that seen in the TMA1 specimen.

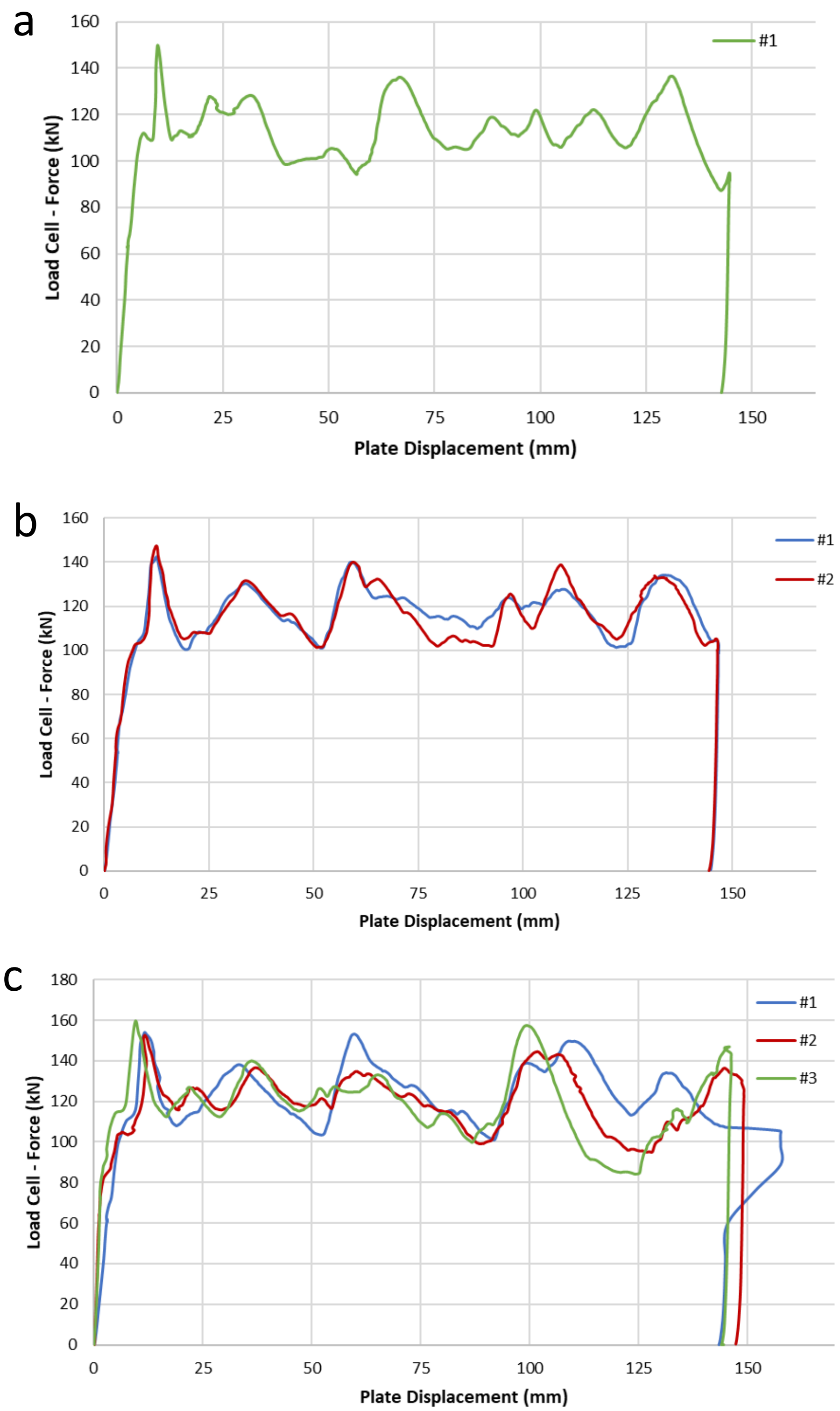

Figure D. Crush load curve for the TMA3 specimens of the AA6xxx series crush alloy. (a) TMA1 (b) TMA2 (c) TMA3.

Figure D displays the different charts collected from the crush tests of all specimens. These charts can be used to determine the energy absorption (EA) behaviour of the material. The EA is calculated from the area under the graphs. Average values for EA are given for conditions where more than one samples are tested. From the results, TMA3 had the greatest energy absorption with an average value of 18581.6 KN*mm. TMA1 and TMA2 had calculated EA values of 17069.9JN*mm and 16557.8 KN*mm respectively.

TMA showed the greatest energy absorption as well as also having the greatest strength out of all investigated samples. This shows the greatest strength-ductility compromise achieved in the material. the use of a lower strain level in this recipe aided in retaining as much ductility as possible.